

Iron, Cobalt, and Nickel
Metalloboranes:
Reactivity, Catalysis, N₂
Activation and
Stabilization of Reactive
N₂H_x Ligands

Thesis by
Mark Allen Nesbit
In Partial Fulfillment of the Requirements for
the degree of
Doctor of Philosophy



CALIFORNIA INSTITUTE OF TECHNOLOGY
Pasadena, California
2018
(Defended: January 8, 2018)

© 2018

Mark Allen Nesbit
All rights reserved

ACKNOWLEDGEMENTS

To the best of my knowledge I've always enjoyed learning and working with my hands. For the last roughly 5.5 years as a graduate student I've had the unique privilege of being able to fill my days with these two things, and while these years have without a doubt been the most challenging, frustrating, and difficult of my life they've also been among the most exciting and rewarding and as much as I am ready to move on, I am genuinely going to miss this place. Having said all that the person to whom I owe the greatest debt of gratitude is Jonas for allowing me to work for and with him in his lab. Jonas has given me a great deal of freedom over the years and allowed me to tinker and pursue chemistry and ideas in which I was personally interested. I've always respected him and the advice he gives (even on those occasions when I didn't listen to him) and I know that working with him and the rest of his lab has made me a better chemist and I am eternally grateful for his guidance. Mentorship, however, is not limited to one's advisor and I feel lucky to have Jonas' input supplemented by an excellent committee which included Profs. Jackie Barton, Greg Fu, and Theo Agapie. I can honestly say that I never walked away from a meeting with my committee without having learned something new, whether it be about chemistry, effective presentation, or just an amusing anecdote. I found their feedback helpful and constructive and am grateful for the time and effort they have devoted to my education.

I think it is also important to acknowledge the people who helped me get into graduate school, my undergraduate advisor Prof. Greg Girolami and the two graduate students (now professors) in his lab whom I work most closely with Profs. Scott Daly and Brian Bellott. These three are the ones who taught me how to use a Schlenk line and a glove box, how to solve a crystal structure, and countless other things that any synthetic inorganic chemist must know. They were the ones who exposed me to the world of synthetic inorganic chemistry with which I fell in love and words cannot sufficiently express how much I owe to them.

I must also thank all of my coworkers past and present (both at Caltech and UIUC). At some point or another I've received a helpful suggestion, insightful comment, or learned something new by just quietly listening from everyone I've worked with in lab and want to thank all my fellow students as a whole for their part in my education. Dan Suess deserves special recognition here for getting me started on a project and showing me around the lab when I first joined and for co-authoring the first paper of my graduate career. In a similar vein I must also thank Paul Oyala for all his help on the EPR studies discussed in Chapter 4. He's devoted a lot of time to teaching me about pulsed-EPR

measurements and I would not have been able to do the majority of that work without his expertise. I must also thank Mike Takase and Larry Henling in the X-ray crystallography facility for teaching me how to mount crystals and all their help with solving structures.

Finally, I have to thank all the people who made my life outside of lab better. I'll start with the people whom I have lived with for the past ~4.5 years in the ramshackle abode we affectionately refer to as "The Lake House": Paul Walton, Trevor Del Castillo, Ben Matson, JingXin Liang, and Jenna Bush. It's been a wild ride these past few years and I'm going to miss all the shenanigans. I'd also like to thank Beau Pritchett and the rest of our band (The 818s) and anyone who came to watch us play or jam with us. Playing music has been a big part of my life since I was very young and some of the most fun I've had these past few years has been had sweating and screaming in the music room with you all and my only regret is that we couldn't have spent more time playing together. My other hobby which I didn't indulge nearly enough was camping and hiking and I want to thank all the people who ventured out into the wilderness with me (especially Kareem Hannoun and Josh Buss), it was always a blast. I also want to thank my family especially my parents for their unwavering support and encouragement. Lastly I want to give an additional special thanks to JingXin Liang, who has been a wonderful concert buddy and partner whose love and support have played an important part in keeping me sane. She's put up with a lot of me at my grouchiest after working long hours and coming home from lab in the middle of the night (and on a few occasions not at all) and I am forever grateful for her patience. There are probably more people who deserve thanks, certainly there are a number of regulars at "The Lake House" who are great friends that I've not listed here by name because this is getting long and I've been rambling for a while... so to anyone I forgot or didn't mention thanks for being you and for having a beer or seven with me all those times, you're pretty all right.

ABSTRACT

The reactivity of Fe and Co compounds supported by a bisphosphinoborane (DPB) ligand ($[(\text{DPB})\text{Fe}]_2(\text{N}_2)$ and $(\text{DPB})\text{Co}(\text{N}_2)$) towards E-H bonds (E = C, N, S, O, Si) is reported along with the catalytic hydrosilylation of ketones and aldehydes. The Fe and Co compounds displayed a mix of 1-electron and 2-electron chemistry. In some cases $[(\text{DPB})\text{Fe}]_2(\text{N}_2)$ and $(\text{DPB})\text{Co}(\text{N}_2)$ facilitated oxidative addition of the E-H bond across the M-B interaction, and in others evolution of H_2 giving a 1-electron oxidized complex of the general form $(\text{DPB})\text{M}(\text{E})$ was observed. The reaction of Ph_2SiH_2 with $(\text{DPB})\text{Co}(\text{N}_2)$ was found to be reversible, similar to the previously reported related nickel complex $(^{\text{Ph}}\text{DPB}^{\text{Mes}})\text{Ni}$. The reactivity of these Fe and Co compounds is compared to previously reported Ni compounds supported by a similar ligand which catalyze olefin hydrogenation and hydrosilylation of substituted benzaldehydes.

The synthesis and metalation with nickel of two new variants of the DPB ligand ($\text{DP}^*\text{B}^{\text{Ph}}$ and $\text{DP}^*\text{B}^{\text{Mes}}$) is described. The primary modification introduced in $\text{DP}^*\text{B}^{\text{Ph}}$ and $\text{DP}^*\text{B}^{\text{Mes}}$ is the incorporation of a tertiary amine moiety into the secondary coordination sphere. This was done with the hypothesis that the amine moiety might act as a proton shuttle and facilitate proton reduction or hydrogen oxidation electrocatalysis. The process of screening these compounds for activity as proton reduction and hydrogen oxidation catalysts is also discussed. Additionally, the stoichiometric reactivity of $[(\text{DP}^*\text{B}^{\text{Ph}})\text{Ni}]_2(\text{N}_2)$ and $(\text{DP}^*\text{B}^{\text{Mes}})\text{Ni}(\text{N}_2)$ with H_2 was studied. We observed that $[(\text{DP}^*\text{B}^{\text{Ph}})\text{Ni}]_2(\text{N}_2)$ slowly decomposed to an unidentified mixture of products while $(\text{DP}^*\text{B}^{\text{Mes}})\text{Ni}(\text{N}_2)$ dimerized to form a phosphine bridged Ni-borohydride dimer $[(\text{DP}^*\text{B}^{\text{Mes}}\text{H})\text{Ni}]_2$. $[(\text{DP}^*\text{B}^{\text{Ph}})\text{Ni}]_2(\text{N}_2)$ and $(\text{DP}^*\text{B}^{\text{Mes}})\text{Ni}(\text{N}_2)$ were also tested as precatalysts for olefin hydrogenation and found to be less active than their previously reported counterpart $(^{\text{Ph}}\text{DPB}^{\text{Mes}})\text{Ni}$. $[(\text{DP}^*\text{B}^{\text{Ph}})\text{Ni}]_2(\text{N}_2)$ and $(\text{DP}^*\text{B}^{\text{Mes}})\text{Ni}(\text{N}_2)$ correspondingly showed no activity for hydrogenation of polar substrates such as ketones, aldehydes, or CO_2 .

Lastly, the synthesis of a new trisphosphinoborane ligand ($^{\text{Ar}}\text{P}_3\text{B}$) with bulky aryl substituents on the phosphines and its metalation with Fe is described. The anionic- N_2 adduct $[(^{\text{Ar}}\text{P}_3\text{B})\text{Fe}(\text{N}_2)][\text{Na}(12\text{-C-4})_2]$ was observed to react with H^+ sources to generate the first observed parent iron-diazenido $(^{\text{Ar}}\text{P}_3\text{B})\text{Fe}(\text{NNH})$ and an iron-hydrazido(2-) $[(^{\text{Ar}}\text{P}_3\text{B})\text{Fe}(\text{NNH}_2)]^+$. $[(^{\text{Ar}}\text{P}_3\text{B})\text{Fe}(\text{NNH}_2)]^+$ was found to have similar spectroscopic properties to the previously reported $[(\text{TPB})\text{Fe}(\text{NNH}_2)]^+$. A thorough characterization of $[(^{\text{Ar}}\text{P}_3\text{B})\text{Fe}(\text{N}_2)][\text{Na}(12\text{-C-4})_2]$, $(^{\text{Ar}}\text{P}_3\text{B})\text{Fe}(\text{NNH})$, and $[(^{\text{Ar}}\text{P}_3\text{B})\text{Fe}(\text{NNH}_2)]^+$ by a variety of continuous wave and pulsed ERP techniques is presented along with ^{57}Fe Mössbauer data. The new $(^{\text{Ar}}\text{P}_3\text{B})\text{Fe}$ system was also canvassed for activity as a

catalyst for conversion of N_2 to NH_3 and found to yield substoichiometric amounts of NH_3 in the presence of KC_8 and $\text{HBAr}_{24}^{\text{F}} \cdot 2\text{Et}_2\text{O}$ while no NH_3 was observed using CoCp^*_2 and $[\text{H}_2\text{NPh}_2][\text{OTf}]$.

PUBLISHED CONTENT AND CONTRIBUTIONS

This dissertation contains material adapted with permission from the following published work(s):

E–H Bond Activations and Hydrosilylation Catalysis with Iron and Cobalt Metalloboranes.

Nesbit, M. A.; Suess, D. L. M.; Peters, J. C.; *Organometallics*, **2015**, *34*, 4741-4752.

DOI: 10.1021/acs.organomet.5b00530

M.A.N. participated in data collection, analysis, and manuscript preparation.

TABLE OF CONTENTS

Acknowledgements.....	iii
Abstract	v
Published Content and Contributions.....	vii
Table of Contents.....	viii
List of Figures	ix
List of Schemes.....	xv
List of Charts.....	xvii
List of Tables	xviii
Abbreviations.....	xx
Chapter 1: Introduction.....	1
1.1 Motivation	1
1.2 Catalysis with Earth Abundant Metals	1
1.3 Ligand Design and Metal Reactivity	2
1.4 Chapter Summaries	5
References.....	9
Chapter 2: E-H Bond activations by iron and cobalt metalloboranes and their application in hydrosilylation catalysis	11
2.1 Introduction	11
2.2 Results and Discussion.....	14
2.3 Catalytic Hydrosilylation of Ketones and Aldehydes	33
2.4 Conclusions	42
2.5 Supporting Information.....	43
References.....	68
Chapter 3: Synthesis and reactivity of nickel metalloboranes with amine groups in the secondary coordination sphere	73
3.1 Motivation	73
3.2 Results and Discussion.....	75
3.3 Conclusions	86
4.4 Supporting Information.....	87
References.....	95
Chapter 4: Synthesis and Characterization of the First Parent Fe-hydrazido Complex	98
4.1 Introduction	98
4.2 Results and Discussion.....	101
4.3 Conclusion	137
4.4 Supporting Information.....	138
References.....	214
Appendix A: Additional Characterization Data and Synthetic Details.....	218
References.....	235

LIST OF FIGURES

<i>Chapter 2</i>	<i>Page</i>
2.1: ORTEP representation of the N ₂ bridged dimer generated by inversion symmetry.....	15
2.2: ORTEP representations of terminal N ₂ adducts from the asymmetric unit of (DPB)Co(N ₂)	16
2.3: ORTEP representation of (DPB)Fe(OPh)	18
2.4: ORTEP representation of [(DPBH)Fe(SPh)] ₂	19
2.5: ORTEP representation of (DPB)Co(OPh)	21
2.6: ORTEP representation of (DPB)Co(SPh)	22
2.7: ORTEP representation of (DPBH)Fe(benzo[h]quinolin-10-yl).	24
2.8: ORTEP representation of of (DPBH)Co(benzo[h]quinolin-10-yl)	25
2.9: ORTEP representation of the major component (90%) of a twinned crystal of (DPBH)Fe(8-amidoquinoline).....	27
2.10: ORTEP representation of the minor component (10%) of a twinned crystal of (DPBH)Fe(8-amidoquinoline).	28
2.11: ¹ H NMR spectra in C ₆ D ₆ of (DPB)Co(N ₂) in the presence of Ph ₂ SiH ₂	31
2.12: X-Band EPR Spectrum of (DPBH)Co(SiHPh ₂) in benzene at 77 K in toluene glass.....	33
2.S1: X-Band EPR Spectrum of (DPBH)Co(SiHPh ₂) in benzene at 77 K in toluene glass.....	56
2.S2: ORTEP Representation of (DPB)CoBr.....	57
2.S3: Variable temperature ¹ H NMR of the reaction mixture of (DPBH)Fe(8-amidoquinoline) in d ₈ -toluene.....	58
2.S4: 77 K X-Band EPR spectrum of (DPBH)Co(benzo[h]quinolin-10-yl) in 2-MeTHF and simulation.	59

2.S5: 77 K X-band EPR spectrum of (DPBH)Co(8-amidoquinoline) in 2-MeTHF and simulation.	60
2.S6: Thin film IR spectrum of (DPBH)Co(8-amidoquinoline) from evaporated C ₆ D ₆	60
2.S7: ¹ H NMR spectrum of (DPB)Fe(OPh) in C ₆ D ₆	61
2.S8: ¹ H NMR of (DPBH)Fe(8-amidoquinoline) in d ₈ -toluene (mixture of isomers). * d ₈ -toluene.	61
2.S9: ¹ H NMR spectrum of (DPB)Co(N ₂) in C ₆ D ₆	62
2.S10: ¹ H NMR Spectrum of (DPB)Co(OPh) in C ₆ D ₆	62
2.S11: ¹ H NMR Spectrum of the reaction mixture of Ph ₂ SiH ₂ with propanal in 5:1 THF:d ₈ -THF catalyzed by (DPB)Co(N ₂)	63
2.S12: ¹ H NMR Spectrum of the reaction mixture of Ph ₂ SiH ₂ with butanal in 4:1 THF:d ₈ THF catalyzed by (DPB)Co(N ₂)	64
2.S13: ¹ H NMR spectrum of the reaction mixture of Ph ₂ SiH ₂ with pentanal in 4:1 THF:d ₈ -THF catalyzed by (DPB)Co(N ₂)	64
2.S14: H NMR spectrum of the reaction mixture of Ph ₂ SiH ₂ with cyclohexanone in 5:1 THF:d ₈ -THF catalyzed by (DPB)Co(N ₂)	65
2.S15: ¹ H NMR spectrum of the reaction mixture of 2-pentanone with Ph ₂ SiH ₂ in C ₆ D ₆ catalyzed by (DPB)Co(N ₂)	65
2.S16: ¹ H NMR spectrum of the reaction mixture of acetophenone with Ph ₂ SiH ₂ in C ₆ D ₆ catalyzed by (DPB)Co(N ₂)	66
2.S17: ¹ H NMR spectrum of the reaction mixture of benzophenone and Ph ₂ SiH ₂ in C ₆ D ₆ catalyzed by (DPB)Co(N ₂)	66
2.S18: ¹ H NMR spectrum of the reaction mixture of benzaldehyde and Ph ₂ SiH ₂ in C ₆ D ₆ catalyzed by (DPB)Co(N ₂)	67
<i>Chapter 3</i>	<i>Page</i>
3.1: ORTEP representation of [(DP [*] B ^{Ph})Ni] ₂ (N ₂)	78
3.2: Cyclic voltammograms of (DP [*] B ^{Ph})NiBr in the presence of 2,6-dichloroanilinium tetrafluoroborate in THF (0.1 M [TBA][PF ₆]).....	79

3.3: Cyclic voltammograms of (DP* ^{B^{Mes}})NiBr in the presence of 2,6-dichloroanilinium tetrafluoroborate in THF (0.1 M [TBA][PF ₆]).....	80
3.4: Cyclic voltammograms of (DP* ^{B^{Ph}})NiBr in the presence of 11.3 equiv. NEt ⁱ Pr ₂ under N ₂ and H ₂ atmospheres	81
3.5: Cyclic voltammograms of (DP* ^{B^{Mes}})NiBr in the presence of 11.8 equiv. NEt ⁱ Pr ₂ under N ₂ and H ₂ atmospheres	81
3.6: ¹ H NMR spectra of the reaction between [(DP* ^{B^{Ph}})Ni] ₂ (N ₂) and H ₂ in d ₈ -THF	83
3.7: ORTEP representation of [(DP* ^{B^{Mes}} H)Ni] ₂	84
3.S1: CW X-band EPR spectra of (DP* ^{B^{Ph}})NiBr (blue trace) and (DP* ^{B^{Mes}})NiBr (red trace) in toluene (77 K)	94
<i>Chapter 4</i>	<i>Page</i>
4.1: DFT (TPSS) optimized structure and space filling model of [(^{Ar} P ₃ B)Fe(N ₂)] ⁻	105
4.2: Reaction progress of [(^{Ar} P ₃ B)Fe(N ₂)] [Na(12-C-4) ₂] with excess HBAr ^F ₂₄ monitored by CW X-band EPR (77 K, 9.44 GHz).	107
4.3: Field Dependent Q-Band ENDOR spectra of [(^{Ar} P ₃ B)Fe(N ₂)] [Na(12-C-4) ₂]	108
4.4: Field Dependent X-Band HYSCORE Spectra of [(^{Ar} P ₃ B)Fe(N ₂)] [Na(12-C-4) ₂] and [(^{Ar} P ₃ B)Fe(¹⁵ N ₂)] [Na(12-C-4) ₂]	109
4.5: Field Dependent X-Band ENDOR spectra of (^{Ar} P ₃ B)Fe(NNH).....	111
4.6: Comparison of (^{Ar} P ₃ B)Fe(NNH) and (^{Ar} P ₃ B)Fe(NN ² H) X-Band ENDOR spectra	112
4.7: X-band HYSCORE spectra (left) and simulations (right) for (^{Ar} P ₃ B)Fe(NNH)	113
4.8: Field Dependent Q-Band ENDOR spectra of (^{Ar} P ₃ B)Fe(NNSiMe ₃)	116
4.9: X-band HYSCORE spectra and simulations for (^{Ar} P ₃ B)Fe(NNSiMe ₃).	117

4.10: Field Dependent Q-Band ENDOR spectra of $[(^A\text{rP}_3\text{B})\text{Fe}(\text{NNH}_2)][\text{BAr}^{\text{F}}_{24}]$	119
4.11: Field Dependent Q-Band ENDOR Comparing Spectra of $[(^A\text{rP}_3\text{B})\text{Fe}(\text{NNH}_2)][\text{BAr}^{\text{F}}_{24}]$ and $[(^A\text{rP}_3\text{B})\text{Fe}(\text{NN}^2\text{H}_2)][\text{BAr}^{\text{F}}_{24}]$	120
4.12: Comparison of Field Dependent X-Band HYSCORE Spectra of $[(^A\text{rP}_3\text{B})\text{Fe}(\text{NNH}_2)][\text{BAr}^{\text{F}}_{24}]$ and $[(^A\text{rP}_3\text{B})\text{Fe}(^{15}\text{N}^{15}\text{NH}_2)][\text{BAr}^{\text{F}}_{24}]$	121
4.13: ^{57}Fe Mössbauer spectra of $[(^A\text{rP}_3\text{B})\text{Fe}(\text{N}_2)][\text{Na}(12\text{-C-4})_2]$	130
4.14: ^{57}Fe Mössbauer spectra of $(^A\text{rP}_3\text{B})\text{Fe}(\text{NNH})$ reaction mixture	131
4.15: ^{57}Fe Mössbauer spectrum of $(^A\text{rP}_3\text{B})\text{Fe}(\text{NNSiMe}_3)$	132
4.16: ^{57}Fe Mössbauer spectrum of $[(^A\text{rP}_3\text{B})\text{Fe}(\text{NNH}_2)][\text{BAr}^{\text{F}}_{24}]$ reaction mixture	133
4.S1: ORTEP representation of $(^A\text{rP}_3\text{B})\text{FeBr}$	150
4.S2: ORTEP representation of $(^A\text{rP}_3\text{B})\text{Fe}(\text{N}_2)$	151
4.S3: ORTEP representation of $(^A\text{rP}_3\text{B})\text{FeOTf}$	152
4.S4: Comparison of field dependent X-band HYSCORE spectra and simulations of $[(^A\text{rP}_3\text{B})\text{Fe}(\text{N}_2)][\text{Na}(12\text{-C-4})_2]$ and $[(^A\text{rP}_3\text{B})\text{Fe}(^{15}\text{N}_2)][\text{Na}(12\text{-C-4})_2]$.	153
4.S5: Comparison of field dependent X-band HYSCORE spectra and simulations of $[(^A\text{rP}_3\text{B})\text{Fe}(\text{NNH}_2)][\text{BAr}^{\text{F}}_{24}]$ and $[(^A\text{rP}_3\text{B})\text{Fe}(^{15}\text{N}^{15}\text{NH}_2)][\text{BAr}^{\text{F}}_{24}]$	154
4.S6: Difference of field dependent ENDOR spectra of $(^A\text{rP}_3\text{B})\text{Fe}(\text{NNH})$ and $(^A\text{rP}_3\text{B})\text{Fe}(\text{NND})$ and simulations	155
4.S7: Difference of field dependent ENDOR spectra of $[(^A\text{rP}_3\text{B})\text{Fe}(\text{NNH}_2)][\text{BAr}^{\text{F}}_{24}]$ and $[(^A\text{rP}_3\text{B})\text{Fe}(\text{NND}_2)][\text{BAr}^{\text{F}}_{24}]$ and simulations	156
4.S8: CW X-Band EPR spectrum of $[(^A\text{rP}_3\text{B})\text{Fe}(\text{N}_2)][\text{Na}(12\text{-C-4})_2]$	157
4.S9: CW X-Band EPR spectrum of $(^A\text{rP}_3\text{B})\text{Fe}(\text{NNH})$	159
4.S10: CW X-band EPR spectrum of $(^A\text{rP}_3\text{B})\text{Fe}(\text{NNSiMe}_3)$	160
4.S11: CW X-Band EPR spectrum of $[(^A\text{rP}_3\text{B})\text{Fe}(\text{NNH}_2)][\text{BAr}^{\text{F}}_{24}]$	161
4.S12: ^{57}Fe Mössbauer spectrum of $(^A\text{rP}_3\text{B})\text{FeBr}$	163
4.S13: ^{57}Fe Mössbauer spectrum of $(^A\text{rP}_3\text{B})\text{Fe}(\text{N}_2)$	163
4.S14: ^{57}Fe Mössbauer spectrum of $(^A\text{rP}_3\text{B})\text{Fe}(\text{OTf})$	164

4.S15: Q-Band 2p-ESEEM trace and exponential fit for T_2 of $[(^{Ar}P_3B)Fe(^{15}N_2)][Na(12-C-4)_2]$ at 40 K.....	164
4.S16: X-Band 2p-ESEEM trace and exponential fit for T_2 of $(^{Ar}P_3B)Fe(NNH)$ at 40 K	165
4.S17: Q-Band 2p-ESEEM trace and exponential fit for T_2 of $(^{Ar}P_3B)Fe(NNSiMe_3)$ at 40 K.....	165
4.S18: Q-Band 2p-ESEEM trace and alternative biexponential fit for T_2 of $(^{Ar}P_3B)Fe(NNSiMe_3)$ at 40 K.....	166
4.S19: Q-Band 2p-ESEEM trace and exponential fit for T_2 of $[(^{Ar}P_3B)Fe(^{15}N^{15}NH_2)][BAr^F_{24}]$ at 40 K	166
4.S20: DFT optimized structure of $[(^{Ar}P_3B)Fe(N_2)]^-$	167
4.S21: DFT optimized structure of a truncated version of $(^{Ar}P_3B)Fe(N_2)$	168
4.S22: DFT optimized structure of a truncated version of $(^{Ar}P_3B)Fe(NNH)$	169
4.S23: DFT optimized structure of a truncated version of $[(^{Ar}P_3B)Fe(NNH_2)]^+$	170
4.S24: DFT optimized structure of $[(^{Ar}P_3B)Fe(NNH)]^+$	171
4.S25: DFT optimized structure of alternative structure B	172
4.S26: DFT optimized structure of alternative structure G	173
4.S27: DFT optimized structure of alternative structure I.....	174
4.S28: Cyclic Voltammogram of $(^{Ar}P_3B)Fe(N_2)$	175
<i>Appendix A</i>	<i>Page</i>
A.1: ORTEP representation of $(P_3B)Co(SH)$	224
A.2: ORTEP representation of $(P_3B)Co(OH)$	225
A.3: ORTEP representation of $(P_3B)Fe(SH)$	226
A.4: ORTEP representation of $(^{Ar}P_3B)CoBr$	227
A.5: ORTEP representation of $(^{Ar}P_3B)Co(N_2)$	228
A.6: ORTEP representation of $[(^{Ar}P_3B)Co][BAr^F_{24}]$	229
A.7: CW X-band EPR spectrum of $(^{Ar}P_3B)Co(N_2)$ in MeCy glass	232

A.8: CW X-band EPR spectrum of ($^{Ar}P_3B$)Co(N ₂) in MeCy glass with simulation	232
A.9: Cyclic Voltammogram of (TPB)CoSH in THF	233
A.10: Cyclic Voltammogram of (TPB)FeSH in THF	233
A.11: Cyclic Voltammograms of (TPB)CoOH in THF	234
A.12: Cyclic Voltammogram of (TPB)FeOH	235

LIST OF SCHEMES

<i>Chapter 1</i>	<i>Page</i>
1.1: Reversible Si-H bond activation and catalytic hydrosilylation of ketones and aldehydes by (DPB)Co(N ₂).....	6
1.2: Hypothesized heterolytic H ₂ cleavage to give a zwitterionic Ni species.....	7
1.3: Protonation of [(^{Ar} P ₃ B)Fe(N ₂)] [Na(12-C-4) ₂] to give (^{Ar} P ₃ B)Fe(NNH) and [(^{Ar} P ₃ B)Fe(NNH ₂)] [BAr ^F ₂₄].....	8
<i>Chapter 2</i>	<i>Page</i>
2.1: M-N ₂ adducts [(DPB)Fe] ₂ (N ₂) and (DPB)Co(N ₂)	14
2.2: E-H bond activations mediated by [(DPB)Fe] ₂ (N ₂).....	17
2.3: E-H bond activations mediated by (DPB)Co(N ₂)	20
2.4: Reversible Si-H activation at (^{Ph} DPB ^{Mes})Ni and (DPB)Co(N ₂)	32
2.5: Possible catalytic cycle for hydrosilylation mediated by (DPB)Co(N ₂).....	40
<i>Chapter 3</i>	<i>Page</i>
3.1: Heterolytic cleavage of H ₂ by (DPB)Ni and Reversible H ₂ cleavage and catalytic olefin hydrogenation by (^{Ph} DPB ^{Mes})Ni.....	74
3.2: Previously reported trisphosphino-silyl ligand with pendant amines and new DPB type ligand target with pendant amines.....	75
3.3: Synthesis of DP [*] B ^{Ph} and DP [*] B ^{Mes} ligands	76
3.4: Synthesis of (DP [*] B ^{Ar})Ni species.	77
3.5: Hypothesized reactivity with H ₂ for (DP [*] B ^{Ar})Ni compounds	82
3.6: Reaction of (DP [*] B ^{Mes})Ni(N ₂) with H ₂ forms [(DP [*] B ^{Mes} H)Ni] ₂	84
<i>Chapter 4</i>	<i>Page</i>
4.1: Limiting mechanistic pathways for N ₂ fixation at a single metal site	99
4.2: Synthetic routes to previously reported Mo-, and W-diazenido species	100

4.3: Previously reported N_β -functionalization with electrophilic reagents on $(P_3Si)Fe$ and $(P_3B)Fe$ platforms	102
4.4: Reactions of $(P_3E)Fe(N_2)]^{0/-}$ with $HAr^F_{24} \cdot 2Et_2O$	102
4.5: Synthesis of $^{Ar}P_3B$	103
4.6: Synthesis of $^{Ar}P_3BFe$ compounds	105
4.7: Reactivity of $[(^{Ar}P_3B)Fe(N_2)][Na(12-C-4)_2]$ with HAr^F_{24}	106
4.8: Synthesis of $(^{Ar}P_3B)Fe(NNSiMe_3)$	115

LIST OF CHARTS

<i>Chapter 1</i>	<i>Page</i>
1.1: TPB and DPB ligand scaffolds	2
1.2: TPB binding modes.....	3
1.3: DPB binding modes	3
1.4: TPB and DPB metal compounds where the borane acts as a hydride acceptor.....	4
1.5: Active sites of hydrogenase enzymes.....	5
<i>Chapter 2</i>	<i>Page</i>
2.1: Select metal-borane compounds that facilitate bond activations via cleavage of the M-B interaction	12
2.2: Selected examples of previously reported Fe and Co carbonyl hydrosilylation catalysts.	34
<i>Chapter 3</i>	<i>Page</i>
3.1: Active sites of hydrogenase enzymes.....	73
3.2: Examples of synthetic Ni-based H ⁺ reduction catalysts which incorporate potential H ⁺ relays.....	75
<i>Chapter 4</i>	<i>Page</i>
4.1: Selected alternative structures considered for (ArP ₃ B)Fe(NNH) and [(ArP ₃ B)Fe(NNH ₂)] ⁺	126

LIST OF TABLES

<i>Chapter 2</i>	<i>Page</i>
2.1: Comparison of $[(DPB)Fe]_2(N_2)$ and $(DPB)Co(N_2)$ to $(^{Ph}DPB^{Mes})Ni$ for Benzaldehyde Hydrosilylation by Ph_2SiH_2	35
2.2: Substituent Effects on Hydrosilylation of Benzaldehyde by Ph_2SiH_2	36
2.3: Comparison of Primary, Secondary and Tertiary Silanes in Hydrosilylation of Benzaldehyde	37
2.4: Summary for Hydrosilylation by Ph_2SiH_2 of Various Aldehydes and Ketones by $[(DPB)Fe]_2(N_2)$ and $(DPB)Co(N_2)$	39
2.5: Comparison of Known Catalysts with $[(DPB)Fe]_2(N_2)$ and $(DPB)Co(N_2)$ for Hydrosilylation of Acetophenone by Ph_2SiH_2	42
2.S1: XRD experimental parameters for $(DPB)Fe(OPh)$, $[(DPBH)Fe(SPh)]_2$, $(DPBH)Fe(benzo[h]quinolin-10-yl)$, $(DPBH)Fe(8-amidoquinoline)$..	54
2.S2: XRD experimental parameters for $(DPB)Co(N_2)$, $(DPB)Co(OPh)$, $(DPB)Co(SPh)$, $(DPBH)Co(benzo[h]quinolin-10-yl)$, $(DPB)CoBr$..	55
<i>Chapter 3</i>	<i>Page</i>
3.1: Catalytic Hydrogenation of Styrene by $(DP^*B^{Ar})Ni$ Compounds and Related Activity Screening Data	86
3.S1: XRD experimental parameters for $[(DP^*B^{Ph})Ni]_2(N_2)$, $[(DP^*B^{Mes}H)Ni]_2$	93
<i>Chapter 4</i>	<i>Page</i>
4.1: Nuclear hyperfine couplings derived from ENDOR and HYSCORE for $[(^{Ar}P_3B)Fe(N_2)][Na(12-C-4)_2]$	110
4.2: Nuclear Hyperfine Couplings Derived from ENDOR and HYSCORE for $(^{Ar}P_3B)Fe(NNH)$	114
4.3: Nuclear Hyperfine Couplings Derived from ENDOR and HYSCORE for $(^{Ar}P_3B)Fe(NNSiMe_3)$	118
4.4: Nuclear hyperfine couplings derived from ENDOR and HYSCORE for $[(^{Ar}P_3B)Fe(NNH_2)]^+$	122

4.5: ^{14}N nuclear quadrupole couplings and asymmetry parameters derived from ENDOR and HYSCORE for N_α	124
4.6: ^{57}Fe Mössbauer Parameters.....	129
4.7: ^{57}Fe Mössbauer fit parameters for $[(^{\text{Ar}}\text{P}_3\text{B})\text{Fe}(\text{N}_2)][\text{Na}(12\text{-C-4})_2]$	130
4.8: ^{57}Fe Mössbauer fit parameters for Generation of $(^{\text{Ar}}\text{P}_3\text{B})\text{Fe}(\text{NNH})$.	131
4.9: ^{57}Fe Mössbauer fit parameters for $(^{\text{Ar}}\text{P}_3\text{B})\text{Fe}(\text{NNSiMe}_3)$	132
4.10: ^{57}Fe Mössbauer Fit components for Generation of $[(^{\text{Ar}}\text{P}_3\text{B})\text{Fe}(\text{NNH}_2)][\text{BAr}^{\text{F}}_{24}]$	133
4.11: NH_3 Production Under Various Conditions	137
4.S1: XRD experimental parameters for $(^{\text{Ar}}\text{P}_3\text{B})\text{FeBr}$, $(^{\text{Ar}}\text{P}_3\text{B})\text{Fe}(\text{N}_2)$, $(^{\text{Ar}}\text{P}_3\text{B})\text{Fe}(\text{OTf})$	149
4.S2: ^{11}B nuclear quadrupole couplings and asymmetry parameters derived from ENDOR and HYSCORE	162
<i>Appendix A</i>	<i>Page</i>
A.1: XRD experimental parameters for $(\text{P}_3\text{B})\text{Fe}(\text{SH})$, $(\text{P}_3\text{B})\text{Co}(\text{SH})$, $(\text{P}_3\text{B})\text{Co}(\text{OH})$	230
A.2: XRD experimental parameters for $(^{\text{Ar}}\text{P}_3\text{B})\text{CoBr}$, $(^{\text{Ar}}\text{P}_3\text{B})\text{Co}(\text{N}_2)$, $[(^{\text{Ar}}\text{P}_3\text{B})\text{Co}][\text{BAr}^{\text{F}}_{24}]$	231

ABBREVIATIONS

A_X	Hyperfine coupling constant due to nucleus X
A_{iso}	isotropic component of a hyperfine coupling constant
A_{aniso}	anisotropic component of a hyperfine coupling constant
Anal	Analysis
Atm	Atmosphere
Avg	Average
$\text{BAr}^{\text{F}}_{24}$	$[\text{B}(3,5\text{-C}_6\text{H}_3(\text{CF}_3)_2)_4]^-$
br	broad
$n\text{Bu}$	n-butyl
C	constant
ca	circa
Calc	calculated
cm	centimeter
cm^{-1}	wave number
CO	carbon monoxide
CO_2	carbon dioxide
Cp	cyclopentadienyl
Cp^*	pentamethylcyclopentadienyl
CV	cyclic voltammogram
d	doublet or deuterium
dd	doublet of doublets
d_x	compound with x deuterium atoms
DFT	density functional theory
DME	1,2-dimethoxyethane
e^-	electron
ENDOR	electron nuclear double resonance
EPR	electron paramagnetic resonance
ESI-MS	electrospray ionization mass spectrometry
eq.	equivalents
equiv.	equivalents
EXAFS	extended X-ray absorption fine structure
eV	electron volt
E	element
E°	reduction or oxidation potential
F	structure factor
G	gauss
g	gram
g	electron g-factor
GC	gas chromatography
GHz	gigahertz

H	enthalpy
Hz	hertz
<i>i</i> Pr	isopropyl
IR	infrared
$^X J_{AB}$	NMR coupling constant between atoms A and B along X number of bonds
<i>J</i>	NMR coupling constant or magnetic coupling constant
K	Kelvin or rate or equilibrium constant
L	Generic neutral dative ligand
kcal	kilocalorie
m	multiplet
M	concentration in molarity
Max	maximum
Me	methyl
mg	milligram
MHz	megahertz
mL	milliliter
mM	millimolar
mm	millimeter
mmol	millimole
mT	millitesla
mV	millivolt
MO	molecular orbital
mol	mole
n	generic number
nm	nanometer
NMR	nuclear magnetic resonance
N _x H _y	generic nitrogenous ligand with x N atoms and y H atoms
<i>o</i>	ortho
OTf	trifluoromethanesulfonate
Ph	phenyl
pK _a	acid dissociation constant
q	quartet
R	generic organic group or R-factor
RT	room temperature
q	quartet
S	entropy
<i>S</i>	spin quantum number
s	singlet or second
t	triplet or time
TBA	tetra- <i>n</i> -butyl ammonium
<i>t</i> Bu	<i>tert</i> -butyl
THF	tetrahydrofuran
2-MeTHF	2-methyltetrahydrofuran
TMS	trimethylsilyl
TPB	<i>o</i> - <i>i</i> Pr ₂ P(C ₆ H ₄)) ₃ B or generically <i>o</i> -R ₂ P(C ₆ H ₄)) ₃ B
UV	ultraviolet

V	volt
Vis	visible
wR	weighted R-factor
X	generic anionic atom or molecule
XAS	X-ray absorption spectroscopy
XANES	X-ray Absorption near edge spectroscopy
XRD	X-ray diffraction
N _α	proximal nitrogen atom of a bound N ₂ H _x ligand
N _β	distal nitrogen atom of a bound N ₂ H _x ligand
γ	high frequency electromagnetic radiation
ΔEq	Mössbauer quadrupole splitting
δ	Mössbauer isomer shift
°	degree
°C	degrees Celcius
ε	Extinction coefficient in units of M ⁻¹ cm ⁻¹
η ^x	hapticity of order x
λ	wavelength
λ _{max}	Wavelength of local maximum intensity
μ	bridging
μ-X	bridging X ligand
μB	Bohr magneton
μ _{eff}	Effective magnetic moment
μL	microliter
Σ	summation
σ	sigma symmetry orbital or interaction
σ*	antibonding sigma symmetry orbital or interaction
π	pi symmetry orbital or interaction
π*	antibonding pi symmetry orbital or interaction
Å	angstrom
12-C-4	12-crown-4
¹ H	hydrogen-1
² H	deuterium (hydrogen-2)
¹¹ B	boron-11
¹³ C	carbon-13
¹⁴ N	nitrogen-14
¹⁵ N	nitrogen-15
³¹ P	phosphorus-31
TPSS	DFT functional
def2-svp	DFT basis set
def2-tzvp	DFT basis set

Chapter 1

INTRODUCTION

1.1 Motivation

The work detailed in this thesis is united thematically by the manipulation of chemical and electronic structure in first row transition metal compounds in order to elicit new reactivity. Although the specific approaches and reactions studied are not necessarily closely related, each chapter describes a study which was motivated by this core goal. This introductory chapter will serve to provide some basic background behind the reactions studied/developed in the context of this overarching theme. The individual chapters will discuss many of the concepts introduced here in more explicit detail.

1.2 Catalysis with Earth-Abundant Metals

Among the most interesting challenges facing inorganic and organometallic chemistry is the development of new chemical transformations that employ abundant chemical feedstocks (N_2 , CO_2 , O_2 , H_2O , etc...) and catalyst species (first row transition metals) in order to facilitate atom efficient and cost effective synthesis of value-added chemical products.^{1,2} Many synthetically and industrially important reactions utilize catalysts based on 2nd- and 3rd-row transition metals. These metals are often rare, expensive, and in some cases toxic. Many of these catalysts are sufficiently high-performing to negate the aforementioned limitations in the short term. However, as the sources for these materials become depleted it will become increasingly important to develop more sustainable catalyst systems based. One

strategy for addressing this problem is the development of catalytic reaction using the more abundant first row transition metals.

Among the most difficult challenges in moving to first row transition metal catalyst systems lies in the divergent reactivity displayed by these metals relative to the second and third row metals. The first row metals have a greater propensity towards single electron reactivity often involving radical intermediates, while the 2nd- and 3rd-row metals are more prone to two-electron reactivity.²⁻⁵ Recent developments in ligand design have been able to overcome this problem of divergent reactivity in several cases. Some researchers have used ligands which employ redox-active moieties in the ligand framework. Others have incorporated Lewis-acidic or –basic functionality into the ligand in order to facilitate the desired 2-electron reactivity.⁶⁻¹⁷

1.3 Ligand Design and Metal Reactivity

1.3.1 Metal-Borane Interactions: A common structural feature among the metal species described in this thesis is presence of a metal-borane interaction. More specifically, the ligands which support the metal center are in all cases based on the neutral L₃Z type ligands originally reported by Borrisou TPB (also referred to as P₃B), and DPB (Chart 1.1).¹⁸

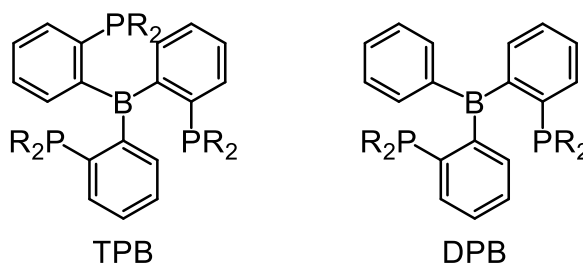


Chart 1.1: TPB and DPB ligand scaffolds.

These ligand scaffolds feature phosphine ligands in the primary coordination sphere which can act as σ -donors and π -acceptors while the borane can act as a σ -acceptor. The M-B interaction in the TPB scaffold can vary from no interaction to a strong interaction and can even develop an η^2 -interaction with the phenylene linker between the borane and phosphine moieties in order to increase the coordination number and electron count at the metal center (Chart 1.2).

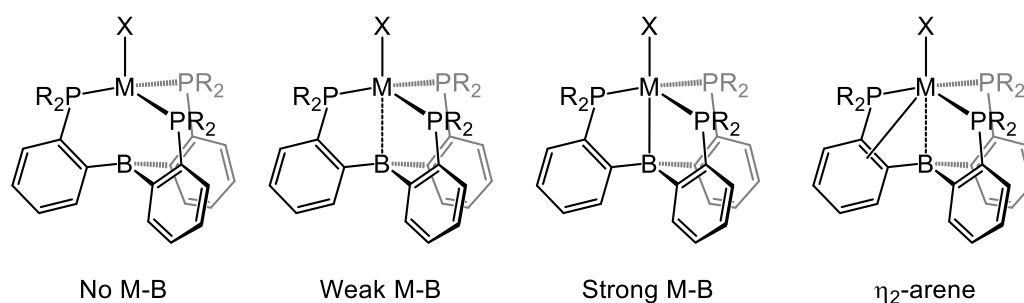


Chart 1.2: TPB binding modes.

The DPB scaffold also features an aryl substituent which can act as both a σ -donor and π -acceptor in addition to two phosphine ligands. The arene ligand additionally may display hemilability providing a mechanism for modulating the coordination number and electron count at the metal center (Chart 1.3).

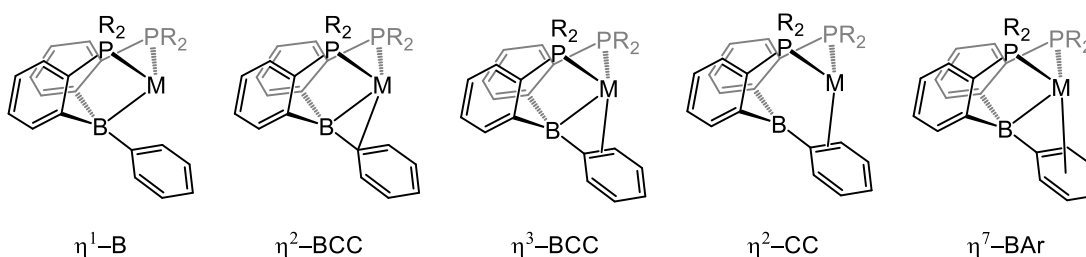


Chart 1.3: DPB binding modes.

An additional degree of flexibility of the TPB and DPB ligands introduce is the ability of the borane to act as a hydride acceptor. Reversible addition of H-H bonds across the M-B

interaction in (TPB)Fe compounds has been employed by our group to facilitate iron catalyzed olefin hydrogenation and similar reversible H-H and Si-H bond oxidative addition in (DPB)Ni has also been used in nickel catalyzed olefin hydrogenation and aldehyde hydrosilylation.^{6,7,19} The ability of the borane to act as a hydride acceptor provides additional stabilization of the metal hydride species and may help facilitate the desirable 2-electron step of oxidative addition requisite for these reactions (Chart 1.4).²⁰

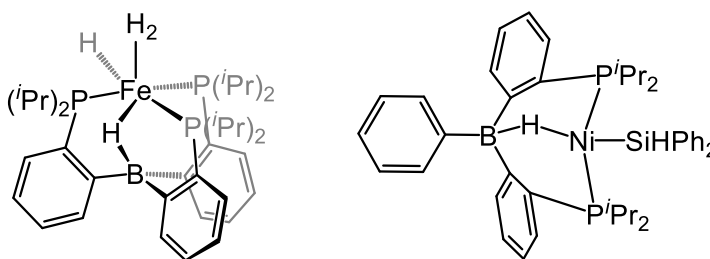


Chart 1.4: TPB and DPB metal compounds where the borane acts as a hydride acceptor.

1.3.2 Appended Lewis Basic Functionalities as H⁺ Shuttles: An additional strategy for imparting the desired reactivity at first row transition metal centers is to take inspiration in ligand design from biological systems which catalyze the desired reaction. These systems have evolved, over millions of years, a unique and complicated structure which enables abundant metals to perform extremely difficult and complex reactions with remarkable efficiency. Reactions of particular interest to me during my studies were reduction of H⁺ to H₂, and its microscopic reverse, H₂ oxidation. These reactions are catalyzed in biological systems by hydrogenase enzymes. Each of the three types of known hydrogenase enzymes contains a moiety which can act as a H⁺ shuttle (Chart 1.5). Similar moieties have been incorporated successfully into synthetic systems and enhanced the catalytic activity of the

transition metal compounds for H^+ reduction and H_2 oxidation and we undertook a similar strategy in our research.^{16,17,21}

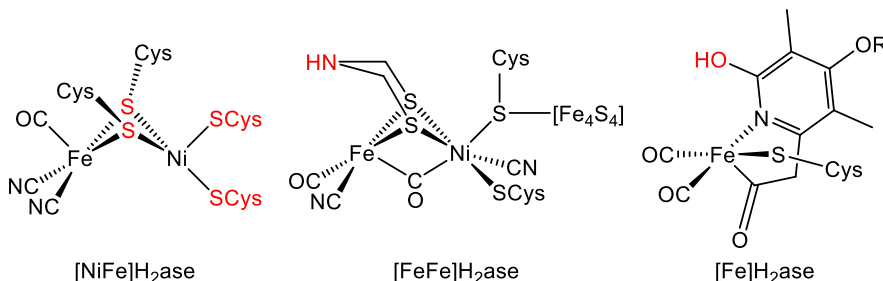
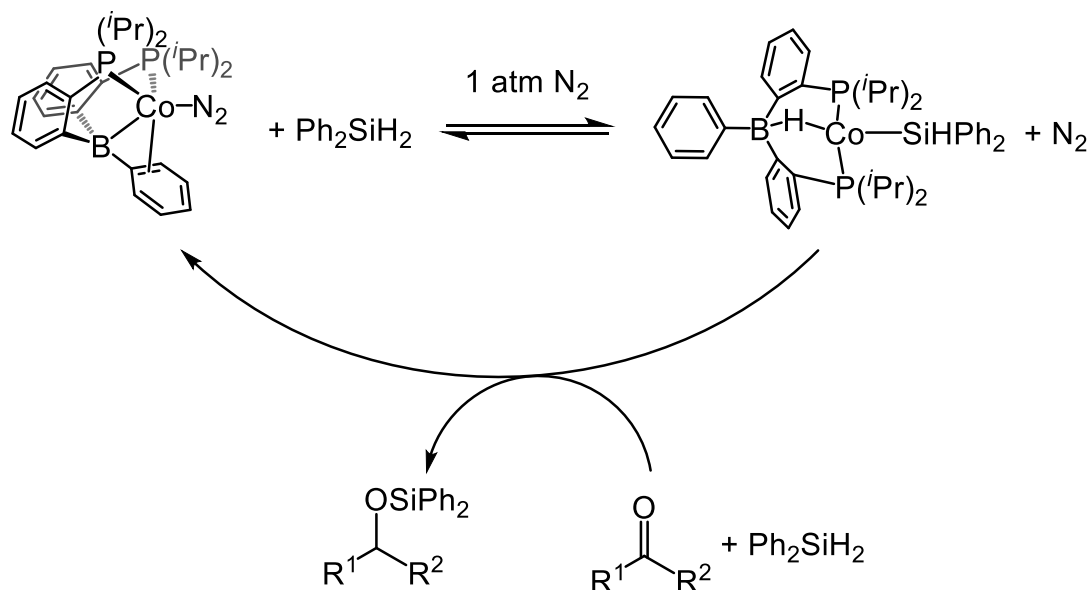


Chart 1.5: Active sites of hydrogenase enzymes. Sites which may act as proton shuttles are shown in red.

1.4 Chapter Summaries

Chapter 2 discusses the synthesis of $(\text{DPB})\text{Co}(\text{N}_2)$ and the reactivity of $(\text{DPB})\text{Co}(\text{N}_2)$ and its analog $[(\text{DPB})\text{Fe}]_2(\text{N}_2)$ in the context of E-H bond activation and ketone and aldehyde hydrosilylation. We were interested in determining whether changing the metal center would open up new reactivity, as our previous studies on $(\text{DPB})\text{Ni}(\text{N}_2)$ and $(^{\text{Ph}}\text{DPB}^{\text{Mes}})\text{Ni}$ had shown that $(\text{DPB})\text{M}$ species were capable of facilitating oxidative addition of E-H substrates (H_2 and Ph_2SiH_2) across the Ni-B interaction. Furthermore, we had shown that the reversible nature of these reactions under some conditions led to productive catalytic reactivity for olefin hydrogenation and hydrosilylation of benzaldehyde substrates. The current study shows that indeed both the Fe and Co analogs display the desired oxidative addition chemistry with C-H and N-H bonds which were unreactive in the presence of $(\text{DPB})\text{Ni}$ species. The Fe and Co analogs also displayed net 1-electron chemistry resulting in formation of H_2 with PhOH as an O-H bond substrate and differing reactivity with PhSH . Finally, reversible Si-H bond activation similar to that observed with $(^{\text{Ph}}\text{DPB}^{\text{Mes}})\text{Ni}$ was observed

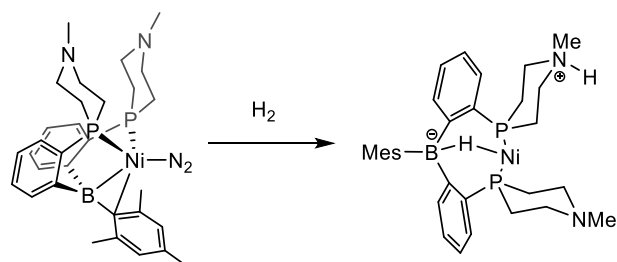
with (DPB)Co(N₂). This prompted us to investigate [(DPB)Fe]₂(N₂) and (DPB)Co(N₂) as precatalysts for hydrosilylation of benzaldehyde substrates similar to (PhDPB^{Mes})Ni. We found that both Fe and Co species served as more active catalysts than the Ni system and were also able to extend the substrate scope to include alkyl aldehydes as well as aryl and alkyl ketone substrates (Scheme 1.1).



Scheme 1.1: Reversible Si-H bond activation and catalytic hydrosilylation of ketones and aldehydes by (DPB)Co(N₂)

Chapter 3 explores the synthesis of two new DPB ligands which utilize an azacycphosphinane moiety to incorporate tertiary amines into the secondary coordination sphere and the metalation of these ligands with nickel. The reactivity of the N₂ adducts of these new ligands [(DP^{*}B^{Ph})Ni]₂(N₂) and (DP^{*}B^{Mes})Ni(N₂) with H₂ was investigated and compared to the reactivity observed with the previously studied (DPB)Ni(N₂) and (PhDPB^{Mes})Ni. Additionally the new compounds were screened for activity as H⁺ reduction and H₂ oxidation catalysts and were found to exhibit little to no catalytic activity towards

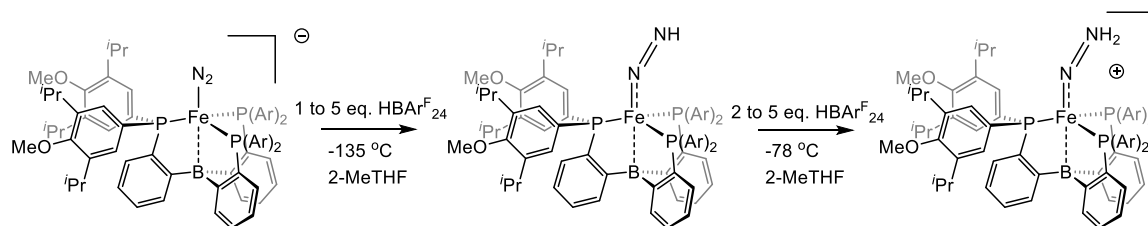
either of these reactions. We had hypothesized that the addition of amines into the secondary coordination sphere might allow for heterolytic H_2 cleavage with delivery of H^+ to the amine moiety and H^- to the borane to give a zwitterionic compound with both acidic and hydridic protons which could be useful in hydrogenation of polar substrates (Scheme 1.2). However, neither $[(\text{DP}^*\text{B}^{\text{Ph}})\text{Ni}]_2(\text{N}_2)$ nor $(\text{DP}^*\text{B}^{\text{Mes}})\text{Ni}(\text{N}_2)$ displayed any observable reactivity towards hydrogenation of ketones, aldehydes, or CO_2 as substrates. $(\text{DP}^*\text{B}^{\text{Ph}})\text{Ni}(\text{N}_2)$ and $(\text{DP}^*\text{B}^{\text{Mes}})\text{Ni}$ were shown to be competent styrene hydrogenation catalysts but underperformed the previously reported $(^{\text{Ph}}\text{DPB}^{\text{Mes}})\text{Ni}$ system. It is possible that the pK_a of the trialkyl amine is too high and that this is the cause of the poor activity in H^+ reduction and H_2 oxidation. An aniline type moiety might have a pK_a which is better matched for proton shuttling and this type of species might display enhanced catalytic activity relative to $(\text{DP}^*\text{B}^{\text{Ph}})\text{Ni}(\text{N}_2)$ and $(\text{DP}^*\text{B}^{\text{Mes}})\text{Ni}$.



Scheme 1.2: Hypothesized heterolytic H_2 cleavage to give a zwitterionic Ni species.

Chapter 4 details the synthesis of a new TPB type ligand ($^{\text{Ar}}\text{P}_3\text{B}$) with bulky electron rich aryl substituents on the phosphines and its metalation with iron. The protonation of the anionic $\text{Fe}-\text{N}_2$ adduct supported by this ligand $[(^{\text{Ar}}\text{P}_3\text{B})\text{Fe}(\text{N}_2)][\text{Na}(12\text{-C-}4)_2]$ led to observation of the first parent Fe-diazenido $(^{\text{Ar}}\text{P}_3\text{B})\text{Fe}(\text{NNH})$ (Scheme 1.3) via EPR, ENDOR, HYSCORE and ^{57}Fe Mössbauer spectroscopies. Subsequent reaction of

$(^{\text{Ar}}\text{P}_3\text{B})\text{Fe}(\text{NNH})$ with excess acid led to the generation of $[(^{\text{Ar}}\text{P}_3\text{B})\text{Fe}(\text{NNH}_2)][\text{BAr}^{\text{F}}_{24}]$ (Scheme 1.3) which showed similar spectroscopic signatures to the previously reported $[(\text{TPB})\text{Fe}(\text{NNH}_2)][\text{BAr}^{\text{F}}_{24}]$.²² The activity of $(^{\text{Ar}}\text{P}_3\text{B})\text{Fe}$ species as catalysts for the conversion of N_2 to NH_3 is discussed under different sets of conditions using KC_8 , $\text{HBAr}^{\text{F}}_{24} \cdot 2\text{Et}_2\text{O}$ and CoCp^*_2 , $[\text{H}_2\text{NPh}_2][\text{OTf}]$ as the reductant/acid cocktails. An in-depth characterization of $[(^{\text{Ar}}\text{P}_3\text{B})\text{Fe}(\text{N}_2)][\text{Na}(12\text{-C-4})_2]$, $(^{\text{Ar}}\text{P}_3\text{B})\text{Fe}(\text{NNH})$ and $[(^{\text{Ar}}\text{P}_3\text{B})\text{Fe}(\text{NNH}_2)][\text{BAr}^{\text{F}}_{24}]$ by ENDOR, and HYSCORE gave hyperfine couplings to the N, P, H, and B atoms in the protonation series and dipolar distance estimates for the $\text{Fe-H}_{\text{N}\beta}$ were consistent with distances predicted by DFT methods. Finally the N-H bond dissociation free energies (BDFEs) were calculated by DFT methods and compared to the corresponding BDFEs calculated for the parent $(\text{P}_3\text{B})\text{Fe}$ system.



Scheme 1.3: Protonation of $[(^{\text{Ar}}\text{P}_3\text{B})\text{Fe}(\text{N}_2)][\text{Na}(12\text{-C-4})_2]$ to give $(^{\text{Ar}}\text{P}_3\text{B})\text{Fe}(\text{NNH})$ and $[(^{\text{Ar}}\text{P}_3\text{B})\text{Fe}(\text{NNH}_2)][\text{BAr}^{\text{F}}_{24}]$.

References

- (1) *Activation of Small Molecules: Organometallic and Bioinorganic Perspectives*; Wiley-VHC: Weinheim, Germany, 2006.
- (2) Crabtree, R. H. *The Organometallic Chemistry of the Transition Metals, 5th Ed.*; John Wiley & Sons Inc.: New York, 2009.
- (3) Bullock, R. M. *Catalysis without Precious Metals*; Wiley-VCH Verlag GmbH & Co. KGaA Weinheim, 2010.
- (4) Chirik, P. J. In *Catalysis without Precious Metals*; Wiley-VCH Verlag GmbH & Co. KGaA: 2010, p 83.
- (5) Miessler, G. L.; Tarr, D. A. *Inorganic Chemistry*; 4th ed.; Prentice Hall: New York, 2011.
- (6) Harman, W. H.; Peters, J. C. *J. Am. Chem. Soc.* **2012**, *134*, 5080.
- (7) MacMillan, S. N.; Hill Harman, W.; Peters, J. C. *Chem. Sci.* **2014**, 590.
- (8) Stephan, D. W.; Erker, G. *Angew. Chem. Int. Ed.* **2010**, *49*, 46.
- (9) Stephan, D. W.; Erker, G. *Angew. Chem. Int. Ed.* **2015**, *54*, 6400.
- (10) Suess, D. L. M.; Peters, J. C. *J. Am. Chem. Soc.* **2013**, *135*, 4938.
- (11) Suess, D. L. M.; Peters, J. C. *J. Am. Chem. Soc.* **2013**, *135*, 12580.
- (12) Sylvester, K. T.; Chirik, P. J. *J. Am. Chem. Soc.* **2009**, *131*, 8772.
- (13) Trovitch, R. J. *Synlett* **2014**, *25*, 1638.
- (14) Das, P.; Stolley, R. M.; van der Eide, E. F.; Helm, M. L. *Eur. J. Inorg. Chem.* **2014**, *2014*, 4611.

- (15) Das, A. K.; Engelhard, M. H.; Bullock, R. M.; Roberts, J. A. S. *Inorg. Chem.* **2014**, *53*, 6875.
- (16) Bediako, D. K.; Solis, B. H.; Dogutan, D. K.; Roubelakis, M. M.; Maher, A. G.; Lee, C. H.; Chambers, M. B.; Hammes-Schiffer, S.; Nocera, D. G. *Proc. Natl. Acad. Sci.* **2014**, *111*, 15001.
- (17) Appel, A. M.; Pool, D. H.; O'Hagan, M.; Shaw, W. J.; Yang, J. Y.; Rakowski DuBois, M.; DuBois, D. L.; Bullock, R. M. *ACS Catal.* **2011**, *1*, 777.
- (18) Bontemps, S.; Gornitzka, H.; Bouhadir, G.; Miqueu, K.; Bourissou, D. *Angew. Chem. Int. Ed.* **2006**, *45*, 1611.
- (19) Fong, H.; Moret, M.-E.; Lee, Y.; Peters, J. C. *Organometallics* **2013**, *32*, 3053.
- (20) Harman, W. H.; Lin, T.-P.; Peters, J. C. *Angew. Chem. Int. Ed.* **2013**, 1081.
- (21) Yang, J. Y.; Bullock, R. M.; Shaw, W. J.; Twamley, B.; Frazee, K.; DuBois, M. R.; DuBois, D. L. *J. Am. Chem. Soc.* **2009**, *131*, 5935.
- (22) Anderson, J. S.; Cutsail, G. E.; Rittle, J.; Connor, B. A.; Gunderson, W. A.; Zhang, L.; Hoffman, B. M.; Peters, J. C. *J. Am. Chem. Soc.* **2015**, *137*, 7803.

*Chapter 2***E-H BOND ACTIVATIONS BY IRON AND COBALT
METALLOBORANES AND THEIR APPLICATION IN
HYDROSILYLATION CATALYSIS**

Reproduced in part with permission from:

Nesbit, M. A.; Suess, D. L. M.; Peters, J. C.; *Organometallics*, **2015**, *34*, 4741-4752.

DOI: 10.1021/acs.organomet.5b0053

© 2015 American Chemical Society

2.1 Introduction

The ability of transition metals to mediate multielectron transformations is critical in organometallic catalysis. Noble metals are prominent in organometallic catalysis due to their tendency to display well-defined multielectron reactivity.¹ E–H bond oxidative additions and reductive eliminations are key steps in many of these catalytic processes, such as olefin hydrogenation and the hydrosilylation of ketones and aldehydes.²⁻⁴ There has been increasing interest in developing well-defined complexes featuring earth-abundant first-row transition metals that can mediate similar two-electron redox steps and thus serve as viable catalysts for these types of transformations.^{5,6}

One promising strategy for imparting nobility to first-row transition metal systems is the use of ligands that incorporate a pendant borane.⁷⁻¹¹ The weak or labile interaction between the transition metal center and the boron atom in the ligand can be considered as an organometallic frustrated Lewis pair wherein the pendant borane formally serves as the Lewis acid and an electron-rich, low-valent metal center serves as the Lewis base.⁹⁻¹⁵ This

point was highlighted by our lab in recent studies of the reactivity of a nickel metalloborane ($^{\text{Ph}}\text{DPB}^{\text{Mes}}\text{Ni}$) (Chart 2.1, A) with hydrogen.⁹ This limiting polarity is inverted from the more typical case where a Lewis acidic metal is paired with a ligand featuring a Lewis basic site.^{5,8,9,16,17}

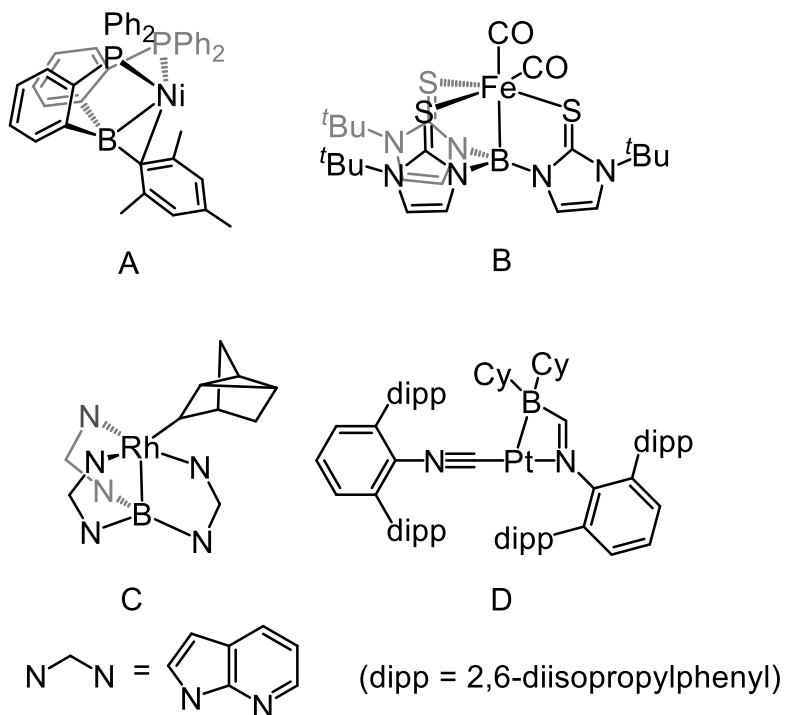
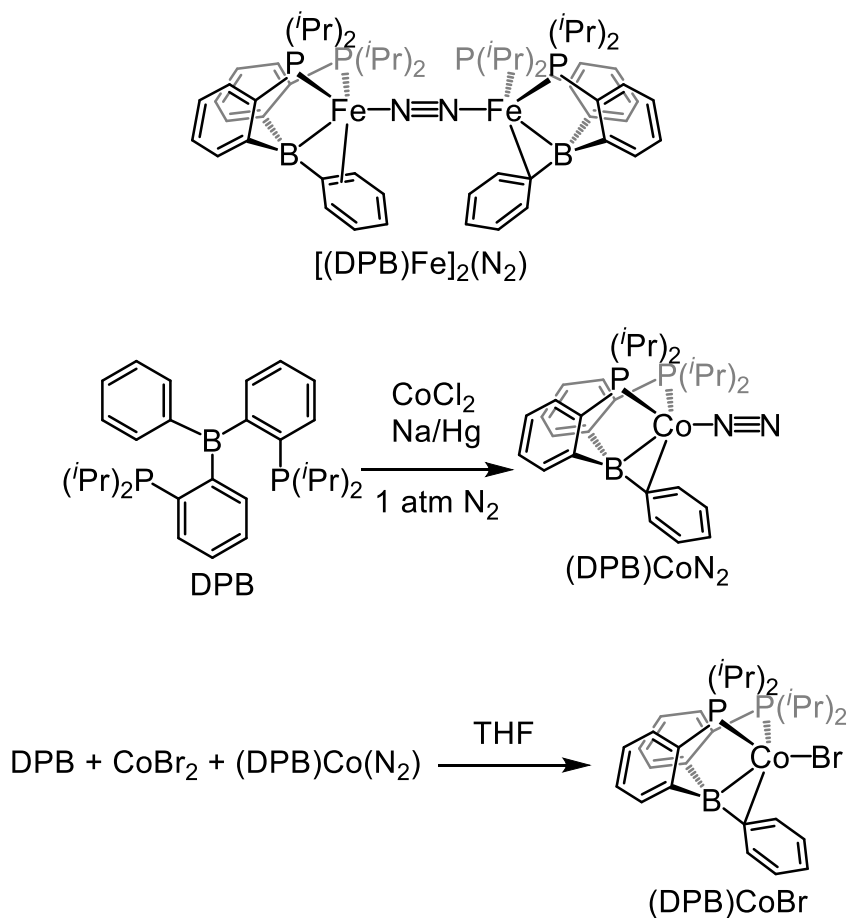


Chart 2.1: Select metal-borane compounds that facilitate bond activations via cleavage of the M-B interaction.

Other metalloborane platforms have also been shown to facilitate oxidative additions across the metal–borane interaction. For instance, Parkin and co-workers showed that Fe and Ni compounds supported by a trismercaptoimidazolylborane ligand (e.g., $(\text{B}(\text{mim}^{\text{tBu}})_3)\text{Fe}(\text{CO})_2$, Chart 2.1, B) facilitate 1,2-addition of a variety of E–X bonds across the transition metal–borane interaction.^{18,19} Related to our own studies of nickel metalloboranes, Owen and co-workers demonstrated that the rhodium compound

Rh[B(azaindoly)₃](nortricyclyl) (Chart 2.1, C) facilitates oxidative addition of H₂ and serves as an olefin hydrogenation catalyst.²⁰ Very recently, Emslie and Figueroa have independently reported platinum compounds bearing a pendant borane that activate H₂ and other E–H bonds (Chart 2.1, D).^{21,22}

Stimulated by these recent advances that show M–B dative interactions can facilitate well-defined multielectron chemistry at base metal centers, we now describe the reactivity of the Fe and Co metalloboranes [(DPB)Fe]₂(N₂), and (DPB)Co(N₂) (Scheme 1.1). We report here a comparative study on the reactivity of [(DPB)Fe]₂(N₂) and (DPB)Co(N₂) in the context of E–H bond activation and catalytic hydrosilylation of ketones and aldehydes, and compare their activity to the Ni analogue (Chart 1.1, A), which has been previously demonstrated to be a competent catalyst for olefin hydrogenation and benzaldehyde hydrosilylation.^{9,11} Ultimately, we find that [(DPB)Fe]₂(N₂) and (DPB)Co(N₂) display enhanced reactivity profiles toward E–H bonds by comparison to the aforementioned Ni system and that (DPB)Co(N₂) serves as a very active precatalyst for the hydrosilylation of organic carbonyls. Furthermore, we have independently prepared several efficient hydrosilylation catalysts reported in the literature^{23–25} to test them against [(DPB)Fe]₂(N₂) and (DPB)Co(N₂) and have found (DPB)Co(N₂) to be the most active cobalt precatalyst under the conditions described herein.



Scheme 2.1: M-N₂ adducts [(DPB)Fe]₂(N₂) and (DPB)Co(N₂)

2.2 Results and Discussion

We have previously described the synthesis of [(DPB)Fe]₂(N₂) (Scheme 2.1, top)²⁶ and have reported Si-H and H-H bond activations by related iron compounds derived from silylation of bound N₂ and CO.^{26,27} A cobalt analogue, (DPB)Co(N₂) (Scheme 2.1, middle), has been synthesized for this study to compare with [(DPB)Fe]₂(N₂). A solution magnetic susceptibility measurement of (DPB)Co(N₂) (1.8 μB at rt) is consistent with an *S* = 1/2 ground state. The presence of a terminally bound N₂ ligand was supported by X-ray crystallographic studies (Figures 2.1, 2.2, and 2.S1), which showed the presence of two

(DPB)Co(N₂) molecules and an N₂-bridged dimer ([(DPB)Co]₂(N₂)) in the asymmetric unit; the nickel derivative (DPB)Ni(N₂) behaves similarly in the solid state.¹⁶ ATR-FTIR and solution IR spectra showed intense N₂ stretching bands at 2098 cm⁻¹, establishing the terminal N₂ adduct as the major species in solution.

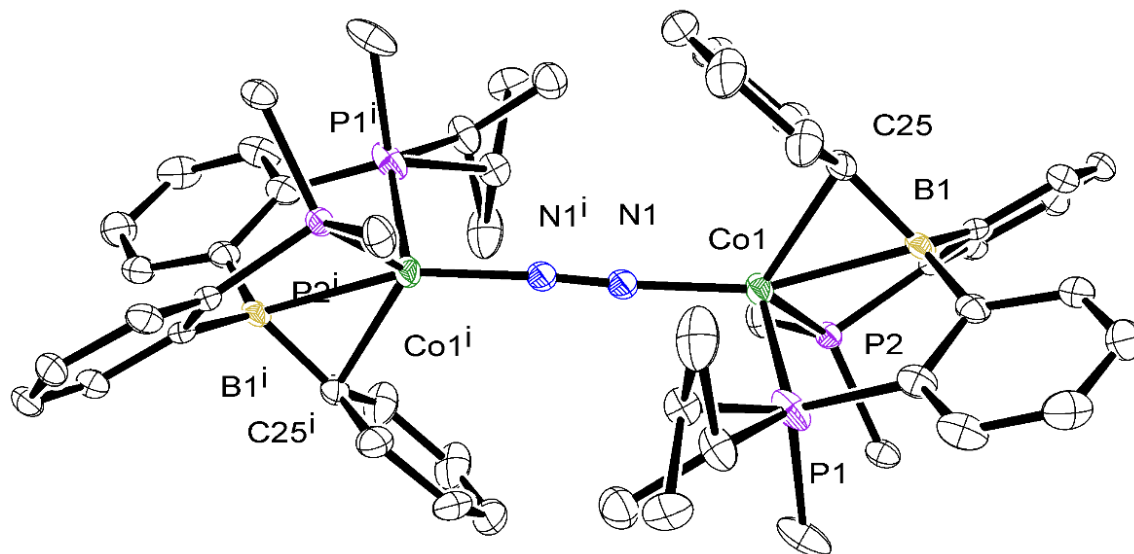


Figure 2.1: ORTEP representation of the N₂ bridged dimer generated by inversion symmetry in the solid-state structure of (DPB)Co(N₂). Selected Bond Distances: Co1-P1 2.2754(9) Å; Co1-P2 2.2890(8) Å; Co1-N1 1.900(2) Å; Co1-B1 2.282(3) Å; Co1-C25 2.113(3) Å. One of the isopropyl groups on P1 is disordered over two positions.

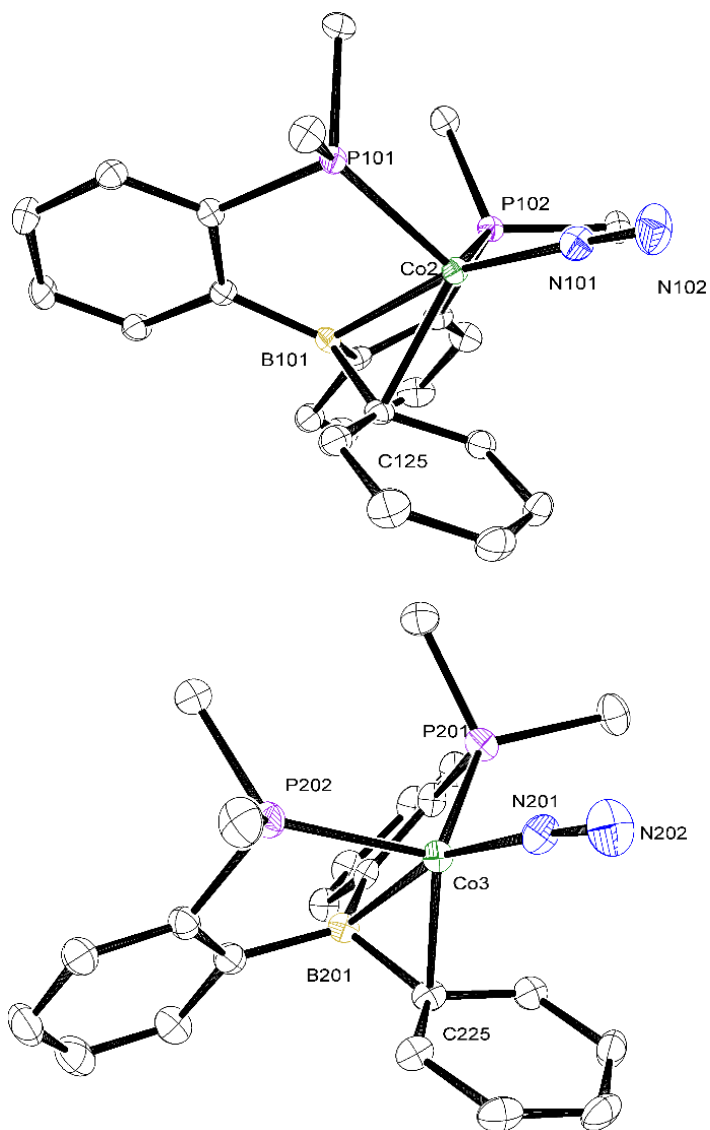
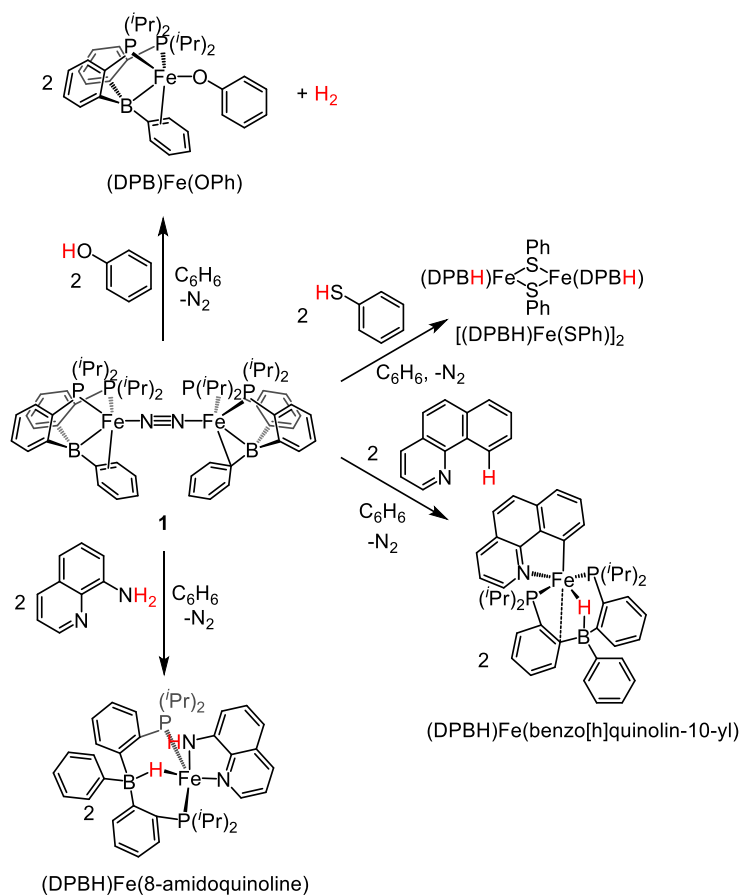


Figure 2.2: ORTEP representations of terminal N₂ adducts from the asymmetric unit of (DPB)Co(N₂) (H atoms and Methyl groups on non-disordered isopropyl substituents omitted for clarity). Selected bond distances Co2-P102 2.2594(8) Å; Co2-P101 2.2616(8) Å; Co2-N101 1.845(2) Å; Co2-C125 2.099(2) Å; Co2-B101 2.240(3) Å; Co3-P201 2.2645(8) Å; Co3-P202 2.2607(9) Å; Co3-N201 1.846(2) Å; Co3-C225 2.054(3) Å; Co3-B201 2.225(3) Å.

2.2.1 Reactivity with PhOH and PhSH. Addition of PhOH (2 equiv.) to $[(\text{DPB})\text{Fe}]_2(\text{N}_2)$ in C_6D_6 results in formation of an unusual Fe(I) terminal phenolate adduct, $(\text{DPB})\text{Fe}(\text{OPh})$, with concomitant release of H_2 (detected by GC; Scheme 2.2). $(\text{DPB})\text{Fe}(\text{OPh})$ is an $S = 3/2$ paramagnet with a solution magnetic moment of $3.9 \mu\text{B}$ (C_6D_6 , 25°C). The $\text{Fe}-\text{P}_{\text{avg}}$ and $\text{Fe}-\text{B}$ distances of 2.38 and $2.340(3) \text{ \AA}$ in $(\text{DPB})\text{Fe}(\text{OPh})$ determined by X-ray crystallographic studies (Figure 2.3) are similar to those observed in the previously reported $S = 3/2$ $(\text{DPB})\text{FeBr}$ ($\text{Fe}-\text{P}_{\text{avg}} = 2.38 \text{ \AA}$, $\text{Fe}-\text{B} = 2.3242(11) \text{ \AA}$, $\mu_{\text{eff}} = 3.8 \mu\text{B}$).²⁶ This fact further supports the formulation of $(\text{DPB})\text{Fe}(\text{OPh})$ as a high-spin Fe(I) phenolate.



Scheme 2.2: E-H bond activations mediated by $[(\text{DPB})\text{Fe}]_2(\text{N}_2)$.

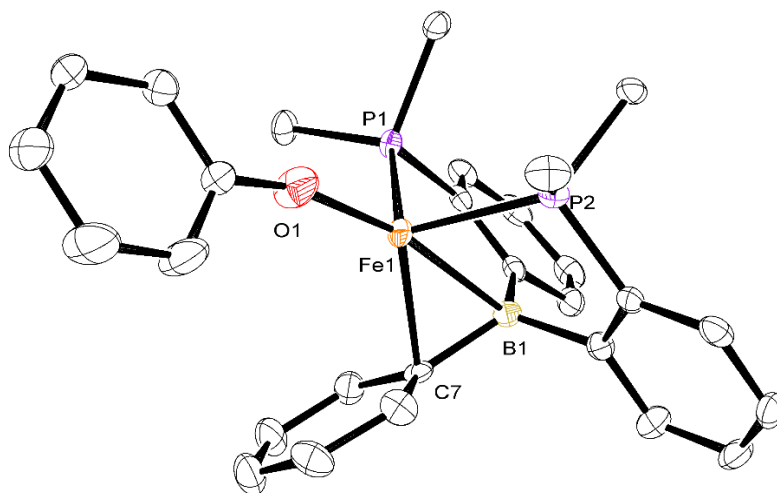


Figure 2.3: ORTEP representation of (DPB)Fe(OPh). Thermal ellipsoids are drawn at the 50% probability level. Methyl substituents on the isopropyl groups and hydrogen atoms attached to carbon have been omitted for clarity. Selected bond distances for (DPB)Fe(OPh): Fe-P1, 2.3736(7) Å; Fe-P2, 2.3777(6) Å; Fe-B, 2.340(3) Å; Fe-O, 1.8665(18) Å; Fe-C7, 2.237(2) Å; Fe-C8, 2.434(3) Å.

In contrast, addition of PhSH to [(DPB)Fe]₂(N₂) gives the dimeric Fe(II) borohydride-phenylthiolate adduct [(DPBH)Fe(SPh)]₂, resulting from formal S–H bond oxidative addition. The ATR-FTIR of [(DPBH)Fe(SPh)]₂ shows a broad absorbance centered at 1949 cm^{−1} that is consistent with the presence of a B–H–Fe moiety.^{26,27} Additionally, the solid-state structure of [(DPBH)Fe(SPh)]₂ shows the absence of a metal–arene interaction and an elongated Fe–B distance of 3.019(2) Å (Figure 2.4) versus 2.3739(7) and 2.3136(7) Å in [(DPB)Fe]₂(N₂) (note: the position of the bridging H atom could not be reliably located

and refined upon for $[(\text{DPBH})\text{Fe}(\text{SPh})]_2$.²⁶

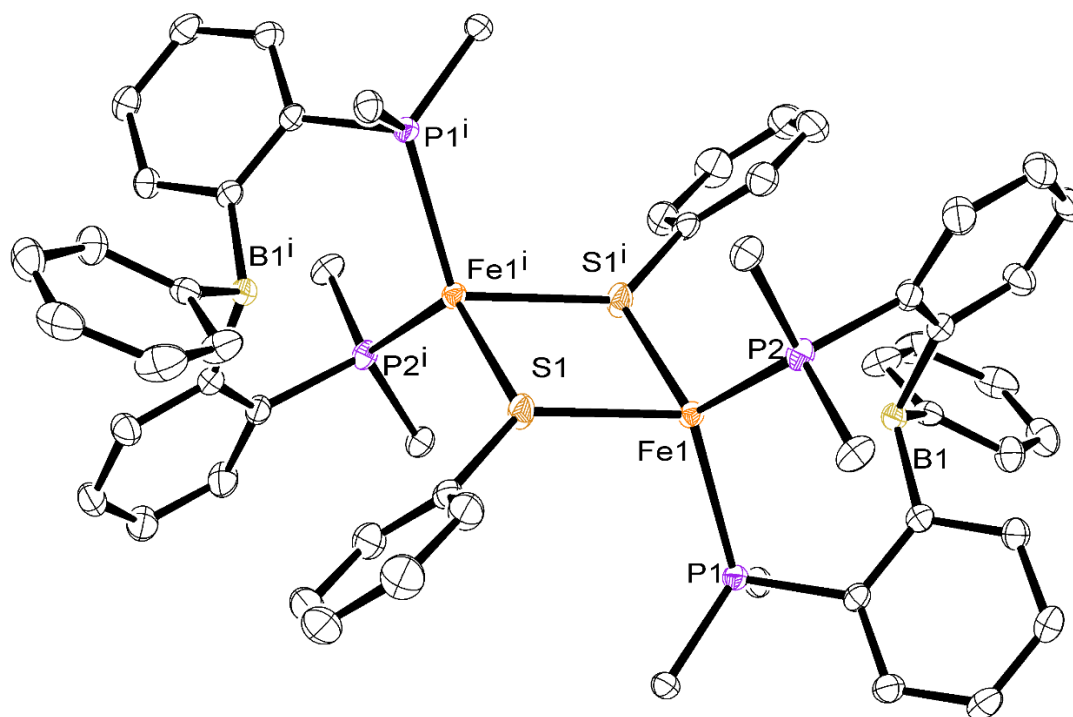
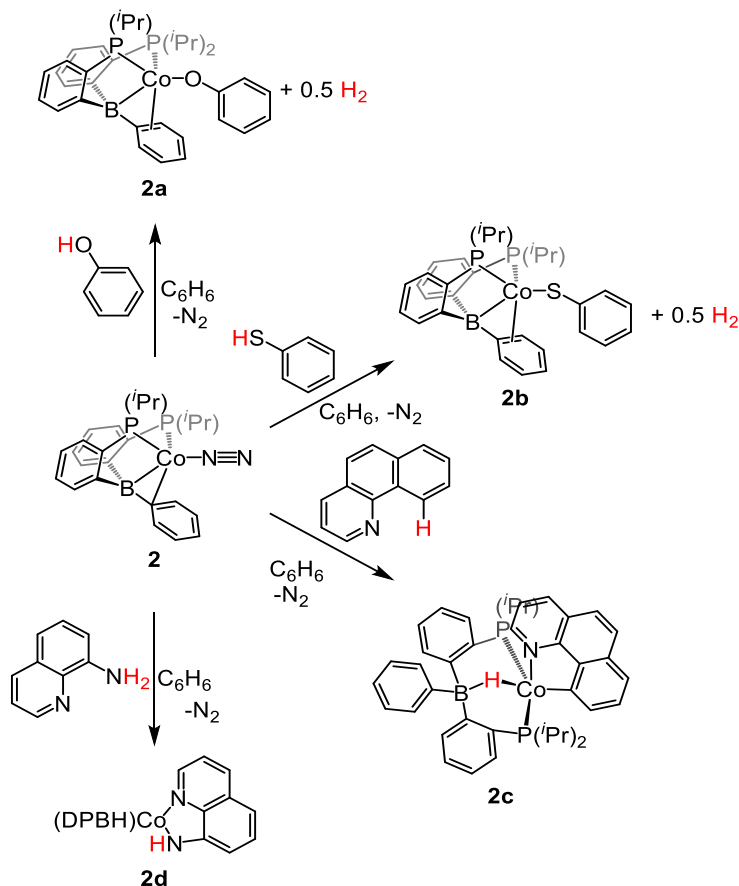


Figure 2.4: ORTEP representation of $[(\text{DPBH})\text{Fe}(\text{SPh})]_2$. Thermal ellipsoids are drawn at the 50% probability level. Methyl substituents on the isopropyl groups and hydrogen atoms attached to carbon have been omitted for clarity. Selected distances for $[(\text{DPBH})\text{Fe}(\text{SPh})]_2$: Fe-P1, 2.49770(13) Å; Fe-P2, 2.5296(2) Å; Fe-B, 3.019(2) Å; Fe-S1, 2.42445(18) Å Fe-S1ⁱ, 2.37283(14).

Treatment of $(\text{DPB})\text{Co}(\text{N}_2)$ with PhOH or PhSH gave the isostructural phenolate and phenylthiolate adducts $(\text{DPB})\text{Co}(\text{OPh})$ ($\mu_{\text{eff}} = 3.2 \mu\text{B}$ at 25 °C), and $(\text{DPB})\text{Co}(\text{SPh})$ ($\mu_{\text{eff}} = 2.6 \mu\text{B}$ at 25°C), respectively (Scheme 2.3), accompanied by the release of H_2 (detected by GC).



Scheme 2.3: E-H bond activations mediated by (DPB)Co(N₂).

The solid-state structures of (DPB)Co(OPh) and (DPB)Co(SPh) are shown in Figure 2.5 and Figure 2.6. The Co–O distance of 1.8904(15) Å in (DPB)Co(OPh) (Figure 2.5) is consistent with the only other structurally characterized Co(I) compound bearing a terminal phenolate ligand, (PPh₃)₃CoOPh; the latter species displays a Co–O distance of 1.9 Å.²⁸ Other Co(II) compounds bearing a terminal phenolate ligand have similar Co–O distances ranging from 1.85 to 1.91 Å.^{29,30} Terminal Co(I) phenylthiolate compounds are more common, and the observed Co–S distance of 2.2483(3) Å in (DPB)Co(SPh) lies within the reported range 2.24–2.35 Å.^{31–35} Furthermore, the Co–P_{avg} distances of 2.29 Å for (DPB)Co(OPh) and 2.33 Å for (DPB)Co(SPh) and the Co–B distances of 2.302(2) Å for

(DPB)Co(OPh) and 2.2828(12) Å for (DPB)Co(SPh) closely match the Co–P_{avg} distance of 2.30 Å and Co–B distance of 2.3070(7) Å in (DPB)CoBr (Figure 2.S2). Additional confirmation of the identities of compounds (DPB)Fe(OPh), (DPB)Co(OPh), and (DPB)Co(SPh) was obtained by independent preparation via reaction of (DPB)FeBr or (DPB)CoBr with NaOPh or NaSPh in THF.

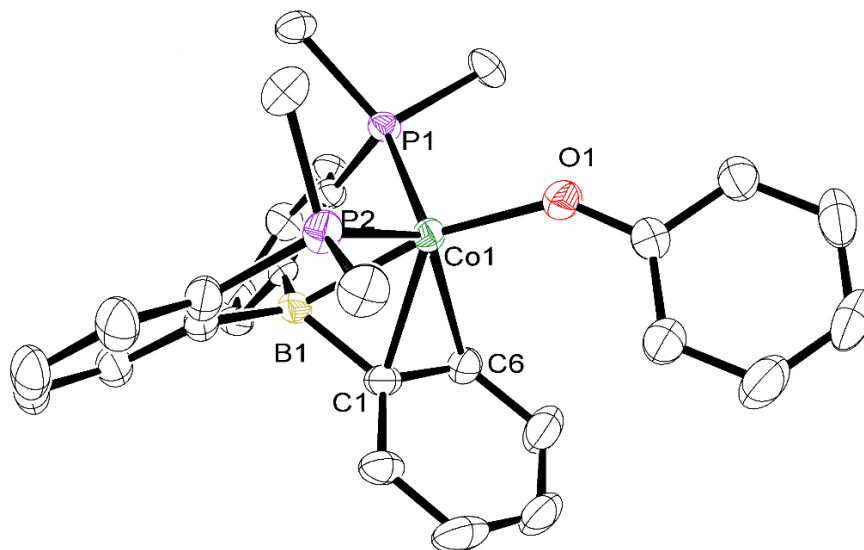


Figure 2.5: ORTEP representation of (DPB)Co(OPh). Thermal ellipsoids are drawn at the 50% probability level. Methyl groups on the isopropyl substituents and hydrogen atoms bonded to carbon have been omitted for clarity. Selected distances for (DPB)Co(OPh): Co–P1, 2.2984(5) Å; Co–P2, 2.2813(6) Å; Co–B, 2.302(2) Å; Co–O, 1.8904(15) Å; Co–C1, 2.245(2) Å; Co–C6, 2.499(2) Å.

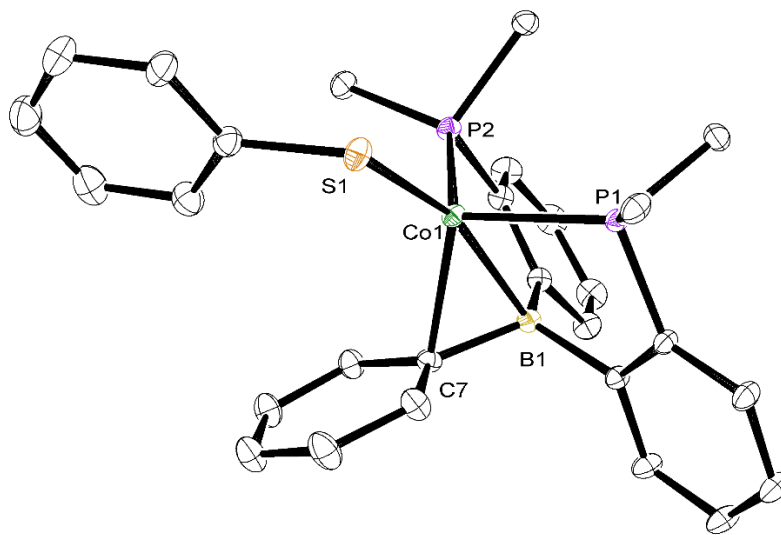


Figure 2.6: ORTEP representation of (DPB)Co(SPh). Thermal ellipsoids are drawn at the 50% probability level. Methyl groups on the isopropyl substituents and hydrogen atoms bonded to carbon have been omitted for clarity. Selected distances for (DPB)Co(SPh): Co-P1, 2.3381(3) Å; Co-P2, 2.3203(3) Å; Co-B, 2.2828 (12) Å; Co-S, 2.2483(3) Å; Co-C7, 2.2390(11) Å.

2.2.2 Reactivity of 1 and 2 with Benzo[h]quinolone. (DPB)Fe(OPh), (DPB)Co(OPh), and (DPB)Co(SPh) can be considered as the products of formal one-electron processes in which [(DPB)Fe]₂(N₂) or (DPB)Co(N₂) acts as a reductant. One plausible mechanistic scenario that could lead to products such as (DPB)Fe(OPh), (DPB)Co(OPh), and (DPB)Co(SPh) is where a four-coordinate Fe(II) or Co(II) borohydride-phenolate or a Co(II) borohydride-phenylthiolate is transiently formed. This transient could then be followed by a bimolecular reductive elimination step to release H₂ and generate the observed monovalent products. While we have not undertaken mechanistic studies of the reactions that produce (DPB)Fe(OPh), (DPB)Co(OPh), and

(DPB)Co(SPh), the isolation of [(DPBH)Fe(SPh)]₂ suggested species of this type might be more generally accessible. The structure of [(DPBH)Fe(SPh)]₂ also indicated that a species formed by oxidative addition of an E–H bond at [(DPB)Fe]₂(N₂) or (DPB)Co(N₂) might be stabilized by increasing the coordination number of the metal center to five. With this in mind, we explored the reactivity of [(DPB)Fe]₂(N₂) and (DPB)Co(N₂) with chelating substrates that could stabilize the products of E–H bond oxidative addition.

Benzo[h]quinolone has been used previously as a substrate in directed C–H bond arylation.^{36–38} Heating benzo[h]-quinoline with [(DPB)Fe]₂(N₂) in benzene to 70 °C for a period of ca. 3 h cleanly afforded the oxidative addition product (DPBH)Fe(benzo[h]quinolin-10-yl) (Scheme 2.2). (DPBH)Fe(benzo[h]quinolin-10-yl) adopts a six-coordinate structure in the solid state and is diamagnetic (Figure 2.7). A broad singlet appears in its ¹H NMR spectrum located at $\delta = -22.80$ ppm, consistent with a borohydride. The bridging B–H–Fe moiety was confirmed via an XRD study, and the bridging hydride was successfully located and refined (Figure 2.7). The Co analogue (DPBH)Co(benzo[h]quinolin-10-yl) (Scheme 2.3), was synthesized under similar conditions and is an $S = 1/2$ paramagnetic species with a solution magnetic moment of 1.79 μ_B (C₆D₆, 25 °C). Complex (DPBH)Co(benzo[h]quinolin-10-yl) displays a broad M–H–B stretch at 2047 cm^{–1} in its thinfilm ATR-FTIR spectrum.

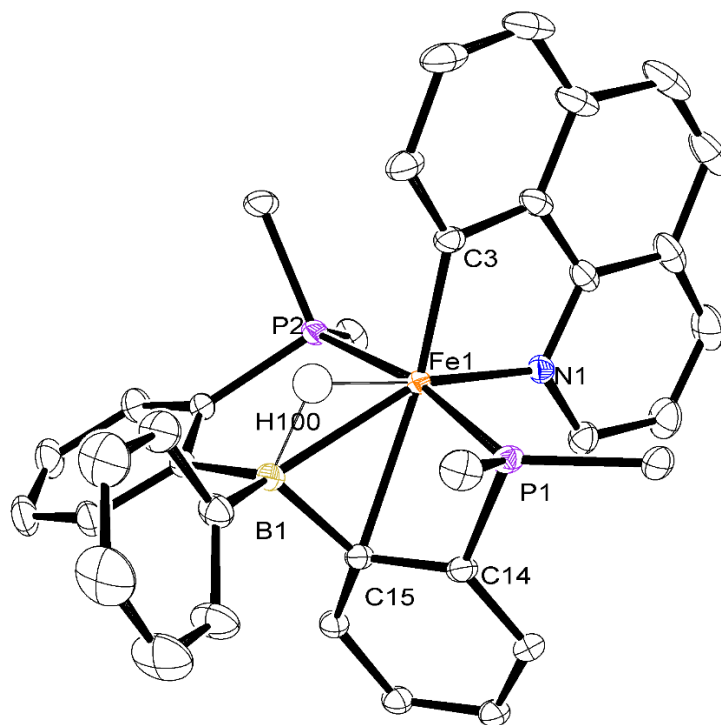


Figure 2.7: ORTEP representation of (DPBH)Fe(benzo[h]quinolin-10-yl). Thermal ellipsoids are drawn at the 50% probability level. Methyl substituents on the isopropyl groups and hydrogen atoms bonded to carbon have been omitted for clarity. Selected distances for (DPBH)Fe(benzo[h]quinolin-10-yl): Fe-P1, 2.2189(3) Å; Fe-P2 2.2665(3) Å; Fe-H100, 1.591(19) Å; Fe-C3, 1.9286(8) Å; Fe-N1, 1.9682(8) Å; Fe-C15, 2.3739(8) Å; Fe-B, 2.3342(9) Å.

Interestingly, the Fe center in (DPBH)Fe(benzo[h]quinolin-10-yl) interacts with one of the ipso carbons on the borane ligand to adopt a distorted octahedral geometry, resulting in an 18-electron, $S = 0$ ground state (Figure 2.7). In contrast (DPBH)Co(benzo[h]quinolin-10-yl) adopts a five-coordinate geometry best described as a distorted square-based pyramid ($\tau_5 = 0.386$) (Figure 6; $\tau_5 = 0$ for ideal square-based pyramid, $\tau_5 = 1$ for ideal trigonal bipyramid)³⁹ to give the observed 17-electron, $S = 1/2$ ground state (Figure 2.8).

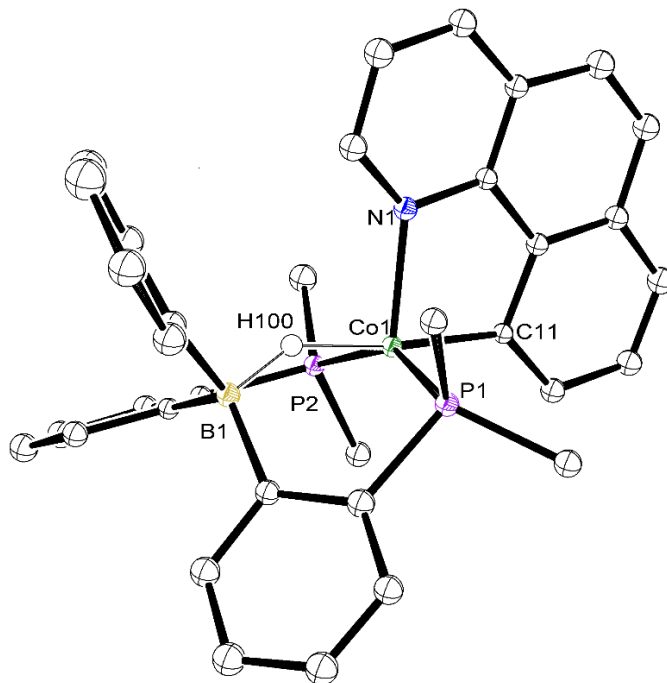


Figure 2.8: ORTEP representation of of (DPBH)Co(benzo[h]quinolin-10-yl). Thermal ellipsoids are drawn at the 50% probability level. Methyl substituents on the isopropyl groups and hydrogen atoms bonded to carbon have been omitted for clarity. Selected distances for (DPBH)Co(benzo[h]quinolin-10-yl): Co-P1, 2.2604(18) Å; Co-P2, 2.2331(18) Å; Co-H100, 1.59(5) Å; Co-N1, 2.040(5) Å; Co-C11, 1.931(6) Å; Co-B, 2.698 Å.

2.2.3 Reactivity of [(DPB)Fe]₂(N₂) and (DPB)Co(N₂) with 8-Aminoquinoline. N–H bond activation and functionalization using Fe and Co is less well established than C–H activation. Reports of N–H bond activation with Fe are primarily limited to relatively acidic amides,^{40,41} and N–H bond activation chemistry of amines by Co is similarly scarce.^{42–45} The N–H bond in 8-aminoquinoline adds across the M–B unit in [(DPB)Fe]₂(N₂) and (DPB)Co(N₂) to afford (DPBH)Fe(8-amidoquinoline) and

(DPBH)Co(8-amidoquinoline) over several hours at room temperature (Schemes 2.2 and 2.3). In the case of (DPB)Co(N₂) the reaction reaches completion more quickly by evacuating the head space via freeze–pump–thaw cycles to remove N₂.

The ¹H NMR spectrum of the reaction mixture producing (DPBH)Fe(8-amidoquinoline) shows more than 30 paramagnetically broadened and shifted peaks, suggesting either a single species with C₁ symmetry in solution or two different C_s symmetric species. The distribution of products does not change when the reaction is run at elevated temperatures (80 °C), and the ¹H NMR spectrum of the reaction mixture in d₈-toluene does not change significantly over the temperature range of 25 to 75 °C. Cooling to low temperatures (–90 °C) results in the disappearance of most of the paramagnetically shifted features with no new diamagnetic signals (Figure 2.S3). Single crystals of the reaction products were highly twinned in many cases; the least twinned crystal of several screened was chosen and showed the anticipated N–H oxidative addition product (DPBH)Fe(8-amidoquinoline) with the major component (~90%) having the amido group located cis to the borohydride and the minor component (~10%) having the amido group trans to the borohydride (Figures 2.9 and 2.10).

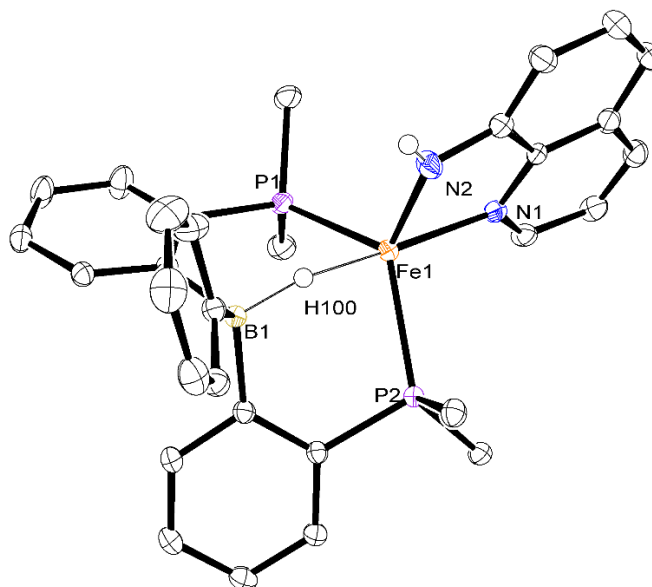


Figure 2.9: ORTEP representation of the major component (90%) of a twinned crystal of (DPBH)Fe(8-amidoquinoline). Ellipsoids are drawn at the 50% probability level. Methyl substituents on the isopropyl groups and hydrogen atoms bonded to carbon have been omitted for clarity. Selected distances for the major component of (DPBH)Fe(8-amidoquinoline): Fe-P1, 2.4324(5) Å; Fe-P2, 2.4552(5) Å, Fe-H100, 1.77(2)Å, Fe-N1, 2.1920(15) Å; Fe-N2, 1.9584(19) Å, Fe-B, 2.9667(17)Å.

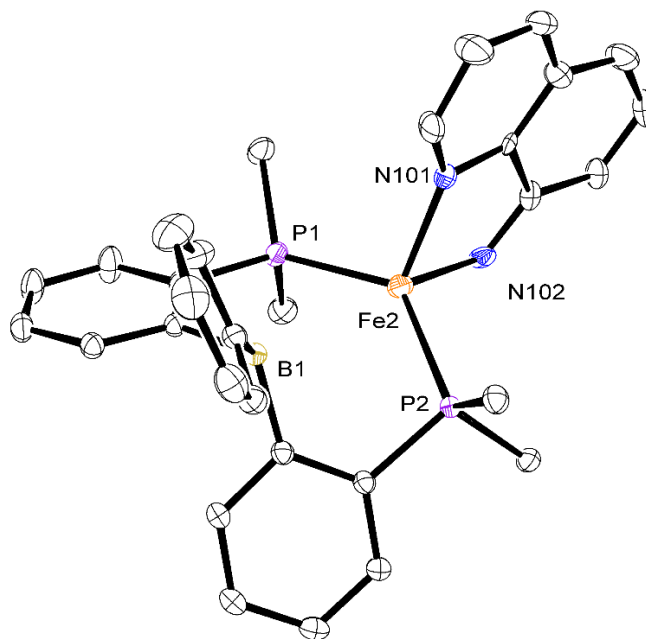


Figure 2.10. ORTEP representation of the minor component (10%) of a twinned crystal of (DPBH)Fe(8-amidoquinoline). Ellipsoids are drawn at the 50% probability level. Methyl substituents on the isopropyl groups and hydrogen atoms bonded to carbon have been omitted for clarity.

The bond metrics of the major component showed a borohydride moiety and elongated Fe–P distances indicative of an $S = 2$ species (Figure 2.9). This assignment is supported by the solution magnetic moment of $5.2 \mu_B$ (C_6D_6 , $25^\circ C$), which is consistent with the presence of high-spin Fe(II) isomers of the appropriate molecular weight. The high-spin ground state observed for (DPBH)Fe(8-amidoquinoline) is interesting since the similar C–H activation product (DPBH)Fe(benzo[h]quinolin-10-yl) is diamagnetic. The difference in spin states is also reflected in the solid-state structure (Figure 2.9) of (DPBH)Fe(8-amidoquinoline); it adopts a five-coordinate distorted trigonal bipyramid geometry ($\tau_5 = 0.82$) as opposed to the six-coordinate pseudo-octahedral geometry

observed in (DPBH)Fe(benzo[h]quinolin-10-yl). This difference in geometry is presumably due to the weaker ligand field exerted by the amido ligand compared to the aryl ligand. As a result, the Fe–H distance in (DPBH)Fe(8-amidoquinoline) lengthens relative to that in (DPBH)Fe(benzo[h]quinolin-10-yl). Evidence in support of this idea can be found in the IR spectrum of (DPBH)Fe(8-amidoquinoline), which shows intense but broad absorptions at 2130 and 2000 cm^{-1} corresponding to B–H–Fe stretches in the two conformational isomers. It remains unclear as to whether formation of the two isomers observed is due to conversion between the two conformations after the N–H bond activation step or if their formation results from differing N–H bond activation pathways.

Reaction of (DPB)Co(N₂) with 8-aminoquinoline proceeds similarly with formation of dark purple (DPBH)Co(8-amidoquinoline) after stirring at room temperature for about 16 h. While single crystals of sufficient quality for X-ray diffraction studies could not be obtained, the proposed connectivity was inferred from the IR spectrum of (DPBH)Co(8-amidoquinoline), which shows a broad B–H–Co stretch at 1961 cm^{-1} and weaker broad N–H stretches at 3384 and 3478 cm^{-1} . Additionally, the 77 K frozen solution X-band EPR spectra of (DPBH)Co(benzo[h]quinolin-10-yl) and (DPBH)Co(8-amidoquinoline) are very similar and suggest similar geometries and spin states at the cobalt center (see Figures 2.S4 and 2.S5 in the Supporting Information). Combustion analysis data are also consistent with this formulation.

2.2.4 Reactivity of (DPB)Co(N₂) with Diphenylsilane. The addition of Ph₂SiH₂ to [(DPB)Fe]₂(N₂) gave a mixture of unidentified products. Addition of 1 equiv. of Ph₂SiH₂ to (DPB)Co(N₂) at room temperature under an atmosphere of N₂ resulted in partial consumption of (DPB)Co(N₂) and formation of a small amount of a new paramagnetic

species as judged by ^1H NMR spectroscopy (Figure 2.11, spectrum A). Upon addition of excess Ph_2SiH_2 (10 equiv.), a new species with paramagnetically shifted resonances can be clearly observed, although $(\text{DPB})\text{Co}(\text{N}_2)$ is still present (Figure 2.11, spectrum B). Increasing the amount of Ph_2SiH_2 to 100 equiv. shows an increase in the concentration of the new paramagnet relative to $(\text{DPB})\text{Co}(\text{N}_2)$ (Figure 2.11, spectrum C). Subjecting the reaction mixture to three freeze–pump–thaw cycles drives complete conversion of $(\text{DPB})\text{Co}(\text{N}_2)$ into the new species (Figure 2.11, spectrum D). Reintroduction of N_2 to the J-Young NMR tube followed by stirring overnight regenerates the spectrum shown in Figure 2.11 spectrum C. These observations suggest that an equilibrium between $(\text{DPB})\text{Co}(\text{N}_2)$ and the new species observed by ^1H NMR spectroscopy (formulated as $(\text{DPBH})\text{Co}(\text{SiHPh}_2)$) exists, as was observed for $(^{\text{Ph}}\text{DPB}^{\text{Mes}})\text{Ni}$ and $(^{\text{Ph}}\text{DPB}^{\text{Mes}}\text{H})\text{Ni}(\text{SiHPh}_2)$ (Scheme 2.4).¹¹ A small amount of an unidentified diamagnetic Co side-product was also observed in the ^1H NMR spectrum, which displays a triplet resonance centered at -17.13 ppm with $^2J_{\text{P-H}} = 44.3$ Hz.

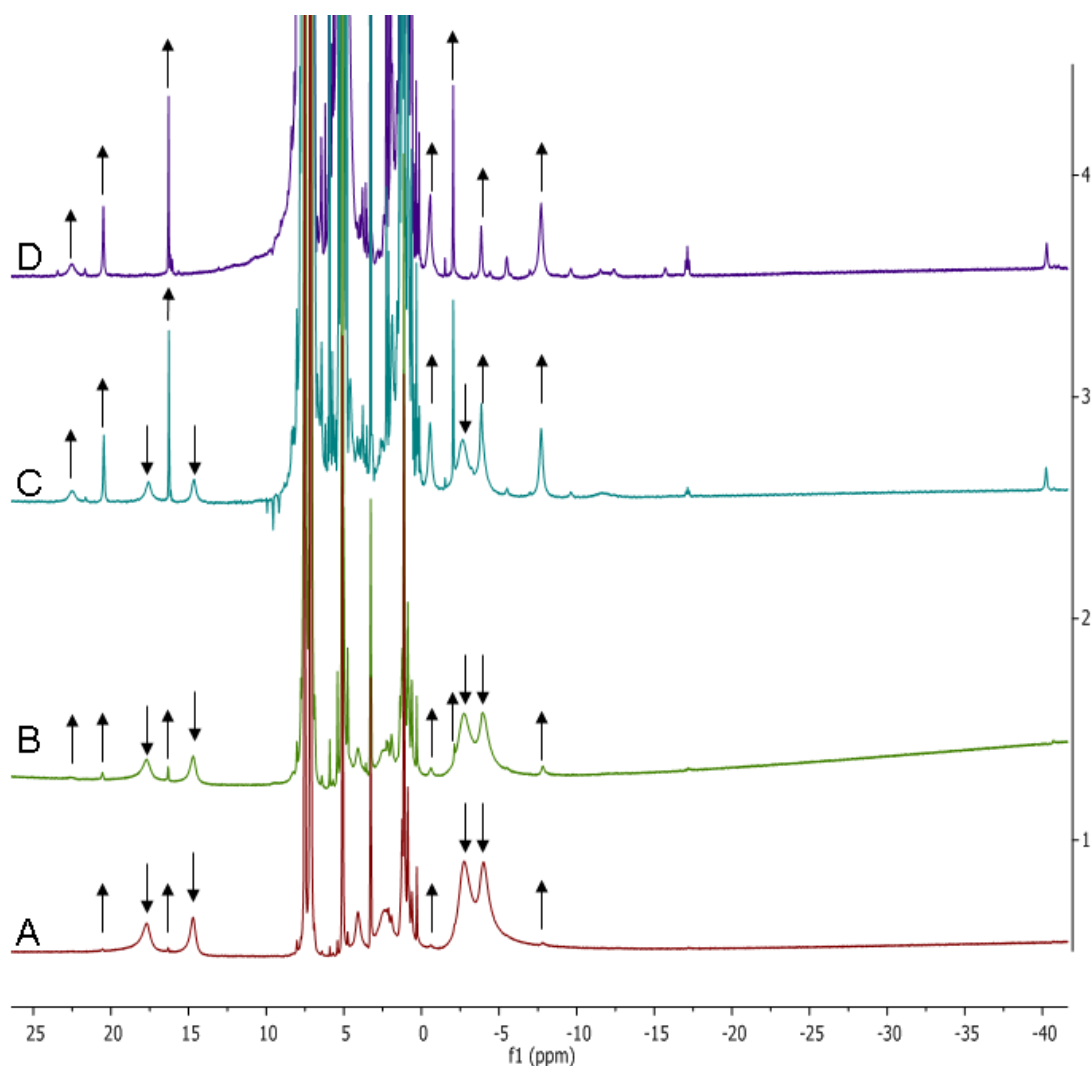
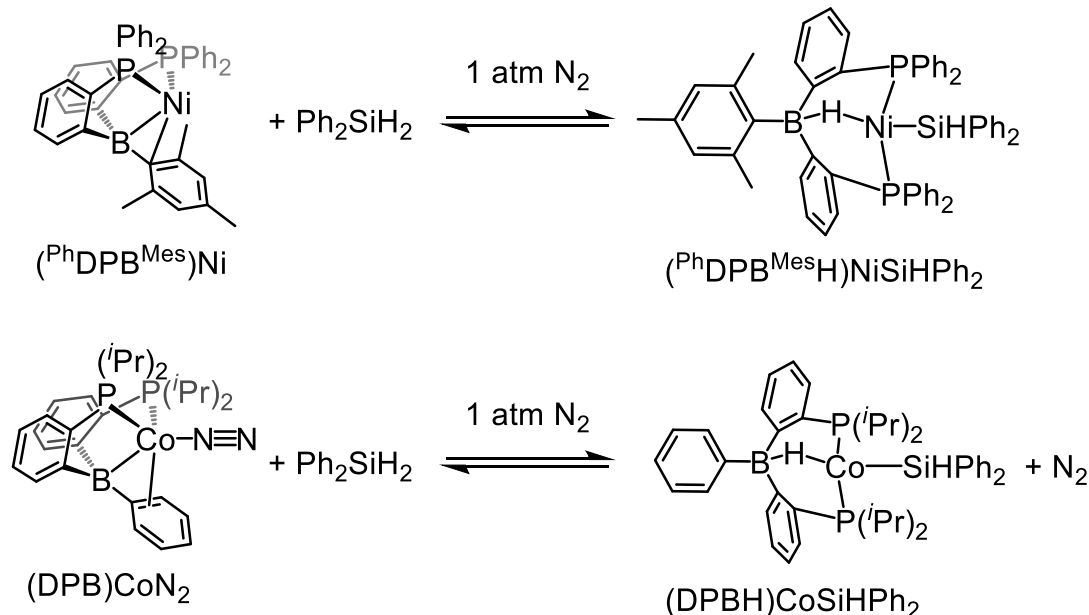


Figure 2.11: ^1H NMR spectra in C_6D_6 of $(\text{DPB})\text{Co}(\text{N}_2)$ in the presence of Ph_2SiH_2 under N_2 (A-C) and vacuum (D). (A) $(\text{DPB})\text{Co}(\text{N}_2)$ + 1 equiv. Ph_2SiH_2 . (B) $(\text{DPB})\text{Co}(\text{N}_2)$ + 10 equiv. Ph_2SiH_2 . (C) $(\text{DPB})\text{Co}(\text{N}_2)$ + 100 equiv. Ph_2SiH_2 . (D) $(\text{DPB})\text{Co}(\text{N}_2)$ + 100 equiv. Ph_2SiH_2 under vacuum. Upward arrows indicate the new paramagnetic species growing in assigned as $(\text{DPBH})\text{Co}(\text{SiHPh}_2)$. Downward arrows indicate consumption of $(\text{DPB})\text{Co}(\text{N}_2)$.



Scheme 2.4: Reversible Si-H Activation at $(\text{PhDPB}^{\text{Mes}})\text{Ni}$ and $(\text{DPB})\text{Co}(\text{N}_2)$

The reaction of $(\text{DPB})\text{Co}(\text{N}_2)$ with 100 equiv. of Ph_2SiH_2 was studied by X-band EPR spectroscopy at 77 K in benzene under vacuum in order to gain further characterization of $(\text{DPBH})\text{Co}(\text{SiHPh}_2)$. Upon degassing the reaction mixture with three freeze–pump–thaw cycles, a slight color change from red-orange to orange was observed and the ^1H NMR spectrum of the reaction mixture confirmed complete consumption of $(\text{DPB})\text{Co}(\text{N}_2)$ (Figure 2.11 spectrum D). The EPR spectrum of the reaction mixture (Figure 2.12) showed clean formation of a new $S = 1/2$ species, which arises from the new paramagnet species observed in the ^1H NMR: $(\text{DPBH})\text{Co}(\text{SiHPh}_2)$ (Figure 2.11). To support the assignment of $(\text{DPBH})\text{Co}(\text{SiHPh}_2)$ we conducted solution IR studies of $(\text{DPB})\text{Co}(\text{N}_2)$ in the presence of 100 equiv. of diphenylsilane under a nitrogen atmosphere. Under these conditions a feature at 1810 cm^{-1} was observed, which can be assigned to a B–H–Co stretching mode.

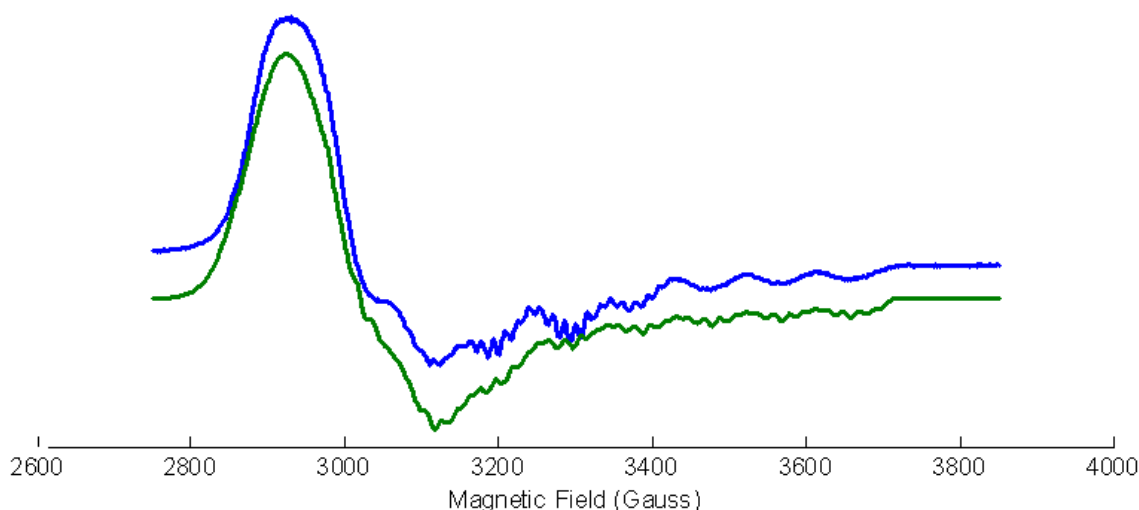


Figure 2.12: X-Band EPR Spectrum of (DPBH)Co(SiHPh₂) in benzene at 77 K in toluene glass (9.49 GHz) (top, blue trace) and simulation (bottom, green trace) ($g_1 = 2.2836$, $g_2 = 2.1703$, $g_3 = 2.0098$; nuclei = Co, P, P, H; $A_{\text{Co}} = 255.346$ MHz, $A_{\text{P1}} = 111$ MHz, $A_{\text{P2}} = 62$ MHz, $A_{\text{H}} = 39$ MHz; $\text{HStrain}_1 = 275.565$ MHz, $\text{HStrain}_2 = 375.565$ MHz, $\text{HStrain}_3 = 35$ MHz).

2.3 Catalytic Hydrosilylation of Ketones and Aldehydes. We next explored the activity of [(DPB)Fe]₂(N₂) and (DPB)Co(N₂) as precatalysts for the hydrosilylation of organic carbonyl compounds and compared their activity to that of (^{Ph}DPB^{Mes})Ni.^{9,11} The ability of transition metal compounds to facilitate catalytic hydrosilylation of ketones and aldehydes has been highlighted for synthetic methodological significance relative to stoichiometric reductants (e.g., LiAlH₄), and the hydrosilylation of carbon–oxygen multiple bonds has been targeted in the context of organic substrate functionalizations and catalytic CO₂ and CO reduction.^{46–55} A number of groups have thus targeted first-row

transition metal catalysts including iron and cobalt to this end.^{23-25,49,56-64} A selection of the most efficient reported iron and cobalt hydrosilylation catalysts is shown in Chart 2.2.

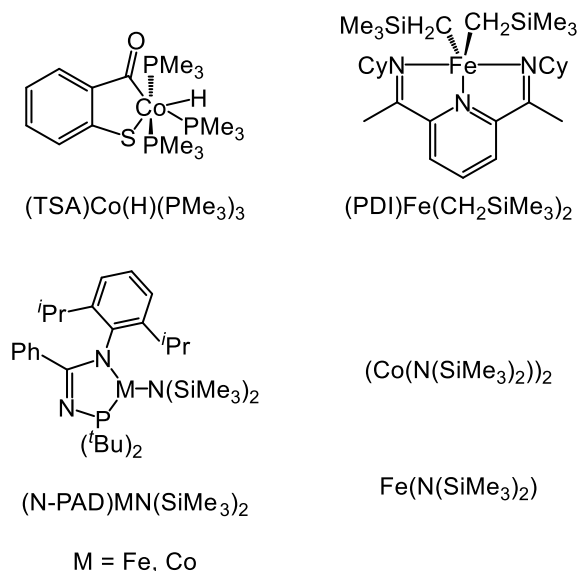


Chart 2.2: Selected examples of previously reported Fe and Co carbonyl hydrosilylation catalysts.

Precatalysts [(DPB)Fe]₂(N₂) and (DPB)Co(N₂) were tested under our previously reported conditions for the catalytic hydrosilylation of benzaldehydes.¹¹ Both [(DPB)Fe]₂(N₂) and (DPB)Co(N₂) are far more active catalysts than (^{Ph}DPB^{Mes})Ni, consistent with their higher degree of reactivity toward E–H bonds relative to (^{Ph}DPB^{Mes})Ni. Full consumption of benzaldehyde was achieved in under 2 min in both cases, while the previously reported (^{Ph}DPB^{Mes})Ni system required several hours to reach completion (Table 2.1).

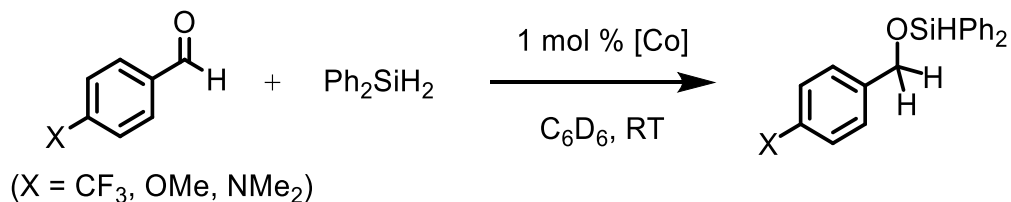
Table 2.1: Comparison of [(DPB)Fe]₂(N₂) and (DPB)Co(N₂) to (^{Ph}DPB^{Mes})Ni for Benzaldehyde Hydrosilylation by Ph₂SiH₂

Entry ^a	Catalyst	Conversion; Time	Yield ^b
1 *	(^{Ph} DPB ^{Mes})Ni	> 98 %; 5.9 hr.	99%
2	[(DPB)Fe] ₂ (N ₂)	>99 %; < 2 min.	99%
3	(DPB)Co(N ₂)	>99 %; < 2 min.	99%

^a1 mmol Ph₂SiH₂, 1 mmol benzaldehyde, 5 mol % catalyst 500 μL C₆D₆. ^bDetermined by ¹H

NMR integration against an internal FeCp₂ standard. * From Reference 11.

The previously reported (^{Ph}DPB^{Mes})Ni benzaldehyde hydrosilylation system showed rate enhancement with electron-donating groups, contrasting Chirik's (PDI)Fe(CH₂SiMe₃)₂ system and other carbonyl reduction catalysts, which have shown rate enhancement with electron-withdrawing substituents.^{11,62,65} Curiously, we found that installing either an electron-withdrawing or electron-donating group led to a dramatic enhancement in the rate of hydrosilylation by (DPB)Co(N₂) with full consumption of the aldehyde in under 2 min when subjected to our standard conditions (Table 2.2).

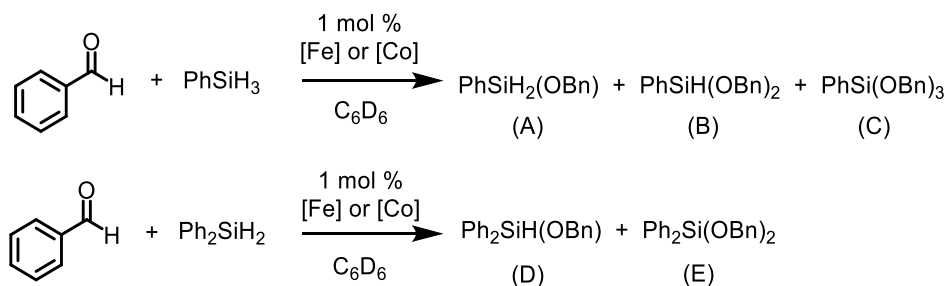
Table 2.2: Substituent Effects on Hydrosilylation of Benzaldehyde by Ph₂SiH₂

Entry ^a	X	Conversion; Time	Yield ^b
1	CF ₃	>99%; <2 min.	88%
2	OMe	>99%; <2 min.	95%
3	NMe ₂	>99%; <2 min.	83%
4	H	>98%; 7.5 hr.	98%

^a1 mmol Ph₂SiH₂, 1 mmol substrate, 1 mol% (DPB)Co(N₂), 500 μL C₆D₆; ^bDetermined by ¹H NMR integration against an internal FeCp₂ standard

Additional studies showed PhSiH₃ to be competent for hydrosilylation of benzaldehyde. The selectivity for a single hydrosilylation product in this reaction was decreased due to the presence of additional Si–H bonds, which facilitated reduction of multiple benzaldehyde equivalents by a single PhSiH₃ molecule. We also found that at lower catalyst loadings the selectivity for a 1:1 stoichiometry of silane to benzaldehyde was reduced and additional products from the reduction of multiple benzaldehyde equivalents were detected in the ¹H NMR spectra and GC-MS traces of the reaction mixtures (Table 2.3, products A–E).

Table 2.3: Comparison of Primary, Secondary and Tertiary Silanes in Hydrosilylation of Benzaldehyde



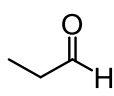
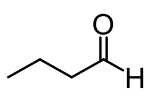
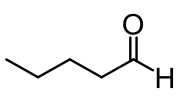
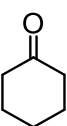
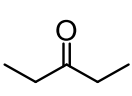
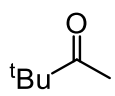
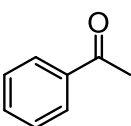
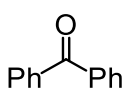
Entry ^a	Catalyst	Silane	Conversion (Time)	Yield ^b
1	[(DPB)Fe] ₂ (N ₂)	PhSiH ₃	>98% (5.6 hr.)	0% (A) 63% (B) 24% (C)
2		Ph ₂ SiH ₂	>97% (10 hr.)	70% (D) 19% (E)
3	(DPB)Co(N ₂)	PhSiH ₃	>98% (2 min)	37% (A) 27% (B) 0% (C)
4		Ph ₂ SiH ₂	>98% (7.5 hr.)	98% (D) 0% (E)

^a1 mmol silane, 1 mmol benzaldehyde, 1 mol % catalyst, 500 μ L C₆D₆. ^bDetermined by ¹H NMR integration against an internal FeCp₂ standard.

The marked enhancement in the rate of hydrosilylation of benzaldehyde by [(DPB)Fe]₂(N₂) and (DPB)Co(N₂) compared to (^{Ph}DPB^{Mes})Ni prompted us to investigate whether [(DPB)Fe]₂(N₂) and (DPB)Co(N₂) would display activity for a larger scope of substrates. While the (^{Ph}DPB^{Mes})Ni system is limited to benzaldehydes, [(DPB)Fe]₂(N₂) and (DPB)Co(N₂) are competent precatalysts for the hydrosilylation of benzaldehydes, alkyl aldehydes, and aryl and alkyl ketones (Tables 2.2, 2.3, 2.4).

Increasing the steric bulk about the carbonyl resulted in a decrease in rate, as evidenced on comparing the hydrosilylation of tert-butyl methyl ketone to that of 2-pentanone (Table 2.4, entries 5, 6, 13, 14). We observed rapid hydrosilylation of 2-pentanone by both $[(DPB)Fe]_2(N_2)$ and $(DPB)Co(N_2)$, whereas hydrosilylation of tertbutyl-methyl ketone was sluggish even at elevated temperatures, showing little conversion after 30 h at 50 °C. The hydrosilylation of benzophenone (a highly activated ketone) proceeds much faster than that of acetophenone despite the increased steric hindrance at the carbonyl.

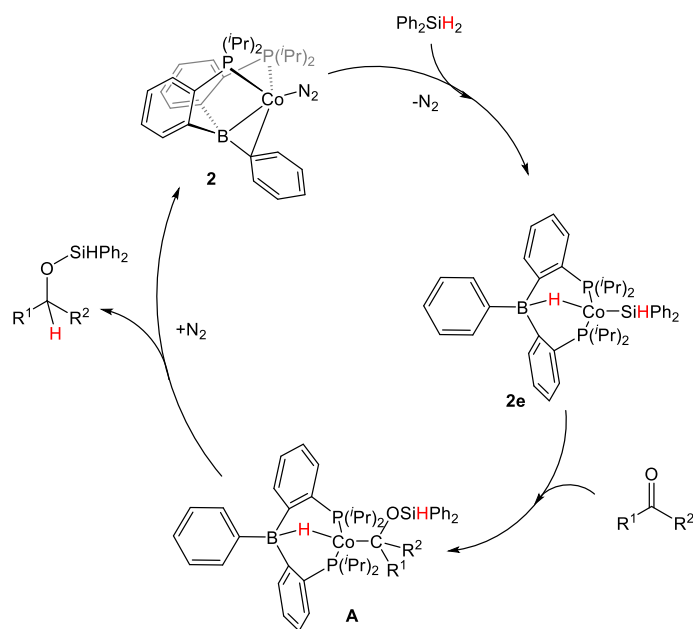
Table 2.4: Summary for Hydrosilylation by Ph_2SiH_2 of Various Aldehydes and Ketones by $[(\text{DPB})\text{Fe}]_2(\text{N}_2)$ and $(\text{DPB})\text{Co}(\text{N}_2)$

							
A	B	C	D	E	F	G	H

Entry ^a	Catalyst	Substrate	Conversion (Time)	Yield ^c
1 ^b	[Fe]	A	>99% ; <5 min.	98%
2 ^b		B	>99%; <10 min.	98%
3 ^b		C	>99%; <10 min.	98%
4 ^b		D	0%; 24 hr.	0%
5		E	>98%; 12 min.	99%
6 ^c		F	<1%; 78 hr.	<1%
7		G	>97%; 21.4 hr.	97%
8		H	>90%; 18.5 hr.	86%
9 ^b	[Co]	A	>99%; < 2 min.	99%
10		B	>99%; <7 min.	99%
11 ^b		C	>98%; <7 min.	97%
12 ^b		D	>96%; 99 hr.	97%
13		E	>99%; 22.4 hr.	99%
14 ^c		F	17%; 78 hr.	16%
15		G	>98%; 3.4 hr.	86%
16		H	>98%; 13 min.	84%

^a1 mmol substrate, 1 mmol silane, 1 mol % catalyst, 500 μL C_6D_6 . ^b1 mmol substrate, 1 mmol Ph_2SiH_2 , 1 mol % catalysts, 500 μL 4:1 THF: d_8 -THF. ^cDetermined by ^1H NMR integration against an internal FeCp_2 standard. ^eReactions were allowed to proceed at room temperature for 48 hours followed by heating to 50 $^\circ\text{C}$ for 30 hours and then worked up.

A plausible mechanistic scenario for the catalytic hydrosilylation of carbonyls by (DPB)Co(N₂) is outlined in Scheme 2.5. This mechanism is similar to the mechanism we have proposed for catalytic hydrosilylation of benzaldehydes by (PhDPB^{Mes})Ni, where we were able to spectroscopically observe a borohydridosiloxyalkyl intermediate during catalytic turnover.¹¹ The structural similarity between (DPB)Co(N₂) and (PhDPB^{Mes})Ni may allow for a similar mechanism, although because the Co-catalyzed cycle involves paramagnetic species, it is not as straightforward to identify intermediates as for the (PhDPB^{Mes})Ni system. We nevertheless speculate that the first step in the catalytic cycle is replacement of the N₂ ligand by silane along with Si–H bond activation to give (DPBH)Co(SiHPh₂). Insertion of the ketone into the Co–Si bond would then give a borohydrido-siloxyalkyl intermediate (Scheme 2.5, A) as demonstrated for (PhDPB^{Mes})Ni. Reductive elimination then releases the hydrosilylation product.



Scheme 2.5: Possible catalytic cycle for hydrosilylation mediated by (DPB)Co(N₂).

It is interesting to note that in almost all cases (DPB)Co(N₂) facilitates the most rapid conversion of the carbonyl to the hydrosilylated product. This contrasts with other reports, comparing isostructural Fe and Co compounds as hydrosilylation catalysts. As an example, Turculet has studied isostructural (N-PAD)M-(N(SiMe₃)₂) (M = Fe, Co; N-PAD = 2,6-diisopropyl-N-di-tertbutylphosphinoamidinate) compounds and demonstrated that the Fe analogues consistently and dramatically outperform the Co system.²⁵ Additionally, the majority of cobalt-catalyzed carbonyl hydrosilylations take place at elevated temperatures and require longer reaction times and greater catalyst loading than those observed in this work.^{23-25,56,60,61} We have prepared and tested several known catalysts under the conditions used herein to accurately compare their performance against [(DPB)Fe]₂(N₂) and (DPB)Co(N₂). These data are summarized in Table 2.5. Li, Klein, and Flörke have reported a Co(III) hydride, (TSA)Co(H)(PMe₃)₃ (TSA= 2-mercaptobenzoyl) (Table 2.5 entry 4), which achieves a TOF of ~50 h⁻¹ when heated to 40 °C or higher.^{24,59} This compound has been cited by Trovitch in a recent perspective as the best reported cobalt catalyst for ketone hydrosilylation.⁵⁹ When tested under identical conditions, (DPB)Co(N₂) significantly outpaces (TSA)Co(H)(PMe₃)₃; (TSA)Co(H)(PMe₃)₃ consumes only a fraction of substrate over the course of several days under our standard conditions. To our knowledge (DPB)Co(N₂) is hence the most active cobalt hydrosilylation catalyst for ketones and aldehydes reported to date, at least under the conditions studied herein. An Fe-based catalyst studied by Tilley, however, was also evaluated for comparison under the present conditions and was found to afford full conversion of substrate slightly more rapidly than for [(DPB)Fe]₂(N₂) or (DPB)Co(N₂) (Table 2.5, entry 3).²³

Table 2.5: Comparison of Known Catalysts with [(DPB)Fe]₂(N₂) and (DPB)Co(N₂) for Hydrosilylation of Acetophenone by Ph₂SiH₂

Entry ^a	Catalyst ^b	Conversion; Time	Yield ^c
1	[(DPB)Fe] ₂ (N ₂)	>97%; 21.4 hr.	97%
2	(DPB)Co(N ₂)	>98%; 3.4 hr.	86%
3	Fe[N(SiMe ₃) ₂] ₂	>96%; 0.8 hr.	100%
4	Co[N(SiMe ₃) ₂] ₂	26%; 5.2 day	26%
5	(TSA)Co(H)(PMe ₃) ₃	15%; 4.1 day	13%

^a1 mmol acetophenone, 1 mmol Ph₂SiH₂, 1 mol % catalyst, 500 μL C₆D₆. ^bSee Chart 2.2.

^cDetermined by ¹H NMR integration against an internal FeCp₂ standard.

2.4 Conclusions

We have shown that the first-row transition metal–borane compounds [(DPB)Fe]₂(N₂) and (DPB)Co(N₂) are capable of facilitating a variety of E–H bond activations and are competent precatalysts for the hydrosilylation of ketones and aldehydes. Reactivity with substrates such as PhOH and PhSH proceeded under mild conditions without use of a directing group, giving terminal Fe and Co phenolates, a dimeric Fe-phenylthiolate-borohydride, and a terminal Co phenylthiolate. The reactivity of [(DPB)Fe]₂(N₂) and (DPB)Co(N₂) with less reactive E–H bonds such as aryl C–H and N–H bonds was facilitated by the use of substrates capable of chelating the metal center. ¹H NMR, X-band EPR, and solution IR studies indicated that reversible activation of the Si–H bonds in diphenylsilane is mediated by (DPB)Co(N₂), prompting us to investigate [(DPB)Fe]₂(N₂) and (DPB)Co(N₂) for applications in hydrosilylation catalysis. We found that [(DPB)Fe]₂(N₂) or (DPB)Co(N₂) are competent precatalysts for the hydrosilylation of aldehydes and ketones under mild conditions, and these catalysts outperform our previously reported and

structurally related Ni system. Additionally, when tested under identical conditions against other reported cobalt hydrosilylation catalysts, we found (DPB)Co(N₂) exhibited the highest catalytic activity. The current study thus highlights the applicability of metalloboranes as precatalysts for hydrosilylation of ketones and aldehydes.

2.5 Supporting Information

2.5.1: Experimental Section

General Considerations: All manipulations were performed using standard Schlenk or glovebox techniques under an atmosphere of N₂. Solvents were degassed and dried by sparging with N₂ gas and passage through an activated alumina column. Deuterated solvents were purchased from Cambridge Isotopes Laboratories, Inc., and were degassed and stored over activated 3 Å molecular sieves prior to use. Reagents were purchased from commercial vendors and used without further purification unless otherwise noted. Propanal, butanal, pentanal, and cyclohexanone were dried over CaSO₄, distilled under nitrogen or vacuum, and stored over 3 Å molecular sieves prior to use. All reagents were checked for purity by ¹H NMR spectroscopy prior to use. DPB⁶⁶ and [(DPB)Fe]₂(N₂)²⁶ were synthesized according to literature procedures. Combustion analyses were performed by Midwest Microlab (Indianapolis, IN, USA) or Robertson Microlit Laboratories (Ledgewood, NJ, USA).

Spectroscopic Measurements. ¹H, ¹³C, ³¹P, and ¹¹B NMR spectra were collected at room temperature on a Varian 400 MHz spectrometer or a Varian 300 MHz spectrometer. ¹H and ¹³C spectra were referenced to residual solvent resonances. ³¹P NMR spectra were referenced to external 85% phosphoric acid (δ = 0 ppm). ¹¹B NMR spectra were referenced to BF₃·Et₂O (δ = 0 ppm). UV–vis measurements were performed with a Cary 50 instrument

with Cary WinUV software. IR spectra were obtained as thin films formed by evaporation or as a solution using a cell with KBr windows using a Bruker Alpha Platinum ATR spectrometer with OPUS software. EPR spectra were recorded on a Bruker EMS spectrometer in frozen solutions at 77 K. EPR simulations used the EasySpin software package.⁶⁷

X-ray Crystallography. X-ray diffraction studies were carried out at the Caltech Division of Chemistry and Chemical Engineering X-ray Crystallography Facility on a Bruker three-circle SMART diffractometer with a SMART 1K CCD detector, APEX CCD detector, or Bruker D8 VENTURE Kappa Duo PHOTON 100 CMOS detector. Data were collected at 100 K using Mo K α radiation ($\lambda = 0.710\ 73\ \text{\AA}$) or Cu K α radiation ($\lambda = 1.541\ 78\ \text{\AA}$). Structures were solved by direct or Patterson methods using SHELXS and refined against F^2 on all data by full-matrix least-squares with SHELXL-2000.⁶⁸ All non-hydrogen atoms were refined anisotropically. With the exception of any μ -B-H-M hydrides that were located on the difference map, all hydrogen atoms were placed at geometrically calculated positions and refined using a riding model. The isotropic displacement parameters of all hydrogen atoms were fixed at 1.2 (1.5 for methyl groups) times the U_{eq} of the atoms to which they are bonded. An A level alert is generated by Checkcif for the structure of (DPBH)Fe(8-amidoquinoline) because of a close H-H contact between H20C (a calculated isopropyl methyl hydrogen) and H108 (a calculated aryl H atom on the minor part of the disordered 8-amidoquinolinyll ligand). Because the close H-H contact is between a calculated methyl H atom and a partially occupied calculated H atom on a highly disordered ligand, we do not anticipate that this is cause for concern or indicative of missing symmetry or a false solution.

Preparation of (DPB)FeOPh: 62.7 mg (0.058 mmol) amount of [(DPB)Fe]₂(N₂) was dissolved in ca. 10 mL of benzene to form a dark red-brown solution. 10.8 mg (0.115 mmol) PhOH dissolved in ca. 5 mL of benzene was added to the solution of [(DPB)Fe]₂(N₂). Over the course of ~1.5 h the solution turned from dark red-brown to dark yellow-brown. The solution was allowed to stir overnight (~16 h). GC analysis of the headspace of the reaction mixture showed formation of H₂. The reaction mixture was lyophilized, leaving a dark residue. Crystals suitable for X-ray diffraction studies were grown by cooling a concentrated solution in Et₂O to -30 °C in a freezer. Yield: 71.1 mg (0.114 mmol), 99.1%. ¹H NMR (400 MHz, C₆D₆): δ 142.34, 109.34, 91.02, 70.19, 5.63, 39.49, 28.01, 21.49, 21.15, 12.18, 11.02, 5.20, -0.14, -0.26, -5.69, -6.69, -11.02, -13.75, -16.56, -18.12, -28.44, -36.17, -52.16. Solution magnetic moment (25 °C, C₆D₆): 3.9 μ_B. UV-vis [toluene, λ(nm){ε(M⁻¹ cm⁻¹)}: 318(sh){5723}, 393{3434}, 877{219}. Combustion analysis for C₃₆H₄₆BFeOP₂: calcd. C 69.36, H 7.44; found C 69.25, H 7.03

Alternative Synthesis of (DPB)Fe(OPh): 17.9 mg (0.03 mmol) of (DPB)FeBr was dissolved in 10 mL of Et₂O, and the mixture was added to a solution of 3.7 mg (0.03 mmol) of NaOPh in 5 mL of Et₂O and stirred for 16 h. The resulting yellow-brown solution was filtered through Celite and evaporated to dryness, leaving a brown residue. This residue was extracted in benzene and lyophilized, giving a fine brown powder, which showed identical spectroscopic features to the product (DPB)Fe(OPh) prepared by the previously described method. Yield: 17.4 mg (0.028 mmol), 93.3%.

Preparation of [(DPBH)Fe(SPh)]: 16.3 mg (0.107 mmol) of [(DPB)Fe]₂(N₂) was dissolved in ca. 10 mL of benzene to form a dark red brown solution. Then 23.6 mg

(0.0214 mmol) of PhSH dissolved in ca. 5 mL of benzene was added to the solution of $[(DPB)Fe]_2(N_2)$. Over the course of ~ 1.5 h the solution turned from dark red-brown to red-orange. The solution was allowed to stir overnight and lyophilized, leaving a fine pale orange powder. Yield: 105.2 mg (0.0821 mmol), 76.7%. 1H NMR (400 MHz, C_6D_6): δ 117.20, 52.99, 48.53, 42.05, 24.28, 13.75, 13.53, 9.11, -7.71 , -8.62 , -15.94 , -21.91 , -24.23 , -25.02 , -27.25 , -44.97 . Solution magnetic moment (25 °C, toluene- d_8): $4.77 \mu_B$ per Fe center. IR (thin film from C_6D_6 , cm^{-1}): 1961 (br, B–H–Fe). UV–vis [toluene, $\lambda(nm)\{\epsilon(M^{-1} cm^{-1})\}$]: 324(sh){9600}, 418(sh){3200}. Combustion analysis for $C_{72}H_{94}B_2Fe_2S_2P_4$: calcd. C 67.52, H 7.40; found C 66.85, H 6.95.

Preparation of (DPBH)Fe(benzo[h]quinolin-10-yl): A solution of $[(DPB)Fe]_2(N_2)$ (19.1 mg, 0.0176 mmol) and benzo[h]quinoline (6.3 mg, 0.035 mmol) in 0.7 mL of C_6D_6 was heated at 70 °C until all of $[(DPB)Fe]_2(N_2)$ was consumed (3 h). Solvent was removed *in vacuo*, and the resulting solids were washed with cold pentane (3×1 mL) and dissolved in minimal Et_2O . Evaporation of the saturated Et_2O solution into HMDSO gave single crystals of $(DPBH)Fe(benzo[h]quinolin-10-yl)$, which were lyophilized from C_6H_6 to give magenta solids. Yield: 14.0 mg (0.0197 mmol), 56%. 1H NMR (500 MHz, C_6D_6): δ 9.02–8.86 (m, 1H), 7.56 (d, $^3J_{HH} = 8.7$ Hz, 1H), 7.47 (d, $^3J_{HH} = 7.9$ Hz, 2H), 7.46 (s, 1H), 7.45–7.41 (m, 4H), 7.39 (d, $^3J_{HH} = 6.6$ Hz, 2H), 7.33–7.28 (m, 4H), 7.25–7.19 (m, 4H), 7.12 (s, 1H), 6.70 (d, $^3J_{HH} = 5.3$ Hz, 1H), 6.41 (dd, $^3J_{HH} = 7.8, 5.4$ Hz, 1H), 1.78–1.50 (m, 4H), 0.87 (d, $^3J_{HH} = 7.0$ Hz, 6H), 0.73 (d, $^3J_{HH} = 6.3$ Hz, 6H), 0.18 (s, 6H), 0.11 (d, $^3J_{HH} = 6.4$ Hz, 6H), -22.80 (s, 1H). ^{11}B NMR (160 MHz, C_6D_6): δ -7.29 . ^{13}C NMR (126 MHz, C_6D_6): δ 160.71, 153.81, 153.63, 147.23, 146.58, 144.03, 135.36, 132.95, 129.87, 129.67,

128.44, 126.20, 125.03, 124.62, 124.41, 122.23, 119.20, 116.80, 26.57, 23.35, 20.97, 18.75, 18.49, 18.36. ^{31}P NMR (202 MHz, C_6D_6): δ 41.26. IR (thin film from C_6D_6 , cm^{-1}): 2279, 2270 (B–H–Fe). UV–vis [toluene, $\lambda(\text{nm})\{\epsilon(\text{M}^{-1} \text{cm}^{-1})\}$]: 287(sh){26,608}, 346(sh){5765}, 366{7761}, 421(sh){3548}, 498{5543}, 537(sh){5211}. Combustion analysis for $\text{C}_{43}\text{H}_{50}\text{BFeNP}_2$: calcd. C 72.80, H 7.10, N 1.97; found C 72.51, H 6.84, N 1.84.

Preparation of (DPBH)Fe(8-amidoquinoline) (Mixture of Two Isomers): A solution of $[(\text{DPB})\text{Fe}]_2(\text{N}_2)$ (17.4 mg, 0.0160 mmol) and 8- aminoquinoline (4.6 mg, 0.032 mmol) in 0.7 mL of C_6D_6 was allowed to stand at RT until all $[(\text{DPB})\text{Fe}]_2(\text{N}_2)$ was consumed (~ 1 h). Volatiles were removed *in vacuo*, and the resulting solids were washed with cold pentane (3×1 mL) and dissolved in minimal Et_2O . Evaporation of the saturated Et_2O solution into hexamethyldisiloxane (HMDSO) furnished crystals of (DPBH)Fe(8-amidoquinoline), which were lyophilized to give a red powder. Yield: 18.0 mg (0.027 mmol), 83%. ^1H NMR (300 MHz, C_6D_6): δ 141.88, 103.99, 85.33, 83.94, 77.91, 72.22, 68.70, 58.27, 57.69, 51.90, 24.40, 22.51, 19.91, 17.52, 17.18, 15.04, 14.47, 12.77, 11.31, 2.17, 0.74, -1.81 , -3.85 , -7.08 , -9.09 , -9.45 , -12.79 , -15.24 , -20.90 , 25.02, -33.79 , -81.35 , -83.00 , -84.84 , -103.43 . Solution magnetic moment (25 $^\circ\text{C}$, C_6D_6): 5.2 μ_{B} . IR (thin film from C_6D_6 , cm^{-1}): 3373 (N–H), 2130 (br, s, B–H–Fe for isomer A), 2000 (B–H–Fe for isomer B). UV–vis [toluene, $\lambda(\text{nm})\{\epsilon(\text{L mol}^{-1} \text{cm}^{-1})\}$]: 297{14 527}, 368(sh){5188}, 415(sh){3761}, 514{2931}. Combustion analysis for $\text{C}_{39}\text{H}_{49}\text{BFeN}_2\text{P}_2$: calcd. C 69.45, H 7.32, N 4.15; found C 68.55, H 7.09, N 3.94.

Preparation of (DPB)Co(N₂): A solution of 0.8483 g (1.79 mmol) of DPB and 0.2316 g (1.78 mmol) of CoCl_2 in tetrahydrofuran (ca. 80 mL) was stirred until no solids remained,

leaving a deep blue solution. Solvent was removed *in vacuo*, and the remaining blue residue was triturated in Et₂O for 15 min. Solvent was removed *in vacuo*, and the blue residue was dissolved in benzene (80 mL). Freshly prepared 1% sodium mercury amalgam (0.0864 g of Na, 3.76 mmol) was added to the dark blue solution and stirred vigorously for 24 h. The resulting dark red-orange solution was decanted and filtered through Celite. Lyophilization afforded a fine dark brown powder. This powder was dissolved in minimal Et₂O and cooled in a freezer to $-30\text{ }^{\circ}\text{C}$, affording red-orange crystals of (DPB)Co(N₂). Yield: 0.850 g (1.51 mmol), 84%. ¹H NMR (400 MHz, C₆D₆): δ 17.79, 14.77, 4.04, 2.42, -2.74 , -4.04 . Solution magnetic moment (25 $^{\circ}\text{C}$, C₆D₆): 1.8 μ_{B} . IR (thin film from C₆D₆, cm⁻¹): 2098 (N₂). UV-vis [toluene $\lambda(\text{nm})\{\epsilon(\text{M}^{-1}\text{ cm}^{-1})\}$]: 288{9346}. Combustion analysis for C₃₀H₄₁BCoN₂P₂ was consistently low in nitrogen and high in carbon and hydrogen, consistent with the labile N₂ ligand; a representative analysis is shown: calcd. C 64.19, H 7.36, N 4.99; found C 64.52, H 7.57, N 4.13.

Preparation of (DPB)CoBr: 57.1 mg (0.12 mmol) of DPB was dissolved in 10 mL of THF with 26.4 mg (0.12 mmol) of CoBr₂, giving a clear blue solution. A dark red-orange solution of (DPB)Co(N₂), 67.6 mg (0.12 mmol), dissolved in 10 mL of THF was added to the stirring solution of DPB and CoBr₂ via pipet, resulting in darkening of the reaction mixture. After stirring for 16 h the solution was yellow-brown. The reaction mixture was filtered through Celite, and volatiles were removed *in vacuo*, leaving a dark brown residue. The residue was extracted in pentane and filtered through Celite, removing some blue and green solids. The brown pentane extract was evaporated to dryness and dissolved in minimal THF. Large brown crystals of (DPB)CoBr were grown by vapor diffusion of a concentrated THF solution into HMDSO. Crystals of suitable quality for X-ray diffraction

were grown by vapor diffusion of Et₂O into HMDSO. Yield: 134.8 mg (0.22 mmol), 91.7%. ¹H NMR (400 MHz, C₆D₆): δ 21.61, 19.58, 16.11, 6.45, 3.82, 2.80, -1.51, -2.09, -6.81, -9.61, -16.16, -40.72. Solution magnetic moment (25 °C, C₆D₆): 3.0 μ_B. UV-vis [toluene, λ(nm){ε(M⁻¹ cm⁻¹)}]: 353{5713}, 404(sh){2863}. Combustion analysis for C₃₀H₄₁BCoP₂Br: calcd. C 58.57, H 6.61; found C 58.76, H 6.74.

Preparation of (DPB)CoOPh: A Schlenk tube was charged with 62.4 mg (0.111 mmol) of (DPB)Co(N₂), 10.5 mg (0.112 mmol) of PhOH, and C₆H₆ (15 mL), and the mixture was stirred for 16 h at room temperature. A color change from red-orange to orange-brown was observed after overnight stirring. GC analysis of the headspace of the reaction mixture showed formation of H₂. The solution was lyophilized, leaving a fine orange-brown powder. Yield: 63.0 mg (0.1 mmol), 90%. ¹H NMR (400 MHz, C₆D₆): δ 58.44, 34.48, 20.37, 19.82, 18.26, 16.38, 15.53, 5.76, 5.39, -3.26, -4.22, -5.48, -6.83, -7.71, -16.92, -18.67, -19.09, -21.05, -21.44, -46.23, -193.33. Solution magnetic moment (25 °C, C₆D₆): 3.2 μ_B. UV-vis [toluene, λ(nm){ε(M⁻¹ cm⁻¹)}]: 287(sh){13 046}, 425{3346}. Combustion analysis for C₃₆H₄₆BCoP₂: calcd. C 69.02, H 7.40; found C 68.14, H 7.46.

Alternative Synthesis of (DPB)Co(OPh): 21.9 mg (0.036 mmol) of (DPB)CoBr was combined with 4.2 mg (0.036 mmol) of NaOPh in ~10 mL of THF, and the mixture was stirred for 16 h. The resulting orange-brown solution was filtered through Celite, and volatiles were removed *in vacuo*. The resulting residue was extracted in benzene and lyophilized, giving a fine orange-brown powder with spectroscopic features identical to

(DPB)Co(OPh) prepared by the previously described method. Yield: 20.9 mg (0.033 mmol), 91.7%.

Preparation of (DPB)CoSPh: 64.2 mg (0.114 mmol) of (DPB)Co(N₂) and 12.6 mg (0.114 mmol) of PhSH were dissolved in benzene (15 mL) in a Schlenk tube, and the mixture was stirred for 16 h at room temperature. The solution color changed from dark red-orange to deep red. GC analysis of the headspace of the reaction mixture showed formation of H₂. The reaction mixture was lyophilized, leaving a dark red powder, which was then dissolved in minimal Et₂O. Crystals suitable for X-ray diffraction studies were obtained by vapor diffusion of an Et₂O solution into HMDSO. Yield: 73.5 mg (0.114 mmol), 100%. ¹H NMR (400 MHz, C₆D₆): δ 184.19, 25.53, 20.79, 15.72, 15.16, 14.22, 13.39, 10.08, 9.77, 5.66, 4.67, 3.05, 1.67, -0.92, -1.09, -1.96, -2.45, -12.17, -17.10, -19.90, -46.22. Solution magnetic moment (25 °C, toluene-d₈): 2.6 μ_B. UV-vis [toluene, λ(nm){ε(M⁻¹ cm⁻¹)}]: 283(sh){18 858}, 355(sh){3705}, 478{3821}. Combustion analysis for C₃₆H₄₆BCoNP₂: calcd. C 67.19, H 7.36; found C 66.97, H 7.09.

Alternative Synthesis of (DPB)Co(SPh): 19.6 mg (0.032 mmol) of (DPB)CoBr was combined with 4.2 mg (0.032 mmol) of NaSPh in 10 mL of THF, and the mixture was stirred for 16 h. The resulting deep red solution was filtered through Celite, and the volatiles were removed *in vacuo*, giving a dark red residue. This residue was extracted in benzene and lyophilized, giving a fine red powder with spectroscopic features identical to (DPB)Co(SPh) prepared by the previously described method. Yield: 19.4 mg (0.030 mmol), 90.9%.

Preparation of (DPBH)Co(benzo[h]quinolin-10-yl): 200.0 mg (0.356 mmol) amount of (DPB)Co(N₂) and 64.1 mg (0.357 mmol) of benzo[h]quinoline were dissolved in ca. 25

mL of benzene in a Schlenk tube. The solution was freeze–pump–thawed for 3×15 min cycles to remove N_2 and heated to $60\text{ }^\circ\text{C}$ for 24 h, turning from dark red-orange to bright red-orange. The solution was lyophilized, leaving a red-orange solid. Dissolving this solid in minimal Et_2O and cooling to $-30\text{ }^\circ\text{C}$ afforded crystals of $(\text{DPBH})\text{Co}(\text{benzo}[\text{h}]\text{quinolin-10-yl})$ suitable for X-ray diffraction studies. Yield: 123.5 mg (0.173 mmol), 48.6%. ^1H NMR (300 MHz, C_6D_6): δ 19.05, 15.79, 10.47, 8.91, 5.49, 3.36, -1.38 . Solution magnetic moment ($25\text{ }^\circ\text{C}$, C_6D_6): $1.8\text{ }\mu_{\text{B}}$. IR (thin film, C_6D_6): 2047 cm^{-1} (B–H–Co). UV–vis [toluene, $\lambda(\text{nm})\{\epsilon(\text{M}^{-1}\text{ cm}^{-1})\}$]: 378{3913}, 406{3563}, 431{3682}, 454{3800}. Combustion analysis for $\text{C}_{43}\text{H}_{50}\text{BCoNP}_2$: calcd. C 72.48, H 7.07, N 1.97; found C 72.23, H 6.78, N 1.94.

Preparation of (DPBH)Co(8-amidoquinoline): 16.1 mg (0.029 mmol) of $(\text{DPB})\text{Co}(\text{N}_2)$ and 4.2 mg (0.029 mmol) of 8-aminoquinoline were dissolved in benzene (ca. 15 mL), and the mixture was freeze–pump–thawed for 3×15 min cycles to remove N_2 . The solution turned from deep red-orange to deep purple after stirring for 24 h. The reaction mixture was lyophilized, giving a dark purple solid, which was dissolved in minimal Et_2O and cooled in a freezer to $-30\text{ }^\circ\text{C}$, affording purple crystals of $(\text{DPBH})\text{Co}(8\text{-amidoquinoline})$. Yield: 17.2 mg (0.025 mmol), 86.2%. ^1H NMR (300 MHz, C_6D_6): δ 37.30, 18.47, 8.99, 8.29, 7.60, 6.52, 5.43, 3.49, 1.86, -0.87 . Solution magnetic moment ($25\text{ }^\circ\text{C}$, C_6D_6): $2.4\text{ }\mu_{\text{B}}$. IR (thin film, C_6D_6): 1961 cm^{-1} (B–H–Co), 3384 cm^{-1} (N–H), 3478 cm^{-1} (N–H). UV–vis [toluene, $\lambda(\text{nm})\{\epsilon(\text{M}^{-1}\text{ cm}^{-1})\}$]: 342(sh) {3874}, 409(sh){2325}, 545{3390}. Combustion analysis for $\text{C}_{39}\text{H}_{49}\text{BCoN}_2\text{P}_2$: calcd C 69.14, H 7.29, N 4.13; found C 68.82, H 7.14, N 4.04.

Generation of (DPBH)Co(SiHPh₂): 6.7 mg (0.012 mmol) of (DPB)Co(N₂) was dissolved in 0.5 mL of C₆D₆, and this was combined with neat Ph₂SiH₂ (220 mg, 1.2 mmol). The solution was divided into two aliquots (0.35 and 0.15 mL) and loaded into an EPR tube and an NMR tube equipped with J-Young gas addition fittings. The EPR and NMR tubes were subjected to three freeze–pump–thaw cycles on a Schlenk line to generate a mixture of the *S* = 1/2 species (DPBH)Co(SiHPh₂) observed by ¹H NMR and X-band EPR and some unidentified diamagnetic impurities. For (DPBH)Co(SiHPh₂): ¹H NMR (400 MHz, C₆D₆): δ 22.44, 20.43, 16.24, 16.12, 16.00, −0.63, −2.10, −3.90, −5.57, −7.76, −9.69, −11.56, −12.47, −15.76, −40.35, −40.84, −41.11. IR (solution in C₆H₆ with 100 equiv. of Ph₂SiH₂): 1810 cm^{−1} (B–H–Co). For impurities: ¹H NMR (400 MHz, C₆D₆): δ −17.13 (t) (*J*_{PH} = 44.3 Hz). ³¹P NMR (162 MHz, C₆D₆): δ 77.96, 58.73, 57.66.

Hydrosilylation Catalytic Protocol: In a typical experiment a J-Young NMR tube was loaded with a 0.005 mmol (100 μL, 0.05 M) solution of [(DPB)Fe]₂(N₂) in C₆D₆ or a 0.01 mmol (100 μL, 0.1 M) solution of (DPB)Co(N₂) in C₆D₆, a 100 μL FeCp₂ solution in C₆D₆ (0.355 M), and 300 μL of C₆D₆ (total volume 500 μL). The tube was then frozen in a cold well cooled by liquid nitrogen. The frozen tube was loaded with 185.8 μL of Ph₂SiH₂ (1.0 mmol) and 1.0 mmol of aldehyde or ketone, sealed, and kept frozen. The frozen tube was rapidly thawed at the NMR spectrometer, shaken vigorously, and monitored by ¹H NMR spectroscopy until all starting materials had been consumed. After completion the reaction mixture was exposed to air, diluted with CH₂Cl₂, filtered through a plug of silica, and analyzed by GC-MS. Hydrosilylation products were identified by comparison of the ¹H NMR spectra and GC-MS traces to those reported in the literature.^{11,23,63,69,70} To aid characterization, (1-(4- trifluoromethylphenyl)methoxy)diphenylsilane was converted to

4-(trifluoromethyl)phenyl methanol by treatment with 1 M HCl; the ^1H NMR and GC-MS data obtained agree with the literature data.⁷¹ Reactions run in the absence of FeCp_2 showed the same distribution of products by ^1H NMR and GC-MS and reached completion in the same amount of time. Control experiments showed little to no reaction of PhSiH_3 or Ph_2SiH_2 with substrates in the absence of $[(\text{DPB})\text{Fe}]_2(\text{N}_2)$ or $(\text{DPB})\text{Co}(\text{N}_2)$ in the time frame in which the catalyzed reaction occurs.

Mercury Drop Test for Homogeneity: A solution of either 0.005 mmol of $[(\text{DPB})\text{Fe}]_2(\text{N}_2)$ or 0.01 mmol of $(\text{DPB})\text{Co}(\text{N}_2)$ in benzene (500 μL) was stirred over excess Hg metal (173–200 equiv.) for 15 min at 25 $^\circ\text{C}$. Benzaldehyde (102 μL , 1.0 mmol) was added to the stirring solution followed by Ph_2SiH_2 (185.8 μL , 1.0 mmol), and the mixture was stirred. ^1H NMR and GC-MS analysis of the reaction mixtures showed full conversion of starting materials into products in the expected time.

2.5.2 Crystallographic Data Tables

Table 2.S1: XRD experimental parameters for (DPB)Fe(OPh), [(DPBH)Fe(SPh)]₂, (DPBH)Fe(benzo[h]quinolin-10-yl), (DPBH)Fe(8-amidoquinoline).

Compound	(DPB)Fe(OPh)	[(DPBH)Fe(SPh)] ₂	(DPBH)Fe(C ₁₃ H ₈ N)	(DPBH)Fe(C ₉ H ₇ N ₂)
Chemical Formula	C ₃₆ H ₄₆ BP ₂ OFe	C ₇₂ H ₉₄ B ₂ P ₄ S ₂ Fe	C ₄₃ H ₅₀ BNP ₂ Fe	C ₃₉ H ₄₉ BN ₂ P ₂ Fe
Formula Weight	623.37	1280.87	709.48	674.44
<i>T</i> (K)	100(2)K	100(2)K	100(2)K	100(2)K
λ (Å)	0.71073	0.71073	0.71073	0.71073
Space Group	C ₂ /c	P2 ₁ /n	P2 ₁ /n	P2 ₁ /n
<i>a</i>	17.9786(7)	11.5444(9)	11.1418(5)	11.9514(10)
<i>b</i>	10.8974(4)	19.5804(15)	12.7713(6)	22.7818(15)
<i>c</i>	33.4789(14)	16.0331(13)	30.2507(13)	13.2520(11)
α	90.00	90.00	90.00	90.00
β	90.6720(11)	110.525(5)	96.033(2)	102.923(5)
γ	90.00	90.00	90.00	90.00
Volume	6558.7(5)	3394.1(5)	4280.7(3)	3516.8(5)
<i>Z</i>	8	4	4	4
Density (calc)	1.2625	1.2532	1.126	1.272
R1, wr2	0.0412, 0.1001	0.0475, 0.1230	0.0522, 0.1565	0.0537, 0.1729

$$R1 = \sum ||F_o| - |F_c|| / \sum |F_o|, \text{ wr2} = \{ \sum [w(F_o^2 - F_c^2)^2] / \sum w(F_o^2)^2 \}^{1/2}$$

Table 2.S2: XRD experimental parameters for (DPB)Co(N₂), (DPB)Co(OPh), (DPB)Co(SPh), (DPBH)Co(benzo[h]quinolin-10-yl), (DPB)CoBr

Compound	(DPB)Co(N ₂)	(DPB)Co(OPh)	(DPB)Co(SPh)	(DPBH)Co(C ₁₃ H ₈ N)	(DPB)CoBr
	C ₃₀ H ₄₆ BN ₂ P ₂ Co	C ₃₆ H ₄₆ BP ₂ OCo	C ₃₆ H ₄₆ BP ₂ SCo	C ₄₃ H ₅₀ BNP ₂ Co	C ₃₀ H ₄₁ BP ₂ BrCo
Formula Weight	561.33	626.45	642.51	712.57	613.25
<i>T</i> (K)	100(2)K	100(2)K	100(2)K	100(2)K	100(2)K
λ (Å)	0.71073	1.54178	0.71073	0.71073	0.71073
Space Group	P-1	P2 ₁ /c	P2 ₁ /n	Pca2 ₁	C2/c
<i>a</i>	10.7517(7)	18.2759(14)	10.0753(4)	19.581(2)	18.8235(11)
<i>b</i>	18.0184(12)	8.9584(6)	19.0012(7)	11.1417(13)	9.9502(6)
<i>c</i>	24.6119(15)	21.2277(15)	17.8659(6)	16.9012(12)	31.4070(19)
α	69.741(5)	90.00	90.00	90.00	90.00
β	81.149(4)	107.184(4)	104.7216(16)	90.00	104.505(3)
γ	74.584(3)	90.00	90.00	90.00	90.00
Volume	4302.0(5)	3320.3(4)	3308.0(2)	3687.2(6)	5695.0(6)
<i>Z</i>	6	4	4	4	8
Density (calc)	1.300	1.252	1.290	1.2835	1.430
R1, wR2	0.0537, 0.1455	0.1088, 0.2698	0.0513, 0.1276	0.0614, 0.1693	0.0293, 0.0658

$$R1 = \sum ||F_o| - |F_c|| / \sum |F_o|, wR2 = \{ \sum [w(F_o^2 - F_c^2)^2] / \sum w(F_o^2)^2 \}^{1/2}$$

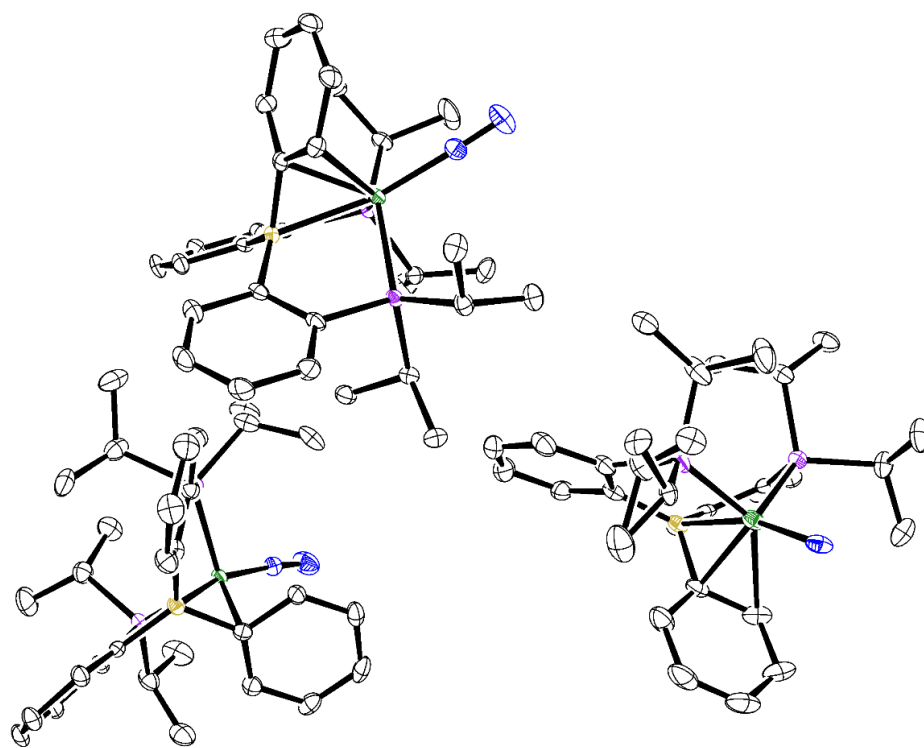


Figure 2.S1: ORTEP representation of the Asymmetric unit for (DPB)Co(N₂) (H atoms omitted for clarity). Color Scheme: blue = nitrogen, purple = phosphorus, gold = boron, green = cobalt, black = carbon.

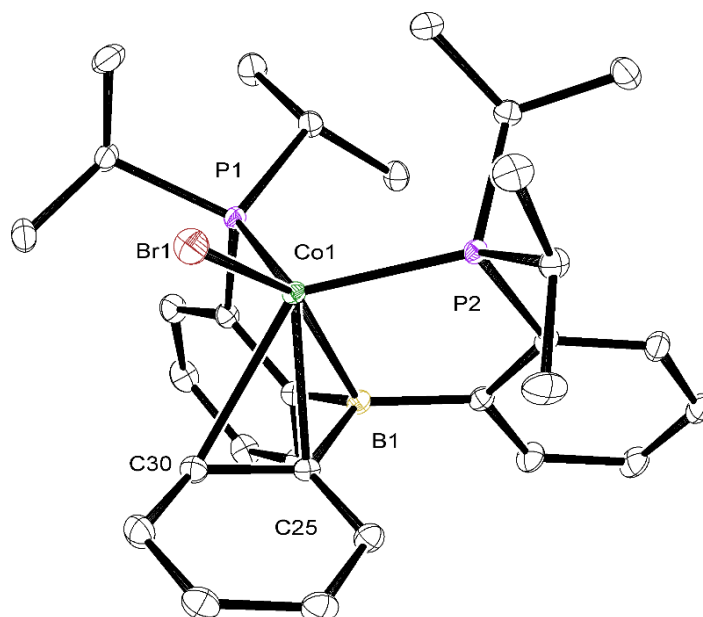


Figure 2.S2. ORTEP Representation of (DPB)CoBr (H atoms omitted for clarity).

Selected Bond distances Co1-P1 2.3088(2) Å; Co1-P2 2.2895(2) Å; Co1-C25 2.2485(6) Å; Co1-C30 2.5286(7) Å; Co1-B1 2.3070(7) Å; Co1-Br1 2.36636(16) Å.

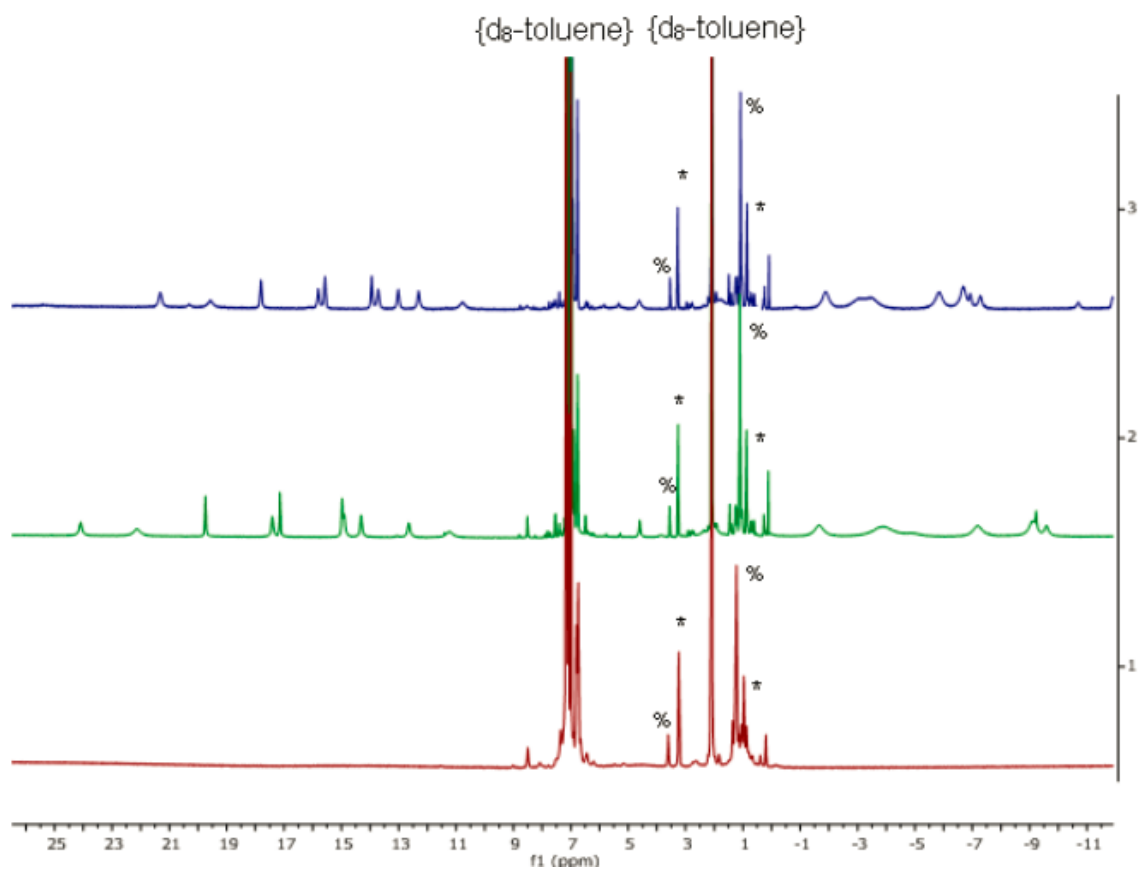


Figure 2.S3. Variable temperature ^1H NMR of the reaction mixture of (DPBH)Fe(8-amidoquinoline) in d_8 -toluene. Red trace is at -90°C , green trace is at 25°C , and blue trace is at 75°C . * Et_2O , % THF.

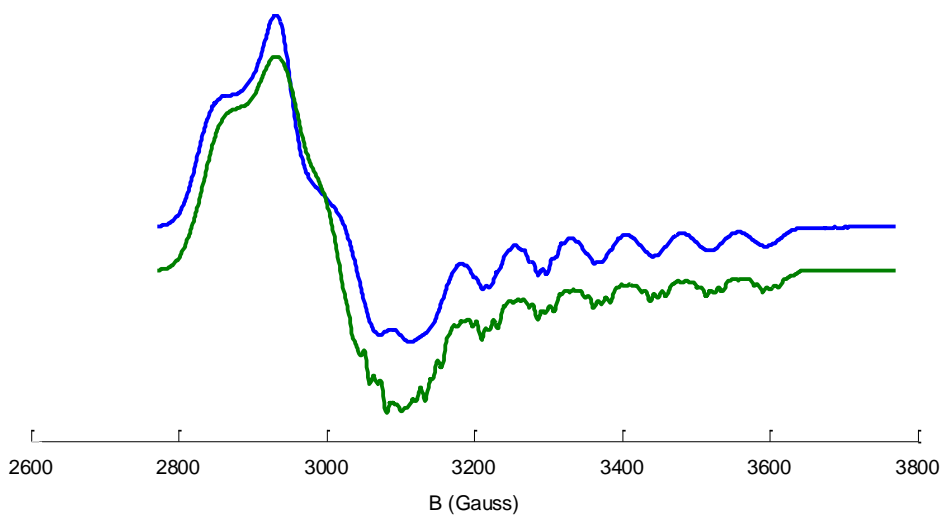


Figure 2.S4: 77 K X-Band EPR spectrum of (DPBH)Co(benzo[h]quinolin-10-yl) in 2-MeTHF (top trace, blue) and simulation (bottom trace, green). Simulation Parameters: g_1 : 2.017, g_2 : 2.199, g_3 : 2.3142. $HStrain_1$: 27.00 MHz, $HStrain_2$: 222.74 MHz, $HStrain_3$: 36.20 MHz. A_{P1} = 63 MHz, 1 MHz, 62.7 MHz; A_{P2} : 63 MHz, 1 MHz, 30.1 MHz; A_H : 30.0 MHz, 1 MHz, 1 MHz; A_N : 30.0 MHz, 160.05 MHz, 141.9 MHz; A_{Co} : 215.1 MHz, 19.7 MHz, 1.0 MHz. Microwave Frequency: 9.398 GHz, Range: 2770 G - 3770 G.

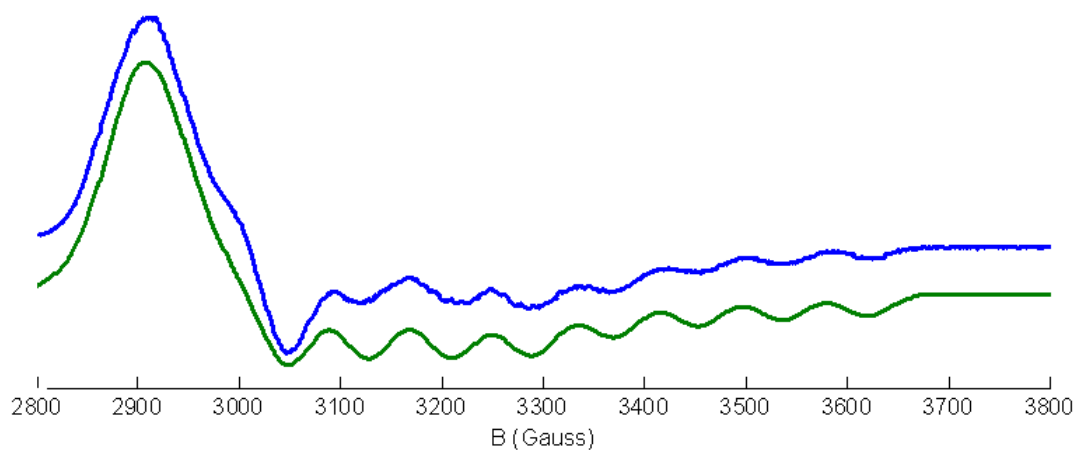


Figure 2.S5: 77 K X-band EPR spectrum of (DPBH)Co(8-amidoquinoline) in 2-MeTHF (top trace, blue) and simulation (bottom trace, green). Simulation Parameters: g_1 : 2.0181, g_2 : 2.1801, g_3 : 2.2679. HStrain₁: 142.23 MHz, HStrain₂: 384.24 MHz, HStrain₃: 226.13 MHz. A_{Co}: 232.51 MHz, 145.42 MHz, 23.80 MHz. Microwave Frequency: 9.412 GHz, Range: 2800 G - 3800 G.

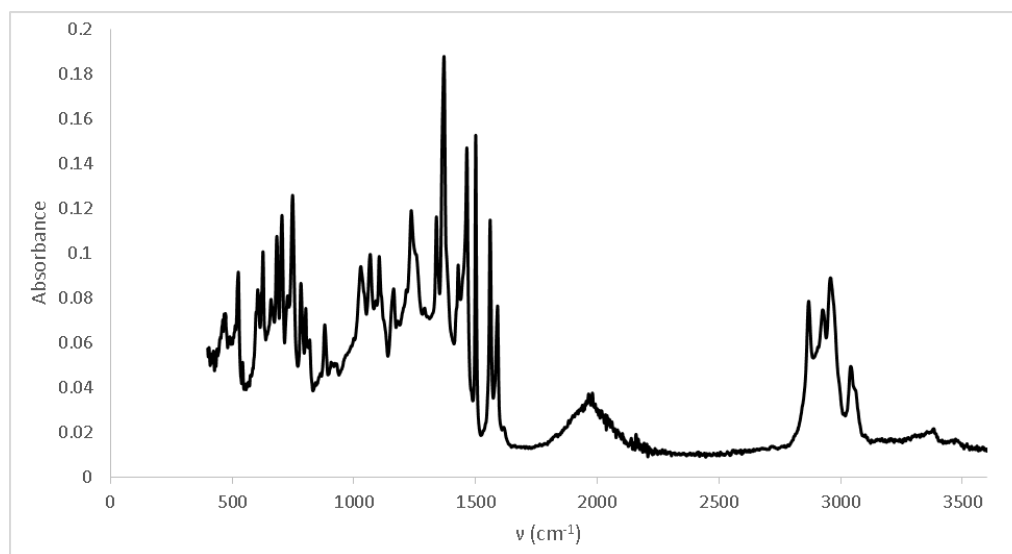


Figure 2.S6: Thin film IR spectrum of (DPBH)Co(8-amidoquinoline) from evaporated C₆D₆.

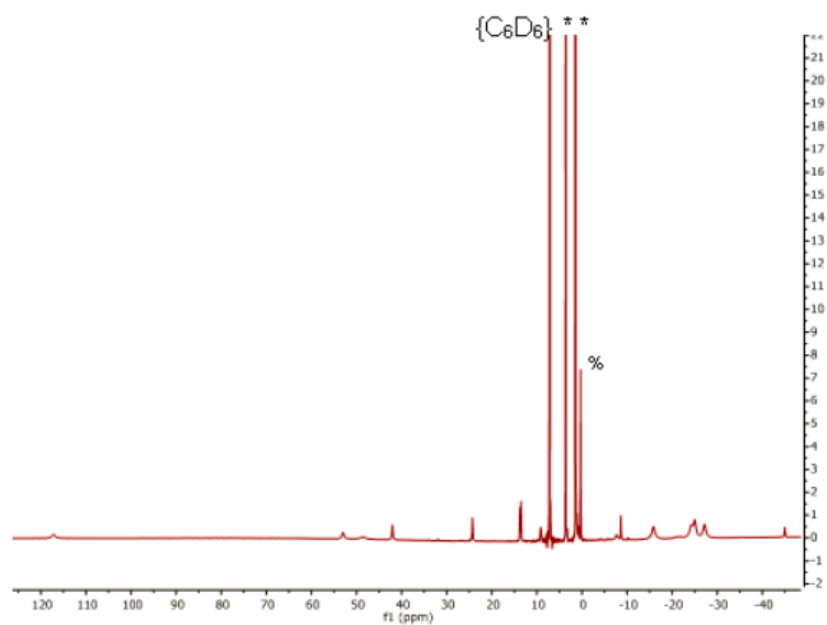


Figure 2.S7: ^1H NMR spectrum of $(\text{DPB})\text{Fe}(\text{OPh})$ in C_6D_6 . * Et_2O , % residual silicone grease.

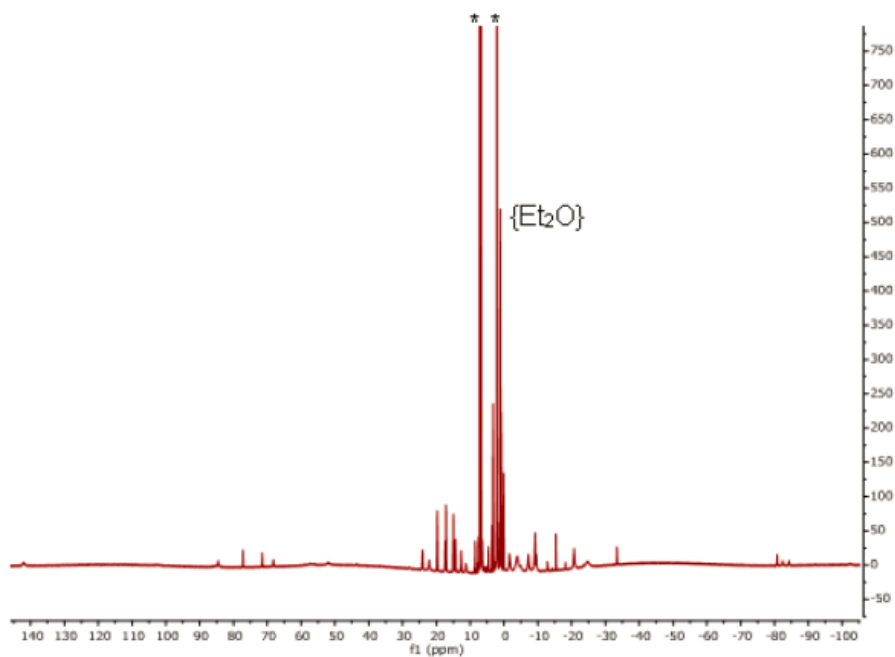


Figure 2.S8: ^1H NMR of $(\text{DPBH})\text{Fe}(\text{8-amidoquinoline})$ in $\text{d}_8\text{-toluene}$ (mixture of isomers). * $\text{d}_8\text{-toluene}$.

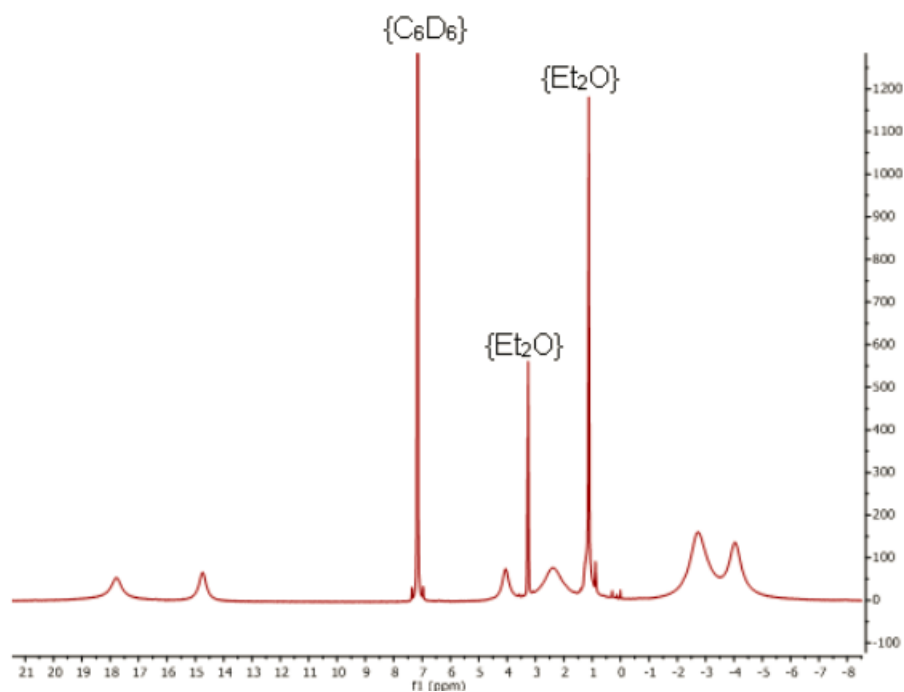


Figure 2.S9: ^1H NMR spectrum of $(\text{DPB})\text{Co}(\text{N}_2)$ in C_6D_6 .

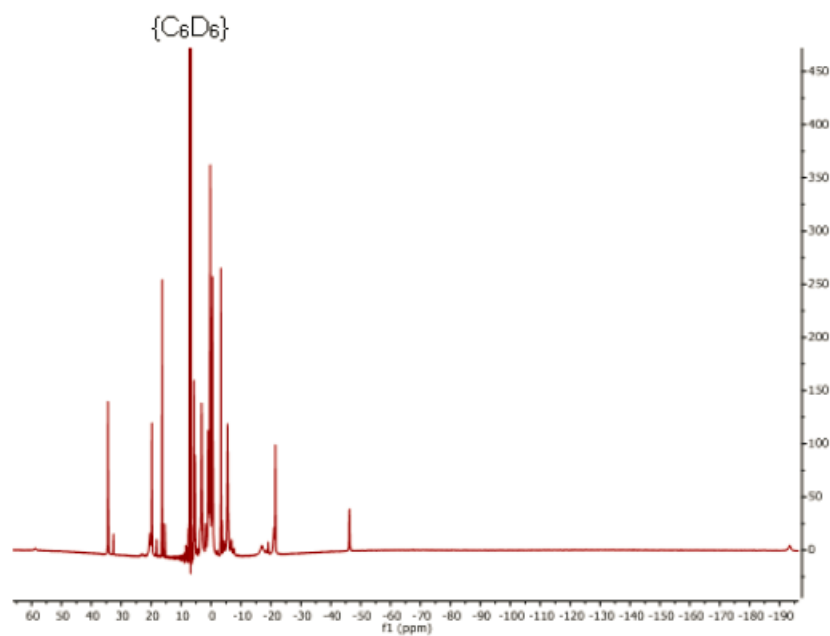


Figure 2.S10: ^1H NMR Spectrum of $(\text{DPB})\text{Co}(\text{OPh})$ in C_6D_6 .

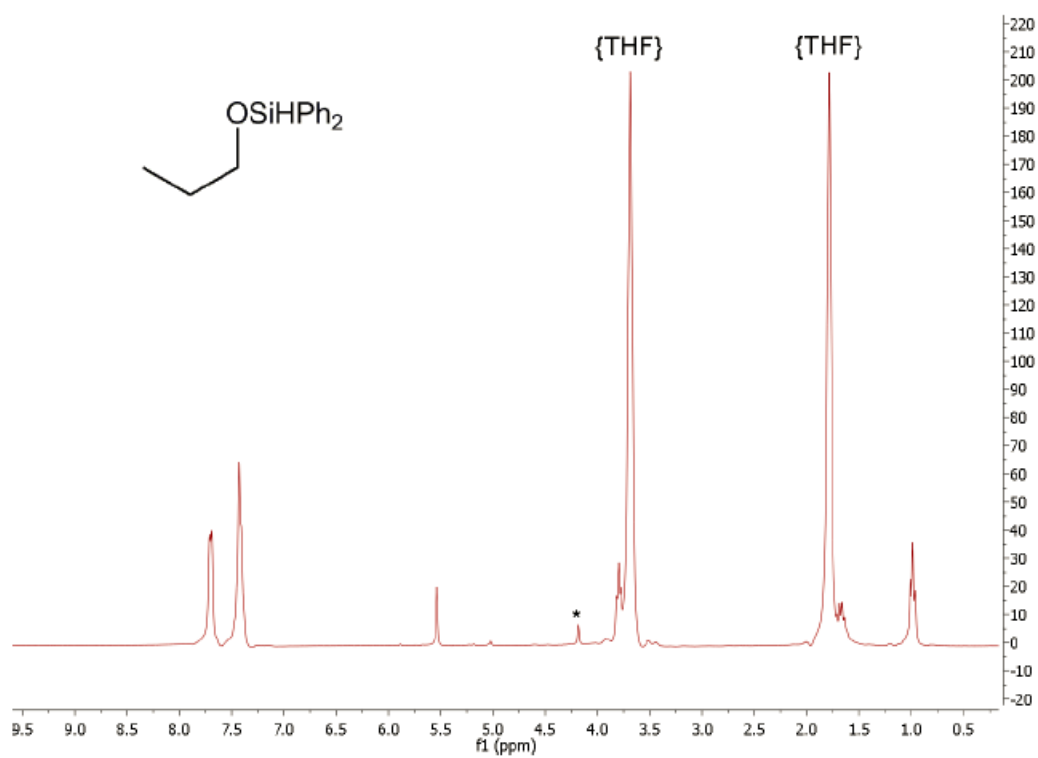


Figure 2.S11: ^1H NMR Spectrum of the reaction mixture of Ph_2SiH_2 with propanal in 5:1 THF: d_8 -THF catalyzed by $(\text{DPB})\text{Co}(\text{N}_2)$. * FeCp_2 internal standard.

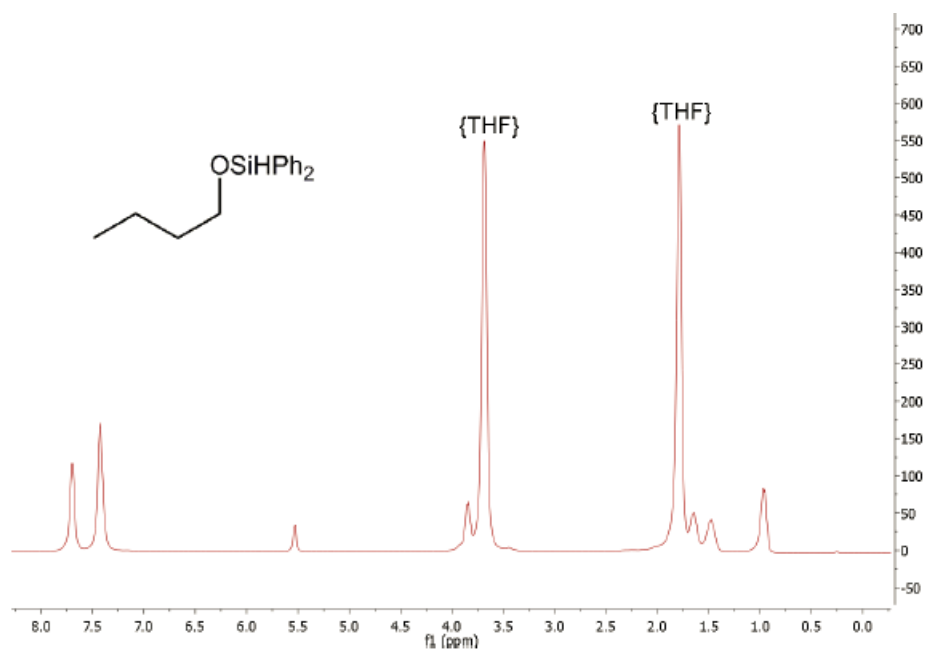


Figure 2.S12: ¹H NMR Spectrum of the reaction mixture of Ph₂SiH₂ with butanal in 4:1 THF:d₈THF catalyzed by (DPB)Co(N₂).

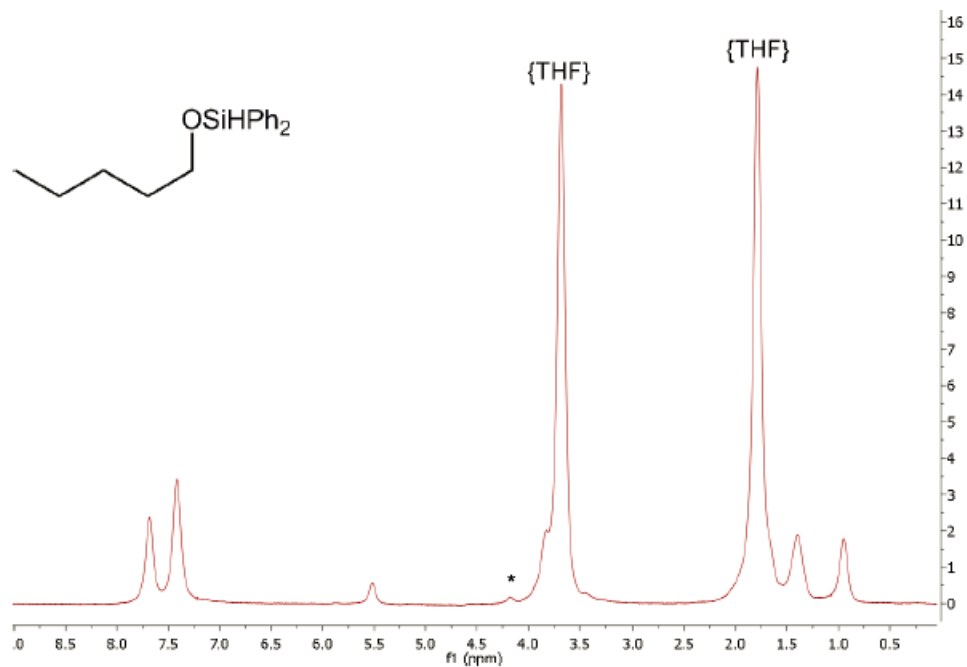


Figure 2.S13: ¹H NMR spectrum of the reaction mixture of Ph₂SiH₂ with pentanal in 4:1 THF:d₈-THF catalyzed by (DPB)Co(N₂). * FeCp₂ internal standard.

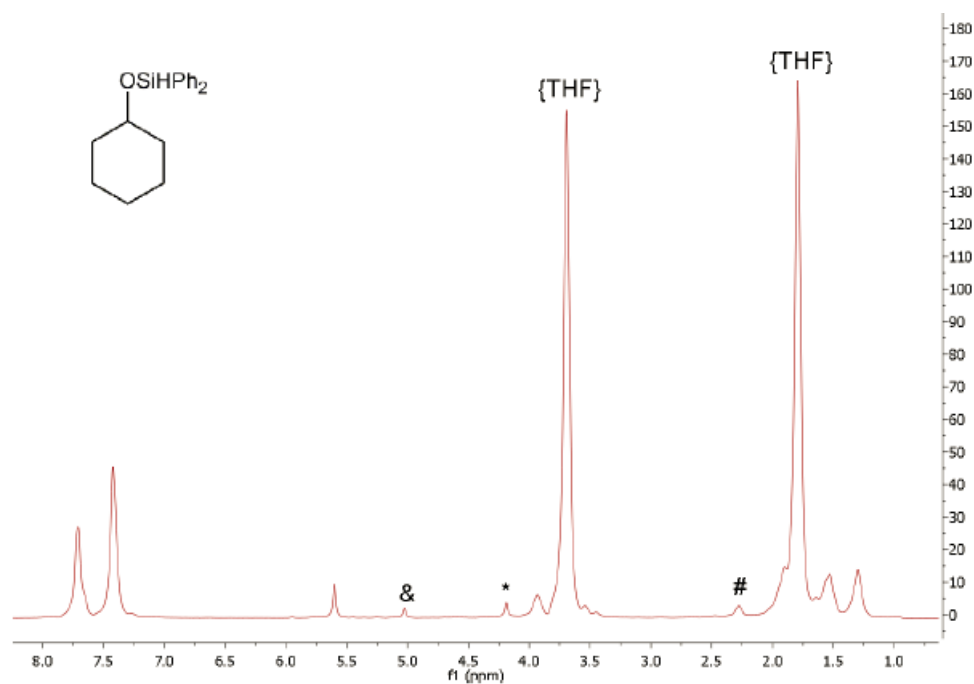


Figure 2.S14: ^1H NMR spectrum of the reaction mixture of Ph_2SiH_2 with cyclohexanone in 5:1 THF: d_8 -THF catalyzed by $(\text{DPB})\text{Co}(\text{N}_2)$. * FeCp_2 internal standard, & Ph_2SiH_2 , # cyclohexanone.

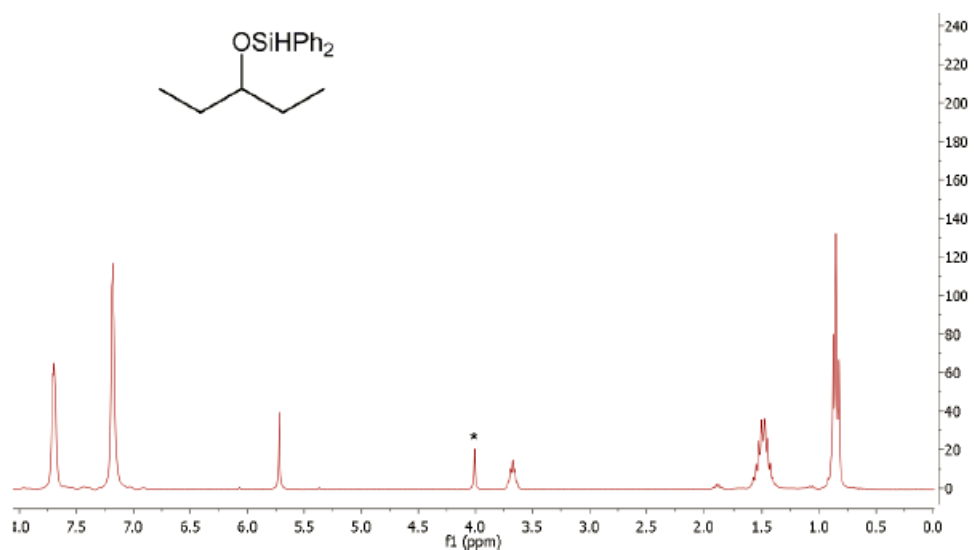


Figure 2.S15: ^1H NMR spectrum of the reaction mixture of 2-pentanone with Ph_2SiH_2 in C_6D_6 catalyzed by $(\text{DPB})\text{Co}(\text{N}_2)$. * FeCp_2 internal standard.

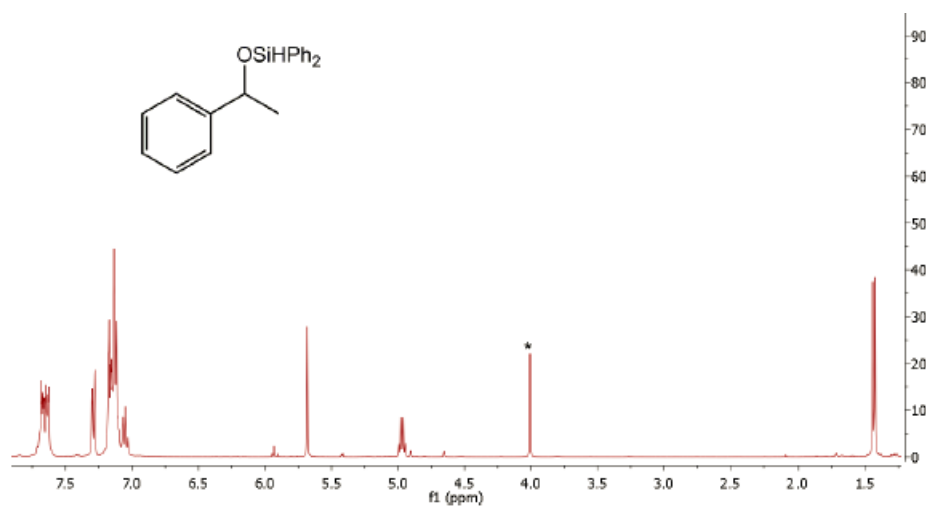


Figure 2.S16: ^1H NMR spectrum of the reaction mixture of acetophenone with Ph_2SiH_2 in C_6D_6 catalyzed by $(\text{DPB})\text{Co}(\text{N}_2)^* \text{FeCp}_2$ internal standard.

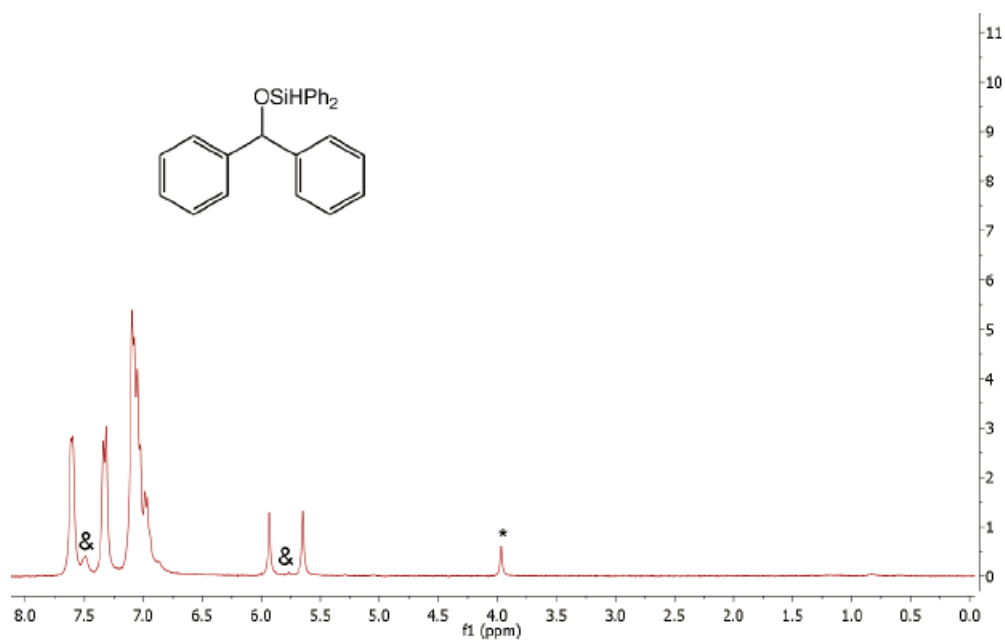


Figure 2.S17: ^1H NMR spectrum of the reaction mixture of benzophenone and Ph_2SiH_2 in C_6D_6 catalyzed by $(\text{DPB})\text{Co}(\text{N}_2)^* \text{FeCp}_2$ internal standard. $\&\text{Ph}_2\text{SiH}_2$.

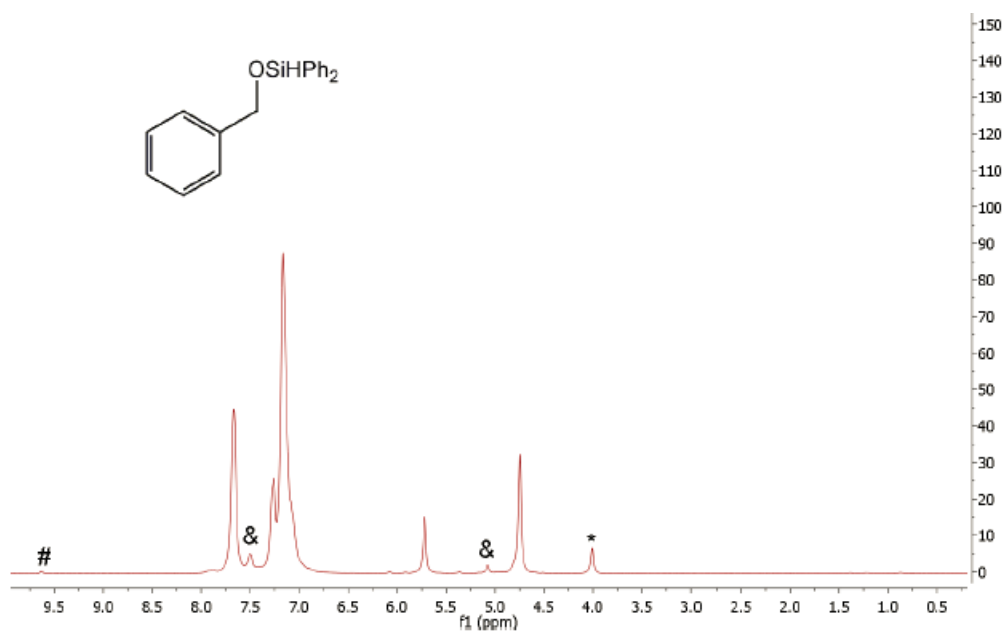


Figure 2.S18: ^1H NMR spectrum of the reaction mixture of benzaldehyde and Ph_2SiH_2 in C_6D_6 catalyzed by $(\text{DPB})\text{Co}(\text{N}_2)$. * FeCp_2 internal standard, & Ph_2SiH_2 , #benzaldehyde.

References

- (1) Crabtree, R. H. *The Organometallic Chemistry of the Transition Metals, 5th Ed.*; John Wiley & Sons Inc.: New York, 2009.
- (2) Miessler, G. L.; Tarr, D. A. *Inorganic Chemistry*; 4th ed.; Prentice Hall: New York, 2011.
- (3) Ojima, I.; Kogure, T.; Kumagai, M.; Horiuchi, S.; Sato, T. *J. Organomet. Chem.* **1976**, *122*, 83.
- (4) Zheng, G. Z.; Chan, T. H. *Organometallics* **1995**, *14*, 70.
- (5) Bullock, R. M. *Catalysis without Precious Metals*; Wiley-VCH Verlag GmbH & Co. KGaA Weinheim, 2010.
- (6) Hu, X. *Chem. Sci.* **2011**, *2*, 1867.
- (7) Owen, G. R. *Chem. Soc. Rev.* **2012**, *41*, 3535.
- (8) Devillard, M.; Bouhadir, G.; Bourissou, D. *Angew. Chem. Int. Ed.* **2014**, n/a.
- (9) Harman, W. H.; Peters, J. C. *J. Am. Chem. Soc.* **2012**, *134*, 5080.
- (10) Fong, H.; Moret, M.-E.; Lee, Y.; Peters, J. C. *Organometallics* **2013**, *32*, 3053.
- (11) MacMillan, S. N.; Hill Harman, W.; Peters, J. C. *Chem. Sci.* **2014**, 590.
- (12) Chapman, A. M.; Haddow, M. F.; Wass, D. F. *J. Am. Chem. Soc.* **2011**, *133*, 18463.
- (13) Bonanno, J. B.; Henry, T. P.; Wolczanski, P. T.; Pierpont, A. W.; Cundari, T. R. *Inorg. Chem.* **2007**, *46*, 1222.
- (14) Stephan, D. W.; Erker, G. *Angew. Chem. Int. Ed.* **2010**, *49*, 46.
- (15) Stephan, D. W.; Erker, G. *Angew. Chem. Int. Ed.* **2015**, *54*, 6400.
- (16) Harman, W. H.; Lin, T.-P.; Peters, J. C. *Angew. Chem. Int. Ed.* **2013**, 1081.
- (17) Frank, N.; Hanau, K.; Langer, R. *Inorg. Chem.* **2014**, *53*, 11335.
- (18) Figueroa, J. S.; Melnick, J. G.; Parkin, G. *Inorg. Chem.* **2006**, *45*, 7056.

- (19) Pang, K.; Tanski, J. M.; Parkin, G. *Chem. Commun.* **2008**, 1008.
- (20) Tsoureas, N.; Kuo, Y.-Y.; Haddow, M. F.; Owen, G. R. *Chem. Commun.* **2011**, 47, 484.
- (21) Cowie, B. E.; Emslie, D. J. H. *Chem. Eur. J.* **2014**, 20, 16899.
- (22) Barnett, B. R.; Moore, C. E.; Rheingold, A. L.; Figueroa, J. S. *J. Am. Chem. Soc.* **2014**, 136, 10262.
- (23) Yang, J.; Tilley, T. D. *Angew. Chem. Int. Ed.* **2010**, 49, 10186.
- (24) Niu, Q.; Sun, H.; Li, X.; Klein, H. F.; Flörke, U. *Organometallics* **2013**, 32, 5235.
- (25) Ruddy, A. J.; Kelly, C. M.; Crawford, S. M.; Wheaton, C. A.; Sydora, O. L.; Small, B. L.; Stradiotto, M.; Turculet, L. *Organometallics* **2013**, 32, 5581.
- (26) Suess, D. L. M.; Peters, J. C. *J. Am. Chem. Soc.* **2013**, 135, 4938.
- (27) Suess, D. L. M.; Peters, J. C. *J. Am. Chem. Soc.* **2013**, 135, 12580.
- (28) Hayashi, Y.; Yamamoto, T.; Yamamoto, A.; Komiya, S.; Kushi, Y. *J. Am. Chem. Soc.* **1986**, 108, 385.
- (29) Archibald, S. J.; Foxon, S. P.; Freeman, J. D.; Hobson, J. E.; Perutz, R. N.; Walton, P. H. *J. Chem. Soc., Dalton. Trans.* **2002**, 2797.
- (30) Buzzeo, M. C.; Iqbal, A. H.; Long, C. M.; Millar, D.; Patel, S.; Pellow, M. A.; Saddoughi, S. A.; Smenton, A. L.; Turner, J. F. C.; Wadhawan, J. D.; Compton, R. G.; Golen, J. A.; Rheingold, A. L.; Doerr, L. H. *Inorg. Chem.* **2004**, 43, 7709.
- (31) Mautz, J.; Huttner, G. *Eur. J. Inorg. Chem.* **2008**, 2008, 1423.
- (32) Jiao, G.; Li, X.; Sun, H.; Xu, X. *J. Organomet. Chem.* **2007**, 692, 4251.
- (33) Wei, G.; Huang, Z.; Lei, X.; Cao, R.; Jiang, F.; Hong, M.; Liu, H. *Acta Crystallogr. Sect. E* **1992**, 48, 2130.
- (34) Vastag, S.; Markó, L.; Rheingold, A. L. *J. Organomet. Chem.* **1990**, 397, 231.

- (35) Mock, M. T.; Potter, R. G.; O'Hagan, M. J.; Camaioni, D. M.; Dougherty, W. G.; Kassel, W. S.; DuBois, D. L. *Inorg. Chem.* **2011**, *50*, 11914.
- (36) Norinder, J.; Matsumoto, A.; Yoshikai, N.; Nakamura, E. *J. Am. Chem. Soc.* **2008**, *130*, 5858.
- (37) Klein, H.-F.; Camadanli, S.; Beck, R.; Leukel, D.; Flörke, U. *Angew. Chem. Int. Ed.* **2005**, *44*, 975.
- (38) Baker, M. V.; Field, L. D. *J. Am. Chem. Soc.* **1986**, *108*, 7433.
- (39) Addison, A. W.; Rao, T. N.; Reedijk, J.; van Rijn, J.; Verschoor, G. C. *J. Chem. Soc., Dalton Trans.* **1984**, 1349.
- (40) Schaad, D. R.; Landis, C. R. *J. Am. Chem. Soc.* **1990**, *112*, 1628.
- (41) Fox, D. J.; Bergman, R. G. *J. Am. Chem. Soc.* **2003**, *125*, 8984.
- (42) Ding, Z.; Yoshikai, N. *Beilstein J. Org. Chem* **2013**, *8*, 1536.
- (43) Zhang, R.; Zhu, L.; Liu, G.; Dai, H.; Lu, Z.; Zhao, J.; Yan, H. *J. Am. Chem. Soc.* **2012**, *134*, 10341.
- (44) Zhang, Z.; Sun, H.; Xu, W.; Li, X. *Polyhedron* **2013**, *50*, 571.
- (45) Ko, J.; Kang, S.; Uhm, J.-K. *Bull. Korean Chem. Soc.* **1994**, *15*, 1122.
- (46) Nishiyama, H. In *Comprehensive Chirality*; Carreira, E. M., Yamamoto, H., Eds.; Elsevier: Amsterdam, 2012, p 318.
- (47) Riener, K.; Högerl, M. P.; Gigler, P.; Kühn, F. E. *ACS Catal.* **2012**, *2*, 613.
- (48) Yamamoto, K. H., T. In *Transition Metals for Organic Synthesis*; Beller, M. B., C., Ed.; Wiley-VCH Verlag GmbH: Weinheim, Germany, 2008, p 167.
- (49) Scheuermann, M. L.; Semproni, S. P.; Pappas, I.; Chirik, P. J. *Inorg. Chem* **2014**, *53*, 9463.

- (50) Frogneux, X.; Jacquet, O.; Cantat, T. *Catal. Sci. Tech.* **2014**, *4*, 1529.
- (51) Jaseer, E. A.; Akhtar, M. N.; Osman, M.; Al-Shammari, A.; Oladipo, H. B.; Garces, K.; Fernandez-Alvarez, F. J.; Al-Khattaf, S.; Oro, L. A. *Catal. Sci. Tech.* **2015**, *5*, 274.
- (52) Iglesias, M.; Fernández-Alvarez, F. J.; Oro, L. A. *ChemCatChem* **2014**, *6*, 2486.
- (53) Aresta, M. In *Activation of Small Molecules*; Wiley-VCH Verlag GmbH & Co. KGaA: 2006, p 1.
- (54) Windle, C. D.; Perutz, R. N. *Coord. Chem. Rev.* **2012**, *256*, 2562.
- (55) Schneider, J.; Jia, H.; Muckerman, J. T.; Fujita, E. *Chem. Soc. Rev.* **2012**, *41*, 2036.
- (56) Inagaki, T.; Phong, L. T.; Furuta, A.; Ito, J.-i.; Nishiyama, H. *Chem. Eur. J.* **2010**, *16*, 3090.
- (57) Zuo, Z.; Sun, H.; Wang, L.; Li, X. *Dalton Trans.* **2014**, *43*, 11716.
- (58) Zhao, H.; Sun, H.; Li, X. *Organometallics* **2014**, *33*, 3535.
- (59) Trovitch, R. J. *Synlett* **2014**, *25*, 1638.
- (60) Sauer, D. C.; Wadepohl, H.; Gade, L. H. *Inorg. Chem* **2012**, *51*, 12948.
- (61) Brunner, H.; Amberger, K. *J. Organomet. Chem.* **1991**, *417*, C63.
- (62) Bullock, R. M. In *Catalysis without Precious Metals*; Wiley-VCH Verlag GmbH & Co. KGaA: 2010, p 51.
- (63) Tondreau, A. M.; Lobkovsky, E.; Chirik, P. J. *Org. Lett.* **2008**, *10*, 2789.
- (64) Gallego, D.; Inoue, S.; Blom, B.; Driess, M. *Organometallics* **2014**.
- (65) Sui-Seng, C.; Freutel, F.; Lough, A. J.; Morris, R. H. *Angew. Chem. Int. Ed.* **2008**, *47*, 940.
- (66) Bontemps, S.; Gornitzka, H.; Bouhadir, G.; Miqueu, K.; Bourissou, D. *Angew. Chem. Int. Ed.* **2006**, *45*, 1611.

- (67) Stoll, S.; Schweiger, A. *J. Magn. Reson.* **2006**, *178*, 42.
- (68) Sheldrik, G. M.; Universität Göttingen: Göttingen, Germany, 2000.
- (69) Wei, Y.; Han, S.; Kim, J.; Soh, S.; Grzybowski, B. A. *J. Am. Chem. Soc.* **2010**, *132*, 11018.
- (70) Masayasu, I.; Tomohiro, M.; Kazuhiko, S.; Wataru, A.; Shigeru, S. *Chem. Lett.* **2014**, *43*, 429.
- (71) Nagendra, G.; Madhu, C.; Vishwanatha, T. M.; Sureshababu, V. V. *Tetrahedron Lett.* **2012**, *53*, 5059.

Chapter 3

SYNTHESIS AND REACTIVITY OF NICKEL METALLOBORANES WITH AMINE GROUPS IN THE SECONDARY COORDINATION SPHERE

3.1 Introduction

The efficient and inexpensive reduction of protons to hydrogen gas is key to development of clean alternative energy sources. One strategy which has led to development of highly active molecular catalysts for proton reduction and H₂ oxidation is to incorporate appended moieties in the secondary coordination sphere of transition metal compounds which can act as proton shuttles and help facilitate the reaction of interest. This strategy takes some inspiration from the active sites of enzymes referred to as hydrogenases (H₂ase) which catalyze hydrogen evolution and oxidation reactions in biological systems (Chart 3.1). Each of the known H₂ase enzymes contains moieties thought to act as proton shuttles, in [NiFe]H₂ase the cysteine residues have been proposed to act as H⁺ shuttles. In [FeFe]H₂ase the pendant amine moiety bridging the two metal centers serves this role and in [Fe]H₂ase the hydroxypyridine moiety of the guanosyl-phosphate ligand can act as a proton shuttle.

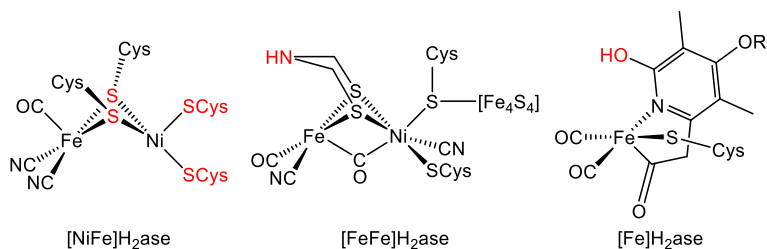
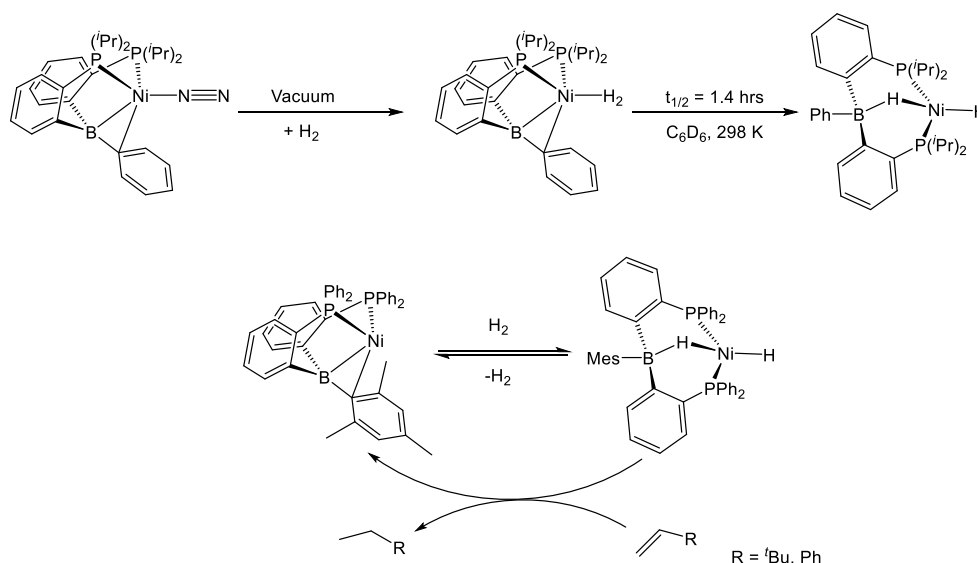


Chart 3.1: Active sites of hydrogenase enzymes. Sites which may act as proton shuttles are shown in red.

A wide variety of synthetic compounds and H₂ase analogs have incorporated these or similar functionalities into their design, some with great success.¹⁻²⁰ Recent work from our lab on the related reaction, heterolytic H₂ cleavage, used the Ni-bisphosphino borane compounds (DPB)Ni(N₂) and (^{Ph}DPB^{Mes})Ni. (DPB)Ni(N₂) was shown to first bind an intact H₂ molecule followed by heterolytic cleavage of the H-H bond across the Ni-B interaction and a related analog (^{Ph}DPB^{Mes})Ni was shown to reversibly activate H₂.^{21,22} The reversible H₂ activation was further utilized in catalytic hydrogenation of olefins (Scheme 3.1).^{21,22} Inspired by the work done on other nickel diphosphine systems pioneer by Bullock, Dubois, and others (Chart 3.2) as well as the presence of proton relays in H₂ase enzymes we sought to synthesize analogs of DPB bearing appended amine functionality and utilize the reactivity of H₂ with the Ni-B moiety present in the compounds in order to facilitate catalytic H⁺ reduction or H₂ oxidation on a (DPB)Ni platform.



Scheme 3.1: Top: Heterolytic cleavage of H₂ by (DPB)Ni. Bottom: Reversible H₂ cleavage and catalytic olefin hydrogenation by (^{Ph}DPB^{Mes})Ni.

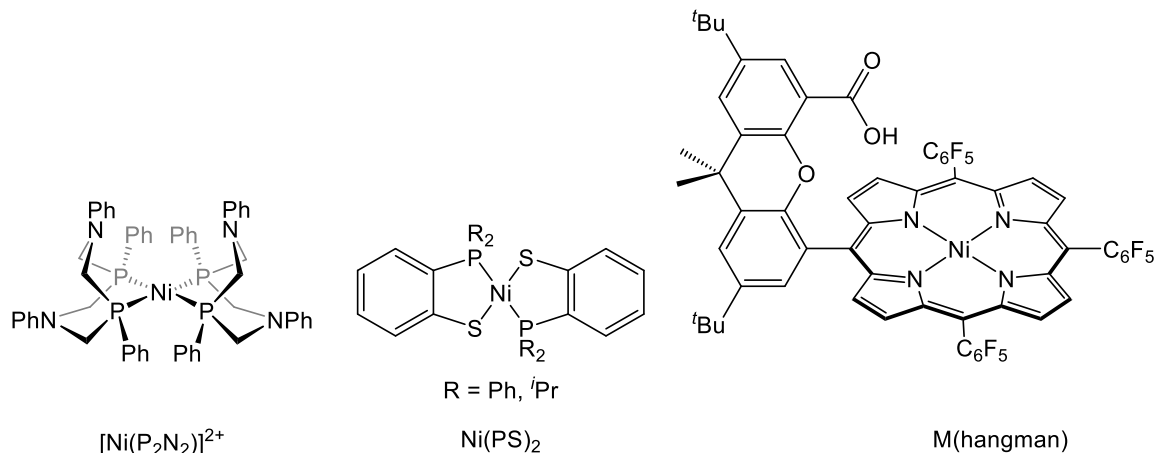
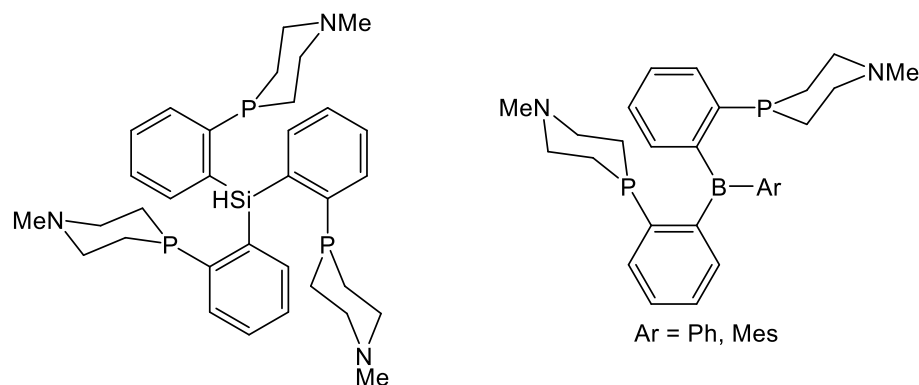


Chart 3.2: Examples of synthetic Ni-based H^+ reduction catalysts which incorporate potential H^+ relays.^{6,17,19}

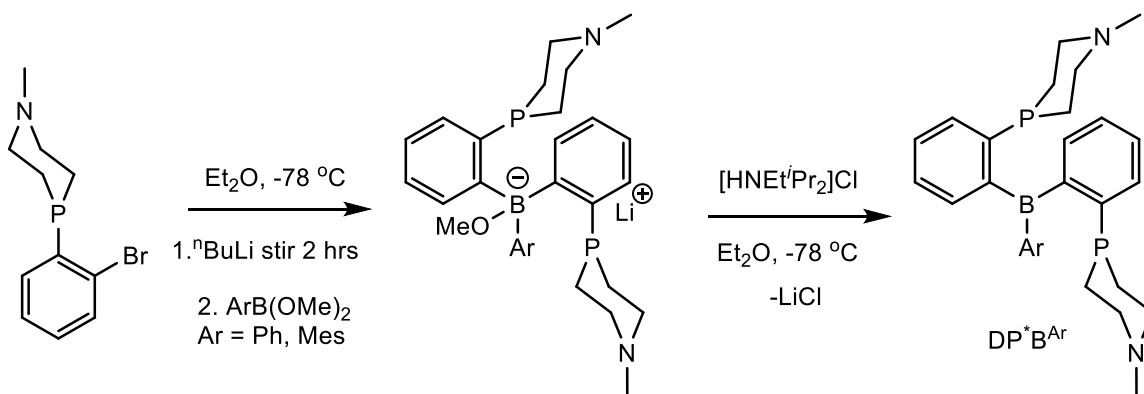
3.2 Results and Discussion

Our lab has previously prepared trisphosphino-silyl ligands which have an appended amine moiety in the context of modelling secondary sphere interaction relevant to nitrogen fixation at iron and we sought to incorporate this functionality into our DPB platform (Scheme 3.2).²³



Scheme 3.2: Left: Previously reported trisphosphino-silyl ligand with pendant amines. Right: New DPB type ligand target with pendant amines.

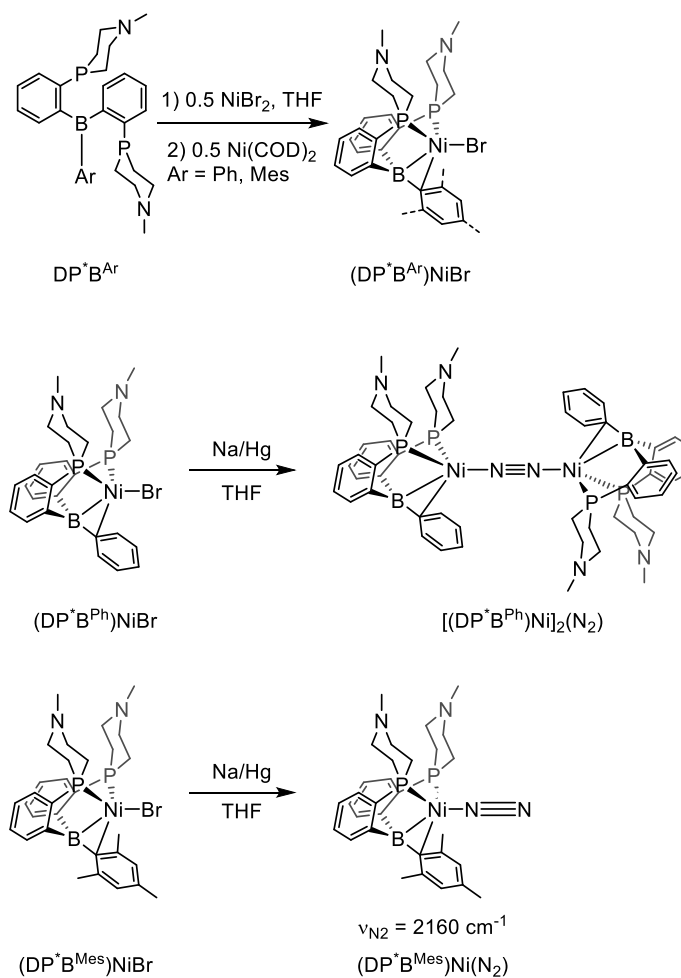
The new ligands were synthesized from 4-(2-bromophenyl)-1-methyl-1,4-azaphosphinane and either PhB(OMe)_2 or MesB(OMe)_2 . Synthesis of these new ligands was achieved via lithiation of the azaphosphinane at -78°C followed by addition of the appropriate arylboronic ester. The resultant borate salt was then isolated by filtration and washed with pentane and suspended in Et_2O followed by addition of $[\text{HNEt}^i\text{Pr}_2][\text{Cl}]$ to yield the desired borane ligand which can be filtered away from lithium chloride and purified by crystallization from a concentrated pentane solution at -35°C (Scheme 3.3).



Scheme 3.3: Synthesis of $\text{DP}^*\text{B}^{\text{Ph}}$ and $\text{DP}^*\text{B}^{\text{Mes}}$ ligands.

Metallation of the $\text{DP}^*\text{B}^{\text{Ar}}$ with 0.5 equiv. Ni(COD)_2 and 0.5 equiv. NiBr_2 afforded the corresponding $S = 1/2$ $(\text{DP}^*\text{B}^{\text{Ar}})\text{NiBr}$. Reduction of the $(\text{DP}^*\text{B})\text{NiBr}$ species with Na/Hg in THF yielded $[(\text{DP}^*\text{B}^{\text{Ph}})\text{Ni}]_2(\text{N}_2)$ similar to the dimeric iron species $[(\text{DPB})\text{Fe}]_2(\text{N}_2)$ (see chapter 1) we had previously reported and $(\text{DP}^*\text{B}^{\text{Mes}})\text{Ni}(\text{N}_2)$ (Scheme 3.4).²⁴ The IR spectrum of $[(\text{DP}^*\text{B}^{\text{Ph}})\text{Ni}]_2(\text{N}_2)$ similar to that of $[(\text{DPB})\text{Fe}]_2(\text{N}_2)$ does not show an N-N stretching frequency and the dimeric structure was confirmed by single crystal X-ray crystallography (Figure 3.1). We were unable to obtain crystals of $(\text{DP}^*\text{B}^{\text{Mes}})\text{Ni}(\text{N}_2)$ of suitable quality for single crystal X-ray diffraction studies but the appearance of $\nu_{\text{N}_2} = 2160$

cm^{-1} in the solid state and solution IR spectra of the compound led us to believe that the species exists with at least a significant component in as a terminal N_2 adduct of Ni.



Scheme 3.4: Synthesis of $(\text{DP}^*\text{B}^{\text{Ar}})\text{Ni}$ species.

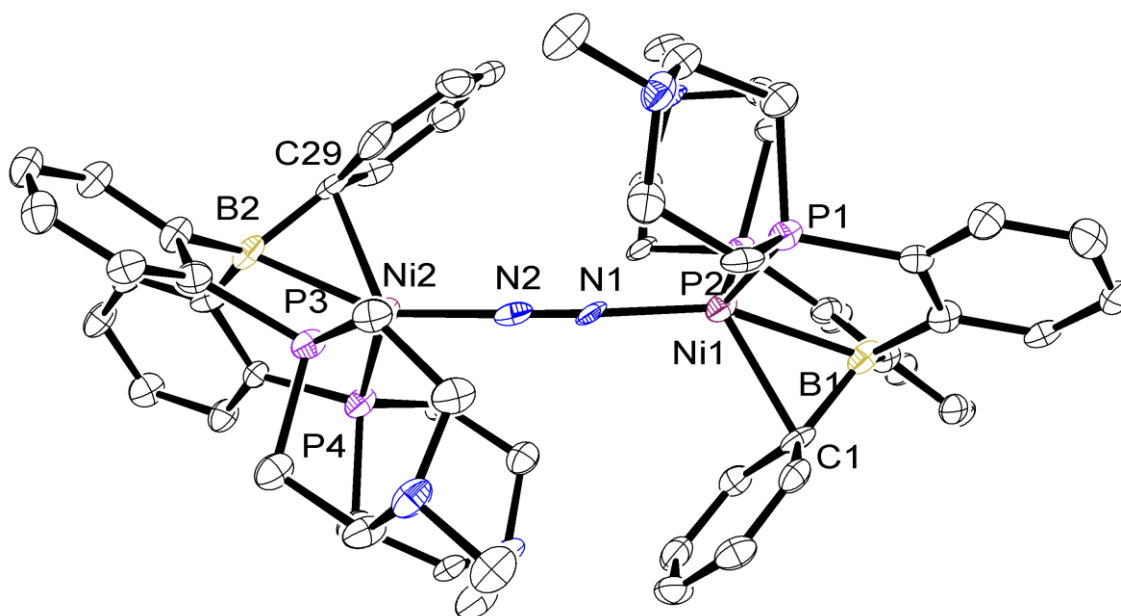


Figure 3.1: ORTEP representation of $[(DP^*B^{Ph})Ni]_2(N_2)$, H atoms have been omitted for clarity.

3.2.1 Electrochemical screening for H^+ reduction and H_2 oxidation activity. In order to determine whether these $(DP^*B^{Ar})Ni$ species had promise as H^+ reduction electrocatalysts, we screened them for catalytic activity in THF (0.1 M [TBA][PF₆]) solution using 2,6-dichloroanilinium tetrafluoroborate $[(2,6-Cl_2C_6H_3)NH_3][BF_4]$ as the acid. We found that neither $(DP^*B^{Ph})NiBr$ nor $(DP^*B^{Mes})NiBr$ exhibited a catalytic current response in the presence of 1-105 equiv. of $[(2,6-Cl_2C_6H_3)NH_3][BF_4]$. In fact the only current response which increased upon addition of acid equivalents was located at roughly the same potential that pure $[(2,6-Cl_2C_6H_3)NH_3][BF_4]$ was reduced at the glassy carbon electrode (approx. -1.1 V vs $FeCp_2/[FeCp_2]^+$) (Figures 3.2 and 3.3). We similarly screened $(DP^*B^{Ph})NiBr$ and $(DP^*B^{Mes})NiBr$ as precatalysts for H_2 oxidation in THF (0.1 M [TBA][PF₆]) in the presence of NEt^iPr_2 and saw no change in the current response under

an atmosphere of H_2 relative to cyclic voltammograms recorded under an atmosphere of N_2 (Figures 3.4 and 3.5).

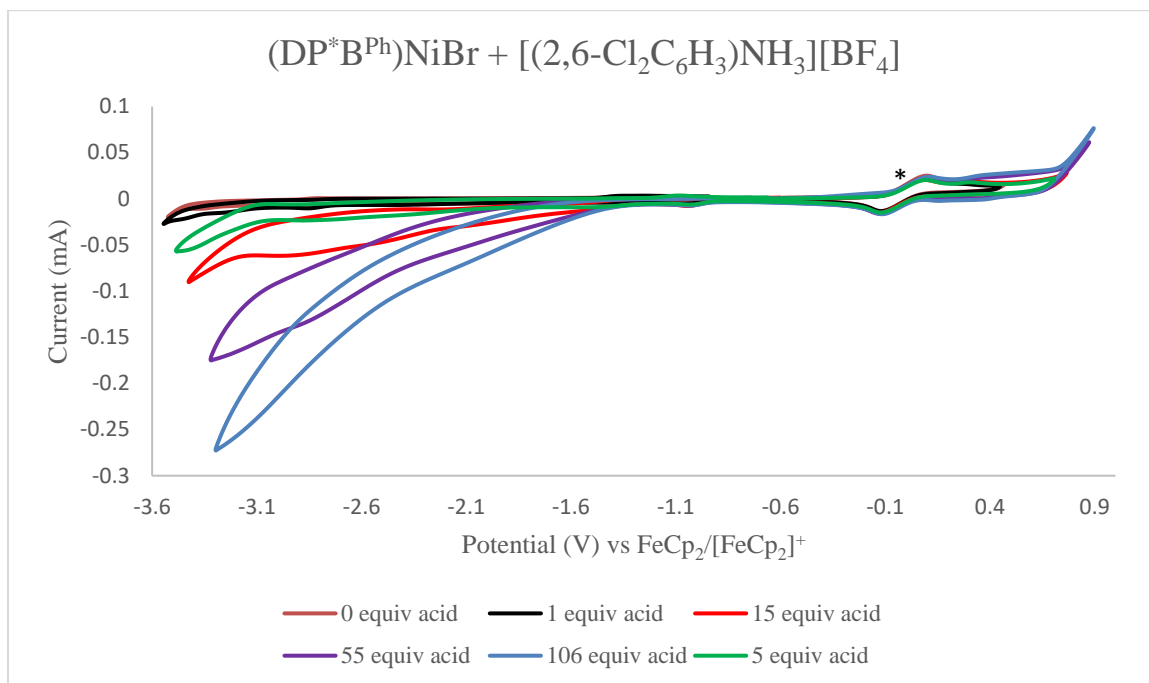


Figure 3.2: Cyclic voltammograms of $(\text{DP}^*\text{B}^{\text{Ph}})\text{NiBr}$ in the presence of 2,6-dichloroanilinium tetrafluoroborate in THF (0.1 M $[\text{TBA}][\text{PF}_6]$). * = $\text{FeCp}_2/[\text{FeCp}_2]^+$.

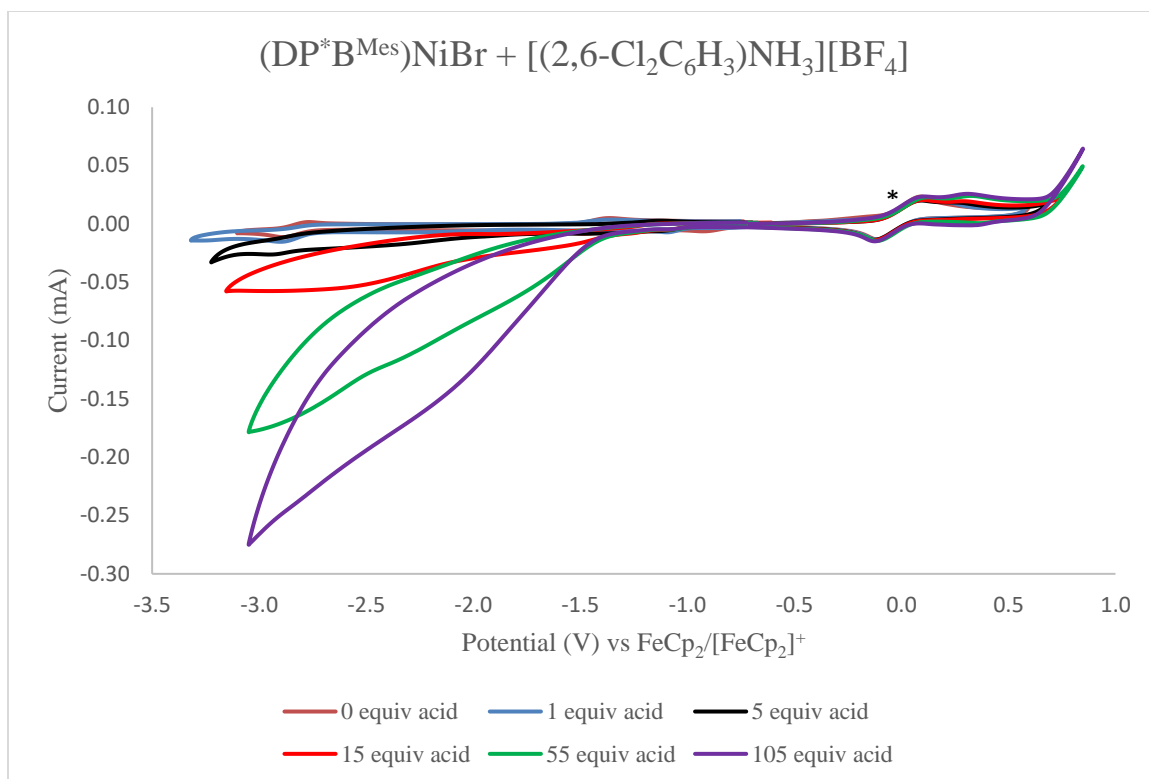


Figure 3.3: Cyclic voltammograms of $(DP^*B^{Mes})NiBr$ in the presence of 2,6-dichloroanilinium tetrafluoroborate in THF (0.1 M $[TBA][PF_6]$). * = $FeCp_2/[FeCp_2]^+$.

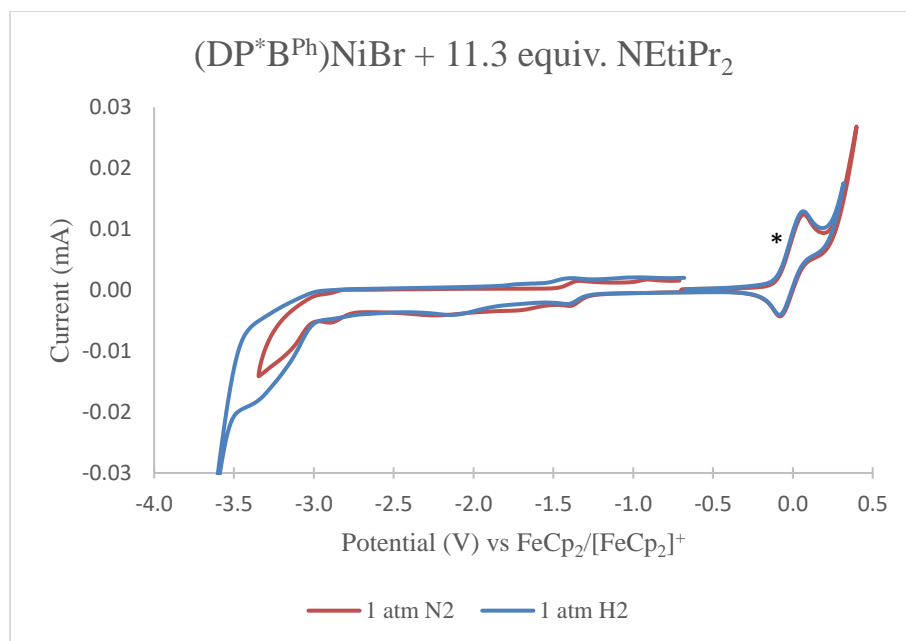


Figure 3.4: Cyclic voltammograms of $(DP^*B^{Ph})NiBr$ in the presence of 11.3 equiv. NEt^iPr_2 under N_2 and H_2 atmospheres. * = $FeCp_2/[FeCp_2]^+$.

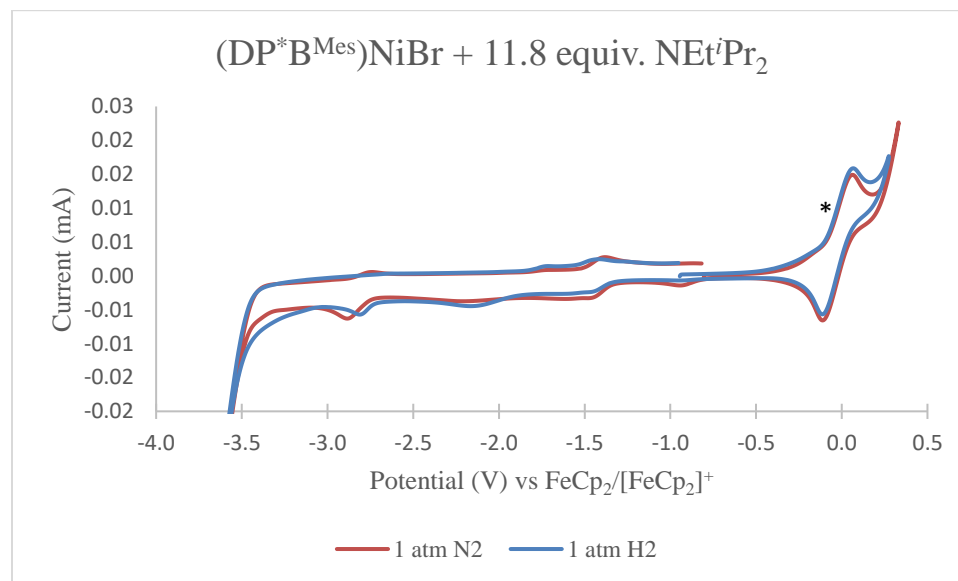
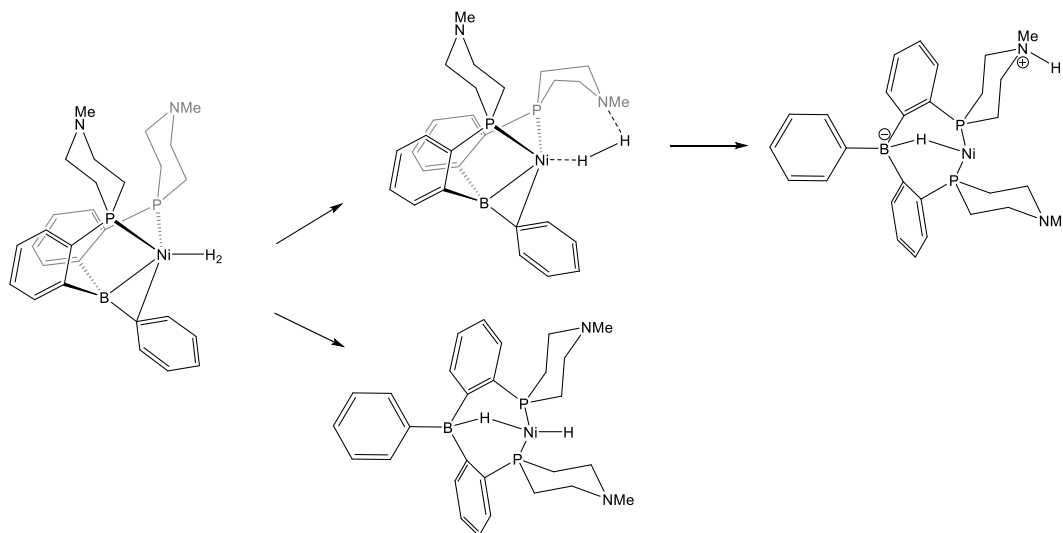


Figure 3.5: Cyclic voltammograms of $(DP^*B^{Mes})NiBr$ in the presence of 11.8 equiv. NEt^iPr_2 under N_2 and H_2 atmospheres. * = $FeCp_2/[FeCp_2]^+$.

3.2.2 Reactivity with H₂ and catalytic hydrogenation of styrene. Despite the unfortunate lack of electrocatalytic activity towards H⁺ reduction and H₂ oxidation determined by our screening attempts we thought that (DP^{*}B^{Ar})Ni species might still display interesting and novel reactivity. We hoped that with the introduction of Lewis basic moieties would lead to new reactivity that would complement our previous studies on reversible H₂ activation and hydrogenation by (PhDPB^{Mes})Ni and the unique H₂ binding and heterolytic cleavage by (DPB)Ni(N₂).^{21,22} More explicitly we hoped that we might be able to bind an H₂ ligand that would then become deprotonated by a pendant amine, giving a zwitterionic nickel complex with both acidic and hydridic moieties which could be useful in the hydrogenation of polar substrates such as aldehydes, ketones, or even CO₂ or CO (Scheme 3.5).



Scheme 3.5: Hypothesized reactivity with H₂ for (DP^{*}B^{Ar})Ni compounds [(DP^{*}B^{Ph}) pictured]. Top path: Deprotonation of an intact H₂ ligand to give a zwitterionic Ni complex. Bottom path: H₂ cleavage across the Ni-B interaction analogous to that observed for (DPB)Ni(H₂).²²

Exposure of $[(DP^*B^{Ph})Ni]_2(N_2)$ to an atmosphere of H_2 for a period of 16 hours resulted in slow decomposition of the starting material to a mixture of benzene (presumably from clipping of the B-C bond on the ligand) and other unidentified diamagnetic materials and a dark insoluble precipitate (Figure 3.6).

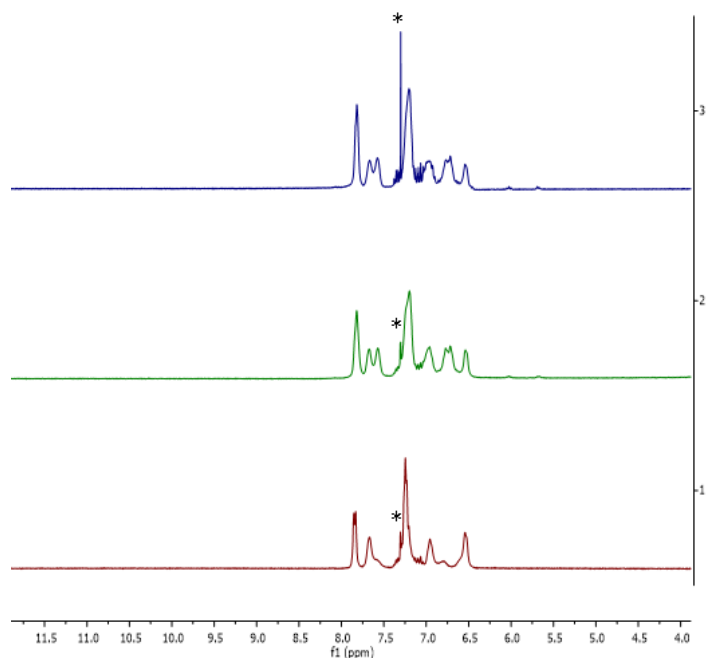
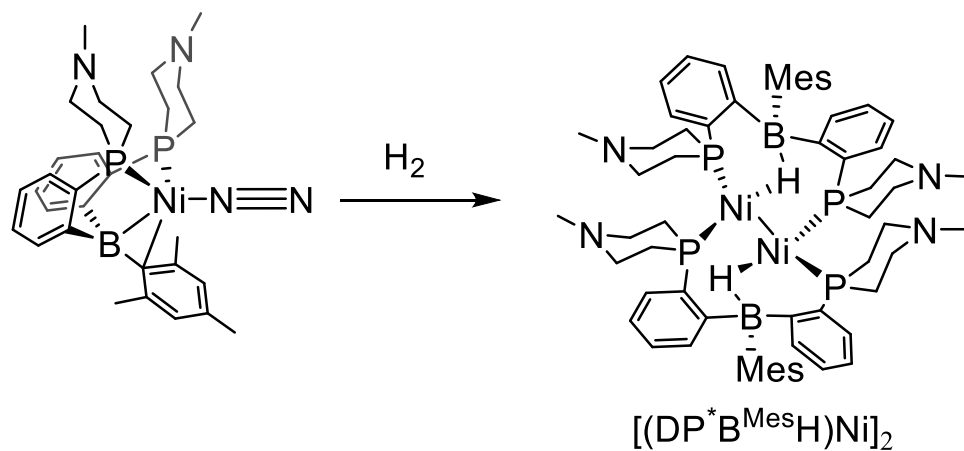


Figure 3.6: 1H NMR spectra of the reaction between $[(DP^*B^{Ph})Ni]_2(N_2)$ and H_2 in d_8 -THF. Bottom: under 1 atm of N_2 . Middle: under 1 atm of H_2 for 1 hour. Top: under 1 atm of H_2 for 16 hours. * = C_6H_6 .

Similar exposure of $(DP^*B^{Mes})Ni(N_2)$ to an atmosphere of H_2 lead to a slow color change from purple to emerald green. The product remained diamagnetic and a new broad resonance in the hydridic region of the 1H NMR spectrum was observed at -5.8 ppm. Crystallization of the green compound by vapor diffusion of Et_2O into HMDSO yielded crystals suitable for single crystal X-ray diffraction studies which revealed the resulting compound to be the dimeric species shown in Scheme 3.6 and Figure 3.7.



Scheme 3.6: Reaction of $(DP^*B^{Mes})Ni(N_2)$ with H_2 forms $[(DP^*B^{Mes}H)Ni]_2$.

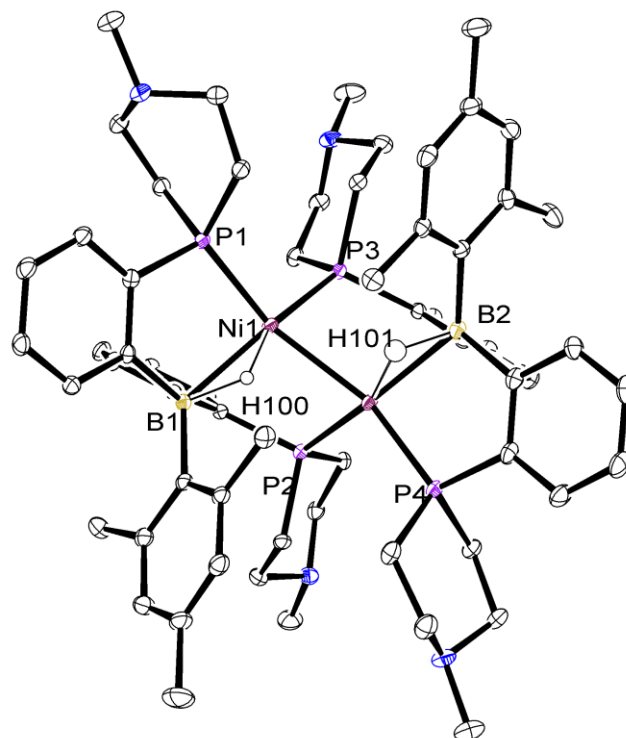


Figure 3.7: ORTEP representation of $[(DP^*B^{Mes}H)Ni]_2$. Ni is shown in magenta, P is shown in purple, N is shown in blue, B is shown in yellow, and C is shown in black. All non-borohydride H atoms have been omitted for clarity. An Et_2O solvent molecule has been omitted for clarity.

In neither case were able to observe formation of a Ni-H₂ adduct like as observed for (DPB)Ni(H₂) nor did we see evidence for reversibility of the reactions with H₂. The dimeric species [(DP*B^{Mes}H)Ni]₂ appeared to be inert towards delivery of the hydride moieties to ketones or aldehydes such as acetophenone and benzophenone nor did it react with styrene. This is somewhat curious because (DP*B^{Mes})Ni(N₂) is a competent precatalyst for the hydrogenation of styrene but becomes deactivated upon complete consumption of styrene as [(DP*B^{Mes}H)Ni]₂. This suggests that some intermediate species between (DP*B^{Mes})Ni(N₂) and [(DP*B^{Mes}H)Ni]₂ exists. Unfortunately, we have not been able to observe or characterize such a species. Both [(DP*B^{Ph})Ni]₂(N₂) and (DP*B^{Mes})Ni(N₂) were capable of facilitating hydrogenation of styrene although both significantly underperformed when compared to the parent (^{Ph}DPB^{Mes})Ni system we have previously reported. Additionally neither [(DP*B^{Ph})Ni]₂(N₂) and (DP*B^{Mes})Ni(N₂) was competent at hydrogenation of polar substrates such as acetophenone or benzaldehyde (Table 3.1).

Table 3.1: Catalytic Hydrogenation of Styrene by (DP^{*}B^{Ar})Ni Compounds and Related Activity Screening Data

Precatalyst ^a	Substrate	Conversion(time)
(DP [*] B ^{Mes})Ni(N ₂)	Styrene	100 % (24 hrs)
[(DP [*] B ^{Ph})Ni] ₂ (N ₂) ^b	Styrene	10 % (16 hrs)
(^{Ph} DPB ^{Mes})Ni ²¹	Styrene	100 % (1 hrs)
(DP [*] B ^{Mes})Ni(N ₂)	Acetophenone	0 % (24 hrs)
[(DP [*] B ^{Ph})Ni] ₂ (N ₂) ^c	Acetophenone	0 % (24 hrs)
(DP [*] B ^{Mes})Ni(N ₂)	Benzaldehyde	0 % (24 hrs)
[(DP [*] B ^{Ph})Ni] ₂ (N ₂) ^c	Benzaldehyde	0 % (24 hrs)

^a Unless otherwise noted reactions were run with 5 mol % precatalyst (per Ni) in C₆D₆ under 1 atm H₂ in a J-Young NMR tube at room temperature. ^b After 16 hours under 1 atm H₂ no apparent reaction had taken place so the pressure of H₂ was increased to ~ 4 atm for 16 hours with minimal conversion of styrene to ethylbenzene observed. Further heating to 40 °C for 16 hours resulted in ~ 10 % conversion to ethylbenzene. ^c Reactions were run under 4 atm H₂.

3.3 Conclusions

We have shown that appended amine moieties can be incorporated into the DPB ligand framework in order to generate the new ligands DP^{*}B^{Ph} and DP^{*}B^{Mes} and have metallated these ligands with nickel. We found that the resultant (DP^{*}B^{Ph})NiBr and (DP^{*}B^{Mes})NiBr were not effective precatalysts for electrocatalytic H⁺ reduction or H₂ oxidation. Furthermore we identified that [(DP^{*}B^{Ph})Ni]₂(N₂) slowly decomposes under an atmosphere of H₂ and that (DP^{*}B^{Mes})Ni(N₂) reacts with H₂ to form the relatively unreactive dimeric species [(DP^{*}B^{Mes}H)Ni]₂ in the absence of styrene. We further found that [(DP^{*}B^{Ph})Ni]₂(N₂) and (DP^{*}B^{Mes})Ni(N₂) are less active catalysts for hydrogenation of styrene to ethylbenzene relative to the parent (^{Ph}DPB^{Mes})Ni system and did not appear to

facilitate hydrogenation of polar substrates such as ketones or aldehydes in the reaction screened. The lack of H^+ reduction activity may possibly be attributed to the basicity of the pendant amines which may be too basic to effectively act as H^+ shuttles (i.e., pK_a is too high) and development of a DP^*B^{Ar} platform which has aniline moieties rather than trialkyl amines as the appended functionality may see improvement in either H^+ reduction or H_2 oxidation. The structural and reactivity differences between $[(DP^*B^{Ph})Ni]_2(N_2)$ and $(DP^*B^{Mes})Ni(N_2)$ highlight the role in which the steric bulk of the aryl group plays in determining the structure and reactivity of metallated species. Finally, we can correlate the poorer catalytic activity for styrene hydrogenation to the irreversible reactivity of both $[(DP^*B^{Ph})Ni]_2(N_2)$ and $(DP^*B^{Mes})Ni(N_2)$ with H_2 . This highlights the importance of having reversible oxidative addition and reductive elimination of the reductant (H_2 or Si-H) that our group has observed in the DPB compounds that perform well at hydrogenation of olefins $[(^{Ph}DPB^{Mes})Ni]$ and hydrosilylation of aldehydes and ketones $[(^{Ph}DPB^{Mes})Ni$ and $(DPB)Co(N_2)]$ (see Chapter 2).^{21,22,25}

3.4 Supporting Information

3.4.1 Experimental Section:

General Considerations: All manipulations were performed using standard Schlenk or glovebox techniques under an atmosphere of N_2 . Solvents were degassed and dried by sparging with N_2 gas and passage through an activated alumina column. Deuterated solvents were purchased from Cambridge Isotopes Laboratories, Inc., and were degassed and stored over activated 3 Å molecular sieves prior to use. Reagents were purchased from commercial vendors and used without further purification unless otherwise noted. All reagents were checked for purity by 1H NMR spectroscopy prior to use. 4-(2-

bromophenyl)-1-methyl-1,4-azaphosphinane, PhB(OMe)_2 , and MesB(OMe)_2 were synthesized according to a literature procedures.^{23,26,27}

Spectroscopic Measurements. ^1H , ^{13}C , ^{31}P , and ^{11}B NMR spectra were collected at room temperature on a Varian 400 MHz spectrometer or a Varian 300 MHz spectrometer. ^1H and ^{13}C spectra were referenced to residual solvent resonances. ^{31}P NMR spectra were referenced to external 85% phosphoric acid ($\delta = 0$ ppm). ^{11}B NMR spectra were referenced to $\text{BF}_3 \cdot \text{Et}_2\text{O}$ ($\delta = 0$ ppm). UV-vis measurements were performed with a Cary 50 instrument with Cary WinUV software. IR spectra were obtained as thin films formed by evaporation or as a solution using a cell with KBr windows using a Bruker Alpha Platinum ATR spectrometer with OPUS software. EPR spectra were recorded on a Bruker EMS spectrometer in frozen solutions at 77 K. EPR simulations used the EasySpin software package.²⁸

X-ray Crystallography. X-ray diffraction studies were carried out at the Caltech Division of Chemistry and Chemical Engineering X-ray Crystallography Facility on a Bruker three-circle SMART diffractometer with a SMART 1K CCD detector, APEX CCD detector, or Bruker D8 VENTURE Kappa Duo PHOTON 100 CMOS detector. Data were collected at 100 K using Mo $K\alpha$ radiation ($\lambda = 0.71073 \text{ \AA}$) or Cu $K\alpha$ radiation ($\lambda = 1.54178 \text{ \AA}$). Structures were solved by direct or Patterson methods using SHELXS and refined against F^2 on all data by full-matrix least-squares with SHELXL-2000. All non-hydrogen atoms were refined anisotropically. With the exception of any $\mu\text{-B-H-M}$ hydrides that were located on the difference map, all hydrogen atoms were placed at geometrically calculated positions and refined using a riding model. The isotropic displacement

parameters of all hydrogen atoms were fixed at 1.2 (1.5 for methyl groups) times the Ueq of the atoms to which they are bonded.

*DP*B^{Ph}*: 1.4914 g (5.48 mmol) of 4-(2-bromophenyl)-1-methyl-1,4-azaphosphinane was dissolved in Et₂O (15 mL) and cooled to -78 °C. ⁿBuLi (3.8 mL, 1.6 M in hexanes) was added dropwise to the stirring solution and allowed to stir for 2 hours at -78 °C, giving a cloudy white suspension. A chilled solution of PhB(OMe)₂ (411.1 mg, 2.74 mmol) in 5 mL Et₂O was added to the stirring solution dropwise and allowed to slowly warm to room temperature overnight (~ 14 hours). The solution was then cooled to -78 °C again and solid [HNEt^tPr₂][Cl] (1.0 g, 6.03 mmol) was added to the stirring solution and stirred cold for 2 hours followed by stirring at room temperature for ~ 12 hours, giving a cloudy white suspension. The suspension was filtered through Celite and volatiles were removed *in vacuo* to give a clear tacky residue which was extracted in pentane. Crystals of *DP*B^{Ph}* were grown from a concentrated Et₂O solution at -35 °C. ¹H NMR (300 MHz, C₆D₆) δ 7.86 (d, ³J_{HH} = 7.4 Hz, 2H), 7.62-7.55 (m, 2H), 7.44 (d, ³J_{HH} = 7.3 Hz, 2H), 7.40-7.33 (m, 2H), 7.27-7.09 (m, 5H), 2.62-2.45 (m, 4H), 2.43-2.28 (m, 4H), 2.02 (s, 6H), 1.94-1.78 (m, 8H). ³¹P NMR (162 MHz, C₆D₆): δ -55.63

*DP*B^{Mes}*: 1.51 g (5.55 mmol) of 4-(2-bromophenyl)-1-methyl-1,4-azaphosphinane was dissolved in Et₂O (30 mL) and cooled to -78 °C. ⁿBuLi (3.8 mL, 1.6 M in hexanes) was added dropwise to the stirring solution and allowed to stir for 2 hours at -78 °C, giving a cloudy white suspension. A chilled solution of PhB(OMe)₂ (532.8 mg, 2.77 mmol) in 5 mL Et₂O was added to the stirring solution dropwise and allowed to slowly warm to room temperature overnight (~ 14 hours), giving a cloudy pale yellow solution. The solution was then cooled to -78 °C again and solid [HNEt^tPr₂][Cl] (1.0073 g, 6.08 mmol) was added to

the stirring solution and stirred cold for 2 hours followed by stirring at room temperature for ~ 12 hours, giving a cloudy pale yellow suspension. The suspension was filtered through Celite and volatiles were removed *in vacuo* to give a yellow residue which was extracted in Et₂O. Crystals of DP*B^{Mes} were grown from a concentrated Et₂O solution at - 35 °C. ESI-MS 515 (M + 1). ¹H NMR (300 MHz, C₆D₆) δ 7.64 (d, ³J_{HH} = 6.7 Hz, 2H), 7.30 (d, J = 6.9 Hz, 2H), 7.19-7.14 (m, 2H), 7.05 (t, J = 7.3 Hz, 2H), 6.79 (s, 2H), 2.81-2.68 (m, 8H), 2.25 (s, 6H), 2.19 (s, 3H), 2.14 – 2.05 (m, 8H), 1.56 (s, 6H). ³¹P NMR (162 MHz, C₆D₆): δ -43.8.

(DP*B^{Ph})NiBr: 247.4 mg of DP*B^{Ph} (0.58 mmol) was stirred in THF (~3 mL) with NiBr₂ (63.5 mg, 0.29 mmol) for 20 minutes giving a cloudy orange suspension. Ni(COD)₂ (79.8 mg, 0.29 mmol) in THF (3 mL) was added dropwise via pipette to the stirring solution causing an immediate color change to dark blood red-orange. The mixture was stirred for 16 hours and filtered through Celite. Removal of all volatiles *in vacuo* left a dark red glaze. The solids were washed with Et₂O (3 x 2 mL). Yield: 128.7 mg, 0.21 mmol (36.2 %) ¹H NMR (300 MHz, C₆D₆) δ 19.85 (s, br), 11.82 (s, br), 3.73 (s, br), 2.75 (s, br), -4.51 (s, br).

(DP*B^{Mes})NiBr: 258.3 mg of DP*B^{Mes} (0.50 mmol) was stirred in THF (~8 mL) with NiBr₂ (55.0 mg, 0.25 mmol) for 20 minutes giving a cloudy orange-brown suspension. Ni(COD)₂ (69.1 mg, 0.25 mmol) in THF (3 mL) was added dropwise via pipette to the stirring solution causing an immediate color change to deep green. After stirring for 2 hours the solution turns red-brown and after stirring overnight (~16 hours) the solution is deep red-orange. The mixture was filtered through Celite and removal of all volatiles *in vacuo* left a dark red glaze. The solids were washed with Et₂O (3 x 2 mL). Yield: 128.7 mg, 0.21

mmol (36.2 %) ^1H NMR (300 MHz, C_6D_6) δ 17.88 (s, br), 11.06 (s, br), 4.60 (s, br), 2.98 (s, br), 2.54 (s, br), -4.30 (s, br).

$[(\text{DP}^*\text{B}^{\text{Ph}})\text{Ni}]_2(\text{N}_2)$: 128.7 mg of $(\text{DP}^*\text{B}^{\text{Ph}})\text{NiBr}$ was dissolved in THF (10 mL) was stirred over freshly prepared 1 % sodium/mercury amalgam (2.52 equiv.) vigorously for three hours. The resulting red-brown solution was filtered through Celite and volatiles were removed *in vacuo* leaving a dark brown glaze in the vial. The solids were dissolved in benzene and lyophilized giving a dark red powder. The red powder was triturated in pentane three times, and lyophilized one additional time. Crystals of $[(\text{DP}^*\text{B}^{\text{Ph}})\text{Ni}]_2(\text{N}_2)$ were grown from a concentrated Et_2O solution at -35°C . ^1H NMR (300 MHz, C_6D_6) δ 8.07 (d, $^3J_{\text{HH}} = 7.2$ Hz, 2H), 7.70 (s, 2H), 7.32-7.2 (m, 5H), 6.95 (s, 2H), 6.86 (d, $^3J_{\text{HH}} = 6.9$ Hz, 2H), 2.90 (s, 2H), 2.69 (s, 2H), 2.52 (s, 2H), 2.40-1.90 (m, 14 H), 1.71 (s, 2H). ^{31}P NMR (121 MHz, C_6D_6) δ 1.65.

$(\text{DP}^*\text{B}^{\text{Mes}})\text{Ni}(\text{N}_2)$: 73.2 mg of $(\text{DP}^*\text{B}^{\text{Mes}})\text{NiBr}$ was dissolved in THF (10 mL) was stirred over freshly prepared 1 % sodium/mercury amalgam (1.09 equiv.) vigorously for 16 hours. The resulting dark solution was filtered through Celite and concentrated to ca. 2 mL and layered with ca. 15 mL pentane and allowed to stand for 16 hours. A green powder crashed out that was later identified $[(\text{DP}^*\text{B}^{\text{Mes}}\text{H})\text{Ni}]_2$. The mother liquor was decanted and volatiles were removed *in vacuo*, leaving a dark solid. The solids were washed with pentane (3 x 1 mL) leaving a purple residue. This residue was extracted in Et_2O and filtered through Celite and pumped down to give $(\text{DP}^*\text{B}^{\text{Mes}})\text{Ni}(\text{N}_2)$ as a dark black-purple solid. Yield: 21 mg (0.035 mmol, 31 %). IR (thin film from C_6D_6) 2160 cm^{-1} (N-N). ^1H NMR (300 MHz, C_6D_6) δ 7.98 (s, br, 4H), 7.39 (s, br, 4H), 5.99 (s, br, 2H), 2.92 (s, br, 2H), 2.73 (s, br, 2H), 2.5-1.5 (m, 27H). ^{31}P NMR (121 MHz, C_6D_6) δ -3.37.

$[(DP^*B^{Mes}H)Ni]_2$: 3.0 mg $(DP^*B^{Mes})Ni(N_2)$ (0.005 mmol) was dissolved in 400 μ L C_6D_6 , degassed with 3 freeze-pump-thaw cycles and exposed to 1 atm H_2 . The solution turned green after ca. 1 hour stirring at room temperature and was allowed to continue stirring overnight. Crystals suitable for single crystal X-ray diffraction studies were grown by slow evaporation of an Et_2O solution into HMDSO. 1H NMR (400 MHz, C_6D_6) δ 8.13 (s, br, 4H), 7.44 (d, $J = 7.1$ Hz, 4H), 7.11-7.06 (m, 8H), 6.97 (m, 4H), 6.85 (s, 4H), 2.93 (s, 6H), 2.68-2.40 (m, 14H), 2.37 (s, 6H), 2.31-2.17 (m, 6H), 1.99 (s, 12H), 1.93-1.84 (m, 6H), 1.82 (s, 6H), 1.73-1.59 (m, 6H), -5.73 (s, br 1H), -5.80 (s, br, 1H). ^{31}P NMR (121 MHz, C_6D_6) δ -19.17 (d, $^2J_{PP} = 32.9$ Hz, 2P), -29.80 (d, $^2J_{PP} = 33.4$ Hz, 2P).

Table 3.S1: XRD experimental parameters for [(DP*^{B^{Ph}})Ni]₂(N₂), [(DP*^{B^{Mes}}H)Ni]₂

Compound	[(DP* ^{B^{Ph}})Ni] ₂ (N ₂)	[(DP* ^{B^{Mes}} H)Ni] ₂ •Et ₂ O
	C ₅₆ H ₇₀ B ₂ N ₆ P ₄ Ni	C ₆₆ H ₉₂ B ₂ N ₄ P ₄ ONi
Formula Weight	1030.42	1222.36
<i>T</i> (K)	100(2)K	100(2)K
λ (Å)	0.71073	0.71073
Space Group	P-1	P2 ₁ /n
<i>a</i>	11.172(12)	13.2739(5)
<i>b</i>	13.516(14)	26.3904(10)
<i>c</i>	19.79(2)	17.7751(6)
α	95.35(2)	90
β	98.705(18)	90.4250(10)
γ	111.104(17)	90
Volume	2720(5)	6226.5(4)
<i>Z</i>	2	4
Density (calc)	1.601	1.305
R1, wR2	0.1198, 0.3481	0.062, 0.1126

$$R1 = \sum ||F_o| - |F_c|| / \sum |F_o|, wR2 = \{ \sum [w(F_o^2 - F_c^2)^2] / \sum w(F_o^2)^2 \}^{1/2}$$

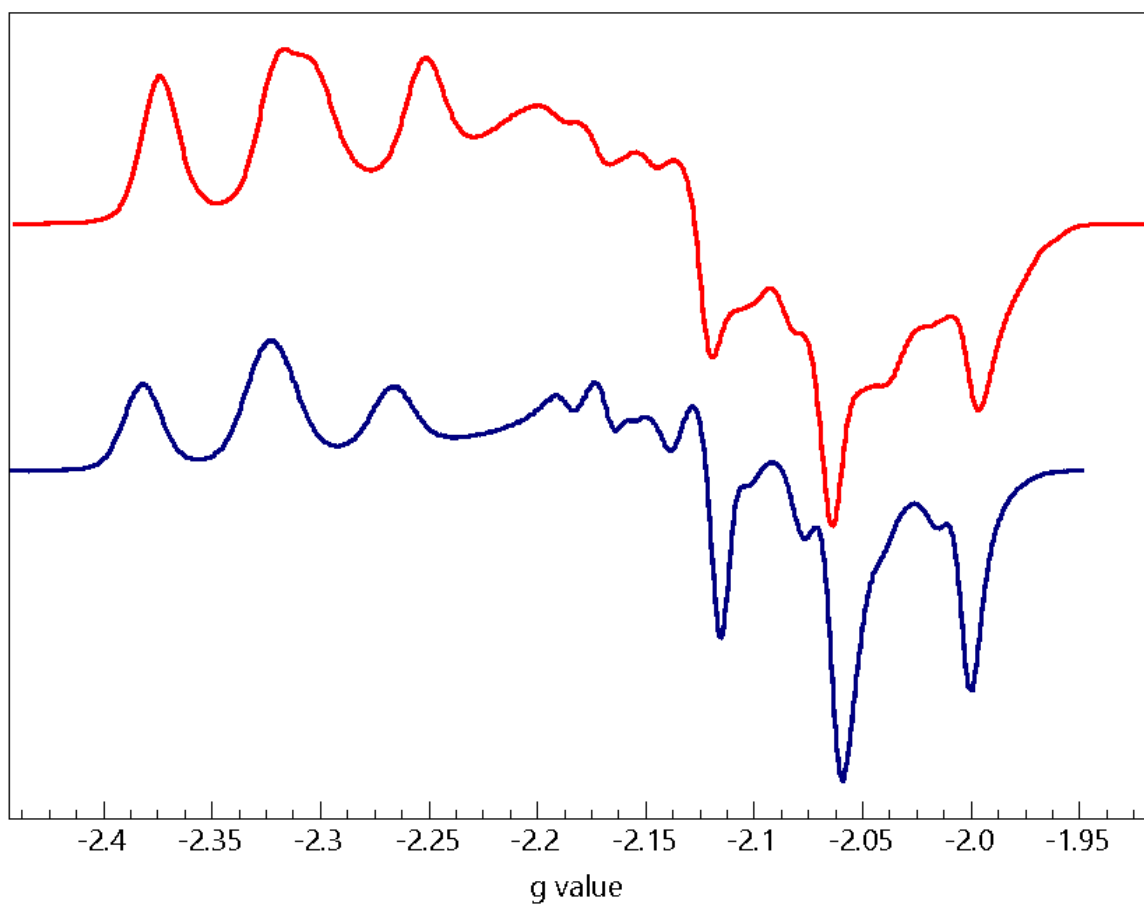


Figure 3.S1: CW X-band EPR spectra of (DP^{*}B^{Ph})NiBr (blue trace) and (DP^{*}B^{Mes})NiBr (red trace) in toluene (77 K).

References

- (1) Simmons, T. R.; Berggren, G.; Bacchi, M.; Fontecave, M.; Artero, V. *Coord. Chem. Rev.* **2014**, 270-271, 127.
- (2) Yang, J. Y.; Bullock, R. M.; Shaw, W. J.; Twamley, B.; Frazee, K.; DuBois, M. R.; DuBois, D. L. *J. Am. Chem. Soc.* **2009**, 131, 5935.
- (3) Kilgore, U. J.; Roberts, J. A. S.; Pool, D. H.; Appel, A. M.; Stewart, M. P.; DuBois, M. R.; Dougherty, W. G.; Kassel, W. S.; Bullock, R. M.; DuBois, D. L. *J. Am. Chem. Soc.* **2011**, 133, 5861.
- (4) Appel, A. M.; Pool, D. H.; O'Hagan, M.; Shaw, W. J.; Yang, J. Y.; Rakowski DuBois, M.; DuBois, D. L.; Bullock, R. M. *ACS Catal.* **2011**, 1, 777.
- (5) O'Hagan, M.; Shaw, W. J.; Raugei, S.; Chen, S.; Yang, J. Y.; Kilgore, U. J.; DuBois, D. L.; Bullock, R. M. *J. Am. Chem. Soc.* **2011**, 133, 14301.
- (6) Helm, M. L.; Stewart, M. P.; Bullock, R. M.; DuBois, M. R.; DuBois, D. L. *Science* **2011**, 333, 863.
- (7) Stewart, M. P.; Ho, M.-H.; Wiese, S.; Lindstrom, M. L.; Thogerson, C. E.; Raugei, S.; Bullock, R. M.; Helm, M. L. *J. Am. Chem. Soc.* **2013**, 135, 6033.
- (8) Huo, P.; Uyeda, C.; Goodpaster, J. D.; Peters, J. C.; Miller, T. F. *ACS Catal.* **2016**, 6, 6114.
- (9) Yang, J. Y.; Smith, S. E.; Liu, T.; Dougherty, W. G.; Hoffert, W. A.; Kassel, W. S.; DuBois, M. R.; DuBois, D. L.; Bullock, R. M. *J. Am. Chem. Soc.* **2013**, 135, 9700.

- (10) Wiese, S.; Kilgore, U. J.; Ho, M.-H.; Raugei, S.; DuBois, D. L.; Bullock, R. M.; Helm, M. L. *ACS Catal.* **2013**, *3*, 2527.
- (11) Franz, J. A.; O'Hagan, M.; Ho, M.-H.; Liu, T.; Helm, M. L.; Lense, S.; DuBois, D. L.; Shaw, W. J.; Appel, A. M.; Raugei, S.; Bullock, R. M. *Organometallics* **2013**, *32*, 7034.
- (12) Das, A. K.; Engelhard, M. H.; Bullock, R. M.; Roberts, J. A. S. *Inorg. Chem.* **2014**, *53*, 6875.
- (13) Brown, H. J. S.; Wiese, S.; Roberts, J. A. S.; Bullock, R. M.; Helm, M. L. *ACS Catal.* **2015**, *5*, 2116.
- (14) Klug, C. M.; O'Hagan, M.; Bullock, R. M.; Appel, A. M.; Wiedner, E. S. *Organometallics* **2017**, *36*, 2275.
- (15) Wiese, S.; Kilgore, U. J.; DuBois, D. L.; Bullock, R. M. *ACS Catal.* **2012**, *2*, 720.
- (16) Das, P.; Stolley, R. M.; van der Eide, E. F.; Helm, M. L. *Eur. J. Inorg. Chem.* **2014**, *2014*, 4611.
- (17) Bediako, D. K.; Solis, B. H.; Dogutan, D. K.; Roubelakis, M. M.; Maher, A. G.; Lee, C. H.; Chambers, M. B.; Hammes-Schiffer, S.; Nocera, D. G. *Proc. Natl. Acad. Sci.* **2014**, *111*, 15001.
- (18) Tsay, C.; Yang, J. Y. *J. Am. Chem. Soc.* **2016**, *138*, 14174.
- (19) Jain, R.; Mashuta, M. S.; Buchanan, R. M.; Grapperhaus, C. A. *Eur. J. Inorg. Chem.* **2017**, *2017*, 3714.
- (20) Seo, J.; Manes, T. A.; Rose, M. J. *Nature Chem.* **2017**, *9*, 552.
- (21) Harman, W. H.; Peters, J. C. *J. Am. Chem. Soc.* **2012**, *134*, 5080.
- (22) Harman, W. H.; Lin, T.-P.; Peters, J. C. *Angew. Chem. Int. Ed.* **2014**, *53*, 1081.
- (23) Creutz, S. E.; Peters, J. C. *Chem. Sci.* **2017**, *8*, 2321.

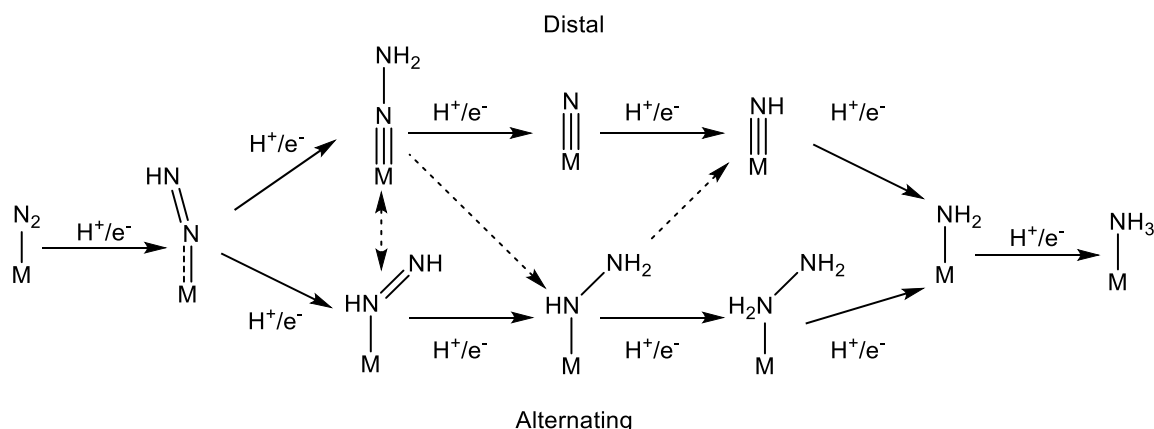
- (24) Suess, D. L. M.; Peters, J. C. *J. Am. Chem. Soc.* **2013**, *135*, 4938.
- (25) Nesbit, M. A.; Suess, D. L. M.; Peters, J. C. *Organometallics* **2015**, *34*, 4741.
- (26) Matsumi, N.; Chujo, Y. *Polymer Bulletin* **1997**, *38*, 531.
- (27) Elkin, P. K.; Levin, V. V.; Dilman, A. D.; Struchkova, M. I.; Belyakov, P. A.; Arkhipov, D. E.; Korlyukov, A. A.; Tartakovsky, V. A. *Tetrahedron Letters* **2011**, *52*, 5259.
- (28) Stoll, S.; Schweiger, A. *J. Magn. Reson.* **2006**, *178*, 42.

Chapter 4

SYNTHESIS AND CHARACTERIZATION OF THE FIRST PARENT IRON DIAZENIDO COMPLEX

4.1 Introduction

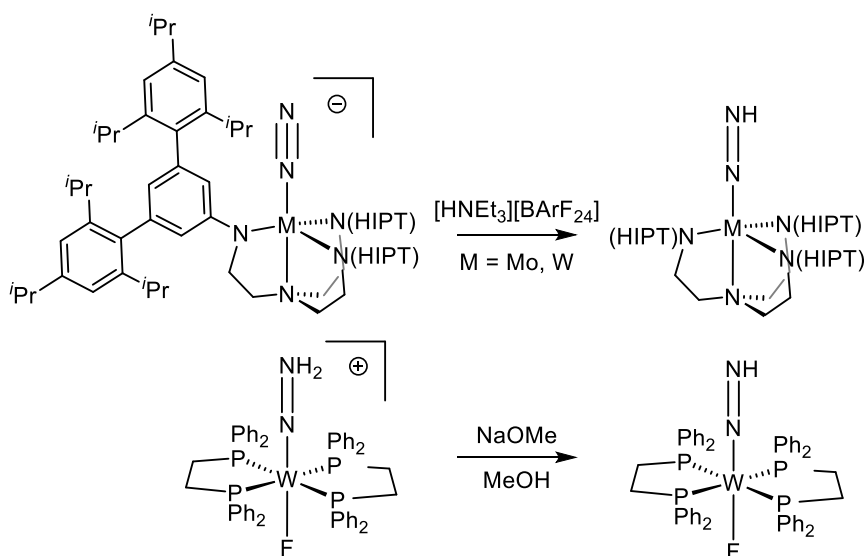
The mechanism of nitrogen fixation in nitrogenase enzymes has been of substantial interest since the discovery and characterization of the iron-molybdenum-cofactor which is the active site in FeMo-nitrogenase enzymes.^{1,2} Hypotheses surrounding the mechanism of N₂ fixation are often framed in the context of two limiting pathways, a distal path where successive protonation occurs at N_β prior to N-N bond cleavage and an alternating path wherein protonation events alternate between N_β and N_α (Scheme 4.1). Early model chemistry from Chatt, Hidai, and others on group VI metals seemed to favor the distal mechanism and studies on the first catalytically active model system from Schrock also showed the viability of a distal pathway on a molybdenum based system.³⁻⁶ Recent work on the biological system has suggested that Fe may be the initial site for N₂ binding, and several Fe based synthetic model systems have shown catalytic activity for N₂ fixation as well as suggesting a potential crossover point between the two limiting paths.⁷⁻¹⁴ Furthermore, recent studies from our lab on the reactivity of [(P₃B)Fe(N₂)]⁻ and [(P₃B)Fe(N₂)]²⁻ with excess acid showed generation of a cationic iron-nitride species [(P₃B)FeN]⁺ and NH₃, a key intermediate in the distal mechanism for N₂ fixation at a single metal site.¹⁴



Scheme 4.1: Limiting mechanistic pathways for N_2 fixation at a single metal site.

Transition metal diazenido ($\text{M}(\text{NNH})$) and hydrazido(2-) ($\text{M}(\text{NNH}_2)$) species are of particular interest in mechanistic studies of N_2 fixation since both are early intermediates in the distal pathway. $\text{M}(\text{NNH})$ species are especially interesting since these species sit at a branching point between the limiting distal and alternating pathways.^{5,8,15,16} Direct observation of these species has been challenging, and $\text{M}(\text{NNH})$ and $\text{M}(\text{NNH}_2)$ species have often proven to be unstable and difficult to observe or isolate. The alkylated and silylated and analogs of metal diazenido and hydrazido(2-) species are fairly well established on a variety of transition metals.¹⁷ Additionally, Lewis acids such as boranes have been used to stabilize the $\text{M}(\text{NNH})$ moiety via formation of $\text{M}(\text{NN}(\text{H})(\text{BR}_3))$ adducts.^{18,19} Despite the precedence for alkyl, aryl, and silyl-diazenido species, only three instances of reliably characterized $\text{M}(\text{NNH})$ species have been reported, all on group VI metal centers (Mo, W) (Scheme 4.2).^{5,15,17,20-22} The Mo- and W-diazenido reported by Schrock and Yandulov were prepared by protonation of anionic $\text{M}-\text{N}_2$ adducts supported by a bulky hexaisopropylterphenyl-substituted triamidoamine ligand using the weak acid $[\text{HNEt}_3][\text{BAr}^{\text{F}}_{24}]$.²² These species been unambiguously identified based on ^1H NMR, ^{15}N NMR, IR and X-ray crystallographic

data.²⁰ The only other reported W-diazenido species was originally reported by Chatt *et al.*, but was not reliably identified until later IR and Raman spectroscopic investigations by Lehnert and Tuzek.^{15,21} Lehnert and Tuzek's studies identified that many of the compounds originally assigned as M(NNH) species by Chatt *et al.* were more appropriately assigned as metal-hydride species and that in some cases an equilibrium between a M(NNH) and M-H species existed in solution.²¹ Instances of well characterized and isolable M(NNH₂) species are more numerous and have been characterized on several group VI systems as well as on iron and other transition metals.^{5,10,15-18,20,23-32}



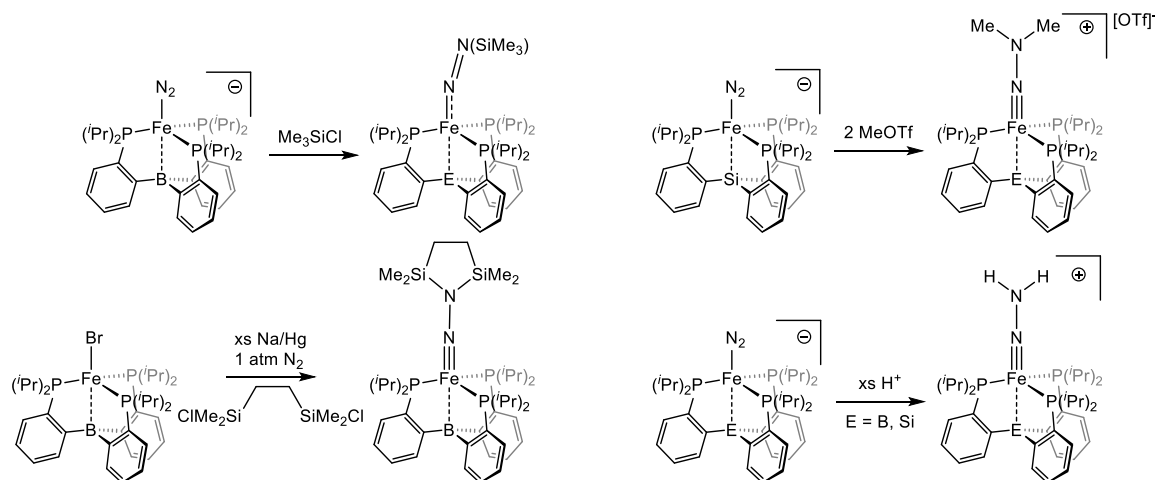
Scheme 4.2: Synthetic routes to previously reported Mo-, and W-diazenido species.^{15,20,22}

Due to the rarity of these species there is substantial interest in characterization of reference compounds whose spectroscopic fingerprints can be used as a point of comparison to guide hypotheses about the identity of potential intermediates in biological nitrogen fixation systems. Herein we report the EPR, ENDOR, HYSCORE, and ⁵⁷Fe Mössbauer spectroscopic characterization of the first directly observed Fe(NNH) species and its

subsequent reaction with H^+ to generate a cationic $[Fe(NNH_2)]^+$. Geometric constraints derived from the spectroscopic data are supported by Density Functional Theory optimized geometries of the proposed $Fe(NNH)$ and $[Fe(NNH_2)]^+$.

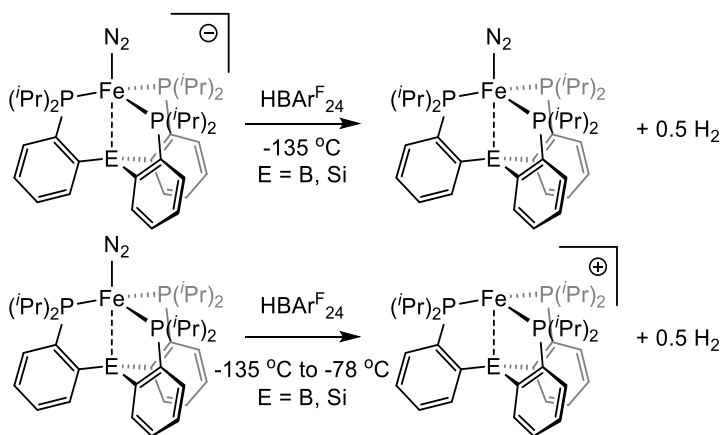
4.2 Results and Discussion

Recent theoretical and experimental investigations from our lab have established that the N-H bonds in $(P_3E)Fe(NNH)$ and $(P_3E)Fe(NNH_2)$ ($E = Si, B$) ($P_3Si = \text{tris}(o\text{-diisopropylphosphinophenyl)silyl}$, $P_3B = \text{tris}(o\text{-diisopropylphosphinophenyl)borane}$) species are very weak (N-H bond dissociation free energy (BDFE) 31.2 kcal/mol for $(P_3B)Fe(NNH)$ and 49.7 kcal/mol for $[(P_3B)Fe(NNH_2)]^+$).³³ The group VI systems have much stronger N-H bonds and seem less prone to deleterious reactivity (for example the predicted N-H bond dissociation enthalpy for $(HIPT)Mo(NNH)$ is ~49 kcal/mol).⁸ Model studies from our lab on $(P_3Si)Fe$ and $(P_3B)Fe$ systems capable of performing catalytic fixation of N_2 suggest that initial functionalization of N_2 with electrophilic reagents such as Me_3SiCl , 1,2-bis-(chlorodimethylsilyl)ethane, and $MeOTf$ takes place at the β -nitrogen generating alkylated and silylated diazenido and hydrazido(2-) species (Scheme 4.3).^{10,16,34-}
³⁷ Additionally, our ability to characterize $[(P_3E)Fe(NNH_2)]^{0/+}$ ($E = Si, B$) species generated by the reaction of anionic $Fe-N_2$ adducts with excesses of acid suggested that a transiently generated $(P_3E)Fe(NNH)$ species was being trapped as the cationic iron hydrazido $[P_3EFe(NNH_2)]^+$ (Scheme 4.3).



Scheme 4.3: Previously reported N β -functionalization with electrophilic reagents on $(\text{P}_3\text{Si})\text{Fe}$ and $(\text{P}_3\text{B})\text{Fe}$ platforms.

Unfortunately, previous attempts to synthesize the hypothesized $\text{Fe}(\text{NNH})$ species using stoichiometric amounts of acid resulted primarily in one electron oxidation of the $[\text{FeN}_2]^-$ starting material to the FeN_2 or oxidation of the FeN_2 to a cationic species with a vacant coordination site along with evolution of 0.5 equivalents of H_2 (Scheme 4.4).

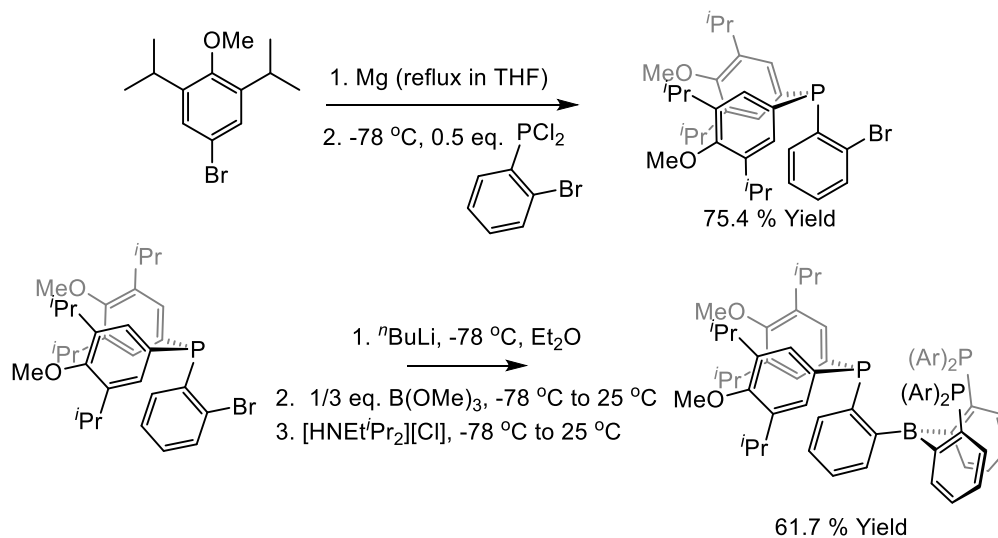


Scheme 4.4: Reactions of $(\text{P}_3\text{E})\text{Fe}(\text{N}_2)]^{0/-}$ with $\text{HBArF}_{24} \cdot 2\text{Et}_2\text{O}$.

Taking these observations from reactions with alkyl and silyl electrophiles, as well as with protic acids, we hypothesized that an $\text{Fe}(\text{NNH})$ species might be observed *en route* to

an $[\text{Fe}(\text{NNH}_2)]^+$. Furthermore we supposed that introduction of sufficient steric bulk around the NNH ligand would slow undesirable side reactions such as H_2 formation via a potential bimolecular coupling pathway thereby stabilizing any species with reactive N-H bonds. We targeted an electron rich tris(diarylphosphino)borane system ($^{\text{Ar}}\text{P}_3\text{B}$) (where Ar = 3,5-diisopropyl-4-methoxyphenyl) as an attractive ligand framework with sufficient vertical steric bulk to create a protective binding pocket for N_2 , and with electron donating properties more similar to the isopropyl substituted phosphines in the catalytically competent $(\text{P}_3\text{B})\text{Fe}$ system.

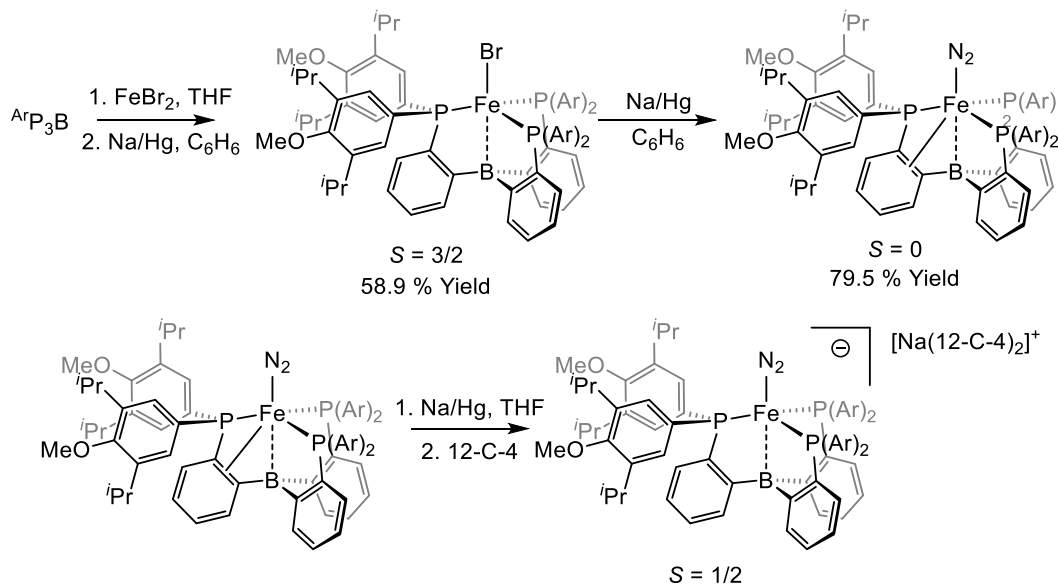
The new $^{\text{Ar}}\text{P}_3\text{B}$ ligand was assembled from previously reported orthobromophenyldichlorophosphine, 4-bromo-2,6-diisopropyl-1-methoxybenzene, and $\text{B}(\text{OMe})_3$ (Scheme 4.5).^{38,39}



Scheme 4.5: Synthesis of $^{\text{Ar}}\text{P}_3\text{B}$.

Metalation of the ligand was achieved by complexation of the ligand with FeBr_2 in THF followed by trituration in Et_2O and reduction in benzene with 1 equiv. of sodium-mercury amalgam to afford the $S = 3/2$ $(^{\text{Ar}}\text{P}_3\text{B})\text{FeBr}$ which was isolated as a dark brown

microcrystalline solid in 58.9 % yield (Figure 4.S1). Further reduction of $(^{\text{Ar}}\text{P}_3\text{B})\text{FeBr}$ by stirring over an excess of sodium-mercury amalgam in benzene afforded diamagnetic $(^{\text{Ar}}\text{P}_3\text{B})\text{Fe}(\text{N}_2)$ which was isolated as a dark green solid in 79.5 % yield (Figure 4.S2). Stirring over an excess of sodium-mercury amalgam in THF yielded $[(^{\text{Ar}}\text{P}_3\text{B})\text{Fe}(\text{N}_2)][\text{Na}(12\text{-C-}4)_2]$ upon treatment with two equivalents of 12-crown-4 (Scheme 4.6). While we were unable to grow crystals of sufficient quality for X-ray diffraction studies, a DFT optimized geometry for $[(^{\text{Ar}}\text{P}_3\text{B})\text{Fe}(\text{N}_2)]^-$ shows a sterically protected N_2 binding pocket that should still be accessible by small electrophiles such as H^+ (Figure 4.1) (TPSS, def2-TZVP on Fe, def2-SVP on C, H, P, B, O, N). The N_2 stretching frequency observed for $(^{\text{Ar}}\text{P}_3\text{B})\text{Fe}(\text{N}_2)$ of 2014 cm^{-1} is very similar to the 2011 cm^{-1} N_2 stretching frequency observed in the parent $(\text{P}_3\text{B})\text{Fe}(\text{N}_2)$ system with isopropyl substituents on the phosphines.⁴⁰ This indicates that the electron rich arylphosphines coupled with the η^2 -arene interaction with the phenylene linker are able to engender a similar degree of N_2 activation as the isopropyl phosphine substituents. However, upon comparison of the N_2 stretching frequencies of $[(^{\text{Ar}}\text{P}_3\text{B})\text{Fe}(\text{N}_2)][\text{Na}(12\text{-C-}4)_2]$ and $[(\text{P}_3\text{B})\text{Fe}(\text{N}_2)][\text{Na}(12\text{-C-}4)_2]$ (1937 cm^{-1} and 1905 cm^{-1} respectively) it becomes apparent that the bulky arylphosphine ligand does not facilitate activation of the N_2 ligand to the extent that the parent ligand does.⁴⁰ However, the significant activation of the N_2 as judged by the N-N stretching frequencies observed in neutral and anionic $(^{\text{Ar}}\text{P}_3\text{B})\text{Fe}(\text{N}_2)$ complexes suggests that they might display similar reactivity to their analogous $(\text{P}_3\text{B})\text{Fe}(\text{N}_2)$ counterparts.



Scheme 4.6.: Synthesis of ArP_3BFe compounds.

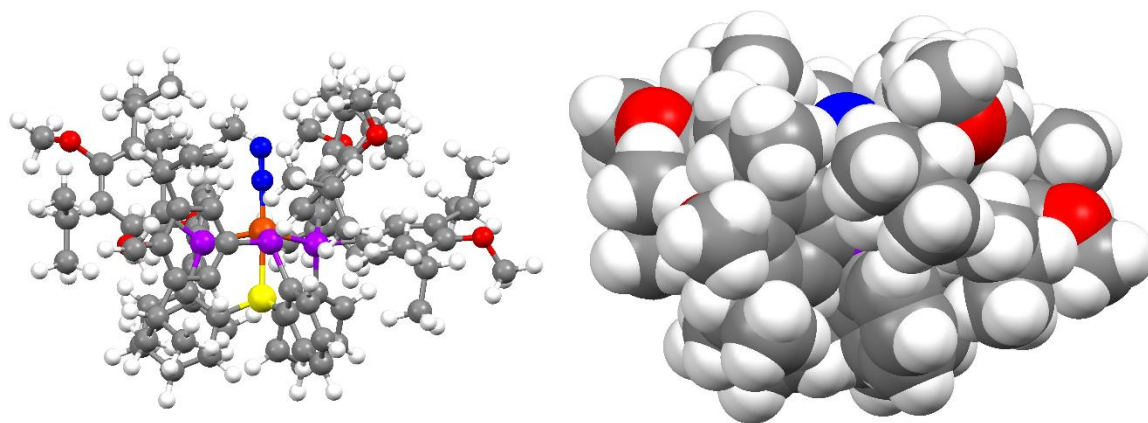
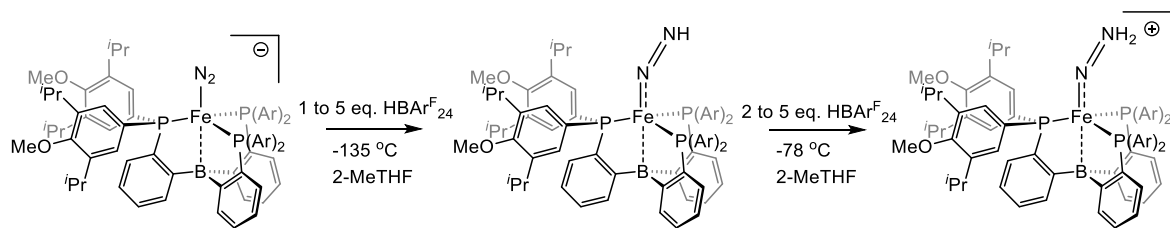


Figure 4.1: Left: DFT optimized structure of $[(\text{ArP}_3\text{B})\text{Fe}(\text{N}_2)]^-$ using the full ArP_3B ligand (TPSS, def2-TZVP on Fe, def2-SVP on all else). Right: Space filling model generated from DFT coordinates.

We investigated the reactivity of $[(\text{ArP}_3\text{B})\text{Fe}(\text{N}_2)][\text{Na}(\text{12-C-4})_2]$ with $\text{HBAr}_{24}^{\text{F}} \cdot 2\text{Et}_2\text{O}$ ($\text{BAr}_{24}^{\text{F}}$ = tetra-(3,5-bistrifluoromethylphenyl)borate) by continuous wave X-band electron paramagnetic resonance spectroscopy (CW-EPR) (Scheme 4.7). Reactions between $[(\text{ArP}_3\text{B})\text{Fe}(\text{N}_2)][\text{Na}(\text{12-C-4})_2]$ and $\text{HBAr}_{24}^{\text{F}} \cdot 2\text{Et}_2\text{O}$ were performed in EPR tubes in thawing

2-MeTHF solutions and mechanically mixed with a stainless steel needle. Mixing of $[(^{\text{Ar}}\text{P}_3\text{B})\text{Fe}(\text{N}_2)][\text{Na}(12\text{-C-4})_2]$ with one equivalent of $\text{HBAr}^{\text{F}}_{24} \cdot 2\text{Et}_2\text{O}$ in thawing 2-MeTHF for 30 minutes lead to observation of a new near-axial $S = 1/2$ species by CW X-band EPR (Figure 4.2, C) assigned as $(^{\text{Ar}}\text{P}_3\text{B})\text{Fe}(\text{NNH})$. This species decays rapidly upon warming to $-78\text{ }^\circ\text{C}$ to generate a mixture of species of which the major product is $(^{\text{Ar}}\text{P}_3\text{B})\text{Fe}(\text{N}_2)$. $(^{\text{Ar}}\text{P}_3\text{B})\text{Fe}(\text{NNH})$ was also generated in the presence of excess acid (2-5 eq.) mixing for only 15 minutes in thawing 2-MeTHF. Warming $(^{\text{Ar}}\text{P}_3\text{B})\text{Fe}(\text{NNH})$ to $-78\text{ }^\circ\text{C}$ for 5 minutes in the presence of excess acid resulted in generation of a signal corresponding to a rhombic $S = 1/2$ species (Figure 4.2, E) assigned as $[(^{\text{Ar}}\text{P}_3\text{B})\text{Fe}(\text{NNH}_2)][\text{BAr}^{\text{F}}_{24}]$. Furthermore, warming a solution of $(^{\text{Ar}}\text{P}_3\text{B})\text{Fe}(\text{NNH})$ in the presence of excess $\text{HBAr}^{\text{F}}_{24}$ to $-78\text{ }^\circ\text{C}$ for 30 seconds followed by rapid freeze quenching gave a mixture of $(^{\text{Ar}}\text{P}_3\text{B})\text{Fe}(\text{NNH})$ and $[(^{\text{Ar}}\text{P}_3\text{B})\text{Fe}(\text{NNH}_2)][\text{BAr}^{\text{F}}_{24}]$ (Figure 4.2, D) which converted completely to $[(^{\text{Ar}}\text{P}_3\text{B})\text{Fe}(\text{NNH}_2)][\text{BAr}^{\text{F}}_{24}]$ upon further warming at $-78\text{ }^\circ\text{C}$ (Figure 4.2).



Scheme 4.7: Reactivity of $[(^{\text{Ar}}\text{P}_3\text{B})\text{Fe}(\text{N}_2)][\text{Na}(12\text{-C-4})_2]$ with $\text{HBAr}^{\text{F}}_{24}$.

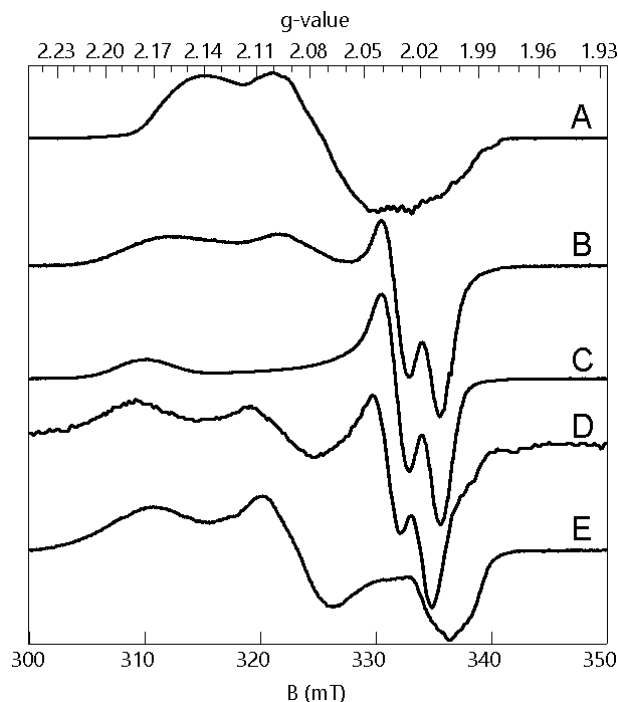


Figure 4.2: Reaction progress of $[(^{\text{Ar}}\text{P}_3\text{B})\text{Fe}(\text{N}_2)][\text{Na}(12\text{-C-4})_2]$ with excess $\text{HBar}^{\text{F}}_{24}$ monitored by CW X-band EPR (77 K, 9.44 GHz, MW power: 6.44 mW, Mod Amp: 0.01 mT, Conversion time: 5.12 ms). A: $[(^{\text{Ar}}\text{P}_3\text{B})\text{Fe}(\text{N}_2)][\text{Na}(12\text{-C-4})_2]$. B: Reaction mixture after mixing for only 15 minutes with 1 eq. $\text{HBar}^{\text{F}}_{24} \cdot 2\text{Et}_2\text{O}$ at $-135\text{ }^{\circ}\text{C}$ showing components of $[(^{\text{Ar}}\text{P}_3\text{B})\text{Fe}(\text{N}_2)][\text{Na}(12\text{-C-4})_2]$ and $(^{\text{Ar}}\text{P}_3\text{B})\text{Fe}(\text{NNH})$. C: Reaction mixture after mixing for 15 minutes with 2.3 eq. $\text{HBar}^{\text{F}}_{24} \cdot 2\text{Et}_2\text{O}$ at $-135\text{ }^{\circ}\text{C}$ showing full conversion to $(^{\text{Ar}}\text{P}_3\text{B})\text{Fe}(\text{NNH})$ (identical spectra were obtained mixing for 30 minutes in the presence of 1 eq. $\text{HBar}^{\text{F}}_{24} \cdot 2\text{Et}_2\text{O}$). D: Reaction mixture from previous trace after warming to $-78\text{ }^{\circ}\text{C}$ for 30 seconds and rapidly freeze quenching in liquid N_2 showing a mixture of $(^{\text{Ar}}\text{P}_3\text{B})\text{Fe}(\text{NNH})$ and $[(^{\text{Ar}}\text{P}_3\text{B})\text{Fe}(\text{NNH}_2)][\text{Bar}^{\text{F}}_{24}]$. E: Reaction mixture from previous trace after warming to $-78\text{ }^{\circ}\text{C}$ for 90 seconds showing complete conversion to $[(^{\text{Ar}}\text{P}_3\text{B})\text{Fe}(\text{NNH}_2)][\text{Bar}^{\text{F}}_{24}]$ (reactions with up to 5 eq. $\text{HBar}^{\text{F}}_{24} \cdot 2\text{Et}_2\text{O}$ showed identical spectra).

To further corroborate our assignments electron nuclear double resonance (ENDOR) and hyperfine sub-level correlation spectroscopies (HYSCORE) were employed on samples of $[(^{\text{Ar}}\text{P}_3\text{B})\text{Fe}(\text{N}_2)]^-$, $(^{\text{Ar}}\text{P}_3\text{B})\text{Fe}(\text{NNH})$, and $[(^{\text{Ar}}\text{P}_3\text{B})\text{Fe}(\text{NNH}_2)]^+$ as well as isotopically enriched analogs generated using $\text{DBar}^{\text{F}}_{24} \cdot 2\text{Et}_2\text{O}$ or $[(^{\text{Ar}}\text{P}_3\text{B})\text{Fe}(^{15}\text{N}_2)]^-$ to gain additional structural information on the observed species.

For the sake of comparison to the protonated species we first studied $[(^A\text{P}_3\text{B})\text{Fe}(\text{N}_2)][\text{Na}(12\text{-C-4})_2]$ by ENDOR and HYSCORE spectroscopies. The Q-band ENDOR spectra are well modeled with hyperfine coupling to ^{11}B and three different ^{31}P environments, with two more strongly coupled than the third (Figure 4.3, Table 4.1). Isotopic labelling with $^{15}\text{N}_2$ aided in determination of the hyperfine coupling constants and quadrupole parameters for ^{14}N and ^{15}N via HYSCORE spectroscopy at X-band (Figures 4.4 and 4.S4).

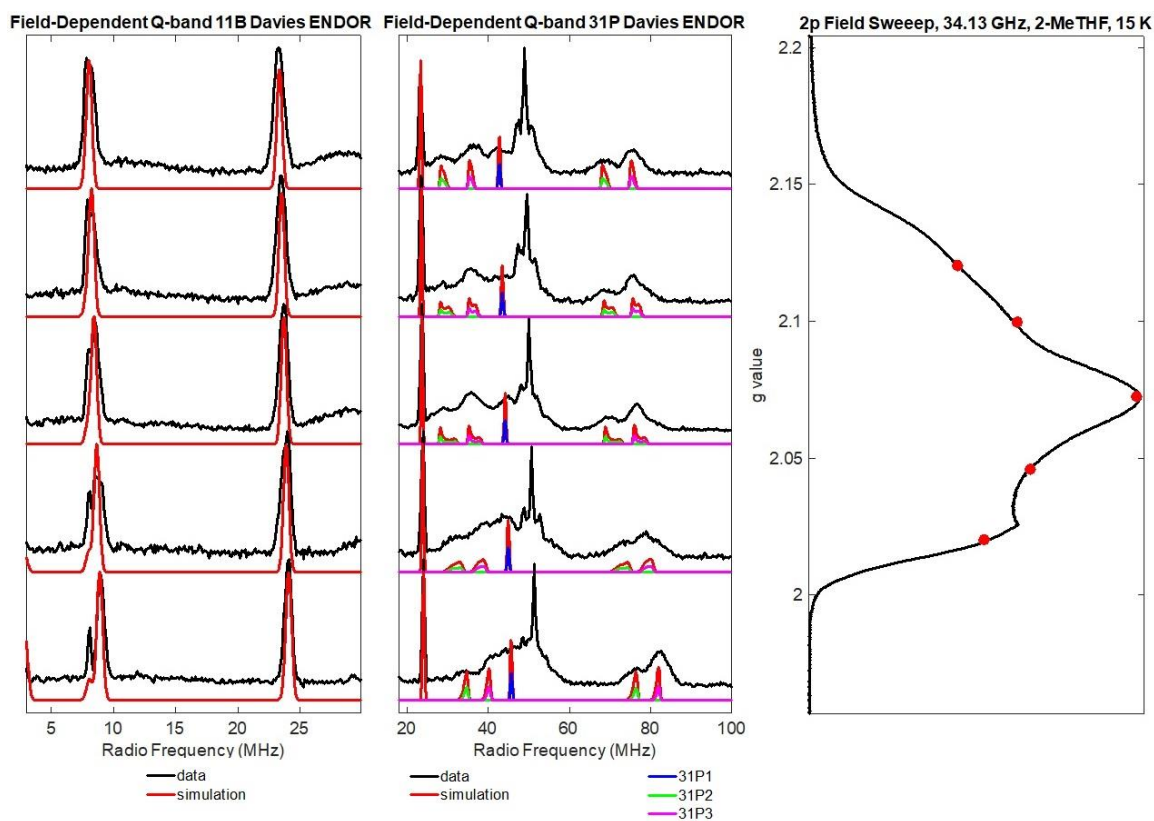


Figure 4.3: Left: Field Dependent Q-Band ENDOR spectra of $[(^A\text{P}_3\text{B})\text{Fe}(\text{N}_2)][\text{Na}(12\text{-C-4})_2]$ with simulation of ^{11}B hyperfine couplings. Middle: Field Dependent Q-Band ENDOR spectra of $[(^A\text{P}_3\text{B})\text{Fe}(\text{N}_2)][\text{Na}(12\text{-C-4})_2]$ with simulation of individual ^{31}P hyperfine couplings. Right: 2 pulse field sweep with ENDOR field positions marked in red. (Experimental Parameters: Temperature = 15 K; MW Frequency = 34.13 GHz; MW Pulse Length ($\pi/2$, π) = 40 ns, 80 ns; RF Pulse Length = 40 μs ; Shot Rep Time = 5000 μs ; τ = 300 ns).

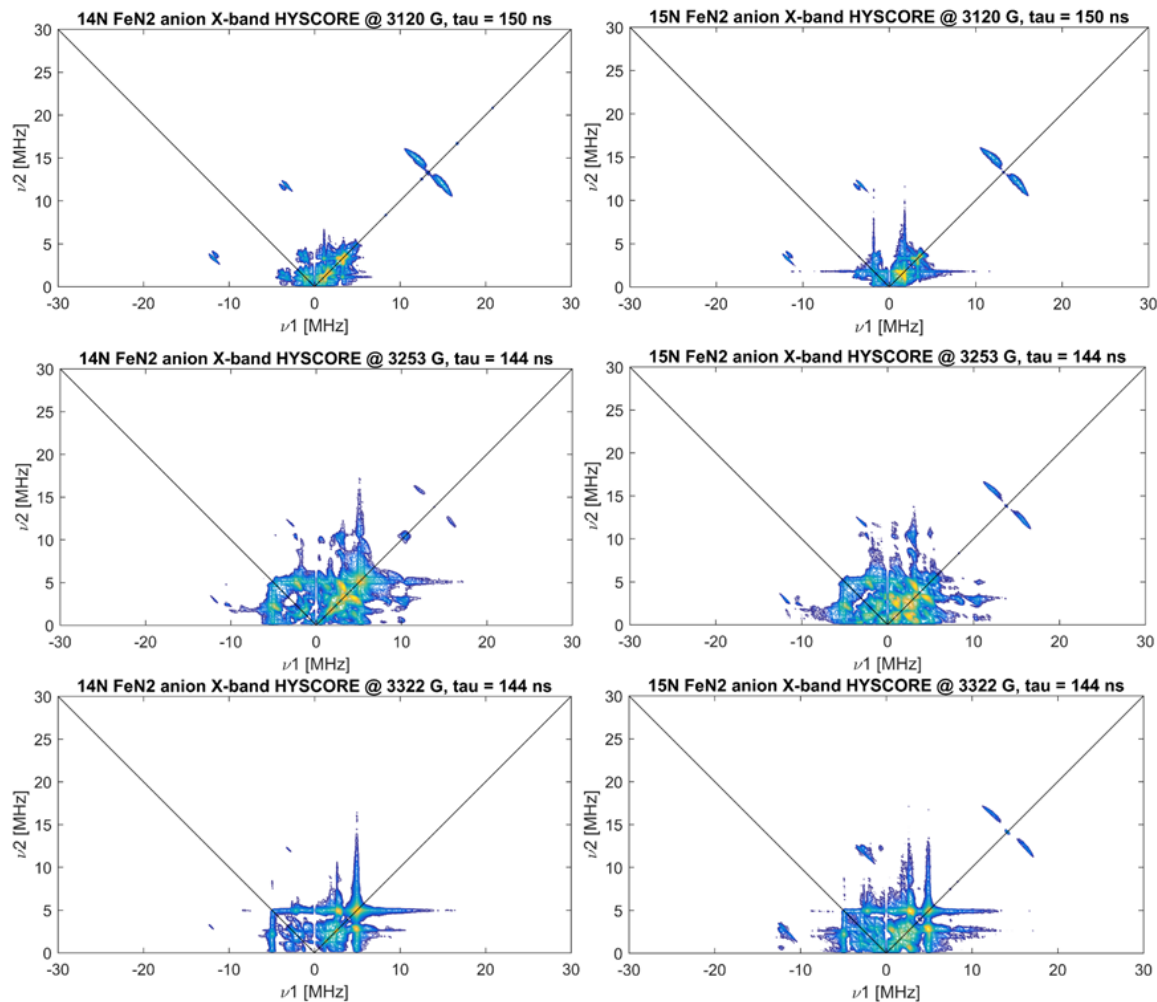


Figure 4.4: Left: Field Dependent X-Band HYSCORE Spectra of $[(^{\text{Ar}}\text{P}_3\text{B})\text{Fe}(\text{N}_2)][\text{Na}(\text{12-C-4})_2]$ (left) and $[(^{\text{Ar}}\text{P}_3\text{B})\text{Fe}(^{15}\text{N}_2)][\text{Na}(\text{12-C-4})_2]$ (right) (20 K, 9.76 GHz) (see Figure 4.S4 for simulations). (9.414 GHz, 20 K).

Table 4.1: Nuclear hyperfine couplings derived from ENDOR and HYSCORE for $[(^{Ar}P_3B)Fe(N_2)][Na(12-C-4)_2]$.

Nucleus	A_I (MHz)	A_2 (MHz)	A_3 (MHz)	A_{iso} (MHz)
^{11}B	15.3	15.3	15.2	15.27
$^{31}P_{(1)}$	45	48	50	47.67
$^{31}P_{(2)}$	96	97	112	101.67
$^{31}P_{(3)}$	110	111	123	114.67
$^{14}N_\alpha$	0.7	-3.2	-1.4	-1.3
$^{15}N_\alpha$	-1.0	4.5	2.0	1.8

The X-band ENDOR spectrum of the putative $Fe(NNH)$ is well modelled with hyperfine coupling to ^{11}B , two different ^{31}P environments (one more strongly coupled and two equivalent weakly coupled) and a single 1H hyperfine (Figure 4.5 and Table 4.2). Isotopic labelling using $DBAr^{F}_{24} \cdot 2Et_2O$ as the acid gave $(^{Ar}P_3B)Fe(NND)$ which appears identical to $(^{Ar}P_3B)Fe(NNH)$ by CW X-band EPR. However, comparison of the ENDOR spectrum of $(^{Ar}P_3B)Fe(NND)$ to that of $(^{Ar}P_3B)Fe(NNH)$ clearly reveals the single 1H hyperfine coupling (Figure 4.6). Note that the small gyromagnetic ratio of D (and by extension Larmor frequency for the D nuclei) causes signals from D coupling to appear at the low frequency end of the ENDOR spectrum where the RF pulses are weak and the peaks resulting from D coupling do not appear in the spectrum.

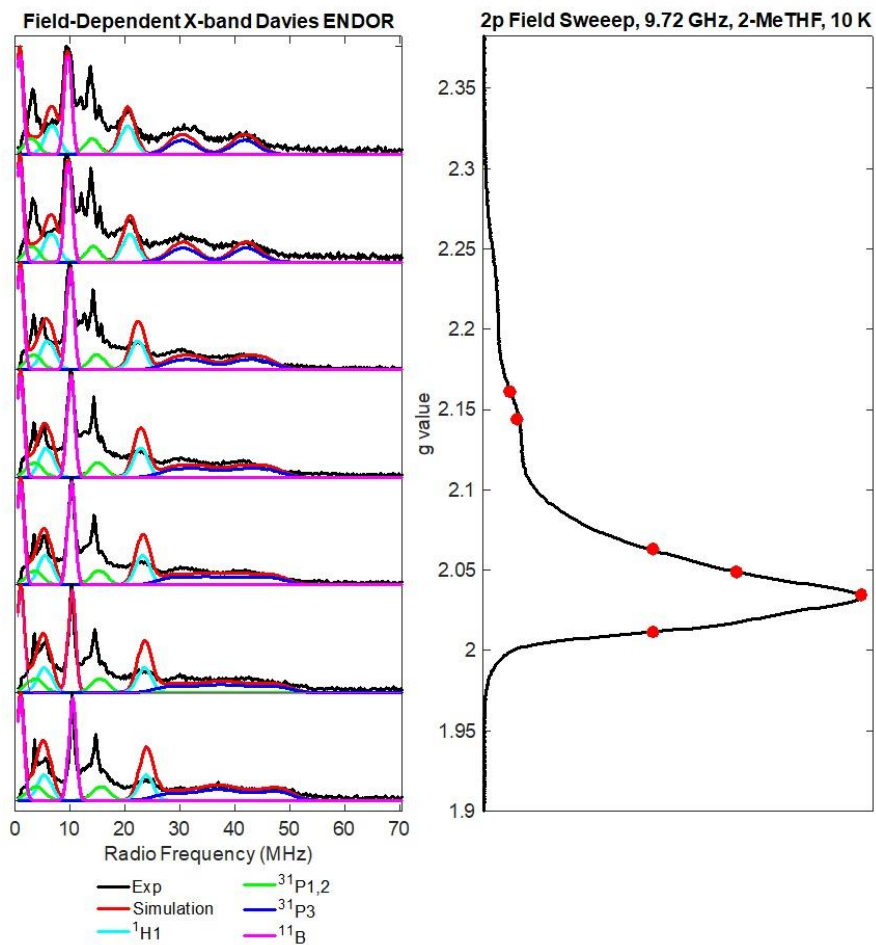


Figure 4.5: Left: Field Dependent X-Band ENDOR spectra of $(^{\text{Ar}}\text{P}_3\text{B})\text{Fe}(\text{NNH})$ with simulation of individual hyperfine couplings. Right: 2 pulse field sweep with ENDOR field positions marked in red. (Experimental Parameters: Temperature = 10 K; MW Frequency = 9.72 GHz; MW Pulse Length ($\pi/2$, π) = 20 ns, 40 ns; RF Pulse Length = 15 μs ; Shot Rep Time = 5000 μs ; τ = 240 ns).

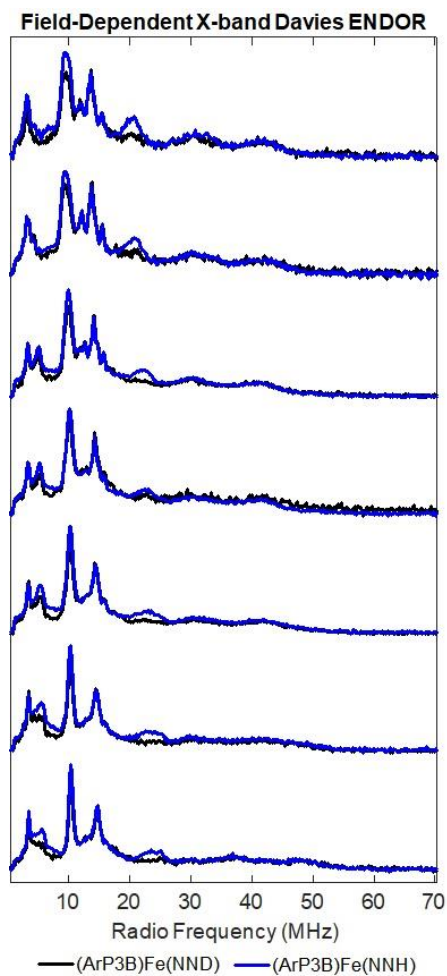


Figure 4.6: Comparison of $(^{Ar}P_3B)Fe(NNH)$ and $(^{Ar}P_3B)Fe(NND)$ X-Band ENDOR spectra (Experimental Parameters: Temperature = 10 K; MW Frequency = 9.72 GHz; MW Pulse Length ($\pi/2, \pi$) = 20 ns, 40 ns; RF Pulse Length = 15 μ s; Shot Rep Time 5000 = μ s; τ = 240 ns).

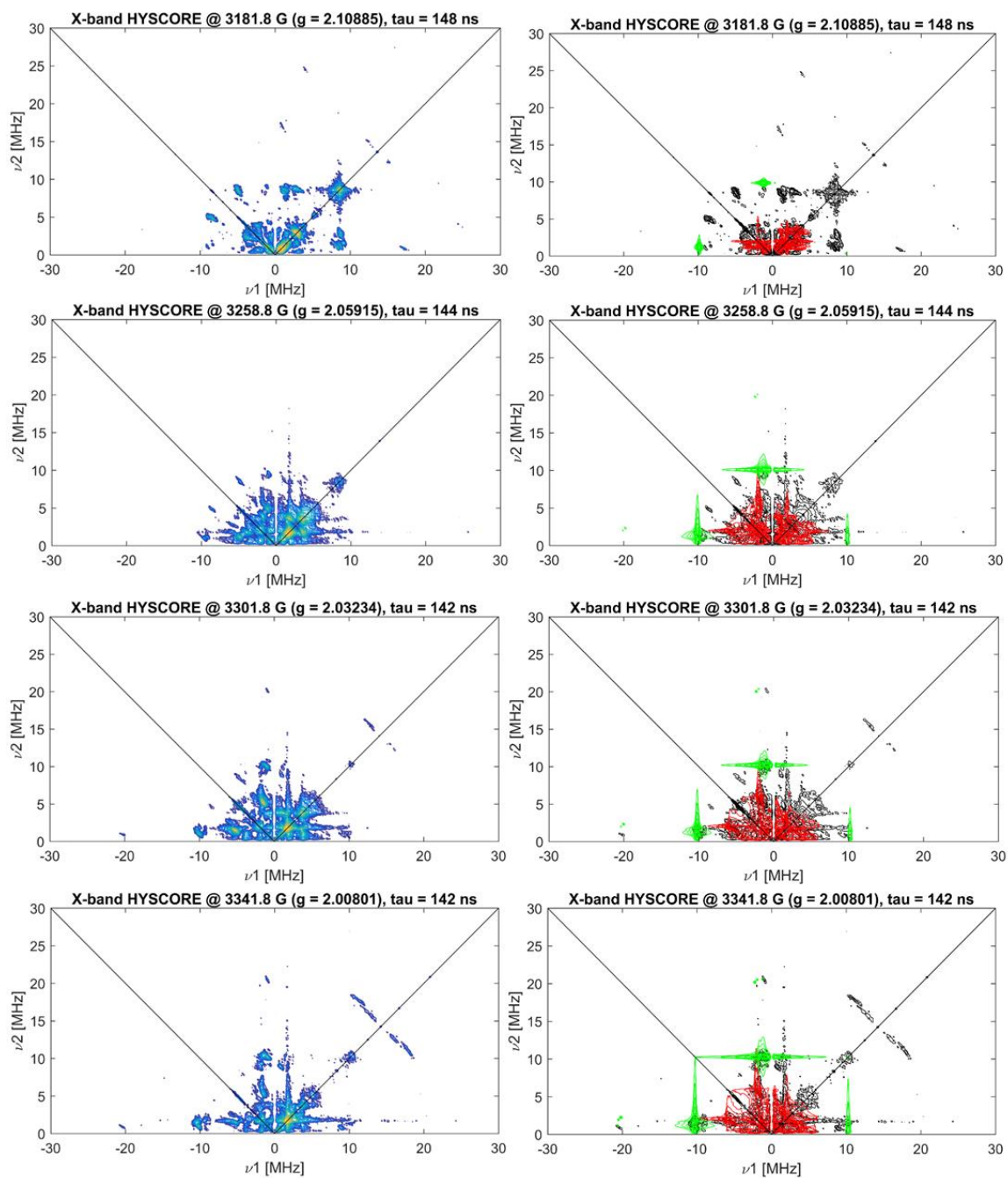


Figure 4.7: X-band HYSCORE spectra (left) and simulations (right) for $(^{\text{Ar}}\text{P}_3\text{B})\text{Fe}(\text{NNH})$. (Experimental data is in black, ^{14}N in red, ^{11}B is in green).

Table 4.2: Nuclear Hyperfine Couplings Derived from ENDOR and HYSCORE for (^{Ar}P₃B)Fe(NNH).

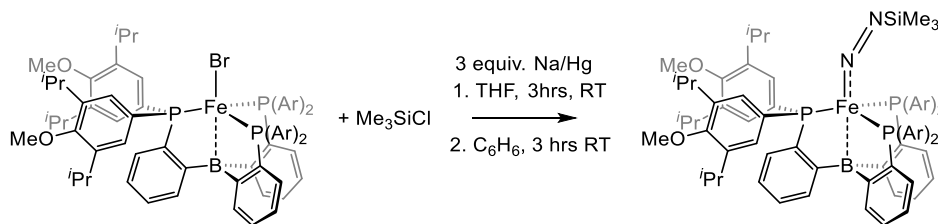
	A_I (MHz)	A_2 (MHz)	A_3 (MHz)	A_{iso} (MHz)
¹ H	12	18.25	19.25	16.5
¹¹ B	15.3	15.3	15.5	15.37
³¹ P _(1,2)	17	17	22	18.67
³¹ P ₍₃₎	71	65	85	73.67
¹⁴ N _α	-1.4	3.8	2	1.47

The ¹H couplings derived from ENDOR spectroscopy can be decomposed into the anisotropic and isotropic components of the hyperfine giving $A_{iso} = 16.8$ MHz (see equations 4.S1 and 4.S2 for $[A_{aniso}]$). The minimum distance of the ¹H from the unpaired spin can be estimated using equation 1 and solving for r by taking the largest value of A_{aniso} as the twice dipolar component of the ¹H hyperfine (2T). The result places the lower limit for the distance of the ¹H from the metal center at 3.31 Å (i.e. $r \geq 3.31$ Å). In order to evaluate whether this distance was consistent for our assignment of (^{Ar}P₃B)Fe(NNH) we performed a DFT geometry optimization on a model structure of (^{Ar}P₃B)Fe(NNH) using the TPSS functional, the def2-TZVP basis set for Fe and def2-SVP for all other atoms (this combination of functional and basis set have been previously used by our group in the study of the related (P₃B)Fe system with good results).³³ The distance between Fe and a proton on the β-nitrogen measured from the DFT optimized structure of (^{Ar}P₃B)Fe(NNH) is ~3.52 Å, which is consistent with this estimated $r \geq 3.31$ Å.

$$T = \frac{\mu_0}{4\pi} \cdot \frac{g_{avg} g_n \mu_B \mu_N}{h r^3}$$

Equation 4.1: T is the dipolar component of the hyperfine coupling, μ_0 is the magnetic vacuum permeability constant, g_{avg} is the average of g value for the compound, g_n is the nuclear gyromagnetic ratio (for ^1H in this case), μ_B is the Bohr magneton, μ_N is the nuclear magneton, and h is Plank's constant.

To further support our assignment of $(^{\text{Ar}}\text{P}_3\text{B})\text{Fe}(\text{NNH})$ we undertook synthesis of the silyl-diazenido analog $(^{\text{Ar}}\text{P}_3\text{B})\text{Fe}(\text{NNSiMe}_3)$ (Scheme 4.8). Previous work from our lab has shown that such species can be more thermally stable and we hoped to generate a species with a similar molecular and electronic structure that would be more thermally stable and amenable to spectroscopic characterization by methods other than low temperature EPR. Vigorously stirring $(^{\text{Ar}}\text{P}_3\text{B})\text{FeBr}$ in the presence of Me_3SiCl (1 equiv.) with 3 equiv. Na/Hg amalgam in THF for 3 hours followed by removal of all volatiles *in vacuo* and subsequent stirring over Hg in benzene for an additional 3 hours gave a dark yellow-brown solution containing $(^{\text{Ar}}\text{P}_3\text{B})\text{Fe}(\text{NNSiMe}_3)$. A thin film IR spectrum of the crude reaction mixture shows an intense stretch at $\nu_{\text{NN}} = 1717\text{ cm}^{-1}$.



Scheme 4.8: Synthesis of $(^{\text{Ar}}\text{P}_3\text{B})\text{Fe}(\text{NNSiMe}_3)$.

The CW X-band EPR spectrum is also very similar to that of $(^{\text{Ar}}\text{P}_3\text{B})\text{Fe}(\text{NNH})$ with a near axial signal with well resolved hyperfine coupling to a single ^{31}P atom at the highest field g value (Figure 4.S10). ENDOR and HYSCORE measurements confirmed that a similar trend in the ^{31}P , ^{11}B and ^{14}N hyperfine coupling tensors. $(^{\text{Ar}}\text{P}_3\text{B})\text{Fe}(\text{NNSiMe}_3)$ has

two similar more weakly coupling ^{31}P nuclei and one significantly stronger coupled ^{31}P nucleus, a fairly isotropic ^{11}B hyperfine coupling tensor, and fairly anisotropic ^{14}N hyperfine coupling tensor. Additionally the nuclear quadrupole coupling constant and asymmetry parameters for $(^{\text{Ar}}\text{P}_3\text{B})\text{Fe}(\text{NNSiMe}_3)$ and $(^{\text{Ar}}\text{P}_3\text{B})\text{Fe}(\text{NNH})$ for $^{14}\text{N}_\alpha$ are identical. This indicates that the silyl-diazenido analog is an appropriate model for $(^{\text{Ar}}\text{P}_3\text{B})\text{Fe}(\text{NNH})$ (Table 4.3, Figures 4.8 and 4.9).

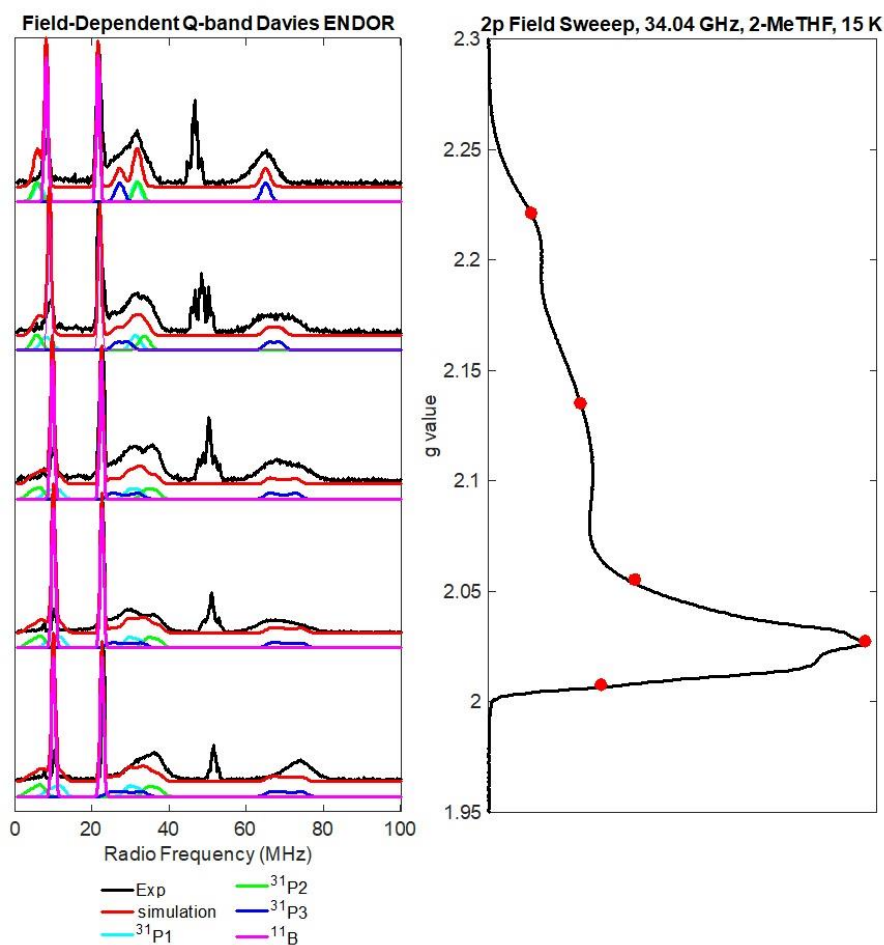


Figure 4.8: Left: Field Dependent Q-Band ENDOR spectra of $(^{\text{Ar}}\text{P}_3\text{B})\text{Fe}(\text{NNSiMe}_3)$ with simulation of individual hyperfine couplings. Right: 2 pulse field sweep with ENDOR field positions marked in red. (Experimental Parameters: Temperature = 15 K; MW Frequency = 34.04 GHz; MW Pulse Length ($\pi/2$, π) = 20 ns, 40 ns; RF Pulse Length = 15 μs ; Shot Rep Time = 5000 μs ; τ = 132 ns).

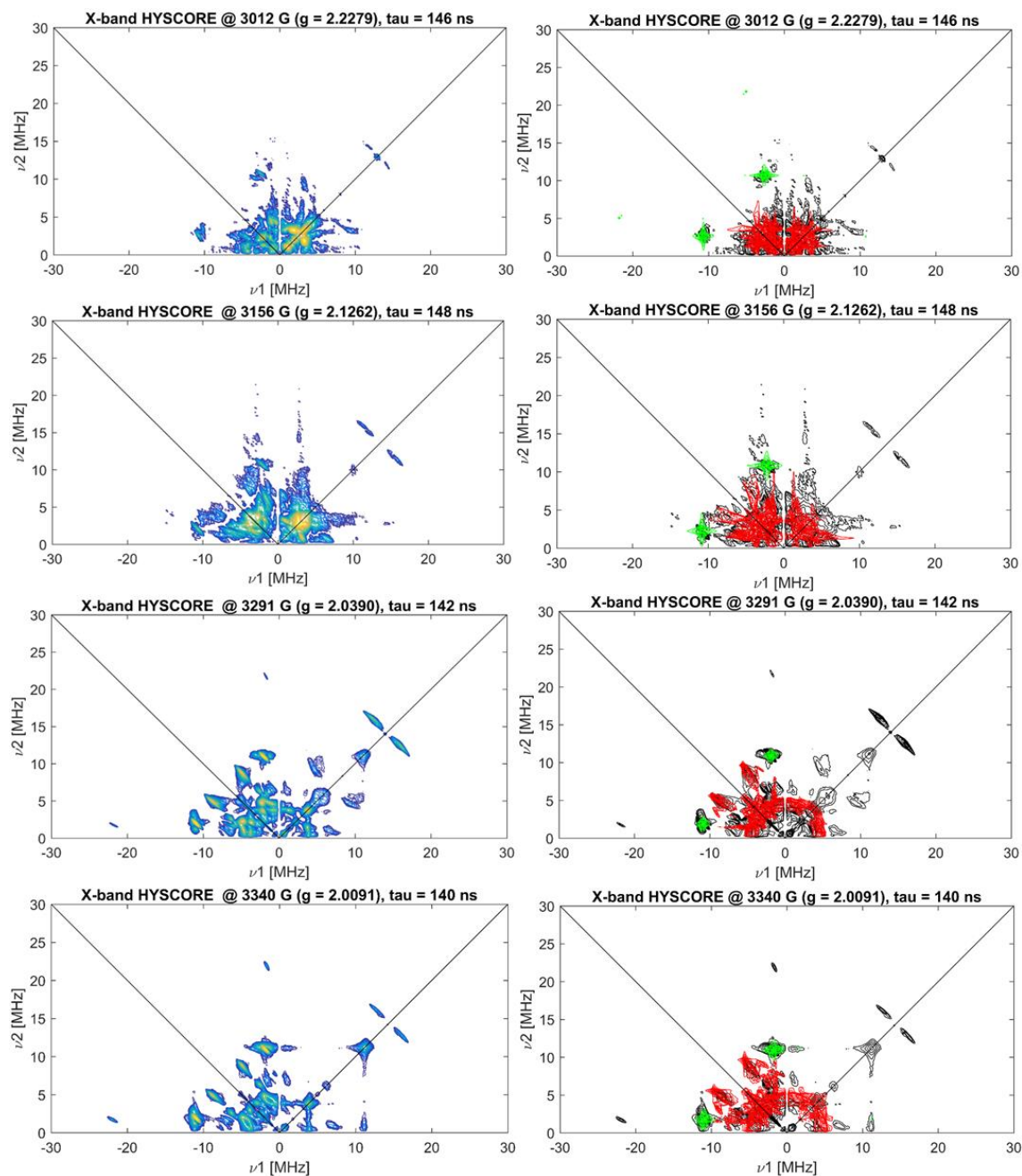


Figure 4.9: X-band HYSCORE spectra and simulations for $(\text{ArP}_3\text{B})\text{Fe}(\text{NNSiMe}_3)$. (Experimental data is in black, ^{14}N is in red, ^{11}B is in green).

Table 4.3: Nuclear Hyperfine Couplings Derived from ENDOR and HYSCORE for $(^{Ar}P_3B)Fe(NNSiMe_3)$.

Nucleus	A_I (MHz)	A_2 (MHz)	A_3 (MHz)	A_{iso} (MHz)
^{11}B	13.50	12.70	12.4	12.87
$^{31}P_{(1)}$	26	16	25	18.67
$^{31}P_{(2)}$	26	26	36	29.33
$^{31}P_{(3)}$	92	90	111	97.67
$^{14}N_\alpha$	-1.0	7.6	5.5	4.7

Similarly the Q-Band ENDOR spectrum of $[(^{Ar}P_3B)Fe(NNH_2)][BAr^{F}_{24}]$ is well modelled with hyperfine coupling to ^{11}B , three ^{31}P environments, and two 1H environments (one more strongly coupled and one more weakly coupled) (Figures 4.10, 4.11, and 4.12 and Table 4.4). Decomposition of the 1H hyperfine couplings into their isotropic and anisotropic components gives $A_{iso} = 19.2$ MHz for the more strongly coupled proton and $A_{iso} = 12.7$ MHz for the weaker 1H coupling (see equations 4.S1, 4.S3, 4.S4). Using equation 1 the estimated minimum r for the two 1H 's is $r_{(1)} \geq 3.08$ Å for the more strongly coupled 1H and $r_{(2)} \geq 3.88$ Å for the more weakly coupled 1H . This is fairly consistent with the predicted Fe-H distances from a DFT optimized structure of $[(^{Ar}P_3B)Fe(NNH_2)][BAr^{F}_{24}]$ of 3.20 Å and 3.73 Å.

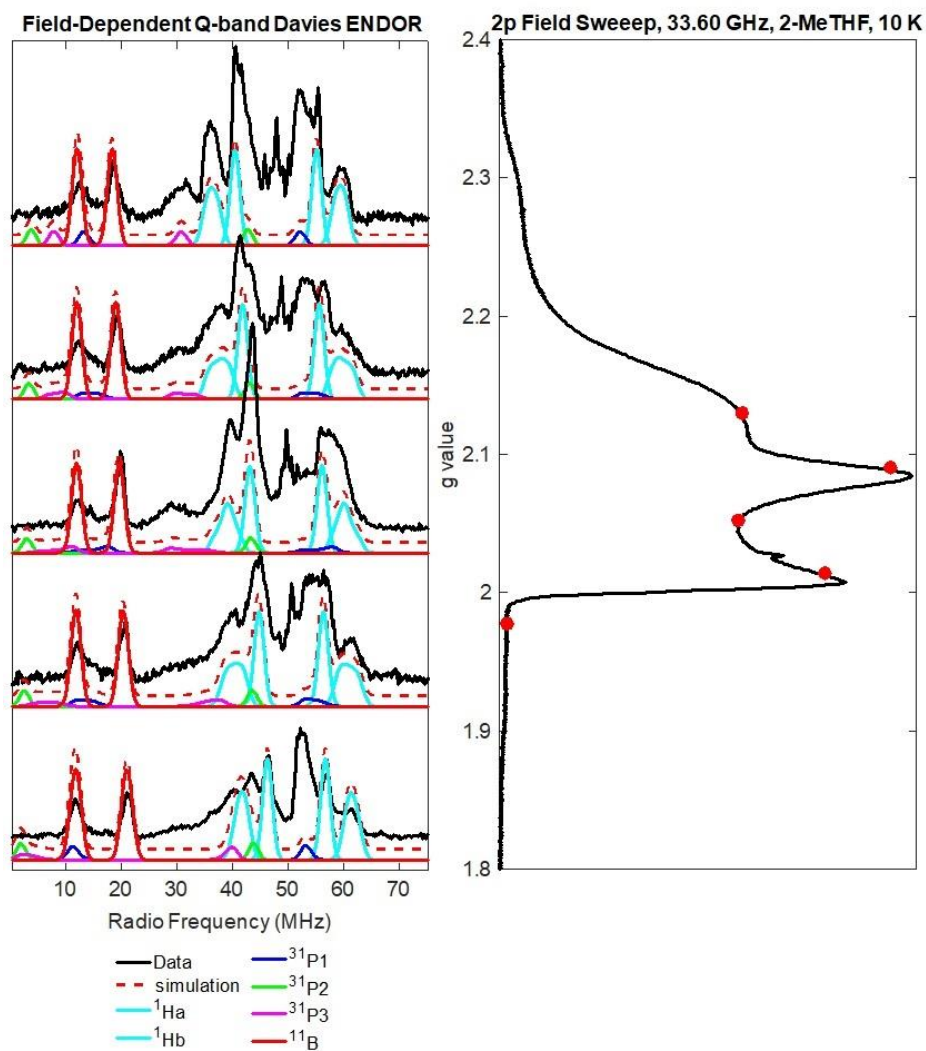


Figure 4.10: Left: Field Dependent Q-Band ENDOR spectra of $[(^{\text{Ar}}\text{P}_3\text{B})\text{Fe}(\text{NNH}_2)][\text{BAr}^{\text{F}}_{24}]$ with simulation of individual hyperfine couplings. Right: 2 pulse field sweep with ENDOR field positions marked in red. (Experimental Parameters: Temperature = 10 K; MW Frequency = 33.60 GHz; MW Pulse Length ($\pi/2$, π) = 20 ns, 40 ns; RF Pulse Length = 15 μs ; Shot Rep Time = 5000 μs , τ = 240 ns).

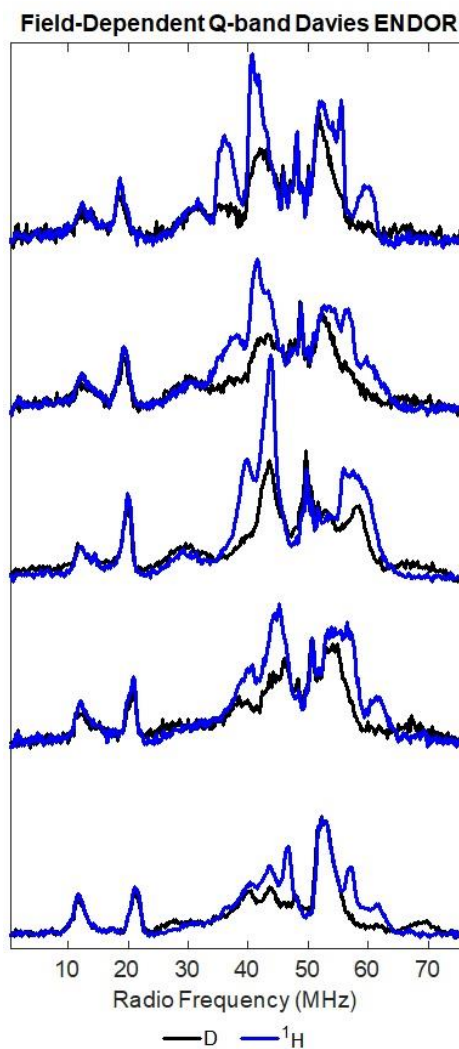


Figure 4.11: Field Dependent Q-Band ENDOR Comparing Spectra of $[(^A\text{P}_3\text{B})\text{Fe}(\text{NNH}_2)][\text{BAr}^{\text{F}}_{24}]$ and $[(^A\text{P}_3\text{B})\text{Fe}(\text{NND}_2)][\text{BAr}^{\text{F}}_{24}]$. (Experimental Parameters: Temperature = 10 K; MW Frequency = 33.60 GHz; MW Pulse Length ($\pi/2, \pi$) = 20 ns, 40 ns; RF Pulse Length = 15 μs ; Shot Rep Time = 5000 μs ; τ = 240 ns).

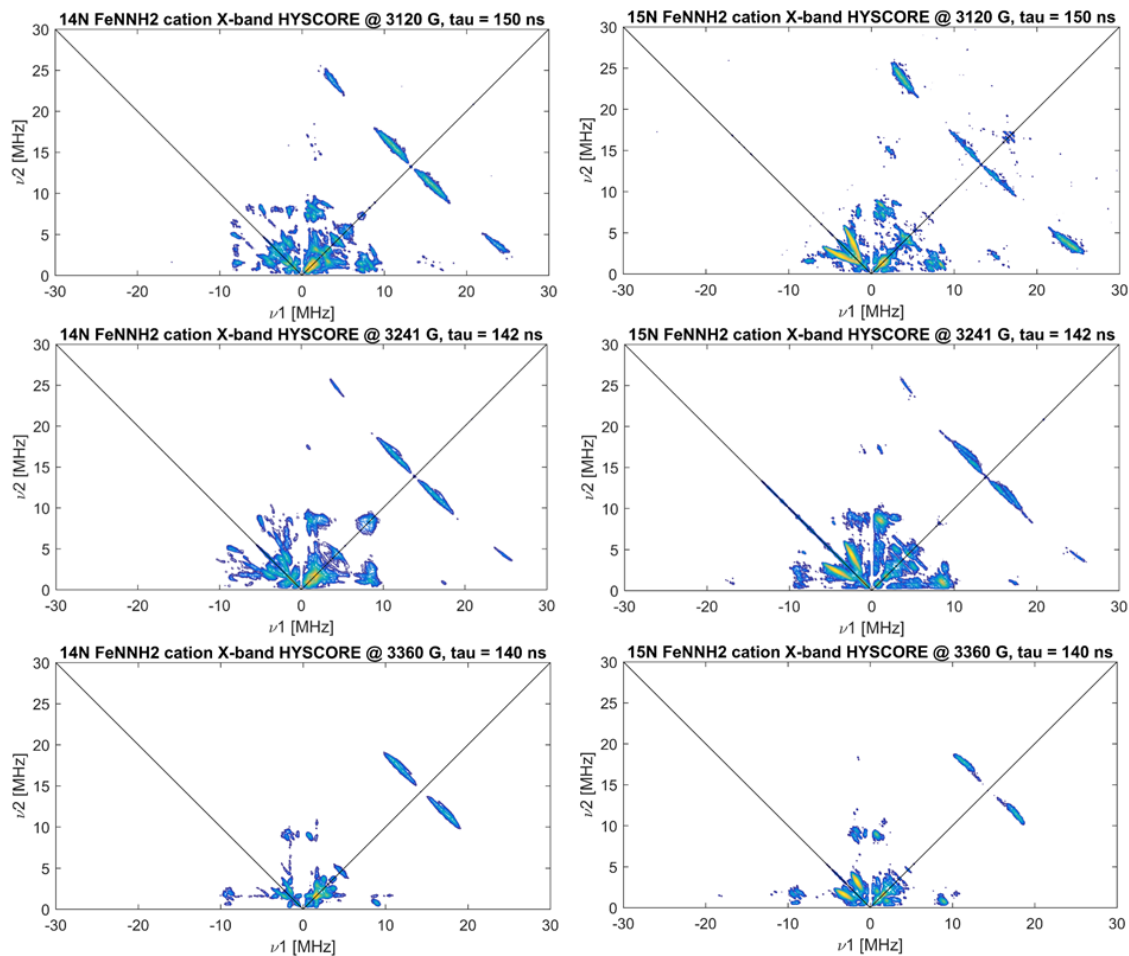


Figure 4.12: Comparison of Field Dependent X-Band HYSCORE Spectra of $[(^{\text{Ar}}\text{P}_3\text{B})\text{Fe}(\text{NNH}_2)][\text{BAr}^{\text{F}}_{24}]$ (left) and $[(^{\text{Ar}}\text{P}_3\text{B})\text{Fe}(^{15}\text{N}^{15}\text{NH}_2)][\text{BAr}^{\text{F}}_{24}]$ (right) (20 K, 9.76 GHz) (see Figure 4.S5 for simulations).

Table 4.4: Nuclear hyperfine couplings derived from ENDOR and HYSCORE for $[(^{\text{Ar}}\text{P}_3\text{B})\text{Fe}(\text{NNH}_2)]^+$.

Nucleus	A_I (MHz)	A_2 (MHz)	A_3 (MHz)	A_{iso} (MHz)
$^1\text{H}_{(1)}$	27	21	16	21.33
$^1\text{H}_{(2)}$	15	13.5	10	12.83
^{11}B	6.0	8.0	9.0	7.67
$^{31}\text{P}_{(1)}$	67	46	55	56
$^{31}\text{P}_{(2)}$	66	64	64	64.67
$^{31}\text{P}_{(3)}$	26.50	20	37	27.53
$^{14}\text{N}_\alpha$	0.07	-7.13	-0.92	2.71
$^{15}\text{N}_\alpha$	-0.1	10	1.3	3.80

A great deal of information about the electronic structure of the NNH_x ($x = 0, 1, 2$) can be gleaned from examination of the nuclear hyperfine couplings, nuclear quadrupole couplings (e^2Qq/h) and asymmetry parameters (η) for N_α and N_β across the series of $[(^{\text{Ar}}\text{P}_3\text{B})\text{Fe}(\text{N}_2)]^-$, $(^{\text{Ar}}\text{P}_3\text{B})\text{Fe}(\text{NNH})$ and $[(^{\text{Ar}}\text{P}_3\text{B})\text{Fe}(\text{NNH}_2)]^+$. These parameters are particularly of interest because of the scarcity of data on these types of iron compounds and their potential worth in the identification of catalytically relevant intermediates in synthetic and biological nitrogen fixation systems. In order to determine the hyperfine couplings to nitrogen as well as the e^2Qq/h and η for the N atoms in the N_2 , NNH , and NNH_2 ligands we

relied on comparison of the X-Band HYSCORE spectra of samples of $[(^{Ar}P_3B)Fe(N_2)][Na(12-C-4)_2]$, $(^{Ar}P_3B)Fe(NNH)$, and $[(^{Ar}P_3B)Fe(NNH_2)][BAr^F_{24}]$ with the X-Band HYSCORE spectra of ^{15}N labelled samples (Figures 4.4, 4.7, and 4.12, Table 4.5). One would expect the magnitude of the hyperfine coupling to N_α to increase with protonation of N_β with $[(^{Ar}P_3B)Fe(N_2)][Na(12-C-4)_2]$ having the smallest A_{N_α} , $[(^{Ar}P_3B)Fe(NNH_2)][BAr^F_{24}]$ having the largest A_{N_α} and A_{N_α} for $(^{Ar}P_3B)Fe(NNH)$ being distributed somewhere between $[(^{Ar}P_3B)Fe(N_2)]^-$ and $[(^{Ar}P_3B)Fe(NNH_2)]^+$. This is in fact the case as $A_{iso} = 1.8$ MHz for $[(^{Ar}P_3B)Fe(N_2)][Na(12-C-4)_2]$, and this value increases by a factor of 1.5 to $A_{iso} = 2.7$ MHz for $[(^{Ar}P_3B)Fe(NNH_2)][BAr^F_{24}]$ with $A_{iso} = 2.4$ MHz for $(^{Ar}P_3B)Fe(NNH)$ lying intermediate between the two. We were unable to prepare samples of $(^{Ar}P_3B)Fe(^{15}N^{15}NH)$ with sufficient isotopic enrichment to show significant differences in the X-band HYSCORE spectra when compared to the ^{14}N analog and prepared samples of the silylated diazenido analog $(^{Ar}P_3B)Fe(NNSiMe_3)$ for use as a point of comparison. The simulations for the X-band HYSCORE of both species gave $e^2Qq/h = 2.0$ and $\eta = 0.6$ for N_α indicating that the bonding environment at N_α for these species is very similar. Additionally, the similarity of $e^2Qq/h = 1.7$ MHz and $\eta = 0.7$ for $[(^{Ar}P_3B)Fe(NNH_2)][BAr^F_{24}]$ to the previously reported values of $e^2Qq/h = 1.74$ MHz and $\eta = 0.64$ for N_α in $[(P_3B)Fe(NNH_2)][BAr^F_{24}]$, indicating that the bonding character/electronic structure of N_α is comparable in both compounds and provides further support for the assignment of $[(^{Ar}P_3B)Fe(NNH_2)][BAr^F_{24}]$ (Table 4.5).^{16,41,42}

Table 4.5: ^{14}N nuclear quadrupole couplings and asymmetry parameters derived from ENDOR and HYSCORE for N_α .

Compound	e^2Qq/h (MHz)	η
$[(^{\text{Ar}}\text{P}_3\text{B})\text{Fe}(\text{N}_2)][\text{Na}(\text{12-C-4})_2]$	3.0	0.1
$(^{\text{Ar}}\text{P}_3\text{B})\text{Fe}(\text{NNH})$	2.0	0.6
$(^{\text{Ar}}\text{P}_3\text{B})\text{Fe}(\text{NNSiMe}_3)$	2.0	0.6
$[(^{\text{Ar}}\text{P}_3\text{B})\text{Fe}(\text{NNH}_2)][\text{BAr}^{\text{F}}_{24}]$	1.7	0.7
$[(\text{P}_3\text{B})\text{Fe}(\text{NNH}_2)][\text{BAr}^{\text{F}}_{24}]$	1.74	0.64

4.2.1 Possible Alternative Structures: In assigning the structures of the $(^{\text{Ar}}\text{P}_3\text{B})\text{Fe}(\text{NNH})$ and $[(^{\text{Ar}}\text{P}_3\text{B})\text{Fe}(\text{NNH}_2)]^+$ we considered several alternative structures (Chart 4.1). Alternative structures for $(^{\text{Ar}}\text{P}_3\text{B})\text{Fe}(\text{NNH})$ where the proton has been delivered to N_α , a phosphine or the metal center to form an iron hydride or borohydride species were considered. DFT geometry optimizations were performed on several of these structures (A, B, G, H, I) in order to evaluate their agreement with the ENDOR derived geometric constraints (TPSS, def2-TZVP on Fe, def2-SVP on C, H, O, P, B; notes: The geometry optimizations were performed using a truncated version of $^{\text{Ar}}\text{P}_3\text{B}$ where ^iPr was replaced with Me; we do not believe these substitutions should cause the core geometry about Fe to differ in a meaningful way since the DFT predicts a singlet ground state for truncated $(^{\text{Ar}}\text{P}_3\text{B})\text{Fe}(\text{N}_2)$ consistent with the experimentally observed diamagnetism of $(^{\text{Ar}}\text{P}_3\text{B})\text{Fe}(\text{N}_2)$. Furthermore the DFT optimized structure for the truncated $(^{\text{Ar}}\text{P}_3\text{B})\text{Fe}(\text{N}_2)$ agrees well with the structure from XRD studies (Figures 4.S2 and 4.S21) and the DFT optimized structures for $[(^{\text{Ar}}\text{P}_3\text{B})\text{Fe}(\text{N}_2)]^+$

and its truncated variant are isostructural (Figures 4.1 and 4.S20)). A structure with the starting connectivity shown in Chart 4.1 A optimized to the structure shown in Chart 4.1 B and alternative structure A was ruled out on this basis. Structure B was ruled out because the DFT predicted Fe-H distance of 2.70 Å is inconsistent with the distance estimated by the dipolar contribution to the ^1H hyperfine of ~ 3.31 Å observed for the acid derived proton (*vide supra*). A phosphine protonated species such as shown in Chart 4.1 C would likely have an extremely small A_{iso} for hyperfine coupling to the acid derived ^1H which is inconsistent with the magnitude of the observed ^1H hyperfine coupling with $A_{\text{iso}} = 16.5$ MHz. The iron hydride or borohydride structures (Chart 4.1 D, E, F) in which the acid derived H atom is directly bonded to the metal center were easily ruled out based on the metal-hydride or metal-borohydride bond distances observed in $(\text{P}_3\text{BH})\text{Fe}(\text{H})(\text{N}_2)$ of ~ 1.47 Å for $d_{\text{Fe-H}}$ and ~ 1.5 Å for $d_{\text{Fe-HB}}$ which are much shorter than the distances estimated from the dipolar contributions to the hyperfine for both compounds (3.52 Å for $(^{\text{Ar}}\text{P}_3\text{B})\text{Fe}(\text{NNH})$, 3.08 Å and 4.13 Å for $[(^{\text{Ar}}\text{P}_3\text{B})\text{Fe}(\text{NNH}_2)]^+$).⁴³ Alternative structures for $[(^{\text{Ar}}\text{P}_3\text{B})\text{Fe}(\text{NNH}_2)]^+$ where both N_α and N_β had been protonated to give either *trans* or *cis*-diazene as a ligand were also considered and ruled out due to the fact that the Fe-H distances for protons on N_α and N_β predicted by DFT are too short for both η^1 -*trans*-diazene (2.51 Å, 3.00 Å; Chart 4.1, G) and η^2 -*cis*-diazene (2.65 Å, 2.68 Å; Chart 4.1, I) isomers compared to the estimated values of 3.08 Å and 4.13 Å from the dipolar contribution to hyperfine couplings). Additionally, DFT geometry optimization starting from the η^1 -*cis*-diazene structure shown in Chart 4.1 H minimized to the η^2 -*cis*-diazene structure shown in Chart 4.1 I and was ruled out on this basis.

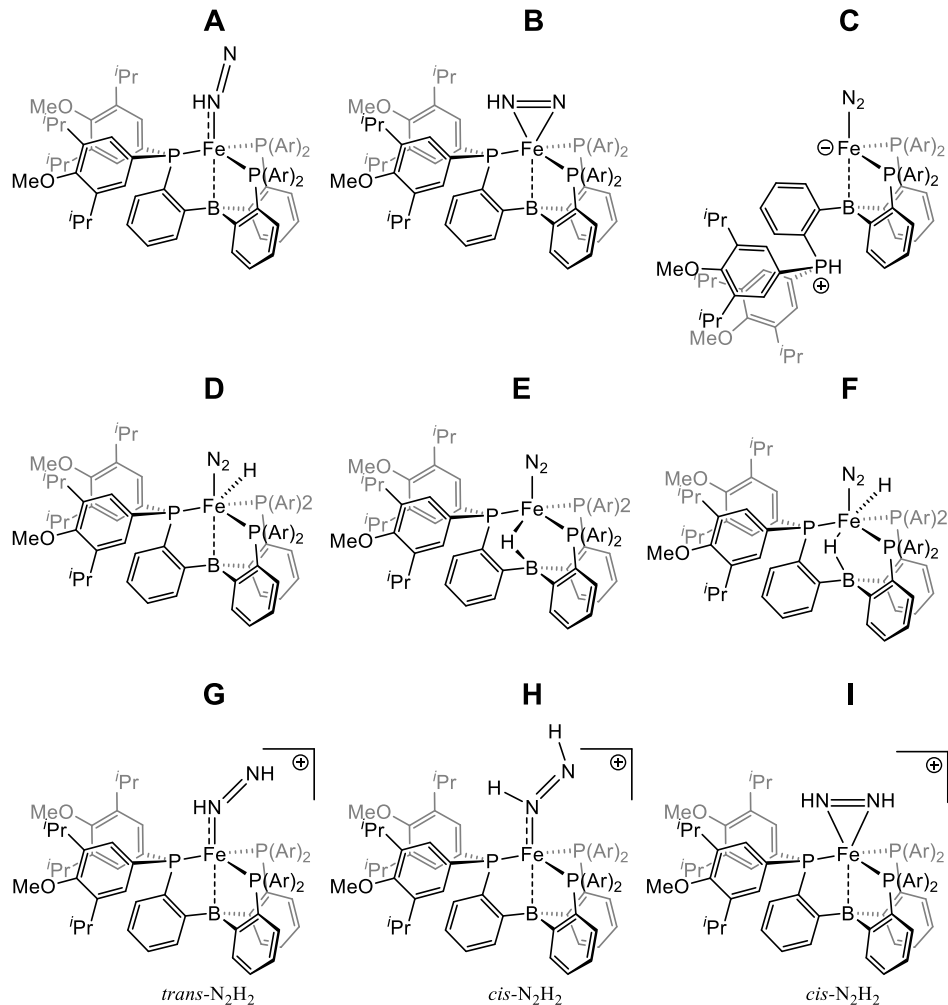


Chart 4.1: Selected alternative structures considered for $(^{\text{Ar}}\text{P}_3\text{B})\text{Fe}(\text{NNH})$ (A-E) and $[(^{\text{Ar}}\text{P}_3\text{B})\text{Fe}(\text{NNH}_2)]^+$ (F-I). (See SI for DFT optimized structures and coordinates).

4.2.2 ^{57}Fe Mössbauer Spectroscopic Studies: ^{57}Fe Mössbauer spectroscopy was also used to characterize the iron speciation of the reactions. Reactions of $[(^{\text{Ar}}\text{P}_3\text{B})\text{Fe}(\text{N}_2)][\text{Na}(12\text{-C-4})_2]$ and $\text{HBAr}^{\text{F}}_{24}$ were mixed in thawing 2-MeTHF in a Delrin Mössbauer cup with a stainless steel spatula in the glovebox coldwell (chilled with an external liquid nitrogen bath) and then frozen and quickly transferred to a liquid N₂ bath and loaded into the spectrometer. The 80 K ^{57}Fe Mössbauer solution phase (2-MeTHF) spectrum of $(^{\text{Ar}}\text{P}_3\text{B})\text{FeBr}$

in the presence of a 50 mT magnetic field oriented parallel to the γ -radiation shows a broad, asymmetric quadrupole doublet that is well fit with $\delta = 0.61$ mm/s and $\Delta E_q = 2.4$ mm/s (Figure S11, Table 4). $(^{Ar}P_3B)Fe(N_2)$ (80 K, 2-MeTHF, 50 mT \parallel) appears as a sharp quadrupole doublet centered at $\delta = 0.42$ mm/s with $\Delta E_q = 1.9$ mm/s (Figure S12, Table 4). The 80 K ^{57}Fe Mössbauer spectrum (2-MeTHF) of $[(^{Ar}P_3B)Fe(N_2)][Na(12-C-4)_2]$ is more complicated and does not appear as a well-defined quadrupole doublet due to unresolved magnetic splitting. Simultaneous fitting of spectra collected in the presence of a 50 mT magnetic field in \parallel and \perp orientations yields $\delta = 0.32$ mm/s with $\Delta E_q = 0.75$ mm/s (Figure 4.13, Table 4.7). The ^{57}Fe Mössbauer spectra (50 mT, \parallel and \perp orientations) of a reaction mixture using the same conditions used to generate $(^{Ar}P_3B)Fe(NNH)$ in the previously described EPR experiments is well fit with a minor component of similar isomer shift and quadrupole splitting to $(^{Ar}P_3B)Fe(N_2)$, a major component with $\delta = 0.24$, $\Delta E_q = 0.94$ which we assign as $(^{Ar}P_3B)Fe(NNH)$ (Figure 4.14, Tables 4.6, 4.8). The ^{57}Fe Mössbauer spectrum of $(^{Ar}P_3B)Fe(NNSiMe_3)$ was also collected for comparison. A freshly prepared sample of $(^{Ar}P_3B)Fe(NNSiMe_3)$ was loaded into a Mössbauer cup as a frozen solution in benzene after being analyzed for purity by 1H and ^{31}P NMR as well as IR spectroscopies to ensure purity. The species appears as a broad asymmetric quadrupole doublet with $\delta = 0.16$, $\Delta E_q = 1.54$ at 80 K in the presence of a 50 mT magnetic field aligned \parallel to the γ -radiation (Figure 4.15, Table 4.9). The 80 K ^{57}Fe Mössbauer (50 mT, \parallel) solution of a reaction mixture prepared using the same conditions used to generate $[(^{Ar}P_3B)Fe(NNH_2)][BAr^F_{24}]$ is well fit as a mixture of two species (an aliquot of the reaction mixture was checked by CW X-band EPR to verify the presence of $[(^{Ar}P_3B)^{57}Fe(NNH_2)][BAr^F_{24}]$ in the sample). The major component

is well fit as $(^{Ar}P_3B)Fe(N_2)$ and the minor species is fit as a quadrupole doublet with $\delta = 0.06$ mm/s and $\Delta E_q = 1.32$ mm/s which is assigned as $[(^{Ar}P_3B)Fe(NNH_2)][BAr^F_{24}]$ (Figure 4.15, Table 4.9). These parameters are very different from those observed for the isoelectronic analog $(P_3Si)Fe(NNH_2)$, which has $\delta = 0.31$ mm/s and $\Delta E_q = 0.86$, as well as the previously reported $[(P_3B)Fe(NNH_2)][BAr^F_{24}]$ with $\delta = 0.35$ mm/s and $\Delta E_q = 1.02$ mm/s.^{10,16} The significant contrast in the ^{57}Fe Mössbauer parameters between $[(^{Ar}P_3B)Fe(NNH_2)]^+$ and its isoelectronic analogs is perhaps explained by significant structural differences between $[(^{Ar}P_3B)Fe(NNH_2)]^+$ and its isoelectronic analogs. The DFT predicted structure of $[(^{Ar}P_3B)Fe(NNH_2)]^+$ using the truncated $^{Ar}P_3B$ ligand predicts an interaction with one of the arene rings on the borane ligand resulting in a T-shaped arrangement of the phosphine ligands around the Fe center (Figure 4.S23) similar to the structure observed crystallographically for $(^{Ar}P_3B)Fe(N_2)$ (Figure 4.S2). The isoelectronic analogs $[(P_3B)Fe(NNH_2)]^+$ and $(P_3Si)Fe(NNH_2)$ do not display such an interaction in their DFT predicted geometries.^{8,10,34} While the ^{57}Fe Mössbauer spectroscopy does not directly provide any structural information, it provides excellent quantification of the Fe containing reaction products and establishes that these reactions proceed fairly cleanly and in moderate to high yield even though $(^{Ar}P_3B)Fe(NNH)$ and $[(^{Ar}P_3B)Fe(NNH_2)][BAr^F_{24}]$ could not be isolated due to thermal instability.

Table 4.6: ^{57}Fe Mössbauer Parameters

Compound	δ (mm/s)	ΔE_Q (mm/s)	Spin State
$(^{\text{Ar}}\text{P}_3\text{B})\text{FeBr}$	0.61	2.40	1.5
$(^{\text{Ar}}\text{P}_3\text{B})\text{Fe}(\text{OTf})$	0.71	2.58	1.5
$(^{\text{Ar}}\text{P}_3\text{B})\text{Fe}(\text{N}_2)$	0.42	1.90	0
$[(^{\text{Ar}}\text{P}_3\text{B})\text{Fe}(\text{N}_2)][\text{Na}(12\text{-C-}4)_2]$	0.32	0.75	0.5
$(^{\text{Ar}}\text{P}_3\text{B})\text{Fe}(\text{NNH})$	0.24	0.94	0.5
$(^{\text{Ar}}\text{P}_3\text{B})\text{Fe}(\text{NNSiMe}_3)$	0.16	1.54	0.5
$[(^{\text{Ar}}\text{P}_3\text{B})\text{Fe}(\text{NNH}_2)][\text{BAr}^{\text{F}}_{24}]$	0.06	1.32	0.5
$(\text{P}_3\text{Si})\text{Fe}(\text{NNH}_2)^{10}$	0.31	0.86	0.5
$[(\text{P}_3\text{B})\text{Fe}(\text{NNH}_2)][\text{BAr}^{\text{F}}_{24}]^{16}$	0.35	1.02	0.5

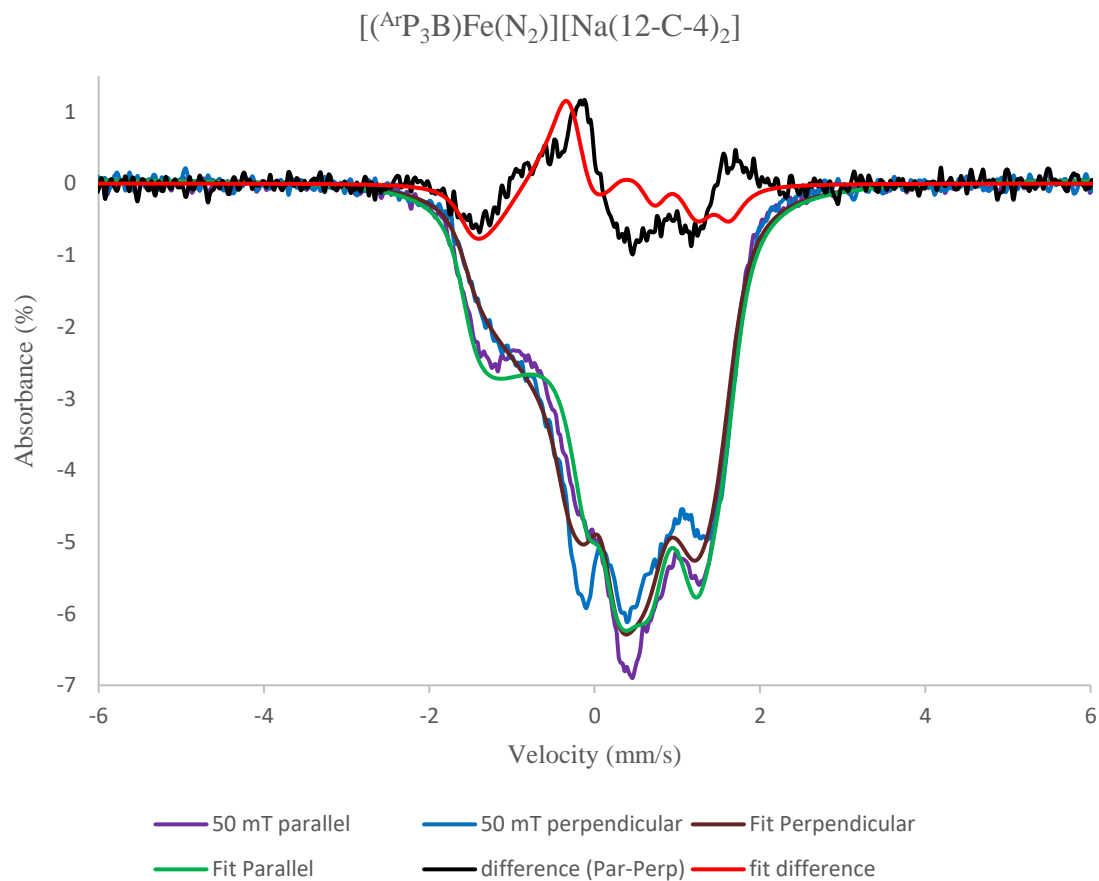


Figure 4.13: ^{57}Fe Mössbauer spectra of $[(^{\text{Ar}}\text{P}_3\text{B})\text{Fe}(\text{N}_2)][\text{Na}(\text{12-C-4})_2]$ in the presence of a 50 mT applied field in \parallel and \perp orientations and difference spectrum with fits (80 K, 2-MeTHF).

Table 4.7: ^{57}Fe Mössbauer fit parameters for $[(^{\text{Ar}}\text{P}_3\text{B})\text{Fe}(\text{N}_2)][\text{Na}(\text{12-C-4})_2]$

Compound	δ (mm/s)	ΔE_{q} (mms/)	$A_{\text{Fe}}(A_1, A_2, A_3)$ (T)	η
$[(^{\text{Ar}}\text{P}_3\text{B})\text{Fe}(\text{N})][\text{Na}(\text{12-C-4})_2]^{\text{a}}$	0.32	0.75	0, 2.0, 0.7	0.63

^a g -values for $[(^{\text{Ar}}\text{P}_3\text{B})\text{Fe}(\text{N}_2)][\text{Na}(\text{12-C-4})_2]$ taken from EPR simulations

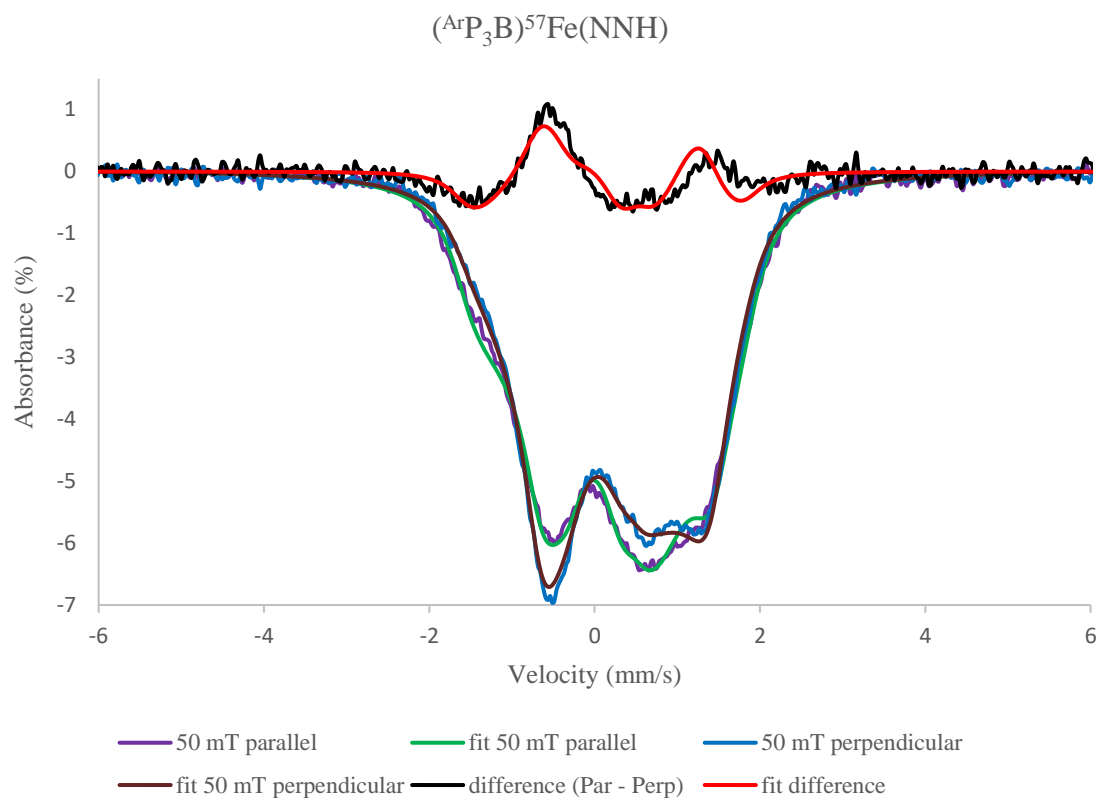


Figure 4.14: ^{57}Fe Mössbauer spectra of $(^{\text{Ar}}\text{P}_3\text{B})\text{Fe}(\text{NNH})$ reaction mixture (80 K, 2-MeTHF,) in the presence of a 50 mT field applied in \parallel and \perp orientations and difference spectrum with fits).

Table 4.8: ^{57}Fe Mössbauer fit parameters for Generation of $(^{\text{Ar}}\text{P}_3\text{B})\text{Fe}(\text{NNH})$

Compound	δ (mm/s)	ΔE_{Q} (mms/)	$A_{\text{Fe}}(A_1, A_2, A_3)$ (T)	η	% Area
$(^{\text{Ar}}\text{P}_3\text{B})\text{Fe}(\text{N}_2)$	0.39	2.06	N/A	N/A	18
$(^{\text{Ar}}\text{P}_3\text{B})\text{Fe}(\text{NNH})^{\text{a}}$	0.24	0.94	1.9, 20.1, 0.6	-0.46	82

^a g -values for $(^{\text{Ar}}\text{P}_3\text{B})\text{Fe}(\text{NNH})$ taken from CW EPR simulations

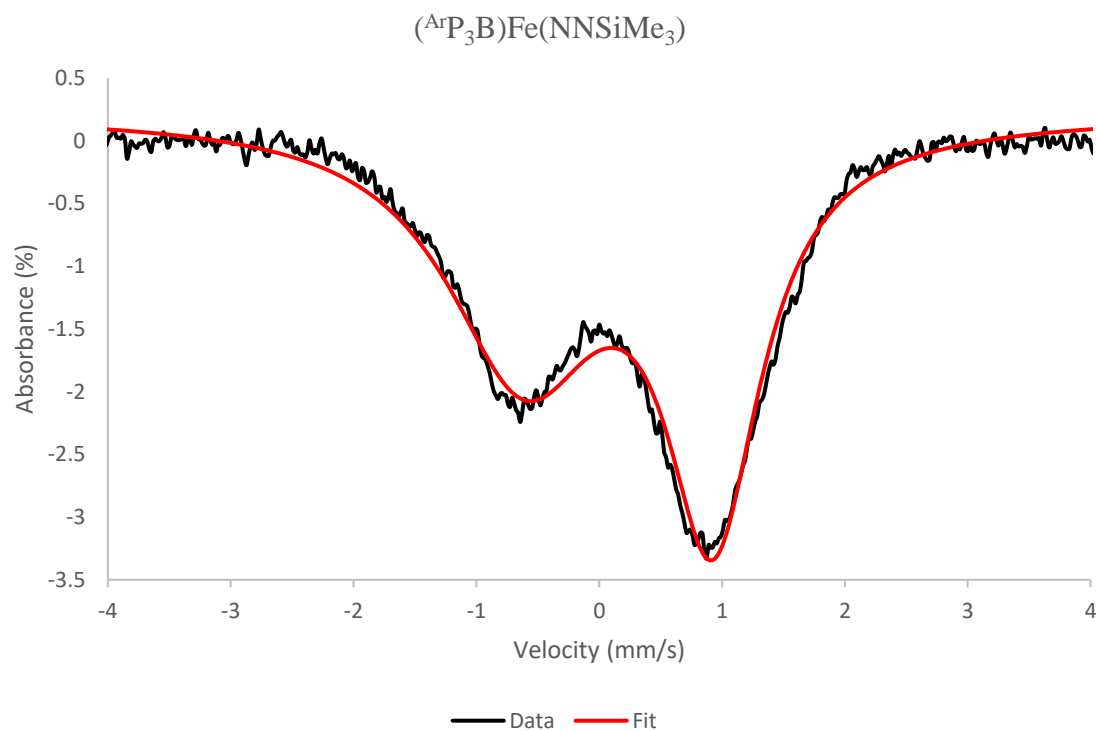


Figure 4.15: ^{57}Fe Mössbauer spectrum of $(^{\text{Ar}}\text{P}_3\text{B})\text{Fe}(\text{NNSiMe}_3)$. (80 K, 2-MeTHF, 50 mT ||).

Table 4.9: ^{57}Fe Mössbauer fit parameters for Generation of $(^{\text{Ar}}\text{P}_3\text{B})\text{Fe}(\text{NNSiMe}_3)$

Compound	δ (mm/s)	ΔE_{q} (mms/)
$(^{\text{Ar}}\text{P}_3\text{B})\text{Fe}(\text{NNSiMe}_3)$	0.16	1.54

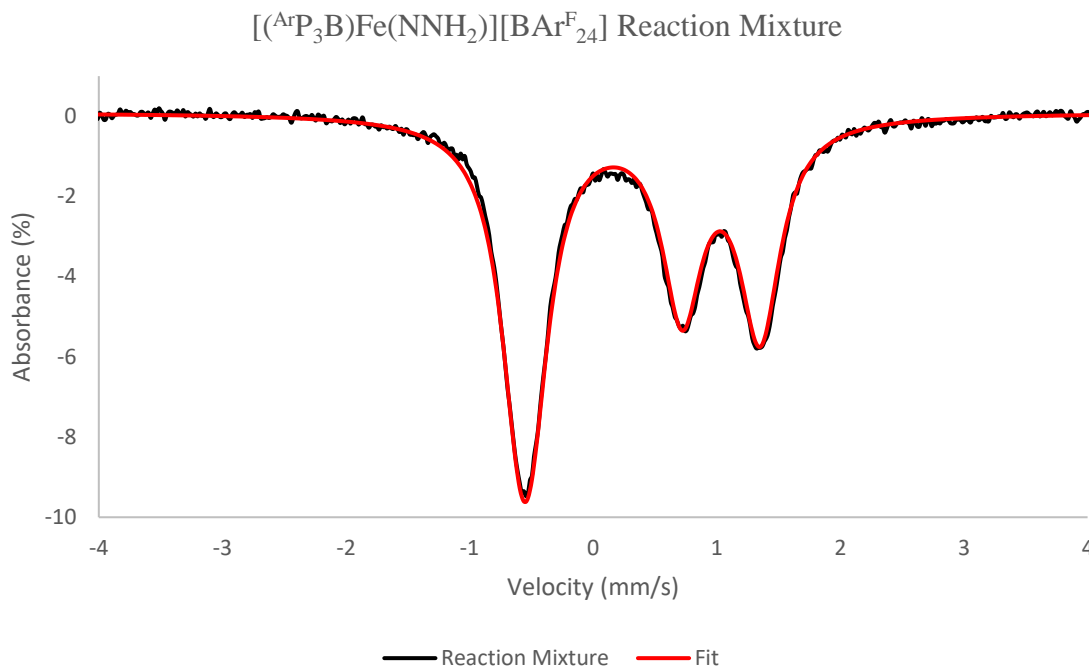


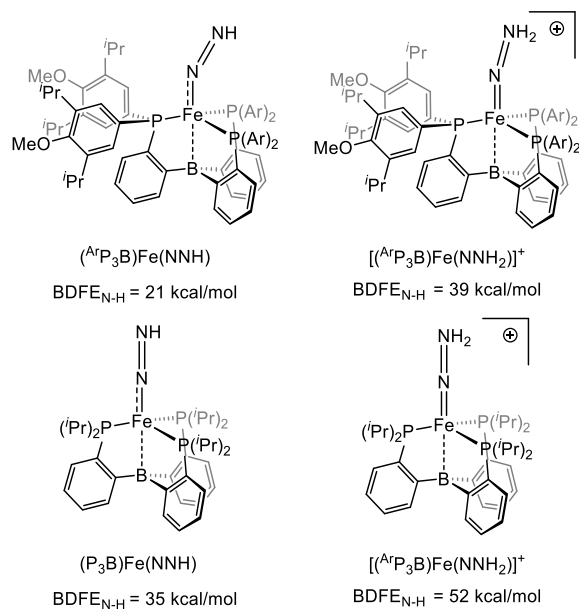
Figure 4.16: ^{57}Fe Mössbauer spectrum of $[(^{\text{Ar}}\text{P}_3\text{B})\text{Fe}(\text{NNH}_2)][\text{BAr}^{\text{F}}_{24}]$ reaction mixture (80 K, 2-MeTHF, 50 mT ||).

Table 4.10: ^{57}Fe Mössbauer Fit components for Generation of $[(^{\text{Ar}}\text{P}_3\text{B})\text{Fe}(\text{NNH}_2)][\text{BAr}^{\text{F}}_{24}]$

Compound	δ (mm/s)	ΔEq (mms/)	% Area
$(^{\text{Ar}}\text{P}_3\text{B})\text{Fe}(\text{N}_2)$	0.42	1.90	53.6
$[(^{\text{Ar}}\text{P}_3\text{B})\text{Fe}(\text{NNH}_2)][\text{BAr}^{\text{F}}_{24}]$	0.07	1.32	46.4

4.2.3 DFT Estimation of N-H Bond Strengths (BDFE) for $(^{\text{Ar}}\text{P}_3\text{B})\text{Fe}(\text{NNH})$ and $[(^{\text{Ar}}\text{P}_3\text{B})\text{Fe}(\text{NNH}_2)][\text{BAr}^{\text{F}}_{24}]$: We were interested to see how the DFT predicted N-H bond strengths in the truncated models of $(^{\text{Ar}}\text{P}_3\text{B})\text{Fe}(\text{NNH}_x)$ ($x = 1, 2$) species compared to those we have previously reported for the parent system and used the same methodology as previously published.³³ We found that for the $^{\text{Ar}}\text{P}_3\text{B}$ system that the N-H bond in

$(^{\text{Ar}}\text{P}_3\text{B})\text{Fe}(\text{NNH})$ is predicted to be significantly weaker than that of the parent system (gas phase $\text{BDFE}_{\text{N-H}} = 21$ kcal/mol for $(^{\text{Ar}}\text{P}_3\text{B})\text{Fe}(\text{NNH})$ and gas phase $\text{BDFE}_{\text{N-H}} = 35$ kcal/mol for $(\text{P}_3\text{B})\text{Fe}(\text{NNH})$) (Scheme 4.9).³³ Similarly, we found that $[(^{\text{Ar}}\text{P}_3\text{B})\text{Fe}(\text{NNH}_2)]^+$ has a predicted gas phase BDFE of 39 kcal/mol while the parent $[(\text{P}_3\text{B})\text{Fe}(\text{NNH}_2)]^+$ has a predicted gas phase BDFE of 52 kcal/mol (Scheme 4.9).³³ The weaker N-H bonds calculated for the truncated $^{\text{Ar}}\text{P}_3\text{B}$ systems relative to the parent system lead us to propose that the enhanced thermal stability of $(^{\text{Ar}}\text{P}_3\text{B})\text{Fe}(\text{NNH})$ and $[(^{\text{Ar}}\text{P}_3\text{B})\text{Fe}(\text{NNH}_2)]^+$ relative to their analogs on the parent system has its origins in kinetic stabilization of these species from the steric bulk provided by the $^{\text{Ar}}\text{P}_3\text{B}$ ligand, rather than from the formation of intrinsically stronger N-H bonds.



Scheme 4.9: DFT predicted N-H BDFE values for $(^{\text{Ar}}\text{P}_3\text{B})\text{Fe}(\text{NNH})$, $[(^{\text{Ar}}\text{P}_3\text{B})\text{Fe}(\text{NNH}_2)]^+$, $(\text{P}_3\text{B})\text{Fe}(\text{NNH})$ and $[(\text{P}_3\text{B})\text{Fe}(\text{NNH}_2)]^+$ (TPSS, def2-TZVP on Fe, def2-SVP on all else).

4.2.4 Production of NH_3 : We also characterized the viability of $(^{\text{Ar}}\text{P}_3\text{B})\text{Fe}$ species as precatalysts for the reduction of N_2 to NH_3 to supplement the thorough spectroscopic

characterization of $[(^{\text{Ar}}\text{P}_3\text{B})\text{Fe}(\text{N}_2\text{H}_x)]^y$ ($x = 0, 1, 2$; $y = -1, 0, +1$) species described above. This was accomplished by screening $[(^{\text{Ar}}\text{P}_3\text{B})\text{Fe}(\text{N}_2)][\text{Na}(12\text{-C-4})_2]$, $(^{\text{Ar}}\text{P}_3\text{B})\text{Fe}(\text{N}_2)$, and $(^{\text{Ar}}\text{P}_3\text{B})\text{FeBr}$ as precatalysts for N_2 fixation using acids, reductants, and reaction conditions previously reported for the parent $[(\text{P}_3\text{B})\text{Fe}(\text{N}_2)][\text{Na}(12\text{-C-4})_2]$ system.^{8,9} We found that substoichiometric amounts of NH_3 (up to 1.07 equiv. per Fe) could be produced using KC_8 and $\text{HBArF}_{24} \cdot 2\text{Et}_2\text{O}$ cocktails. We also observed that quenching $[(^{\text{Ar}}\text{P}_3\text{B})\text{Fe}(\text{N}_2)][\text{Na}(12\text{-C-4})_2]$ with small excesses of $\text{HBArF}_{24} \cdot 2\text{Et}_2\text{O}$ without added reductant generated small amounts of NH_3 (Table 4.11), although the amount of ammonia produced was significantly less than observed under the same conditions using the parent $[(\text{P}_3\text{B})\text{Fe}(\text{N}_2)][\text{Na}(12\text{-C-4})_2]$ system. An additional contrast between the $^{\text{Ar}}\text{P}_3\text{B}$ and parent P_3B systems is that the CoCp^*_2 and $[\text{Ph}_2\text{NH}_2][\text{OTf}]$ cocktail produces no detectable ammonia. We have rationalized the attenuation in catalytic activity for the $^{\text{Ar}}\text{P}_3\text{B}$ system relative to the parent P_3B system in several ways. The increased steric profile may very well have the effect of slowing the kinetics of protonation of the N_2 ligand, subsequently inhibiting the formation of NH_3 relative to the background reaction of HBArF_{24} with KC_8 to produce H_2 . Additionally, the N_2 ligand in $[(^{\text{Ar}}\text{P}_3\text{B})\text{Fe}(\text{N}_2)][\text{Na}(12\text{-C-4})_2]$ is significantly less activated than that of the parent system, as judged by N-N vibration observed in their respective IR spectra ($\nu_{\text{N}_2} = 1937 \text{ cm}^{-1}$ for $^{\text{Ar}}\text{P}_3\text{B}$ versus 1905 cm^{-1} for P_3B). This attenuated activation of the N_2 ligand is likely correlated with attenuated NH_3 yields as has been hypothesized for other systems.^{8,9,12,44,45} Furthermore, the fact that $(^{\text{Ar}}\text{P}_3\text{B})\text{Fe}(\text{N}_2)$ is a diamagnetic $18 e^-$ compound while $(\text{P}_3\text{B})\text{Fe}(\text{N}_2)$ is an $S = 1$, $16 e^-$ compound makes the reduction of $(^{\text{Ar}}\text{P}_3\text{B})\text{Fe}(\text{N}_2)$ into the anionic state presumed to be requisite for catalysis significantly less favorable and may further attenuate any formation of NH_3 .^{8,12} This is made apparent upon comparison of the cyclic voltammograms of

$(^{\text{Ar}}\text{P}_3\text{B})\text{Fe}(\text{N}_2)$ and $(\text{P}_3\text{B})\text{Fe}(\text{N}_2)$. For $(^{\text{Ar}}\text{P}_3\text{B})\text{Fe}(\text{N}_2)$ an irreversible reduction feature with a peak potential at -2.62 V vs $\text{FeCp}_2/[\text{FeCp}_2]^+$ is observed when scanning cathodically corresponding to $(^{\text{Ar}}\text{P}_3\text{B})\text{Fe}(\text{N}_2)/[(^{\text{Ar}}\text{P}_3\text{B})\text{Fe}(\text{N}_2)]^-$ while the $(\text{P}_3\text{B})\text{Fe}(\text{N}_2)/[(\text{P}_3\text{B})\text{Fe}(\text{N}_2)]^-$ couple is reversible with $E_{1/2} = -2.08$ V vs $\text{FeCp}_2/[\text{FeCp}_2]^+$ with a peak potential at -2.17 V vs $\text{FeCp}_2/[\text{FeCp}_2]^+$.¹⁴ The 450 mV difference in peak potentials for the $\text{Fe}(\text{N}_2)/[\text{Fe}(\text{N}_2)]^-$ is indicative of a significantly more difficult reduction to the anionic state requisite for catalytic activity in the $^{\text{Ar}}\text{P}_3\text{B}$ system relative to the parent system and explains the corresponding attenuation in NH_3 when using either the $\text{KC}_8/\text{HBAr}^{\text{F}}_{24}$ or the $\text{CoCp}^*_2/[\text{H}_2\text{NPh}_2][\text{OTf}]$ cocktails. The irreversibility in the $(^{\text{Ar}}\text{P}_3\text{B})\text{Fe}(\text{N}_2)/[(^{\text{Ar}}\text{P}_3\text{B})\text{Fe}(\text{N}_2)]^-$ couple likely results from the significant geometric rearrangement which occurs as the η^2 -arene interaction is lost and the Fe center goes from a 6-coordinate $18 e^-$ configuration to a 4-coordinate $17 e^-$ configuration (Figure 4.S27).

Table 4.11: NH₃ Production Under Various Conditions

Precatalyst	Reductant (equiv.)	Acid (equiv.)	Yield (equiv./Fe)
(^{Ar} P ₃ B)FeBr ^a	KC ₈ (56)	HBArF ₂₄ •2Et ₂ O (46)	1.07
(^{Ar} P ₃ B)Fe(N ₂) ^a	KC ₈ (56)	HBArF ₂₄ •2Et ₂ O (46)	.015
[(^{Ar} P ₃ B)Fe(N ₂)] [Na(12-C-4) ₂] ^a	KC ₈ (56)	HBArF ₂₄ •2Et ₂ O (46)	.095
[(P ₃ B)Fe(N ₂)] [Na(12-C-4) ₂] ⁹	KC ₈ (56)	HBArF ₂₄ •2Et ₂ O (46)	7.0
[(^{Ar} P ₃ B)Fe(N ₂)] [Na(12-C-4) ₂] ^b	CoCp ₂ [*] (53)	[H ₂ NPh ₂][OTf] (108)	0.0
[(P ₃ B)Fe(N ₂)] [Na(12-C-4) ₂] ⁸	CoCp ₂ [*] (54)	[H ₂ NPh ₂][OTf] (108)	12.8
[(^{Ar} P ₃ B)Fe(N ₂)] [Na(12-C-4) ₂] ^c	None	HBArF ₂₄ •2Et ₂ O (2)	0.22
[(^{Ar} P ₃ B)Fe(N ₂)] [Na(12-C-4) ₂] ^c	None	HBArF ₂₄ •2Et ₂ O (5)	0.25

^a Precatalyst, acid, reductant and Et₂O were sealed in a Schlenk tube at 77 K and then warmed to -78 °C and stirred for 45 minutes followed by stirring for 30 minutes while warming room temperature prior to NH₃ quantification workup. ^b Precatalyst, acid, reductant and Et₂O were sealed in a Schlenk tube at 77 K and then warmed to -78 °C and stirred for 6 hours followed by stirring for 30 minutes while warming to room temperature prior to NH₃ quantification workup. ^c Precatalyst, acid, and Et₂O were sealed in a Schlenk tube at 77 K and then warmed to -78 °C and stirred for 15 minutes followed by stirring for 30 minutes while warming to room temperature prior to NH₃ quantification workup.

4.3 Conclusion

The present study has described the synthesis of an anionic Fe-N₂ adduct supported by a tris(diarylphosphine)borane ligand which creates a sterically protected N₂ binding pocket. This additional steric protection present in other Fe-N₂ adducts allows for the observation and characterization of the first Fe(NNH) species which is converted into an [Fe(NNH₂)]⁺ in the presence of 2-5 equivalents of acid. The *S* = ½ ground state of [(^{Ar}P₃B)Fe(N₂)] [Na(12-C-

4)₂] and its more reactive products from protonation (^AP₃B)Fe(NNH) and [(^AP₃B)Fe(NNH₂)] [BAr^F₂₄] were particularly well suited to study by EPR methods which is selective for these species, and all species were extensively characterized by CW-EPR, ENDOR and HYSCORE spectroscopies. These methods are well suited to the study of reactive species which must be handled at cryogenic temperatures in order to be observed. This strategy had previously been employed successfully by our lab to study model systems as well as by others who study metallo-enzyme mechanism and reactivity. Additional support for the assignments is provided by the ⁵⁷Fe Mössbauer spectra of reaction mixtures which show major components which have isomer shifts and quadrupole splittings similar to previously characterized and isoelectronic Fe-silyl-diazenido and iron-hydrazido(2-) species. Furthermore these observations provide direct evidence that the first two protonation steps in (P₃B)Fe(N₂) species occur at N_β and that formation of [Fe(NNH₂)]⁺ goes through an Fe(NNH) on (P₃B)Fe platforms. The characterization of these species also provides well-determined physical observables, namely nuclear hyperfine coupling constants, nuclear quadrupole coupling constants, and their associated asymmetry parameters. These values may serve as useful benchmarks for comparison to intermediates observed under turnover in the study of biological nitrogen fixing metallo-cofactors and synthetic nitrogen reduction catalyst systems.

4.4 Supporting Information

4.4.1 Experimental:

General Considerations: All operations were carried out using standard Schlenk or glovebox techniques under inert atmospheres of N₂ or argon. Unless otherwise noted all solvents were deoxygenated and dried by thoroughly sparging with N₂ gas followed by

passage through an activated alumina column in the solvent purification system by SG Water, USA LLC and storage over 3 Å molecular sieves prior to use. Non-halogenated solvents were tested with a standard purple solution of sodium benzophenone ketyl in tetrahydrofuran in order to confirm effective oxygen and moisture removal. All reagents were purchased from commercial vendors and used without further purification unless otherwise stated. 4-bromo-2,6-diisopropylanisole, 2-bromophenylphosphorusdichloride, [Na][BAr^F₂₄], [H(OEt₂)₂][BAr^F₂₄], KC₈, Cp^{*}₂Co, [Ph₂NH₂][OTf], and anhydrous ⁵⁷FeCl₂ were synthesized following literature procedures.^{12,39,46-50} Deuterated solvents were purchased from Cambridge Isotope Laboratories, Inc., degassed and stored over activated 3 Å molecular sieves prior to use. Elemental analyses were performed by California Institute of Technology's Elemental Analysis facility or by Midwest Microlab, LLC, Indianapolis, IN.

Nuclear Magnetic Resonance Spectroscopy: ¹H and ¹³C chemical shifts are reported in ppm relative to tetramethylsilane, using residual solvent resonances as internal standards. ³¹P chemical shifts are reported in ppm and referenced externally to 85% aqueous H₃PO₄. ¹⁹F chemical shifts are reported in ppm and referenced externally to trifluorotoluene at -63.72 ppm. ¹¹B chemical shifts are reported in ppm and referenced externally to BF₃•Et₂O at 0 ppm. Solution phase magnetic measurements were performed by the method of Evans.

Infrared Spectroscopy: Solid IR measurements were obtained on a Bruker Alpha spectrometer equipped with a diamond ATR probe.

EPR Spectroscopy: Continuous wave X-band EPR spectra were obtained on a Bruker EMX spectrometer on 2-9 mM solutions prepared as frozen glasses in 2-MeTHF. Pulsed

EPR measurement including ESEEM, HYSCORE, and ENDOR measurements were performed at X and Q-bands on a Bruker ELEXSYS spectrometer. Spectra (CW, ENDOR, HYSCORE) were simulated using the EasySpin suite of programs with Matlab 2016.⁵¹

X-Ray Crystallography: XRD studies were carried out at the Beckman Institute Crystallography Facility on a Bruker AXS KAPPA APEXII diffractometer (Mo K α radiation) or a Bruker AXS D8 VENTURE (Mo K α or Cu K α). Structures were solved using SHELXS or SHELXT and refined against F² on all data by full-matrix least squares with SHELXL.⁵² The crystals were mounted on a mitegen loops under Paratone N oil.

Electrochemistry. Electrochemical measurements were carried out using a CD instruments 600B electrochemical analyzer. A freshly-polished glassy carbon electrode was used as the working electrode and a graphite rod was used as the auxiliary electrode. Solutions (THF) of electrolyte (0.1 M tetra-n-butylammonium hexafluorophosphate) contained ferrocene (0.1 mM), to serve as an internal reference, and analyte (0.2 mM). All reported potentials are referenced to the ferrocene/ferrocenium couple, [Cp₂Fe]⁺/CpFe.

⁵⁷Fe Mössbauer Spectroscopy. Spectra were recorded on a spectrometer from SEE Co (Edina, MN) operating in the constant acceleration mode in a transmission geometry. The sample was kept in an SVT-400 cryostat from Janis (Wilmington, MA). The quoted isomer shifts are relative to the centroid of the spectrum of a metallic foil of α -Fe at room temperature. Solid samples were prepared by grinding polycrystalline material into a fine powder and then mounted in a Delrin cup fitted with a screw-cap as a boron nitride pellet. Solution samples were transferred to a sample cup chilled to 77K inside of the glovebox. Upon freezing of the solution, the cup was quickly removed from the glovebox and immersed in liquid N₂ until being mounted in the cryostat. Data analysis was performed

using the program WMOSS (www.wmoss.org) and quadrupole doublets were fit to Lorentzian line shapes.

DFT Calculations. Geometry optimizations and frequency calculations were performed using dispersion-corrected density functional theory (DFT-D₃) using Grimme's dispersion correction.⁵³ All calculations were performed using ORCA version 4.0.1.2 with the TPSS functional, the def2-SVP basis set for C, H, P, B, N, and O atoms, and the def2-TZVP basis set for Fe. Frequency calculations were performed on optimized geometries to ensure true minima and to obtain gas-phase free energy values at 195 K. Mössbauer parameters were calculated using the TPSSH functional, the def2-SVP basis set for C, H, and O atoms, the def2-TZVP basis set for P, B, and N atoms and the CP(PPP) basis set for Fe and a COSMO solvation model in methanol according to a previously reported methodology.¹⁴

4.4.2 Synthetic Procedures

bis(3,5-diisopropyl-4-methoxyphenyl)-o-bromophenylphosphine: Mg turnings (16.6 g, 682.99 mmol) were stirred vigorously under N₂ for 2 hours followed by addition of 400 mL THF and 0.5 mL 1,2-dibromoethane. The suspension was heated to reflux for a period of 1 hour to activate the Mg turnings and then allowed to cool to room temperature. 44.3501 g (163.53 mmol) of 4-bromo-2,6-diisopropylanisole in 25 mL THF was added dropwise via addition funnel to the stirring suspension, no exotherm was observed. The reaction vessel was again heated to reflux for 12 hours and again cooled to room temperature. The dark cloudy solution was then added to a solution of 21.0662 g (81.69 mmol) 2-bromophenylphosphorusdichloride in 250 mL THF at -78 °C dropwise via cannula over 2 hours. After addition was completed the reaction mixture was allowed to stir overnight (10

hours) while slowly warming to room temperature. After overnight stirring 750 mL DI H₂O was added to the reaction mixture and the solution was transferred to a separatory funnel and extracted with 3 x 400 mL Et₂O. The combined organic layers were dried with MgSO₄ and filtered. Removal of solvent left a viscous oil. The oil was taken up in HMDSO and allowed to stand at room temperature overnight as white solids crashed out of solution. Further cooling of the mother liquor to -35 °C overnight furnished an additional small crop of white solids. The solids were collected on a frit, washed with HMDSO and dried under vacuum. Yield: 35.09 g, 75.4% Elemental Analysis % C; H; N: Found (Calc): C: 67.23 (67.48); H: 7.78 (7.43); N: -0.06 (0.00) ¹H NMR (400 MHz, C₆D₆, 298 K): δ 7.40 (dd, 1H, ³J_{HH} = 7.7, ⁴J_{HH} = 3.2 Hz), 7.34 (s, 2H), 7.32 (s, 2H), 7.13 (d, 1H, ³J_{HH} = 7.7 Hz), 6.77 (dt, 2H, J_{HH} = 53.0, 7.4 Hz), 3.44 (s, 6H), 3.34 (hept, 4H, 7.0 Hz), 1.12 (d, 24H, ³J_{HH} = 6.8 Hz). ³¹P{¹H} NMR (202.4 MHz, C₆D₆, 298 K, ppm): δ -3.76 (s), ¹³C{¹H} NMR (101 MHz, C₆D₆, 298 K, ppm): δ 156.10, 142.45 (d, J = 7.2 Hz), 141.42, 141.25 (d, J = 15.0 Hz), 134.76, 133.29 (d, J = 2.1 Hz), 132.55 (d, J = 10.7 Hz), 130.7 (d, J = 31 Hz) 130.57 (J = 21.1 Hz), 130.14, 127.47, 61.88, 24.12, 24.07.

^{Ar}P₃B: 5.0926 g (8.94 mmol) of arm was dissolved in 200 mL Et₂O and cooled to -78 °C. 6.2 mL ⁿBuLi (1.6 M in hexanes) was added dropwise to the reaction mixture causing it to turn golden. The solution was stirred cold for 1 hour and then allowed to warm to room temperature over 1 hour and stirred an additional 30 minutes at room temperature. The solution was then chilled to -78 °C and a solution of B(OMe)₃ (312.4 mg, 3.00 mmol) in Et₂O (40 mL) was added dropwise and the mixture was allowed to slowly warm to RT overnight. All volatiles were removed from the reaction mixture, leaving a tacky cream colored solid. This solid was suspended in pentane and filtered through Celite, leaving a white solid behind

on the Celite pad. The white solid was then washed with Et₂O (5 x 30 mL) and the washings were collected and cooled to -78 °C. Solid [HNEtⁱPr₂]Cl (504.7 mg, 3.05 mmol) was added to the stirring mixture and the reaction was allowed to slowly warm to RT and stirred overnight. The resulting bright yellow solution was pumped down to a yellow foam. The foam was extracted in pentane, filtered through Celite, concentrated, and stored at -35 °C resulting in the formation of bright yellow crystals of ^{Ar}P₃B. Yield: 2.7241 g (61.7%). Elemental Analysis % C; H; N: Found (Calc): C: 77.54 (77.92); H: 9.18 (8.58); N: -0.02 (0.00) ¹H NMR (300 MHz, C₆D₆, 298 K, ppm): δ 7.62 (d, 3H, ³J_{HH} = 7.4 Hz), 7.26 (s, br, 12H), 7.12 (d, 3H, ³J_{HH} = 7.4 Hz), 6.81 (dt, 6H, J_{HH} = 79.7, 7.6 Hz), 3.5 (s, 18H), 3.36 (hept, 12H, ³J_{HH} = 5.6 Hz), 1.16 (t, 72H, ³J_{HH} 6.8 Hz). ³¹P{¹H} NMR (202.4 MHz, C₆D₆, 298 K, ppm) -9.49 (s), ¹¹B (128 MHz, C₆D₆, 298 K, ppm). 3.79 (s, br) ¹³C{¹H} NMR (101 MHz, CDCl₃, 298 K, ppm) δ 154.22, 142.73 (m), 140.22, 135.47, 134.81 (m), 129.84 (d, J = 7.3 Hz), 129.71 (d, J = 7.7 Hz), 128.94, 128.46, 126.51, 62.28, 26.52, 24.28, 23.93

(^{Ar}P₃B)FeBr: ^{Ar}P₃B (504.7 mg, 0.34 mmol) and FeBr₂ (79.4mg, 0.37 mmol) were stirred in THF (ca. 10 mL) until all solids had dissolved giving a clear yellow solution. All volatiles were removed and the resulting solid was triturated in Et₂O and evacuated to dryness. The resulting solid was then dissolved in benzene and combined with Na/Hg amalgam and stirred vigorously overnight giving a dark red-brown solution. The solution was filtered through Celite and all volatiles were removed *in vacuo*, giving a dark brown solid. This solid was dissolved in pentane and allowed to stand at room temperature overnight while tan solids precipitated from solution. The dark brown mother liquor was decanted and filtered through Celite and concentrated and stored at -35 °C, giving (^{Ar}P₃B)FeBr as a dark brown microcrystalline powder. Yield: 324.5 mg (58.9 %). X-ray diffraction quality crystals were

obtained by slow vapor diffusing from a pentane solution of (^{Ar}P₃B)FeBr into HMDSO. Elemental Analysis % C; H; N: Found (Calc): C: 71.78 (71.73); H: 8.35 (7.86); N: 0.03 (0.00) ¹H NMR (300 MHz, C₆D₆, 298 K, ppm): δ 30.19 (s, br), 25.03 (s, br), 9.80 (s, br), 3.95 (s, br), 3.45 (s, br), 3.31 (s, br), 2.41 (s, br), 1.46 (s, br), 0.85 (s, br), 0.75 (s, br), -2.06 (s, br), -24.14 (s, br). μ_{eff} (C₆D₆, 298 K, 300 MHz): 3.7 μB

(^{Ar}P₃B)Fe(N₂): (^{Ar}P₃B)FeBr (142.9 mg, 0.088 mmol) was dissolved in benzene and stirred vigorously over excess sodium amalgam (2.3 eq.) for 12 hours resulting in formation of a dark forest green solution. The solution was filtered through Celite and volatiles were removed *in vacuo*. The resulting dark forest green solids were extracted in pentane, filtered through Celite again, concentrated, and stored in a freezer at -35 °C, giving (^{Ar}P₃B)Fe(N₂) as a dark microcrystalline solid. X-ray diffraction quality crystals were obtained by slow vapor diffusion from a pentane solution of (^{Ar}P₃B)Fe(N₂) into HMDSO. Yield: 109.2 mg (79.5 %). Elemental Analysis % C; H; N: Found (Calc): C: 74.16 (73.74); H: 8.50 (8.12); N: 1.69 (1.79). ¹H NMR (400 MHz, C₆D₆) δ 7.37 (s, br, 9H), 6.94-6.49 (m, br, 15H), 3.50 (s, 9H), 3.41-3.29 (m, br, 15H), 3.11 (m, br, 6H), 1.27 (s, br, 18H), 1.14 (s, br, 18H), 1.03 (d, ³J_{HH} = 6.8 Hz, 18H), 0.96 (s, br, 18H). ³¹P NMR {¹H} NMR (202.4 MHz, C₆D₆, 298 K, ppm) 79.07 (s, br, 2P), 20.25 (s, br, 1P). ¹¹B (128 MHz, C₆D₆, 298 K, ppm) 16.08 (s, br). IR (thin film from C₆D₆, 298 K) ν_{N2} = 2016 cm⁻¹.

[(^{Ar}P₃B)Fe(N₂)]/[Na(12-C-4)₂]: (^{Ar}P₃B)Fe(N₂) was dissolved in THF and stirred vigorously over excess sodium amalgam (5 eq.) for 12 hours, resulting in formation of a dark red solution. The solution was filtered through Celite and volatiles were removed *in vacuo*. The resulting dark red solids were extracted in Et₂O, and filtered through Celite again and neat 12-crown-4 was added. The solution was allowed to stand for 10 minutes and then was

concentrated, layered with pentane, and stored in a freezer at $-35\text{ }^{\circ}\text{C}$, yielding $[(^{\text{Ar}}\text{P}_3\text{B})\text{Fe}(\text{N}_2)][\text{Na}(12\text{-C-}4)_2]$ as a dark red microcrystalline solid. This solid was then washed with pentane until the washings came out colorless (typically 3-5 x 1 mL washes). (note: Et_2O and Pentane were additionally dried by passage through a short pipette column of activated alumina prior to use). Elemental Analysis % C; H; N: Found (Calc): C: 69.04 (69.38); H: 8.19 (8.21); N: 0.39 (1.44). Note: The N content of samples prepared for elemental analysis was consistently low while remaining within acceptable limits on C and H. This is consistent with a labile N_2 ligand, additional evidence of the lability of the N_2 ligand was observed in the rapid exchange of $^{15}\text{N}_2$ for $^{14}\text{N}_2$ in solution at low temperatures and even in the solid state. ^1H NMR (300 MHz, C_6D_6) δ 11.82 (s, br), 10.01 (s, br), 3.75-2.78 (multiple broad overlapping signals), 1.85 (s, br), 1.70-0.70 (multiple broad overlapping signals), -1.36 (s, br). μ_{eff} (C_6D_6 , 298 K, 300 MHz): 1.7 μB . IR (thin film from THF, 298 K) $\nu_{\text{N}_2} = 1937\text{ cm}^{-1}$.

$[(^{\text{Ar}}\text{P}_3\text{B})^{57}\text{Fe}(\text{N}_2)][\text{Na}(12\text{-C-}4)_2]$: $^{\text{Ar}}\text{P}_3\text{B}$ (300.0 mg, 0.203 mmol) and $^{57}\text{FeCl}_2$ (27.8mg, 0.217 mmol) were stirred in THF (ca. 10 mL) until all solids had dissolved, giving a clear yellow solution. All volatiles were removed and the resulting solid was triturated in Et_2O and evacuated to dryness. The resulting solid was then dissolved in benzene and combined with freshly prepared 1 % Na/Hg (1.14 equiv.) amalgam and stirred vigorously overnight, giving a dark red-brown solution. The solution was filtered through Celite and all volatiles were removed *in vacuo* giving a dark brown solid. This solid was dissolved in pentane and allowed to stand at room temperature overnight while tan solids precipitated from solution. The dark brown pentane mother liquor was evaporated to dryness and then dissolved in ca. 5 mL C_6H_6 and stirred vigorously over excess 1 % Na/Hg (10 equiv.) for 16 hours, giving a dark green

solution. This solution was filtered through Celite, extracted in pentane, filtered through Celite again, and evaporated to dryness, leaving a dark green foam. The green foam was dissolved in ca. 5 mL THF and stirred vigorously over excess 1 % Na/Hg (10 equiv.) for 12 hours. The resulting dark red solution was decanted and evaporated to dryness, leaving a dark red film. The film was extracted in ca. 3 mL Et₂O and filtered through Celite. A 70 μ L aliquot of 12-Crown-4 was added to the filtrate and allowed to stand for 15 minutes before layering with ca. 15 mL pentane. The vial was then sealed and placed in a -35 °C freezer overnight. After ~ 48 hours the mother liquor was decanted and $[(^{Ar}P_3B)^{57}Fe(N_2)][Na(12-C-4)_2]$ was collected as a red microcrystalline powder after washing with 3 x 2 mL portions of pentane. The isolated product displayed spectroscopic signatures identical to the unlabeled material by IR, ¹H NMR, and X-Band CW-EPR spectroscopies. (note: Et₂O and Pentane were additionally dried by passage through a short pipette column of activated alumina prior to use). Yield: 121.7 mg (30.9 %).

$(^{Ar}P_3B)Fe(OTf)$: 99.4 mg (0.064 mmol) $(^{Ar}P_3B)Fe(N_2)$ was dissolved in Et₂O (ca. 5 mL) and chilled to -78 °C. Upon chilling the solution was added dropwise to a stirring suspension of $[FeCp_2][OTf]$ (21.3 mg, 0.064 mmol) at -78 °C and stirred for 1 hour. The solution turned from deep forest green to orange-brown and was allowed to warm to room temperature while stirring for an additional 2 hours. All volatiles were removed *in vacuo* leaving a tan solid. This solid was slurried in pentane and filtered to remove FeCp₂, leaving behind $(^{Ar}P_3B)Fe(OTf)$ as a tan solid. X-ray diffraction quality crystals were grown from vapor diffusion of a concentrated THF solution into HMDSO. ¹H NMR (300 MHz, C₆D₆, 298 K) δ 32.58 (s, br), 27.28 (s, br), 3.69 (s, br), 3.59 (s, br), 3.31 (s, br), 2.88 (s, br), 2.28 (s,

br), 1.42-0.12 (m, br), -2.97 (s, br), -27.31 (s, br). ^{19}F NMR (282 MHz, C_6D_6 , 298 K) δ - 27.70 (s, br).

$(^{\text{Ar}}\text{P}_3\text{B})\text{Fe}(\text{NNSiMe}_3)$: 81.2 mg (50.2 μmol) $(^{\text{Ar}}\text{P}_3\text{B})\text{FeBr}$ and 7.0 μL (55.0 μmol) Me_3SiCl were combined in ca. 7 mL THF. Freshly prepared 1% Na/Hg (3.0 eq.) was added and the mixture was stirred vigorously for 3 hours) resulting in a dark red-brown solution. Volatiles were removed *in vacuo* and the reaction mixture was stirred vigorously in ca. 7 mL benzene for an additional 3 hours giving a dark green-brown solution. This solution was filtered through Celite and lyophilized, giving a fine dark green-brown powder. Yield 77.2 mg (94.0 %). ^1H NMR (300 MHz, C_6D_6) δ 11.31 (s, br), 3.23 (s, br), 2.93 (s, br), 2.63 (s, br), 0.68 (s, br), -0.97 (s, br), -2.33 (s, br). (note: this compound is nearly NMR silent at 25 $^\circ\text{C}$ and signals can only be clearly observed in very concentrated solutions (~ 120 mM). This compound slowly decomposes over time in solution and in the solid state to give $(^{\text{Ar}}\text{P}_3\text{B})\text{Fe}(\text{N}_2)$ and hexamethyldisilane and attempts to crystallize this compound resulted in near quantitative recovery of $(^{\text{Ar}}\text{P}_3\text{B})\text{Fe}(\text{N}_2)$. However, the IR and ^{57}Fe Mössbauer spectra of freshly prepared samples generated by the above method show either no component or a very small component of $(^{\text{Ar}}\text{P}_3\text{B})\text{Fe}(\text{N}_2)$. Additionally, no other species were detected in the crude material by ^1H or ^{31}P NMR. As such this material is best used freshly prepared and purity should be evaluated by IR, ^1H and ^{31}P spectroscopies. IR(thin film from C_6H_6 , 298 K) $\nu_{\text{N}_2} = 1717\text{ cm}^{-1}$.

Generation of $(^{\text{Ar}}\text{P}_3\text{B})\text{FeNNH}$: In a typical experiment 5.4 mg (2.8 μmol) of $[(^{\text{Ar}}\text{P}_3\text{B})\text{Fe}(\text{N}_2)][\text{Na}(12\text{-C-4})_2]$ was dissolved in 150 μL 2-MeTHF and transferred into a 4 mm diameter quartz EPR tube and frozen in the glovebox cold well cooled with a liquid nitrogen bath. 2.9 mg $\text{HBAr}^{\text{F}}_{24}$ (2.9 μmol) was dissolved in 150 μL thawing 2-MeTHF and

the acid solution was layered into the EPR tube and allowed to freeze. The two layers were then mechanically mixed for a period of 30 minutes with a stainless steel needle in the EPR tube keeping intermittent contact with the chilled sides of the cold well to keep the solutions at or near -135 °C. The resulting brown solutions were then analyzed by EPR methods. Alternative preparations using excesses of $\text{HBAr}^{\text{F}}_{24}$ (up to 5 equivalents) and HOTF (up to 20 equivalents) yielded identical spectroscopic signatures as judged by CW-X-band EPR.

Generation of $[(^{\text{Ar}}\text{P}_3\text{B})\text{Fe}(\text{NNH}_2)][\text{BAr}^{\text{F}}_{24}]$: In a typical experiment 5.4 mg (2.8 μmol) of $[(^{\text{Ar}}\text{P}_3\text{B})\text{Fe}(\text{N}_2)][\text{Na}(12\text{-C-4})_2]$ was dissolved in 150 μL 2-MeTHF and transferred into a 4 mm diameter quartz EPR tube and frozen in the glovebox cold well cooled with a liquid nitrogen bath. 6.0 mg $\text{HBAr}^{\text{F}}_{24}$ (5.9 μmol) was dissolved in 150 μL thawing 2-MeTHF and the acid solution was layered into the EPR tube and allowed to freeze. The two layers were then mechanically mixed for a period of 15 minutes with a stainless steel needle in the EPR tube, keeping intermittent contact with the chilled sides of the cold well to keep the solutions at or near -135 °C. The resulting brown solutions were then warmed to -78 °C for 3 minutes, flash frozen in liquid N_2 , and analyzed by EPR methods. Alternative preparations using excesses of $\text{HBAr}^{\text{F}}_{24}$ (up to 5 equivalents) yielded identical spectroscopic signatures as judged by CW-X-band EPR.

Table 4.S1: XRD experimental parameters for (^{Ar}P₃B)FeBr, (^{Ar}P₃B)Fe(N₂),
(^{Ar}P₃B)Fe(OTf)

Compound	(^{Ar} P ₃ B)FeBr	(^{Ar} P ₃ B)Fe(N ₂)	(^{Ar} P ₃ B)Fe(OTf)
Chemical Formula	C ₉₆ H ₁₂₆ BO ₆ P ₃ FeBr	C ₉₆ H ₁₂₆ Fe(N ₂)•C ₅ H ₁₂	C ₉₇ H ₁₂₆ BF ₃ O ₉ P ₃ SFe
Formula Weight	1615.44	1635.70	1684.60
<i>T</i> (K)	100(2)K	100(2)K	100(2)K
λ (Å)	1.54178	0.71073	1.54178
Space Group	P-1	P-1	P2 ₁ /C
<i>a</i>	13.3439(11)	11.8779(8)	27.2077(10)
<i>b</i>	13.9184(11)	14.7827(9)	25.6324(10)
<i>c</i>	25.1806(19)	27.0968(17)	13.4428(5)
α	93.843(5)	86.055(3)	90
β	90.086(5)	81.569(3)	94.115(2)
γ	109.902(5)	89.245(3)	90
Volume	4386.0(6)	4695.3(5)	9350.8(6)
<i>Z</i>	2	2	4
Density (calc)	1.223	1.157	1.197
R1, wr2	0.1122, 0.2874	0.1263, 0.1623	0.1007, 0.2149
$R1 = \sum F_o - F_c / \sum F_o , wR2 = \{ \sum [w(F_o^2 - F_c^2)^2] / \sum w(F_o^2)^2 \}^{1/2}$			

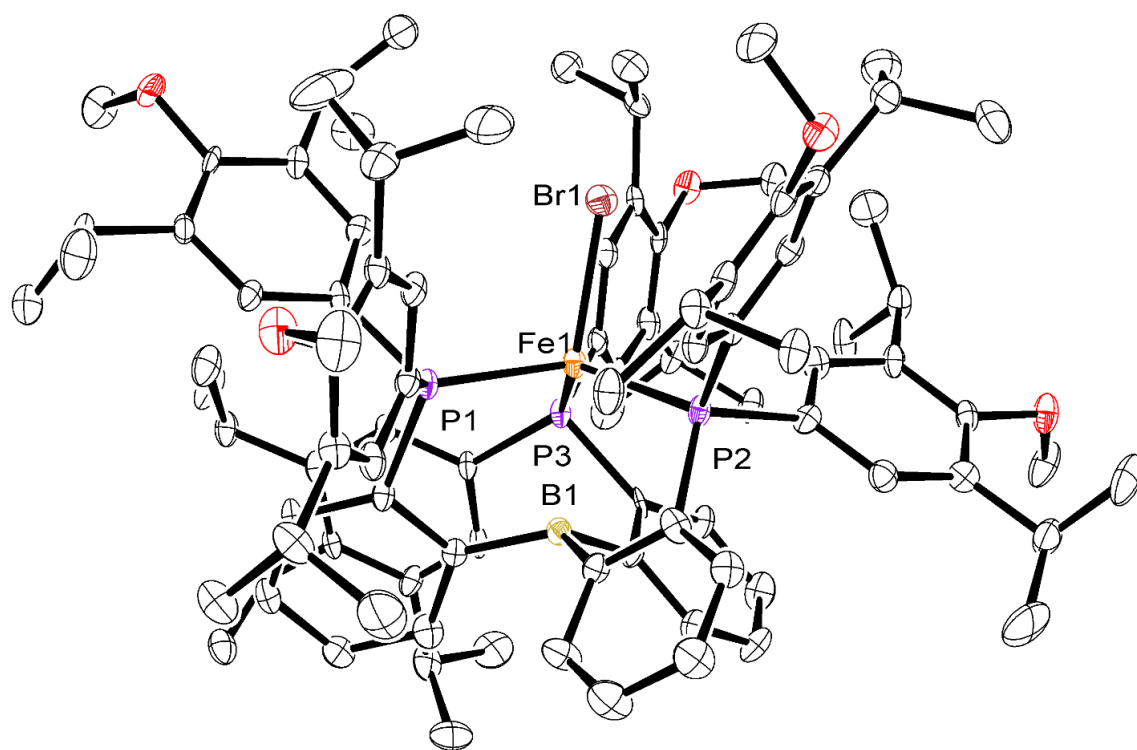


Figure 4.S1: ORTEP representation of $(^{\text{Ar}}\text{P}_3\text{B})\text{FeBr}$ (H atoms omitted for clarity). Thermal ellipsoids are drawn at the 50% probability level.

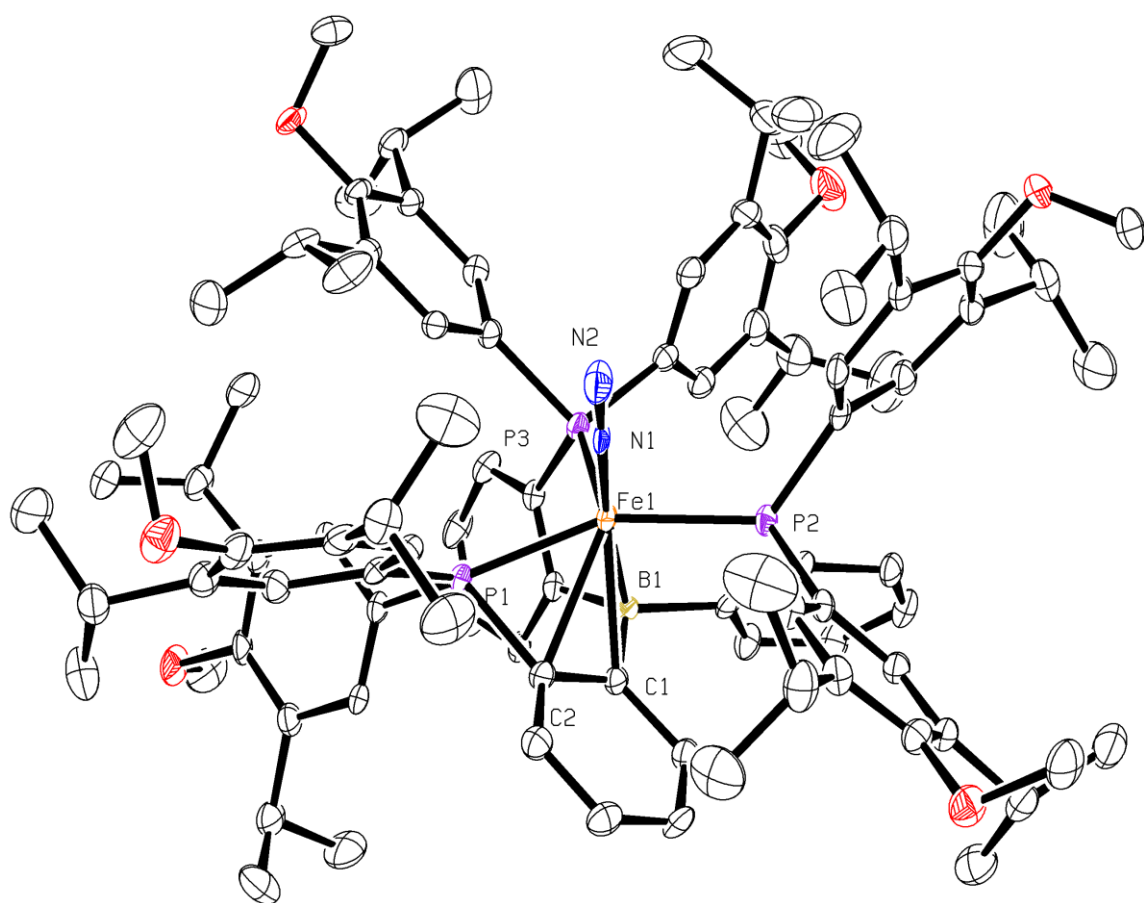


Figure 4.S2: ORTEP representation of (^{Ar}P₃B)Fe(N₂) (H atoms omitted for clarity and a pentane solvent molecule). Thermal ellipsoids are drawn at the 50% probability level.

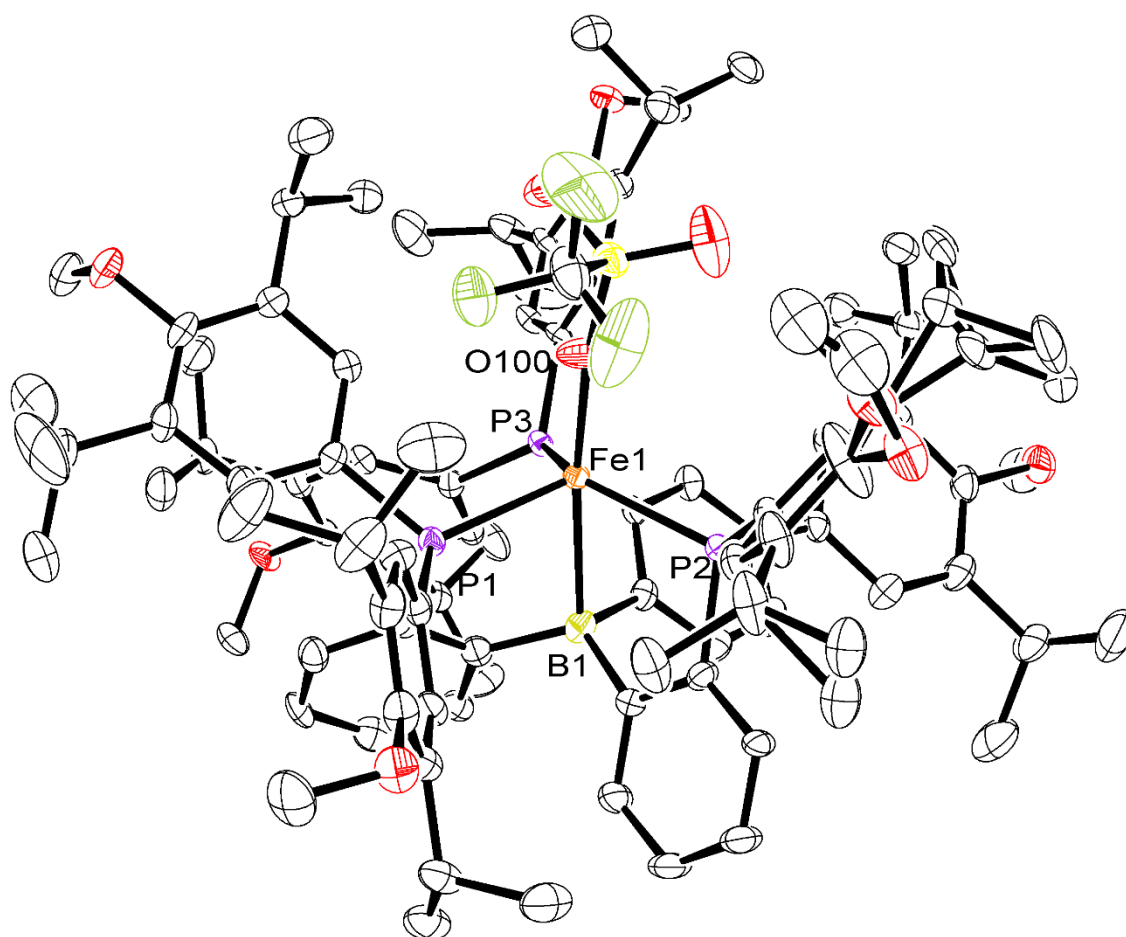


Figure 4.S3: ORTEP representation of $(^{\text{Ar}}\text{P}_3\text{B})\text{FeOTf}$ (H atoms omitted for clarity). Thermal ellipsoids are drawn at the 50% probability level.

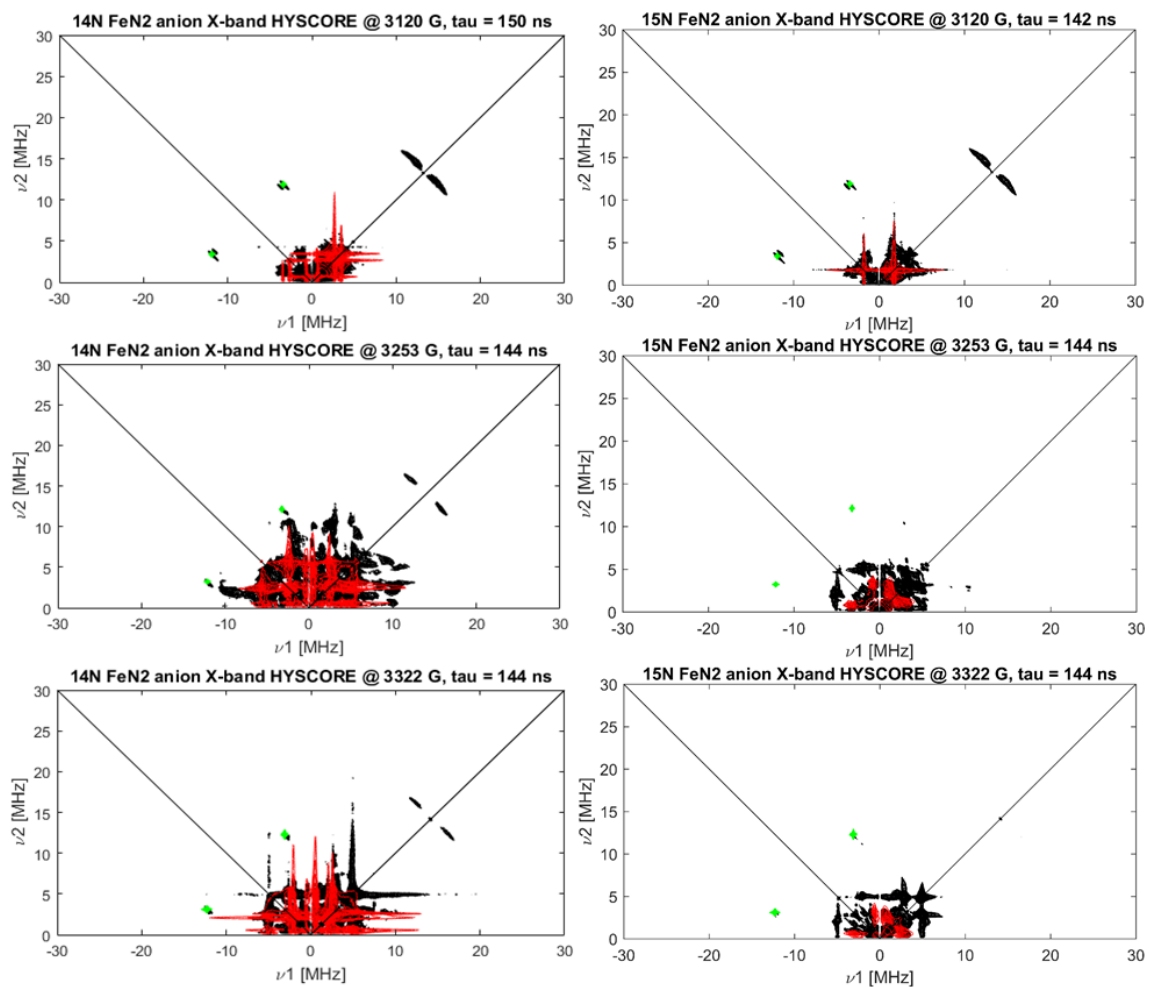


Figure 4.S4: Comparison of field dependent X-band HYSCORE spectra and simulations of $[(^{\text{Ar}}\text{P}_3\text{B})\text{Fe}(\text{N}_2)][\text{Na}(12\text{-C-4})_2]$ (left) and $[(^{\text{Ar}}\text{P}_3\text{B})\text{Fe}(^{15}\text{N}_2)][\text{Na}(12\text{-C-4})_2]$ (right). (9.414 GHz, 20K). (Experimental data is in black, ^{14}N or ^{15}N is in red, ^{11}B is in green).

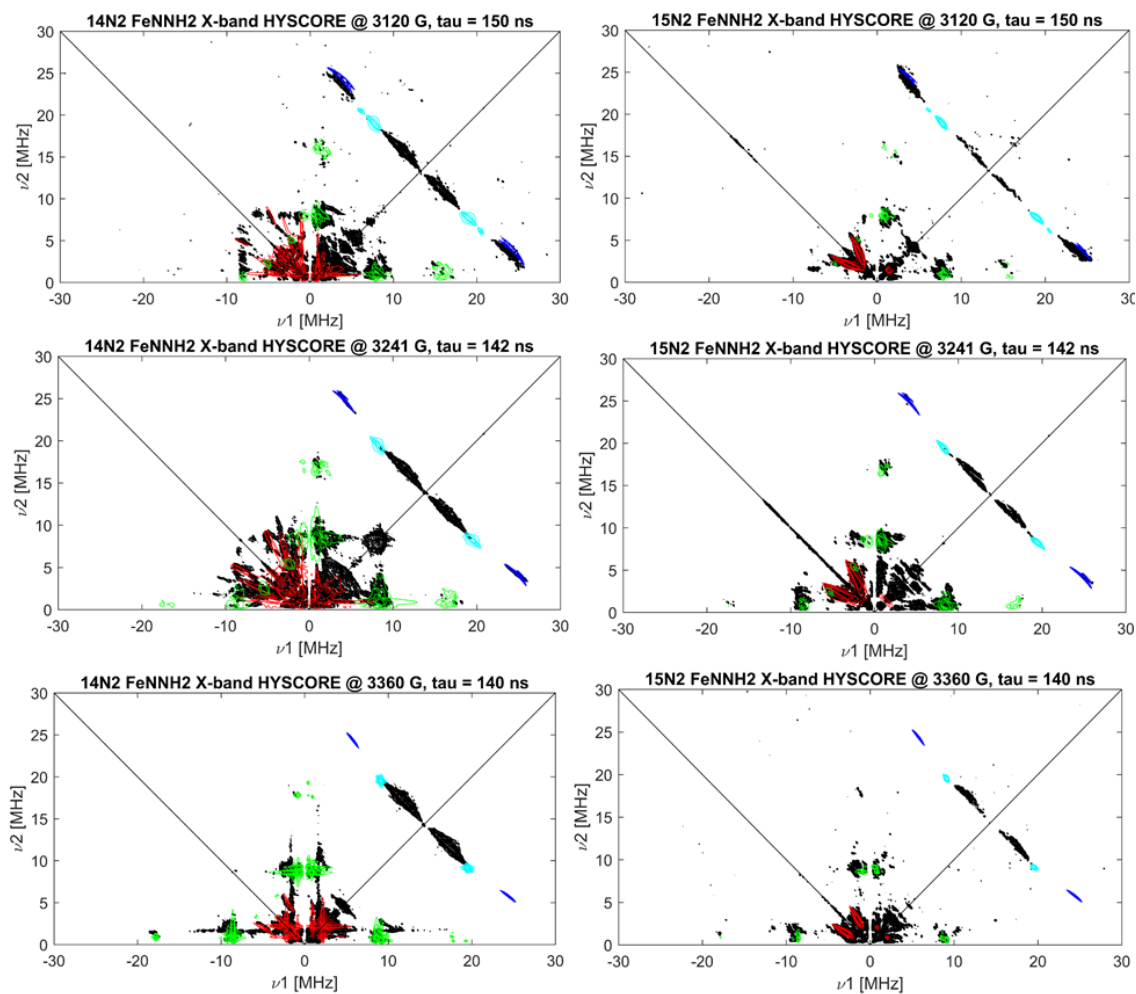


Figure 4.S5: Comparison of field dependent X-band HYSCORE spectra and simulations of $[(^{\text{Ar}}\text{P}_3\text{B})\text{Fe}(\text{NNH}_2)][\text{BAr}^{\text{F}}_{24}]$ (left) and $[(^{\text{Ar}}\text{P}_3\text{B})\text{Fe}(^{15}\text{N}^{15}\text{NH}_2)][\text{BAr}^{\text{F}}_{24}]$ (right) (Experimental data is in black, ^{14}N or ^{15}N is in red, ^{11}B is in green, ^1H is in dark and light blue).

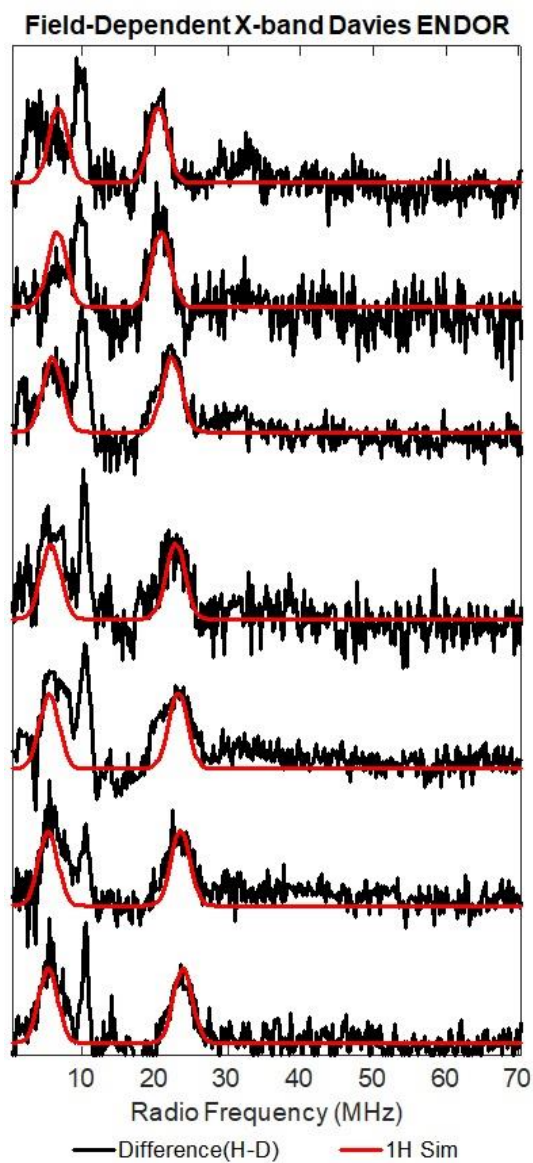


Figure 4.S6: Difference of field dependent ENDOR spectra of ($^{Ar}P_3B$)Fe(NNH) and ($^{Ar}P_3B$)Fe(NND) and simulations. (Experimental Parameters: Temperature = 10 K; MW Frequency = 9.72 GHz; MW Pulse Length ($\pi/2$, π) = 20 ns, 40 ns; RF Pulse Length = 15 μ s; Shot Rep Time 5000 = μ s; τ = 240 ns).

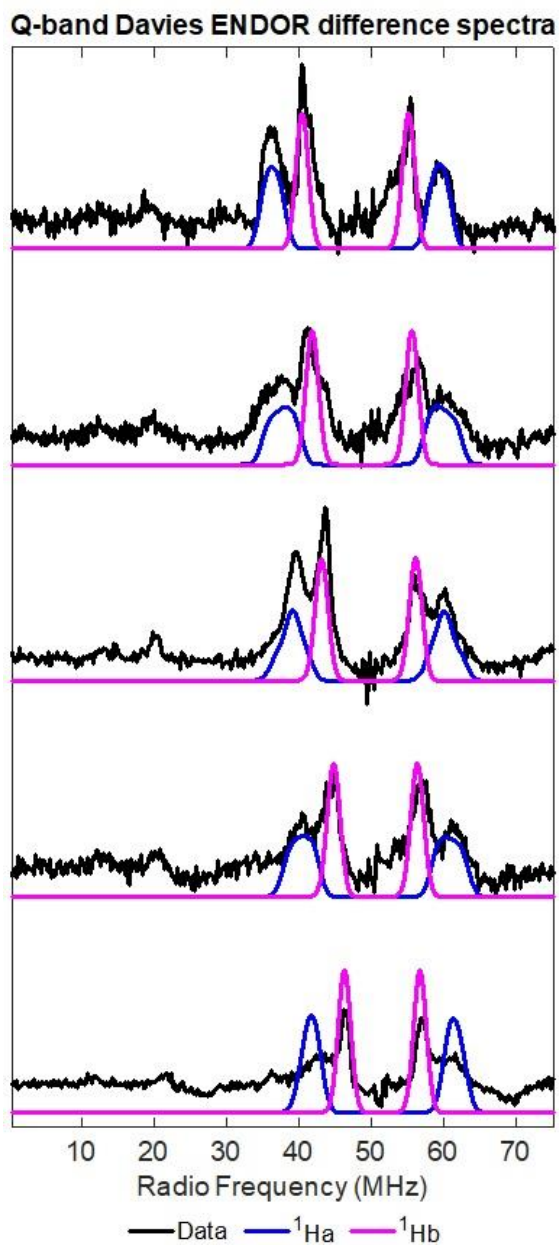


Figure 4.S7: Difference of field dependent ENDOR spectra of $[(^A\text{P}_3\text{B})\text{Fe}(\text{NNH}_2)]\text{BAr}^{\text{F}}_{24}$ and $[(^A\text{P}_3\text{B})\text{Fe}(\text{NND}_2)]\text{BAr}^{\text{F}}_{24}$ and simulations. (Experimental Parameters: Temperature = 10 K; MW Frequency = 33.60 GHz; MW Pulse Length ($\pi/2$, π) = 20 ns, 40 ns; RF Pulse Length = 15 μs ; Shot Rep Time = 5000 μs ; τ = 240 ns).

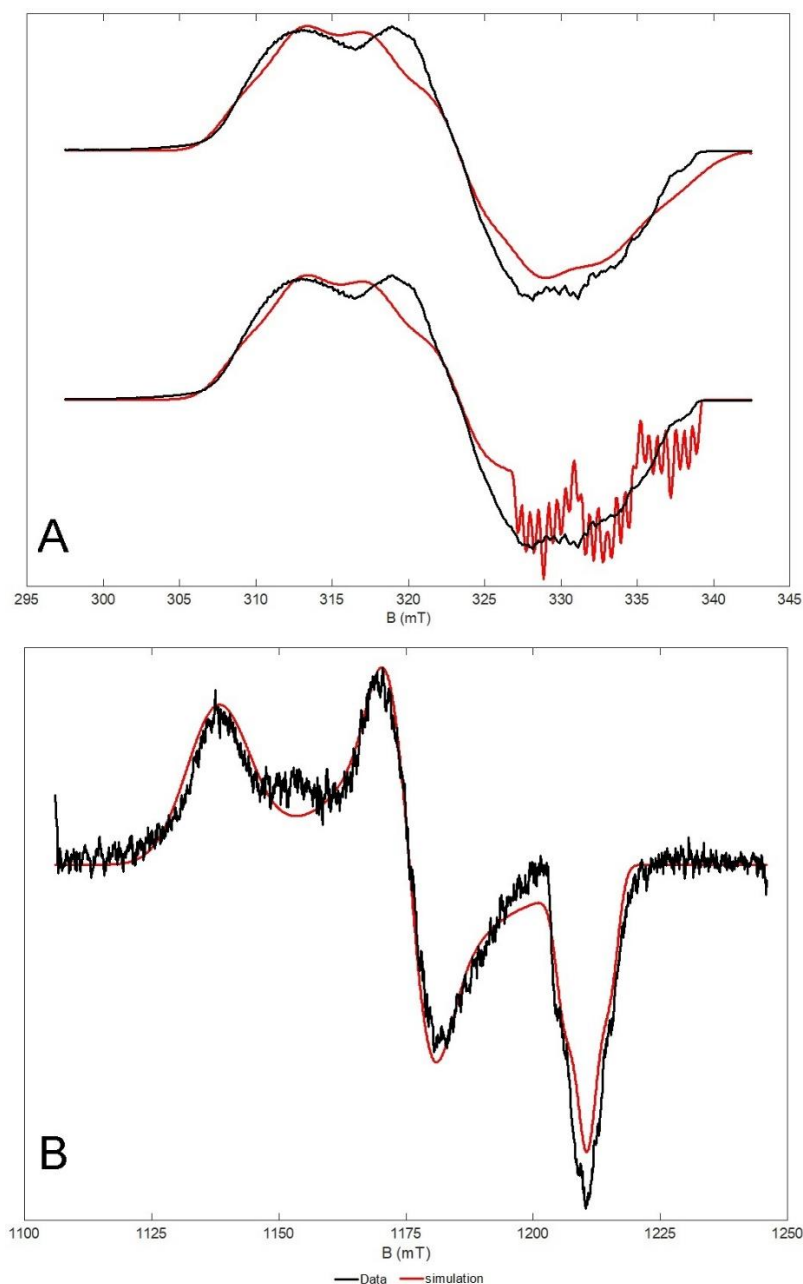


Figure 4.S8: A: (Top): CW X-Band EPR spectrum of $[(^A\text{rP}_3\text{B})\text{Fe}(\text{N}_2)][\text{Na}(12\text{-C-4})_2]$ with simulation capturing overall line shape (77 K, 2-MeTHF, 9.387 GHz). g : [2.143 2.074 2.014]. HStrain (MHz): [95 86 114]. gStrain (MHz): [0.0003 0.003 0.0002]. A: (Bottom): CW X-Band EPR spectrum of $[(^A\text{rP}_3\text{B})\text{Fe}(\text{N}_2)][\text{Na}(12\text{-C-4})_2]$ with simulation capturing fine structure at the highest field g value (77 K, 2-MeTHF, 9.387 GHz). g : [2.143 2.074 2.014]. HStrain (MHz): [95 86 1]. gStrain (MHz): [0.0003 0.003 0.002]. B: Pseudo-modulated Q-Band EPR spectrum of $[(^A\text{rP}_3\text{B})\text{Fe}(\text{N}_2)][\text{Na}(12\text{-C-4})_2]$ with simulation (15 K, 2-MeTHF, 34.122 GHz). g : [2.143 2.073 2.014]. Line Width: 3.2 (MHz). HStrain (MHz): [380 220 9]. gStrain (MHz): [0.0005 0.0003 0.0001].

Notes on simulation of the CW X-band EPR spectrum of $[(^{\text{Ar}}\text{P}_3\text{B})\text{Fe}(\text{N}_2)][\text{Na}(\text{12-C-4})_2]$: We were unable to generate a simulated spectrum which adequately fits the CW X-band EPR spectrum of $[(^{\text{Ar}}\text{P}_3\text{B})\text{Fe}(\text{N}_2)][\text{Na}(\text{12-C-4})_2]$ at the highest field g value. To address this we have included two simulations, one which captures the overall line shape (Figure 4.S8A top) but does not capture the fine structure which can be observed in the experimental spectrum from ~326mT to 340 mT. In the first simulation (Figure 4.S8A bottom) included an additional simulation with much narrower line broadenings which shows that this fine structure aligns nicely with the simulated splitting from the three ^{31}P nuclei and ^{11}B . We have also included a pseudo-modulated spectrum (Figure 4.S8B) generated from a Q-band 2-pulse field sweep (34.12 GHz, 15 K) which is well simulated using the same g values and hyperfine couplings as the X-band data.

We attribute the broad linewidths observed to inhomogeneity in the ^{31}P couplings. The effects of this can be observed in the ENDOR data for $[(^{\text{Ar}}\text{P}_3\text{B})\text{Fe}(\text{N}_2)][\text{Na}(\text{12-C-4})_2]$ where the ^{31}P peaks are much broader than the relatively sharp ^{11}B peaks. One possible origin for the inhomogeneity and broadness is the presence of an isoelectronic species $[(^{\text{Ar}}\text{P}_3\text{B})\text{Fe}(\text{L})][\text{Na}(\text{12-C-4})_2]$ where L is either a vacant coordination site or a solvent molecule (although we think a solvent is unlikely due to the steric bulk of both the $^{\text{Ar}}\text{P}_3\text{B}$ ligand and 2-MeTHF). The fact that the $^{15}\text{N}_2$ ligand is exchanged for $^{14}\text{N}_2$ in solution even at low temperatures (-135 to -78 °C) is consistent with a labile N_2 ligand that may be replaced via a dissociative mechanism generating $[(^{\text{Ar}}\text{P}_3\text{B})\text{Fe}][\text{Na}(\text{12-C-4})_2]$ as an intermediate which has similar EPR parameters to the species shown in our simulations.

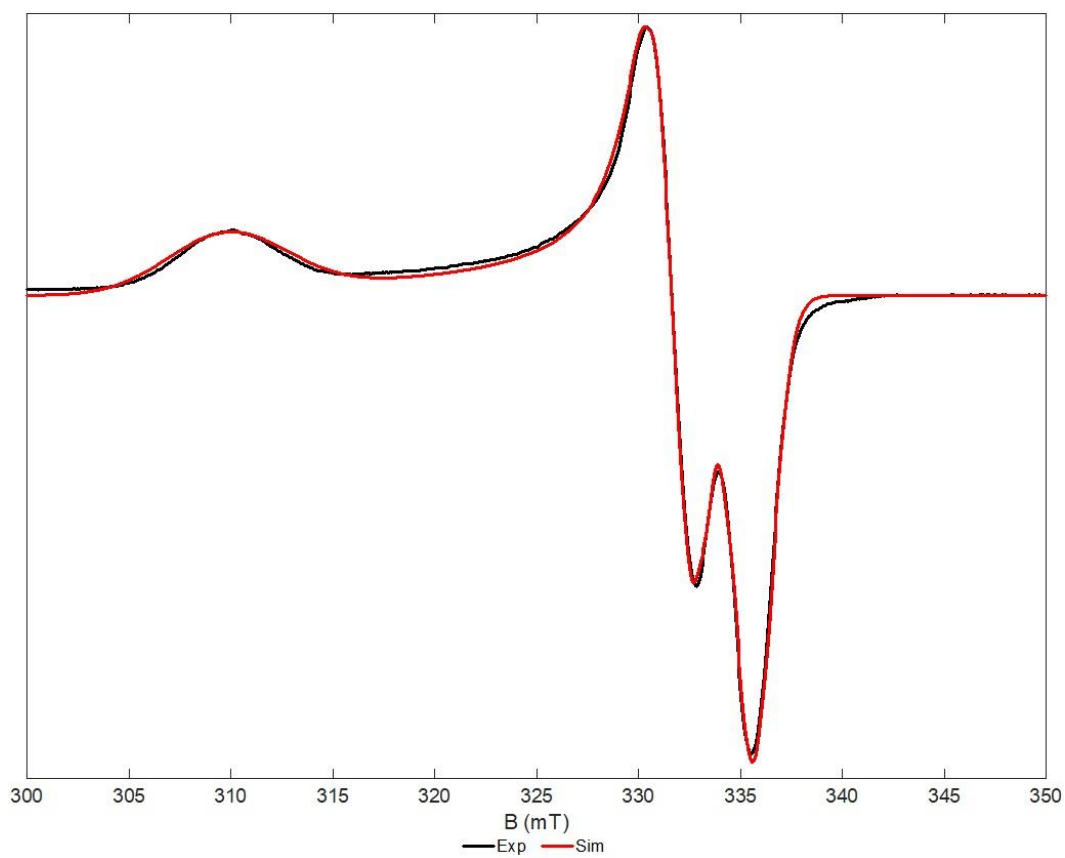


Figure 4.S9: CW X-Band EPR spectrum of ($^{\text{Ar}}\text{P}_3\text{B}$)Fe(NNH) (77 K, 2-MeTHF, 9.44 GHz). g : [2.1771 2.02317 2.02068]. HStrain (MHz): [182 79 17].

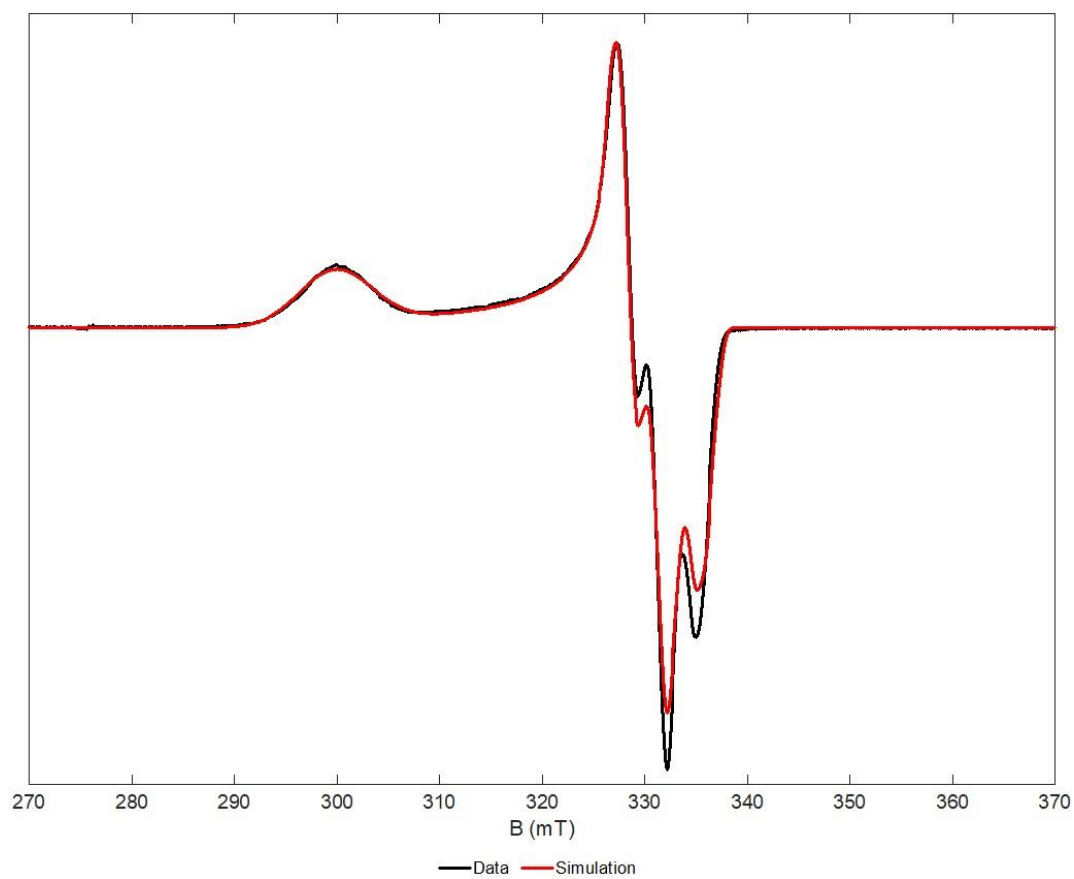


Figure 4.S10: CW X-band EPR spectrum of ($^{Ar}P_3B$)Fe(NNSiMe₃) (77K, 2-MeTHF, 9.37 GHz) g : [2.234 2.03 2.008]. HStrain (MHz): [226 21.3 30].

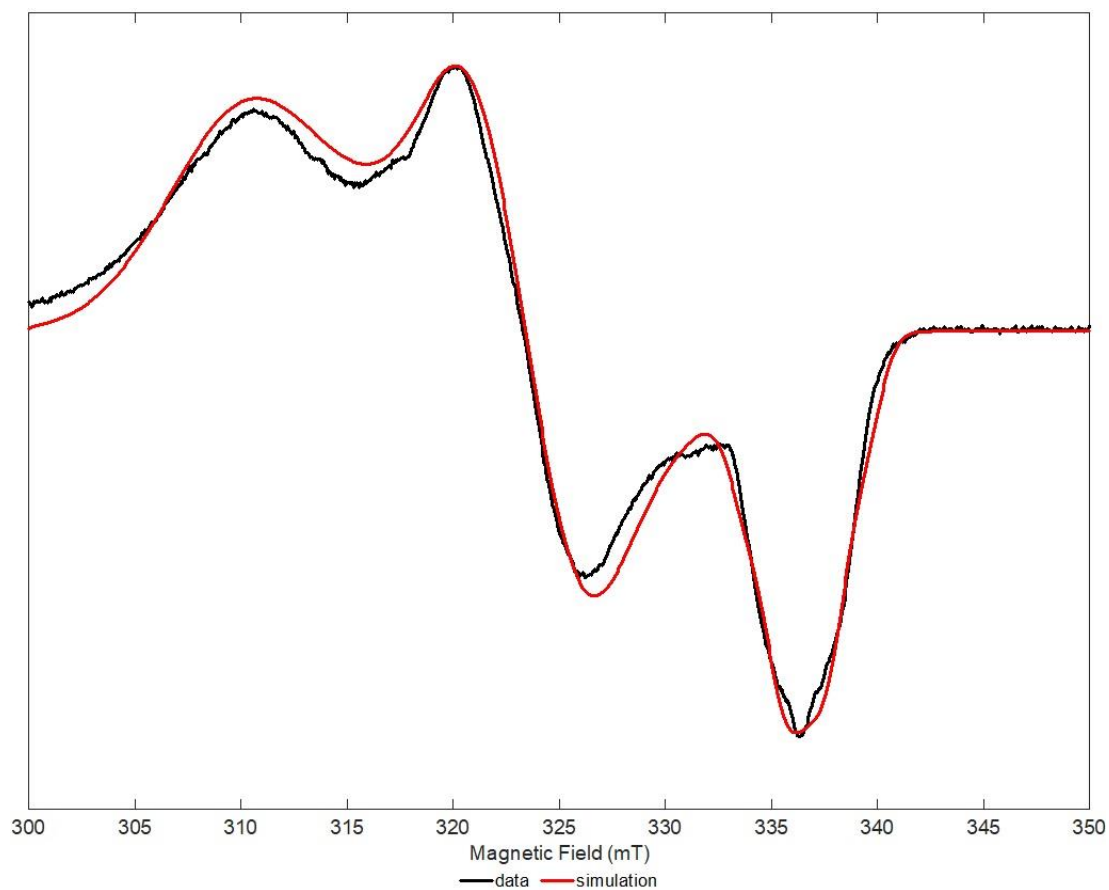


Figure 4.S11: CW X-Band EPR spectrum of $[(^{\text{Ar}}\text{P}_3\text{B})\text{Fe}(\text{NNH}_2)][\text{BAr}^{\text{F}}_{24}]$ (77 K, 2-MeTHF, 9.44 GHz) g : [2.176 2.087 2.004]. HStrain (MHz): [215 105 35].

$$\begin{matrix} A_1 \\ A_2 \\ A_3 \end{matrix} = A_{\text{iso}} + \begin{matrix} A_{1\text{aniso}} \\ A_{2\text{aniso}} \\ A_{3\text{aniso}} \end{matrix}$$

Equation 4.S1: Decomposition of A_{H} into A_{iso} and A_{aniso} components.

$$\begin{matrix} 12 \\ 18.25 \\ 19.25 \end{matrix} = 16.5 + \begin{matrix} -4.5 \\ 1.75 \\ 2.75 \end{matrix}$$

Equation 4.S2: Decomposition of A_{H} into A_{iso} and A_{anis} components for the proton in $(^{\text{Ar}}\text{P}_3\text{B})\text{Fe}(\text{NNH})$.

$$\begin{array}{rcccl} 27 & & & 5.67 & \\ & 21 & & & \\ & 16 & = 21.33 + & -0.33 & \\ & & & & -5.33 \end{array}$$

Equation 4.S3: Decomposition of A_H into A_{iso} and A_{anis} components for the more strongly coupled proton in $[(^{Ar}P_3B)Fe(NNH_2)][BAr^F_{24}]$.

$$\begin{array}{rcccl} 15 & & & 2.17 & \\ & 13.5 & = 12.83 + & 0.67 & \\ & 10 & & & -2.83 \end{array}$$

Equation 4.S4: Decomposition of A_H into A_{iso} and A_{aniso} components for the more weakly coupled proton in $[(^{Ar}P_3B)Fe(NNH_2)][BAr^F_{24}]$.

Table 4.S2: ^{11}B nuclear quadrupole couplings and asymmetry parameters derived from ENDOR and HYSCORE.

Compound	e^2Qq/h (MHz)	η
$[(^{Ar}P_3B)Fe(N_2)][Na(12-C-4)_2]$	0.3	0.1
$(^{Ar}P_3B)Fe(NNH)$	1.0	0.3
$(^{Ar}P_3B)Fe(NNSiMe_3)$	1.0	0.3
$[(^{Ar}P_3B)Fe(NNH_2)][BAr^F_{24}]$	1.0	0.3

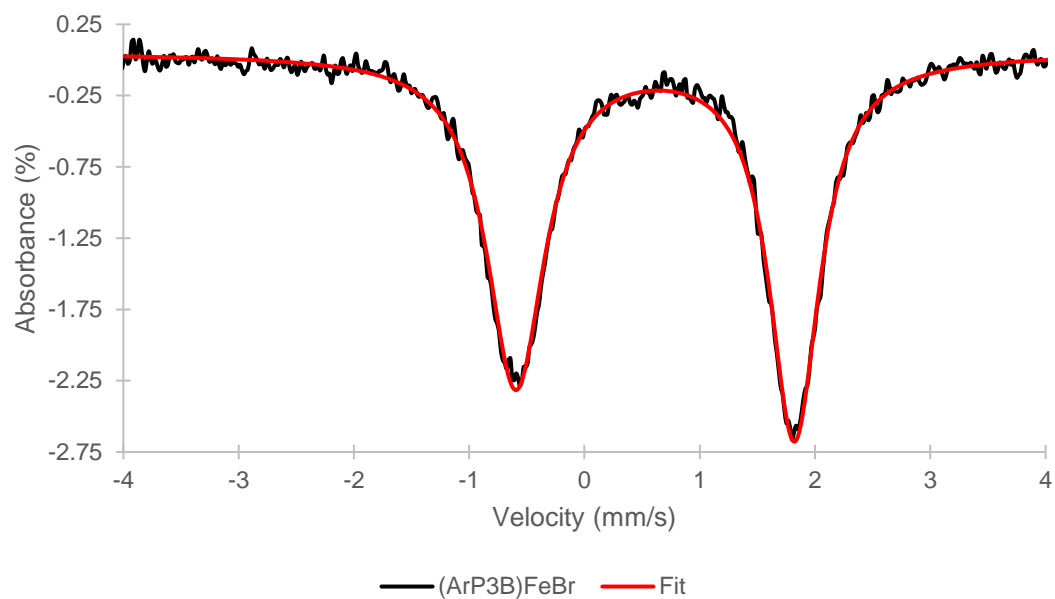


Figure 4.S12: ^{57}Fe Mössbauer spectrum of $(^{\text{Ar}}\text{P}_3\text{B})\text{FeBr}$ (80 K, 2-MeTHF, 50 mT ||) $\delta = 0.61$ mm/s, $\Delta E_{\text{q}} = 2.4$ mm/s.

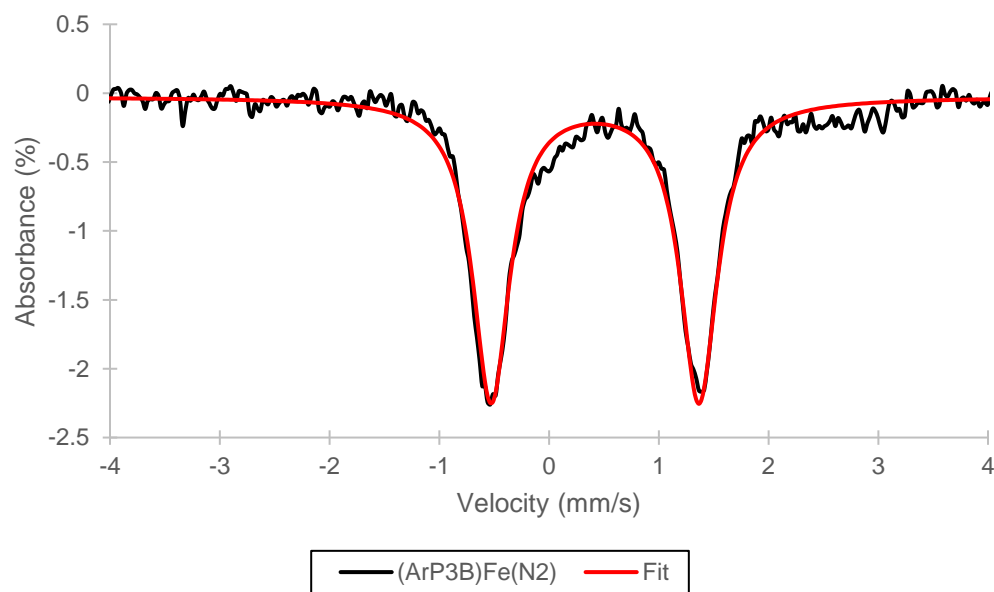


Figure 4.S13: ^{57}Fe Mössbauer spectrum of $(^{\text{Ar}}\text{P}_3\text{B})\text{Fe}(\text{N}_2)$ (80 K, 2-MeTHF, 50 mT ||) $\delta = 0.42$ mm/s, $\Delta E_{\text{q}} = 1.9$ mm/s.

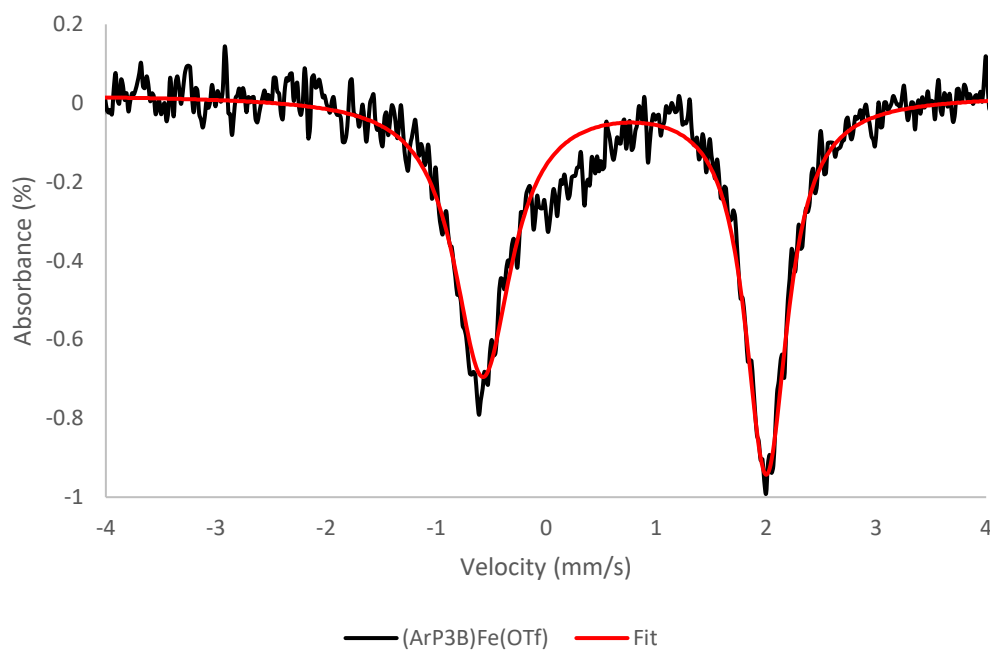


Figure 4.S14: ^{57}Fe Mössbauer spectrum of $(^{\text{Ar}}\text{P}_3\text{B})\text{Fe}(\text{OTf})$ (80 K, 2-MeTHF, 50 mT ||) $\delta = 0.71$ mm/s, $\Delta E_{\text{q}} = 2.6$ mm/s.

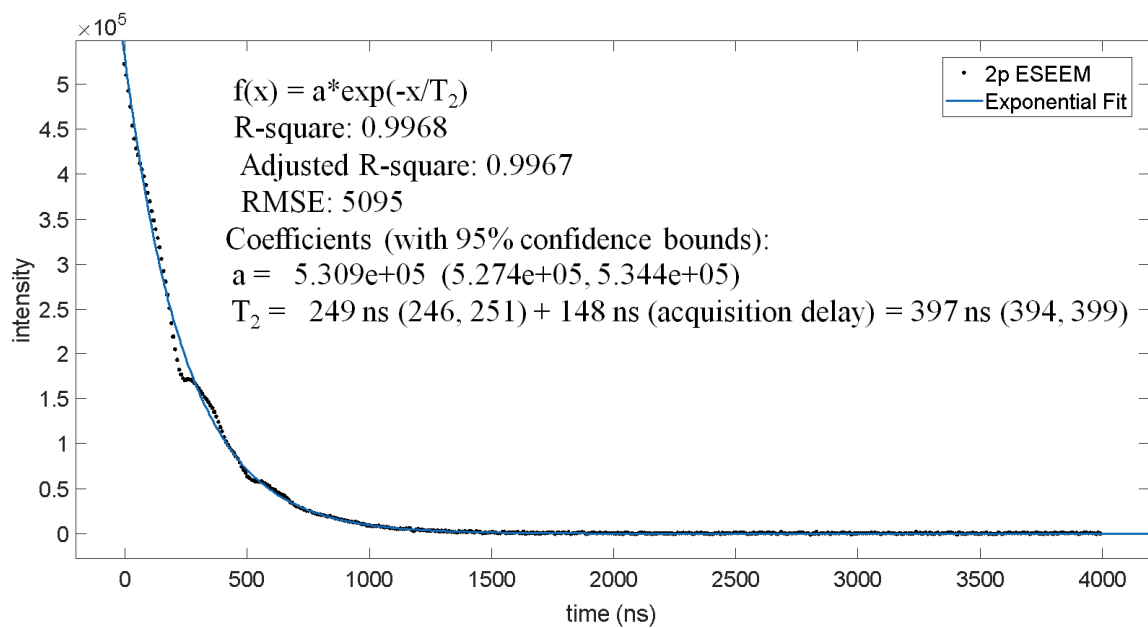


Figure 4.S15: Q-Band 2p-ESEEM trace and exponential fit for T_2 of

$[(^{\text{Ar}}\text{P}_3\text{B})\text{Fe}(^{15}\text{N}_2)][\text{Na}(12\text{-C-}4)_2]$ at 40 K.

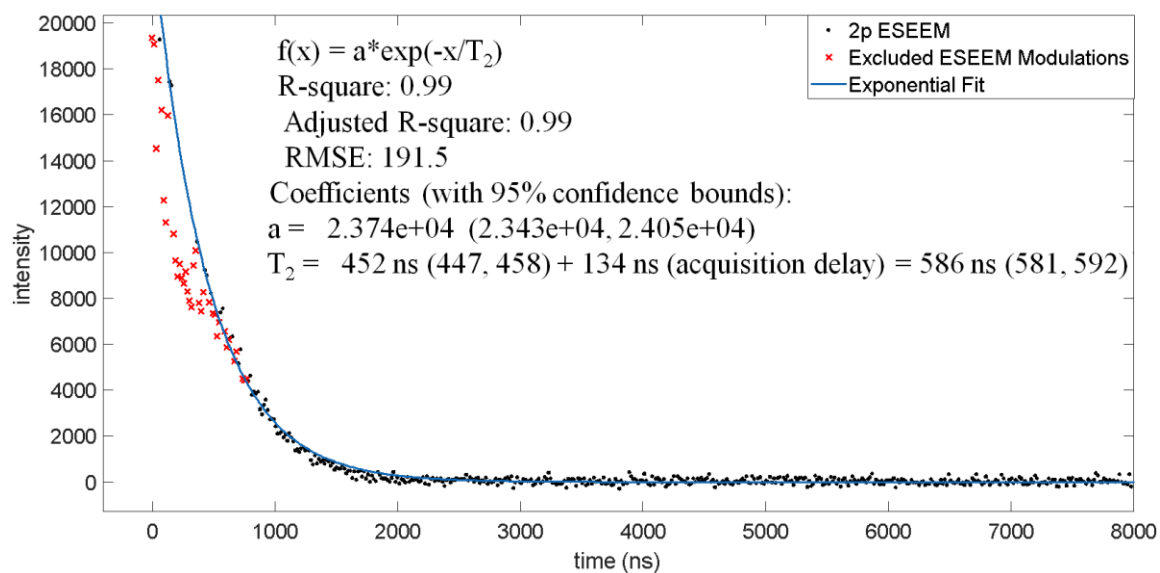


Figure 4.S16: X-Band 2p-ESEEM trace and exponential fit for T_2 of $(^{Ar}P_3B)Fe(NNH)$ at 40 K.

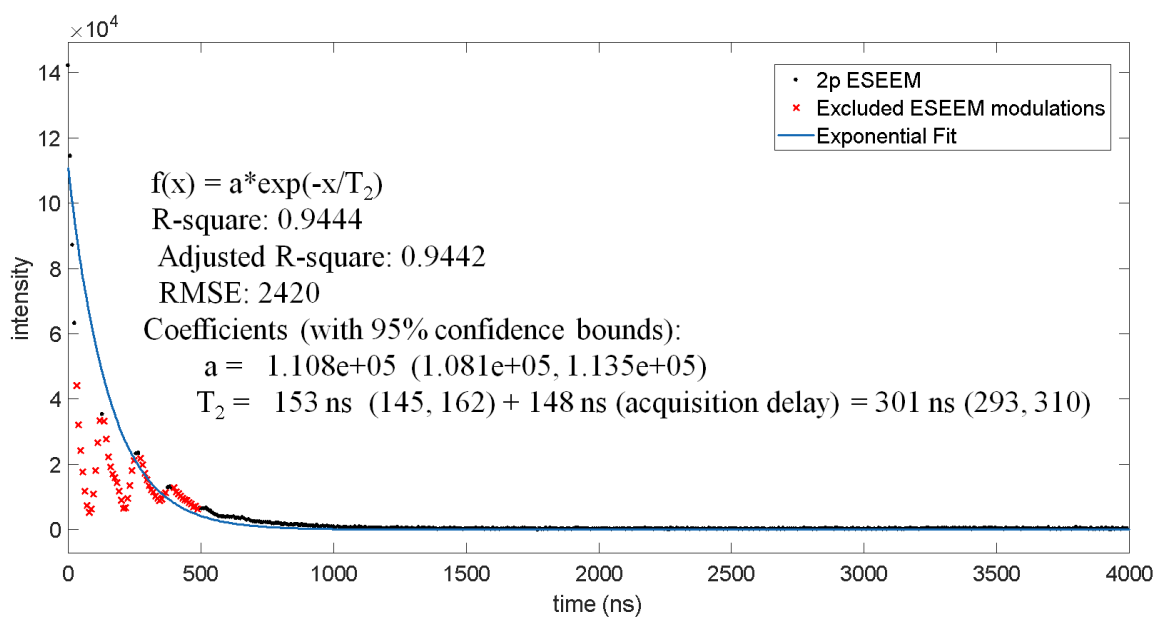


Figure 4.S17: Q-Band 2p-ESEEM trace and exponential fit for T_2 of $(^{Ar}P_3B)Fe(NNSiMe_3)$ at 40 K.

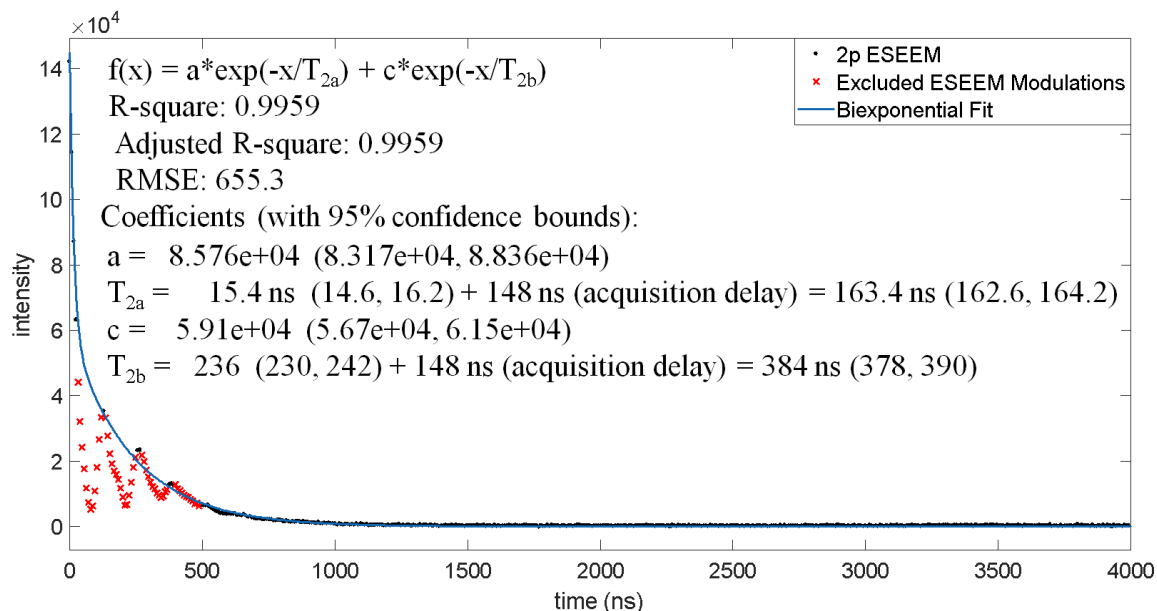


Figure 4.S18: Q-Band 2p-ESEEM trace and alternative biexponential fit for T_2 of

$(^{Ar}P_3B)Fe(NNSiMe_3)$ at 40 K.

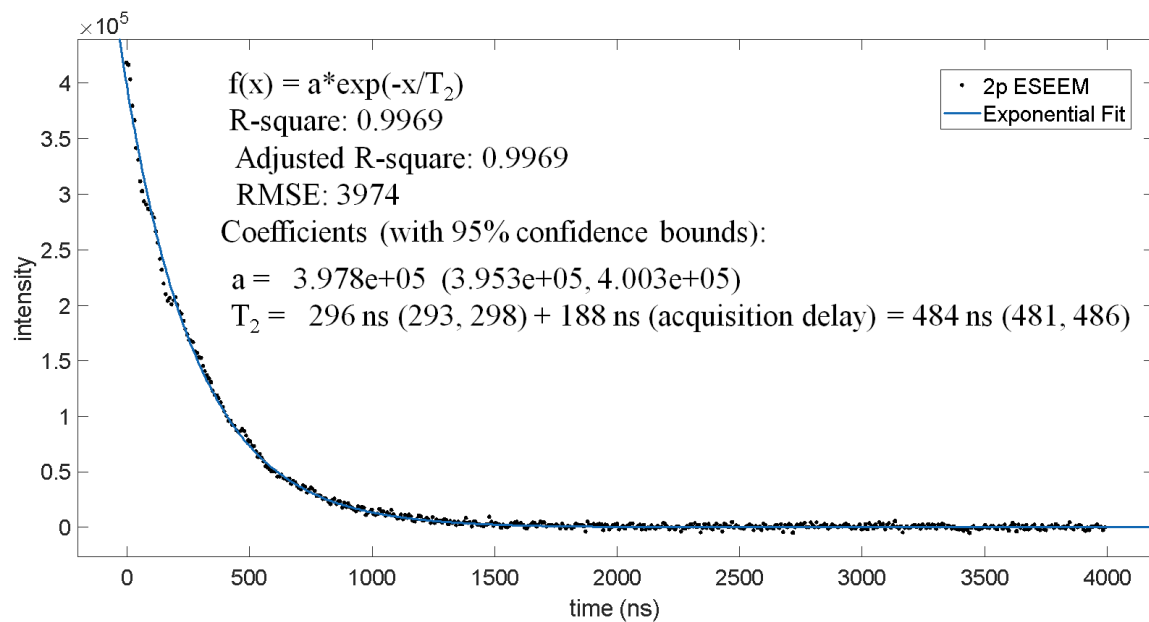


Figure 4.S19: Q-Band 2p-ESEEM trace and exponential fit for T_2 of

$[(^{Ar}P_3B)Fe(^{15}N^{15}NH_2)][BArF_{24}]$ at 40 K.

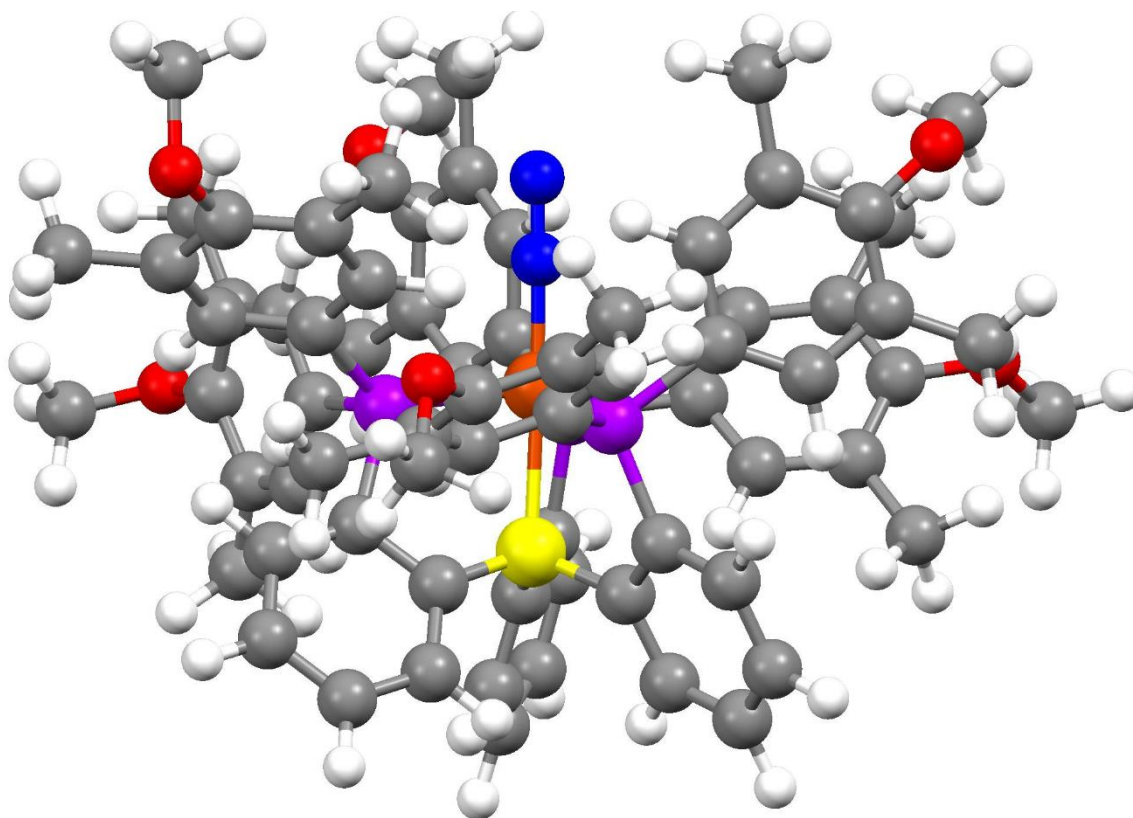


Figure 4.S20: DFT optimized structure of a truncated version of $[(^{\text{Ar}}\text{P}_3\text{B})\text{Fe}(\text{N}_2)]^-$ (TPSS, def2-TZVP on Fe, def2-SVP on all other atoms) (Isopropyl groups on arene rings replaced with methyl groups). (Fe shown in orange, P shown in purple, B shown in yellow, O shown in red, H shown in white, C shown in gray).

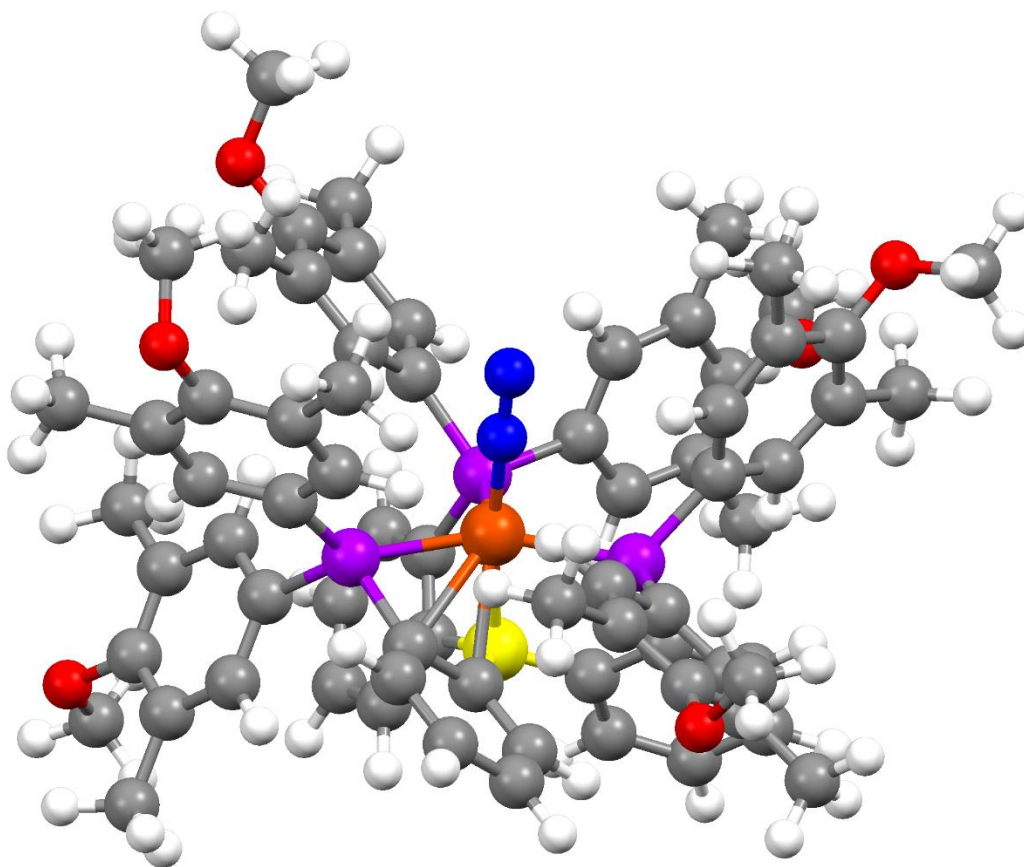


Figure 4.S21: DFT optimized structure of a truncated version of (ArP_3B)Fe(N₂) (TPSS, def2-TZVP on Fe, def2-SVP on all other atoms) (Isopropyl groups on arene rings replaced with methyl groups). (Fe shown in orange, P shown in purple, B shown in yellow, O shown in red, H shown in white, C shown in gray).

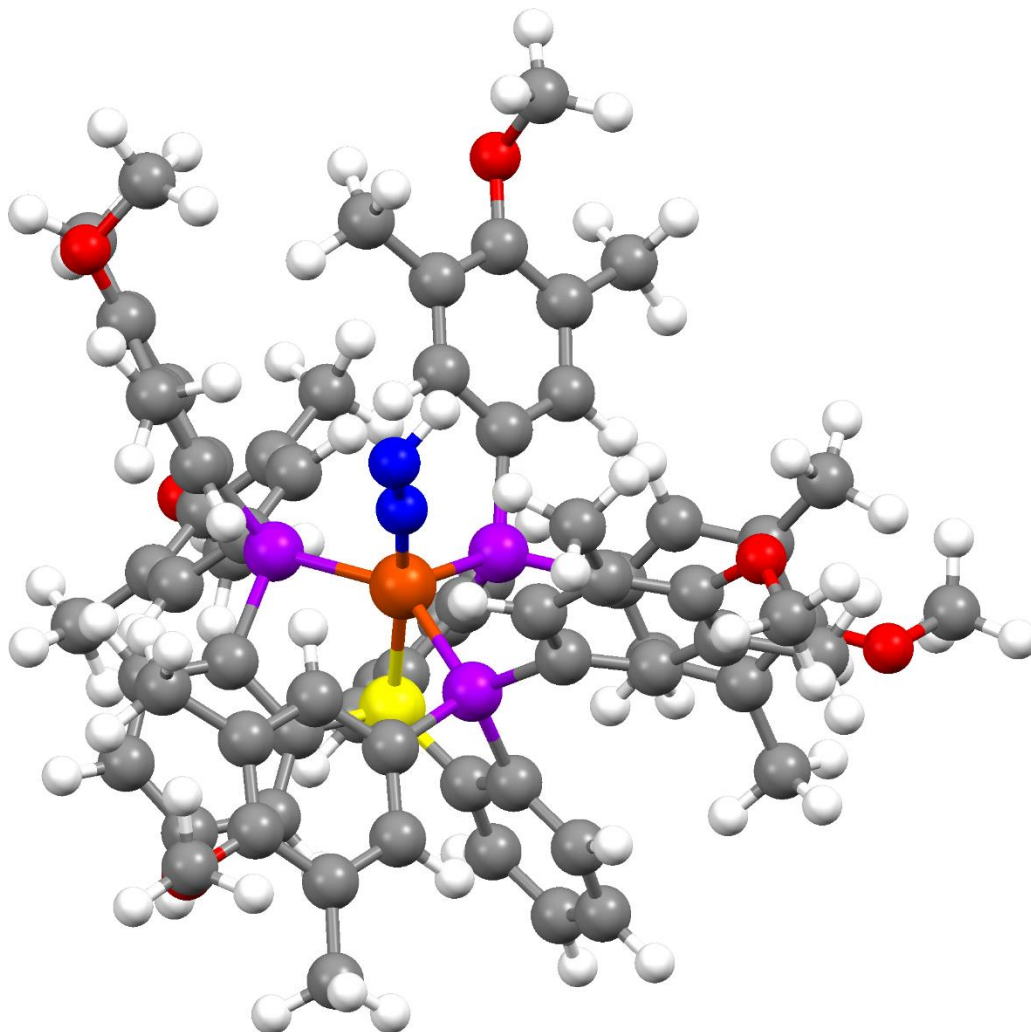


Figure 4.S22: DFT optimized structure of a truncated version of ($^{\text{Ar}}\text{P}_3\text{B}$)Fe(NNH) (TPSS, def2-TZVP on Fe, def2-SVP on all other atoms) (Isopropyl groups on arene rings replaced with methyl groups). Fe shown in orange, P shown in purple, B shown in yellow, O shown in red, H shown in white, C shown in gray.

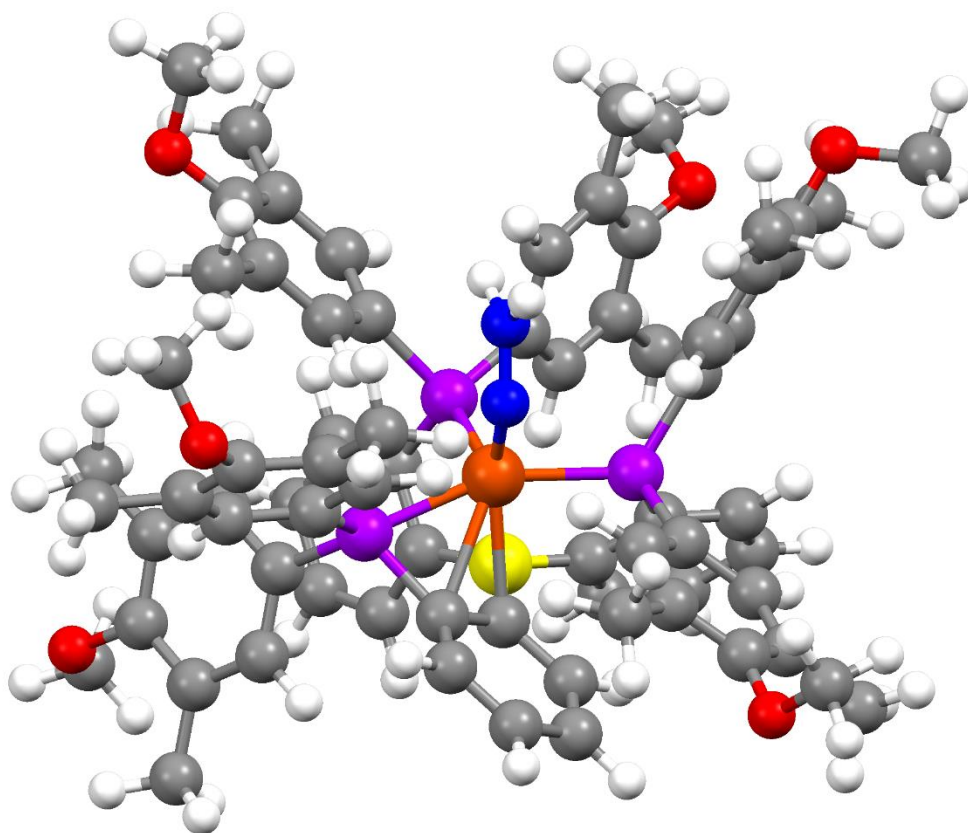


Figure 4.S23: DFT optimized structure of a truncated version of $[(^{\text{Ar}}\text{P}_3\text{B})\text{Fe}(\text{NNH}_2)]^+$ (TPSS, def2-TZVP on Fe, def2-SVP on all other atoms) (Isopropyl groups on arene rings replaced with methyl groups). Fe shown in orange, P shown in purple, B shown in yellow, O shown in red, H shown in white, C shown in gray.

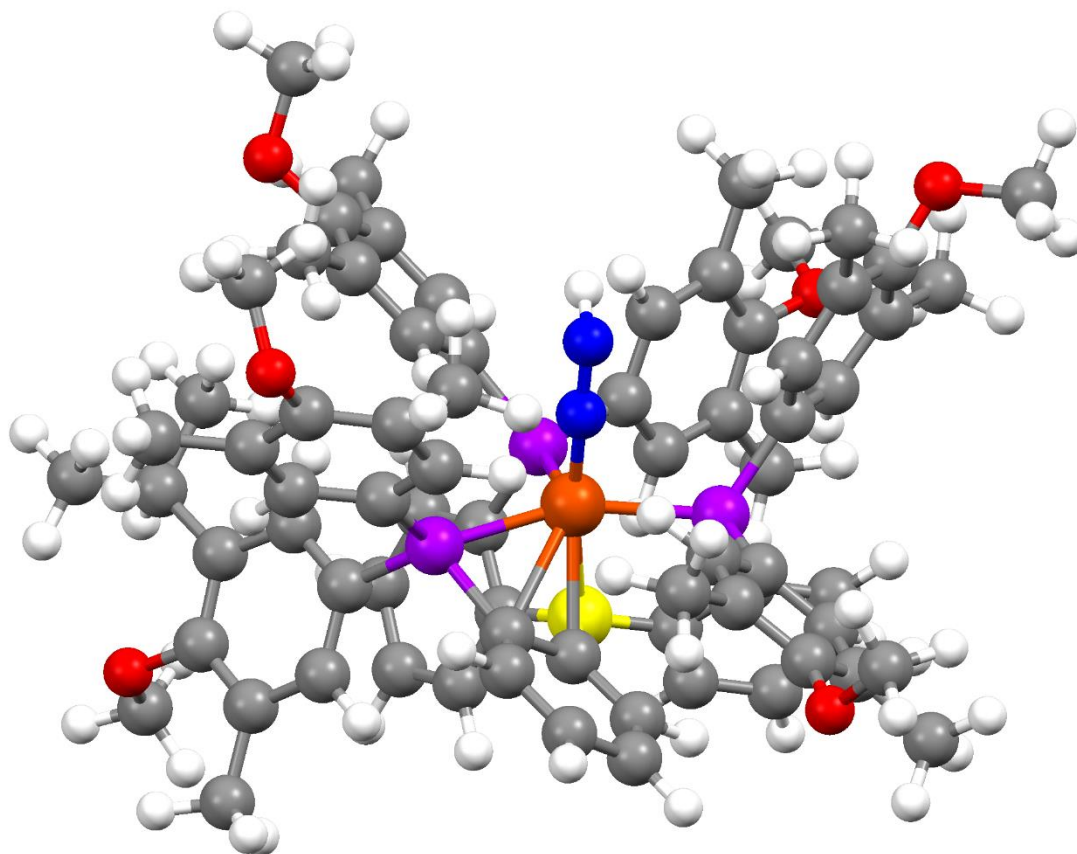


Figure 4.S24: DFT optimized structure of $[(^{\text{Ar}}\text{P}_3\text{B})\text{Fe}(\text{NNH})]^+$ (TPSS, def2-TZVP on Fe, def2-SVP on all other atoms) (Isopropyl groups on arene rings replaced with methyl groups). Fe shown in orange, P shown in purple, B shown in yellow, O shown in red, H shown in white, C shown in gray.

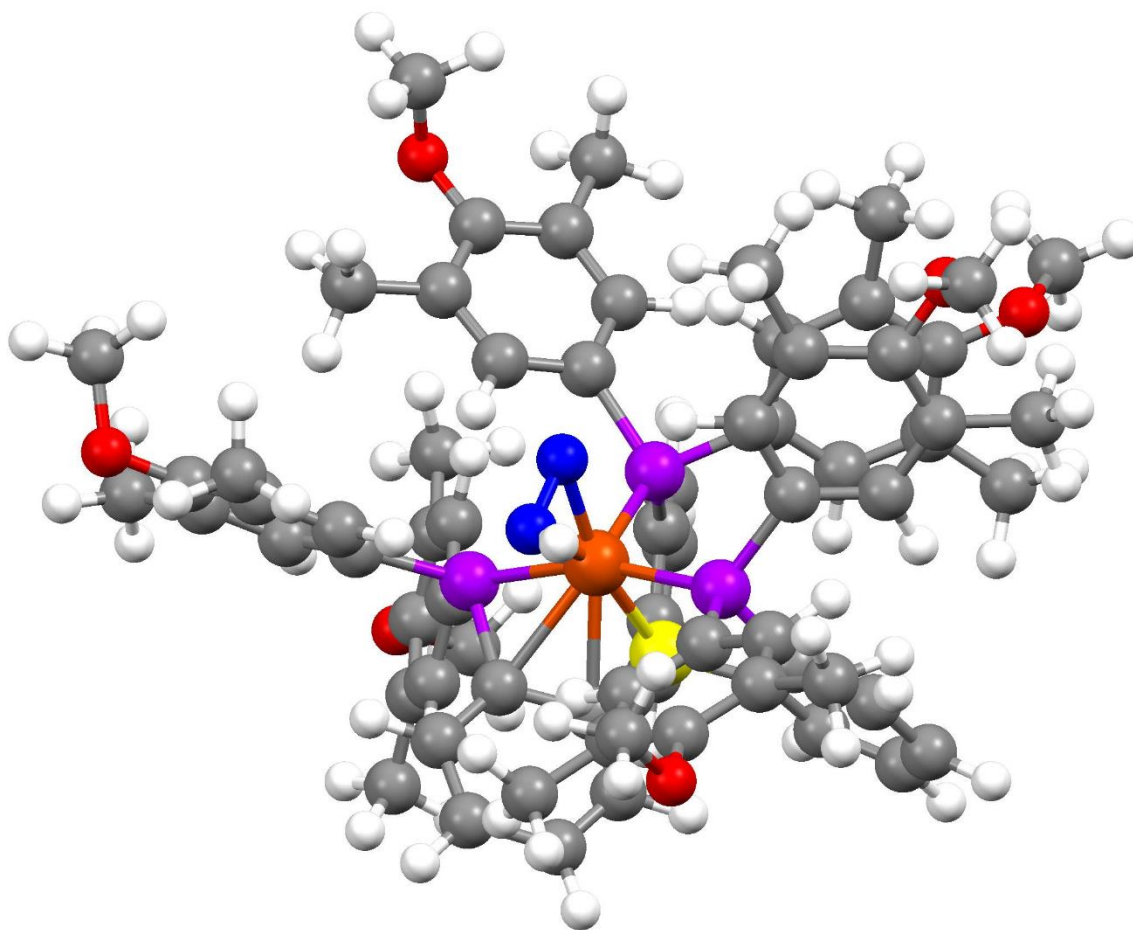


Figure S25: DFT optimized structure of alternative structure B (TPSS, def2-TZVP on Fe, def2-SVP on all other atoms) (Isopropyl groups on arene rings replaced with methyl groups). Fe shown in orange, P shown in purple, B shown in yellow, O shown in red, H shown in white, C shown in gray.

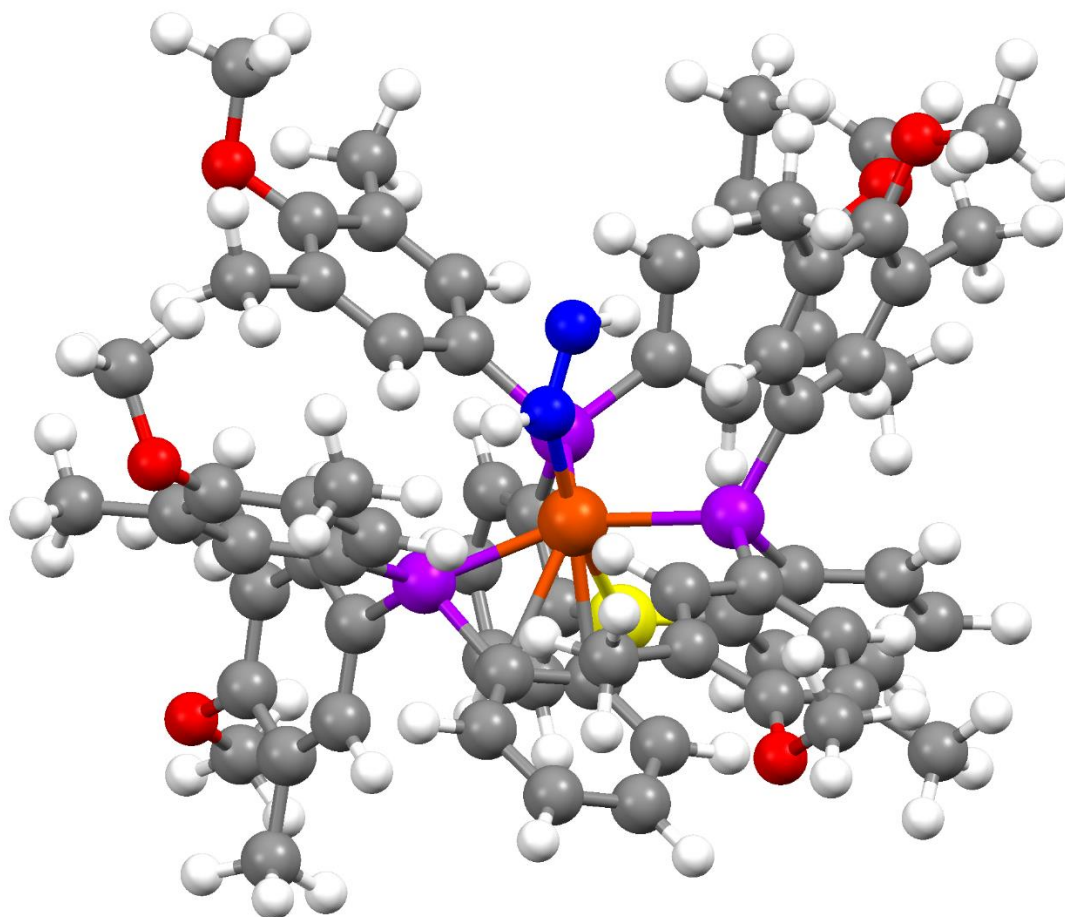


Figure 4.S26: DFT optimized structure of alternative structure G (TPSS, def2-TZVP on Fe, def-2SVP on all other atoms) (Isopropyl groups on arene rings replaced with methyl groups). Fe shown in orange, P shown in purple, B shown in yellow, O shown in red, H shown in white, C shown in gray.

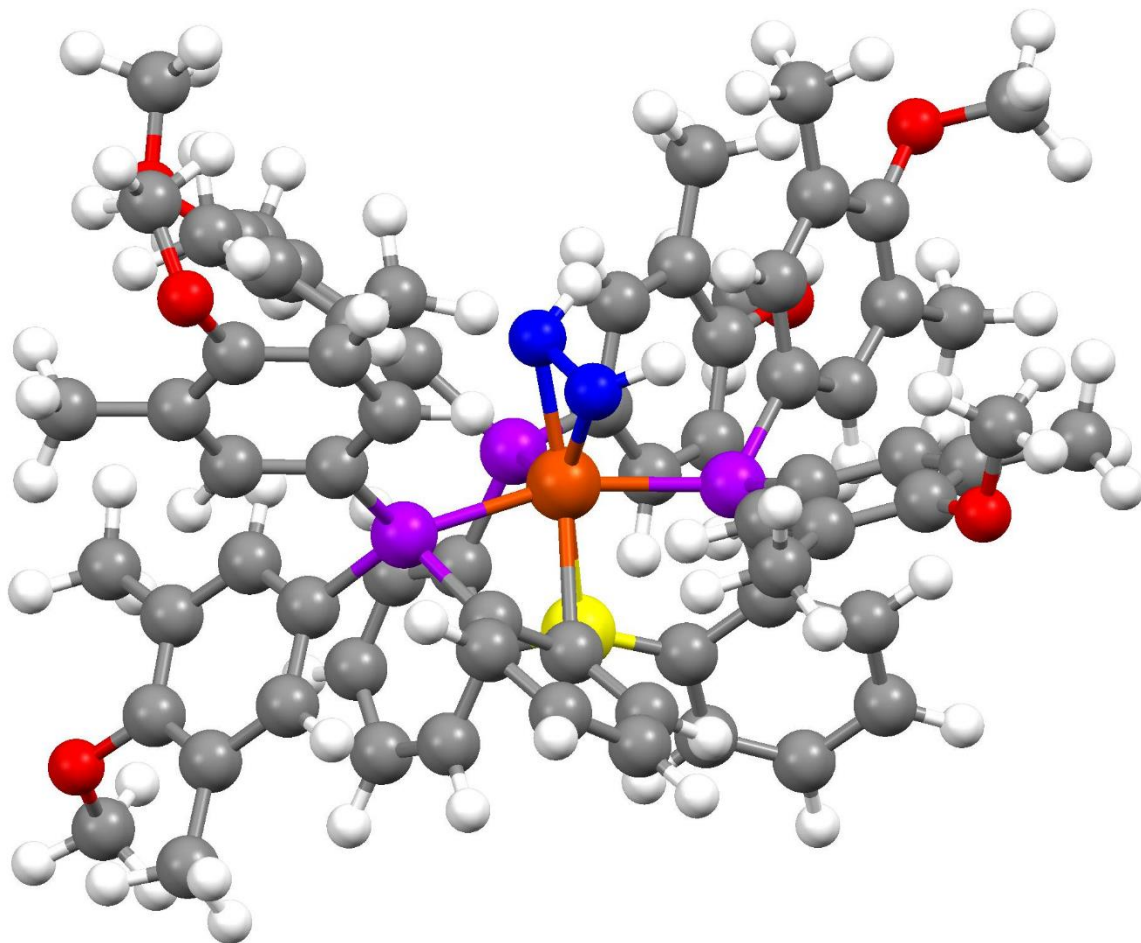


Figure 4.S27: DFT optimized structure of alternative structure I (TPSS, def-2TZVP on Fe, def-2SVP on all other atoms). (Isopropyl groups on arene rings replaced with methyl groups). (Fe shown in orange, P shown in purple, B shown in yellow, O shown in red, H shown in white, C shown in gray).

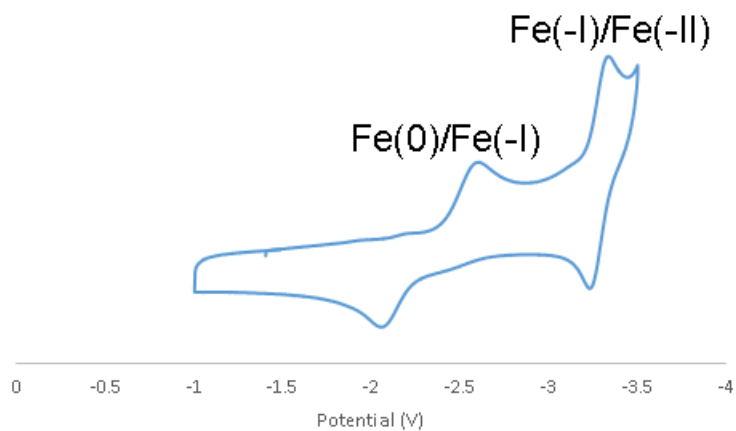


Figure 4.S28: Cyclic Voltammogram of $(^{\text{Ar}}\text{P}_3\text{B})\text{Fe}(\text{N}_2)$ (THF, 0.1 M $[\text{TBA}][\text{PF}_6]$).

4.4.2 Optimized Structure Coordinates for $[(^{\text{Ar}}\text{P}_3\text{B})\text{Fe}(\text{N}_2)]^-$ (TPSS)

P	2.123882	0.308698	0.836816
P	-1.256603	-1.824674	0.614257
P	-1.230023	1.623842	0.504794
O	5.173527	5.551277	0.672540
O	-0.304315	6.280931	-3.270258
O	6.283776	-2.754903	-2.319815
O	-5.589732	-3.716642	-3.185354
O	2.686287	-6.431013	0.237231
O	-7.240169	0.886501	0.253485
C	1.279256	-0.558939	3.259762
C	4.421096	1.967269	0.319525
H	4.923814	1.046729	0.014271
C	-3.997696	-2.385039	-0.133911
H	-4.268089	-2.096995	0.884052
C	5.139859	3.171363	0.308050
C	3.114173	4.333822	1.116810
C	1.460277	-1.125135	4.544964
H	0.585653	-1.486463	5.099309
C	2.429005	3.104120	1.096031
H	1.377364	3.065679	1.400231
C	-4.997033	-2.864626	-1.001123
C	4.469694	4.344899	0.721123
C	2.458959	-0.164512	2.583723
C	3.069020	1.915455	0.709690
C	3.490536	-0.501364	-1.486306
H	2.879803	0.274228	-1.957131
C	-1.938319	-1.992188	2.307375
C	1.236175	-5.023183	1.614006
C	-4.617767	-3.201715	-2.322490
C	-3.072411	1.416782	0.433130
C	3.726893	-0.194568	3.191984
H	4.605009	0.178976	2.650613
C	1.760803	-5.391814	0.357113
C	0.098274	3.076012	-1.486456
H	0.791960	2.231543	-1.408192
C	3.298431	-0.779539	-0.115857
C	-2.649036	-2.286656	-0.537431
C	4.066067	-1.792035	0.477511
H	3.912956	-2.029357	1.534111
C	-5.130403	1.238863	-0.892662
C	-0.105768	-3.289496	0.502729
C	-1.036602	3.065783	-0.662590
C	-0.391298	1.463939	3.070455

C	-3.737820	1.390334	-0.805378
H	-3.153500	1.515631	-1.724138
C	3.865725	-0.733468	4.479011
H	4.852424	-0.783640	4.955546
C	-2.808607	-2.996825	2.778256
H	-3.174577	-3.775128	2.098971
C	-3.821833	1.225706	1.606202
H	-3.304850	1.225843	2.572008
C	-1.939045	4.142471	-0.745133
H	-2.847012	4.129159	-0.130678
C	-1.824702	-1.024766	4.505360
H	-1.466103	-0.249631	5.193641
C	1.450357	-4.661289	-0.816552
C	6.579745	3.247894	-0.196463
H	7.117213	3.970562	0.445280
C	2.727002	-1.225062	5.140048
H	2.827099	-1.672745	6.136680
C	2.412088	5.612559	1.562130
H	3.113556	6.445838	1.380130
C	-0.560792	5.197387	-2.428179
C	0.347598	4.116493	-2.397304
C	0.282197	-3.989863	1.657339
H	-0.147729	-3.705264	2.622462
C	-1.373034	-1.018034	3.161492
C	4.463217	-1.170404	-2.242722
C	-6.450932	-3.064357	-0.565007
H	-6.718172	-4.100277	-0.853759
C	-3.312555	-2.972958	-2.804148
C	0.538781	-3.603119	-0.711549
H	0.342234	-2.991982	-1.592747
C	2.102277	-5.025013	-2.149063
H	3.132457	-5.352161	-1.917933
C	-5.216462	1.057045	1.570357
C	7.332202	1.906834	-0.121793
H	8.391843	2.051834	-0.398696
H	6.909332	1.159570	-0.816226
H	7.296025	1.477386	0.895441
C	5.259951	-2.145112	-1.591528
C	-1.408469	3.662821	2.581447
H	-1.899311	4.339739	1.874463
C	5.079101	-2.465899	-0.231335
C	-1.017567	2.370965	2.180835
C	-1.150925	4.096076	3.889358
H	-1.436050	5.107687	4.200624
C	1.699542	-5.681504	2.911695

H	2.543774	-6.346773	2.658581
C	-2.712524	-1.999136	4.982820
H	-3.036156	-1.978229	6.031158
C	-0.112333	1.947629	4.372419
H	0.417716	1.297121	5.079516
C	-1.702849	5.236357	-1.593217
C	-0.486272	3.236395	4.780177
H	-0.251149	3.578608	5.795813
C	-2.347763	-2.515575	-1.892048
H	-1.338374	-2.323239	-2.258534
C	5.789538	5.922598	1.905074
H	6.355890	6.848470	1.710954
H	6.484515	5.136655	2.264170
H	5.038470	6.112973	2.696480
C	-3.192293	-3.004650	4.125061
H	-3.874937	-3.776501	4.500694
C	-5.856767	1.082727	0.311818
C	1.141889	5.892017	0.735900
H	1.371068	5.974971	-0.339588
H	0.676903	6.839976	1.064282
H	0.391716	5.091580	0.857238
C	2.094357	5.555726	3.071265
H	3.009804	5.399890	3.669701
H	1.401556	4.727364	3.295154
H	1.618400	6.496181	3.407815
C	-5.585998	-5.140079	-3.274789
H	-6.429106	-5.420376	-3.927804
H	-5.720574	-5.609458	-2.279767
H	-4.642183	-5.519820	-3.715040
C	-6.007792	0.907985	2.866364
H	-7.052433	0.682277	2.588297
C	6.022873	-3.416677	0.501051
H	6.782041	-3.748394	-0.228686
C	-6.660695	-2.933660	0.951327
H	-7.702465	-3.194195	1.210992
H	-6.489902	-1.895615	1.282982
H	-5.987894	-3.593568	1.526548
C	2.224492	-4.633401	3.914146
H	3.003811	-3.996782	3.463166
H	2.652980	-5.129244	4.804788
H	1.420549	-3.961132	4.255813
C	4.730561	-0.836991	-3.708174
H	4.930840	-1.794047	-4.227184
C	-2.629820	6.448851	-1.575391
H	-2.222269	7.178878	-2.295782

C	-5.830148	1.293995	-2.248183
H	-6.879020	0.989025	-2.089105
C	0.576836	-6.528466	3.548960
H	0.203056	-7.299180	2.851121
H	-0.279448	-5.887741	3.826468
H	0.934213	-7.034209	4.465456
C	6.603520	3.817137	-1.633394
H	7.642425	3.930534	-1.995557
H	6.109503	4.801679	-1.664372
H	6.069164	3.139576	-2.322222
C	2.184108	-3.838100	-3.123018
H	2.764349	-4.121489	-4.020066
H	2.666070	-2.965671	-2.655609
H	1.186832	-3.520669	-3.474196
C	-2.946530	-3.201512	-4.267858
H	-3.868580	-3.514534	-4.788810
C	1.376354	-6.216583	-2.814110
H	1.867436	-6.492347	-3.766163
H	0.326504	-5.954150	-3.032782
H	1.374776	-7.104959	-2.161614
C	-5.989420	2.228573	3.669173
H	-6.603595	2.142194	4.584692
H	-6.379048	3.071503	3.070184
H	-4.958362	2.485848	3.972050
C	-5.481092	-0.253963	3.728435
H	-5.489511	-1.206214	3.173444
H	-6.098688	-0.377083	4.636998
H	-4.440954	-0.079060	4.049199
C	-7.420442	-2.123081	-1.315102
H	-7.278782	-2.200335	-2.404780
H	-7.270733	-1.078311	-0.998635
H	-8.466792	-2.395547	-1.078226
C	-0.913752	6.183881	-4.556744
H	-0.654308	7.107072	-5.101739
H	-2.017090	6.102387	-4.479325
H	-0.535407	5.309159	-5.121190
C	6.771423	-2.663470	1.623881
H	7.518233	-3.323544	2.104230
H	6.072562	-2.317277	2.406331
H	7.295912	-1.777952	1.223434
C	6.007815	0.024937	-3.831705
H	6.868657	-0.486486	-3.370088
H	5.864055	0.994185	-3.322377
H	6.245105	0.226759	-4.892671
C	5.955669	-4.050794	-2.824609

H	6.856643	-4.429222	-3.335122
H	5.117089	-4.001594	-3.546110
H	5.675683	-4.746577	-2.010350
C	-4.065493	6.087085	-2.006239
H	-4.708337	6.986614	-2.023809
H	-4.520295	5.359143	-1.310009
H	-4.078200	5.632289	-3.012048
C	5.294928	-4.656643	1.052956
H	4.799717	-5.236458	0.257591
H	4.509978	-4.367536	1.772799
H	6.005406	-5.323567	1.577242
C	-2.620868	7.123096	-0.186130
H	-1.594515	7.397743	0.109277
H	-3.022331	6.443609	0.588283
H	-3.242754	8.037355	-0.189301
C	2.179674	-7.753407	0.402066
H	2.957090	-8.437829	0.023284
H	1.246899	-7.904024	-0.174806
H	1.977354	-7.993840	1.463808
C	-8.028947	2.071610	0.320211
H	-9.083118	1.752951	0.262477
H	-7.808554	2.756723	-0.522005
H	-7.864299	2.616789	1.270705
C	3.541966	-0.158222	-4.406807
H	2.603945	-0.720555	-4.266139
H	3.740847	-0.064096	-5.489496
H	3.377698	0.860224	-4.015642
C	-1.896642	-4.320922	-4.417282
H	-2.237407	-5.261265	-3.949060
H	-0.949115	-4.033411	-3.930375
H	-1.680414	-4.521376	-5.482568
C	-5.822171	2.734010	-2.806978
H	-6.286897	3.446907	-2.103178
H	-6.370516	2.786779	-3.765914
H	-4.786553	3.074033	-2.984506
C	-5.202189	0.319985	-3.261616
H	-5.781781	0.308734	-4.202501
H	-5.167674	-0.704934	-2.861196
H	-4.167548	0.616737	-3.507977
C	-2.455132	-1.896123	-4.931193
H	-2.205843	-2.075468	-5.993491
H	-1.554118	-1.501236	-4.429013
H	-3.234607	-1.117530	-4.885109
C	1.288075	2.970223	-4.425298
H	0.373572	3.191178	-5.004600

H	1.152093	1.975375	-3.966650
H	2.137766	2.914029	-5.131241
C	2.864877	3.784384	-2.601455
H	2.861687	2.810288	-2.083587
H	3.061331	4.556458	-1.839194
H	3.709652	3.780597	-3.314303
C	1.540218	4.045835	-3.344629
H	1.621251	5.029724	-3.839849
B	-0.142300	-0.089924	2.598640
N	0.166194	-0.205910	-1.517629
N	0.225291	-0.292618	-2.663554
Fe	0.041578	-0.124804	0.261969

4.4.3 Optimized Structure Coordinates for Truncated (^{Ar}P₃B)Fe(N₂) (TPSS)

Fe	-0.068012	0.646503	-0.188199
P	2.053201	1.264148	-0.287748
P	0.299178	-1.484242	-0.380260
P	-2.264044	0.771204	-0.580294
O	4.097691	-3.915133	3.673513
O	-6.105864	-2.161400	3.038520
O	-3.824159	6.592133	-0.133061
O	6.707897	-0.525191	-3.635194
O	4.507600	3.549808	4.713110
N	-0.292833	0.791350	1.592522
O	-4.225228	-5.474831	-0.281189
N	-0.450621	0.767464	2.722926
C	1.129869	-0.687388	-2.809393
C	1.386156	-2.245280	0.935059
C	-2.845252	2.526721	-0.411561
C	2.072651	-1.434164	1.853593
H	1.912168	-0.353648	1.844390
C	1.595958	-3.639249	0.983833
H	1.045605	-4.296735	0.301220
C	-1.089464	-2.699932	-0.378765
C	1.877795	-0.708440	-4.005042
H	1.837559	0.154597	-4.680864
C	3.925703	1.523033	-2.371923
H	3.431002	2.477702	-2.582571
C	2.024676	-2.921846	-2.274152
H	2.104746	-3.775220	-1.593740
C	3.461136	0.715891	-1.319626
C	1.236072	-1.805588	-1.947894
C	-2.136731	3.368163	0.461110
H	-1.278076	2.965637	1.007550
C	3.171819	-3.365033	2.797927
C	-3.607573	0.269164	1.824771
H	-3.013637	1.105629	2.207200
C	2.493820	-4.216910	1.895326
C	2.057149	2.763741	2.085585
H	0.994859	2.914207	1.875214
C	2.970406	-1.969516	2.794533
C	-2.611633	0.246689	-2.306114
C	2.591444	3.270647	3.278216
C	4.095905	-0.506490	-1.041708
H	3.737871	-1.136139	-0.219131
C	2.856086	2.064285	1.159170
C	-1.664870	-3.149423	-1.578466

H	-1.288942	-2.772965	-2.535600
C	-1.425306	-0.005407	-3.044092
C	0.140708	1.926421	-2.113314
C	-3.888135	0.053715	-2.869779
H	-4.791698	0.257974	-2.285715
C	-3.481415	-0.126785	0.479790
C	-3.894475	3.067769	-1.177274
H	-4.434837	2.441494	-1.893838
C	-3.516575	5.238955	-0.177467
C	-4.253255	-1.206446	0.014867
H	-4.132052	-1.571428	-1.008328
C	3.964245	3.055502	3.537300
C	4.229472	1.908511	1.424790
H	4.869724	1.390600	0.702867
C	-5.268888	-1.442577	2.192994
C	1.056806	2.495682	-1.145646
C	-4.471061	-0.397987	2.708486
C	-1.580884	-0.520113	-4.350895
H	-0.686693	-0.753321	-4.940582
C	1.093330	3.896617	-0.876140
H	1.819131	4.285333	-0.154268
C	3.568361	-4.302889	4.944155
H	3.143774	-3.436364	5.488432
H	4.409457	-4.718500	5.521590
H	2.780277	-5.074479	4.837231
C	5.615530	-0.128104	-2.877605
C	2.743005	-2.924333	-3.478354
H	3.365094	-3.787411	-3.742310
C	-5.184451	-1.849638	0.845528
C	-1.615583	-3.147705	0.848771
H	-1.197699	-2.770294	1.788634
C	-0.693097	4.236513	-2.479437
H	-1.369130	4.917693	-3.008032
C	-4.241024	4.423791	-1.077056
C	5.006200	1.112568	-3.167954
C	-0.752553	2.875961	-2.728470
H	-1.481176	2.501087	-3.455619
C	2.681695	-1.810407	-4.332732
H	3.261395	-1.806527	-5.262769
C	0.235072	4.756874	-1.541389
H	0.271948	5.833992	-1.343845
C	-3.179723	-4.559088	-0.327269
C	5.186118	-0.944356	-1.808135
C	-2.726082	-4.073003	-1.573091
C	-4.006842	-0.444940	-4.174687

H	-4.998451	-0.615348	-4.608422
C	4.803304	2.399666	2.610511
C	-2.453183	4.730416	0.595457
C	-2.847658	-0.744291	-4.908764
H	-2.934784	-1.148661	-5.923837
C	-2.652893	-4.089513	0.897571
C	-4.665913	6.983813	0.954567
H	-4.844053	8.064829	0.841200
H	-4.184288	6.794523	1.934064
H	-5.634473	6.447361	0.928811
C	-7.376264	-1.560514	3.300223
H	-7.929671	-2.263121	3.943861
H	-7.944611	-1.395730	2.363917
H	-7.271070	-0.591243	3.825946
C	6.394415	-1.373432	-4.743441
H	5.737840	-0.858637	-5.472121
H	5.893964	-2.303609	-4.414159
H	7.351345	-1.623191	-5.227508
C	4.519438	2.615862	5.797733
H	3.494919	2.284544	6.055930
H	4.962144	3.139299	6.659527
H	5.130322	1.723564	5.557922
B	0.001440	0.371459	-2.384056
C	-3.845738	-6.833190	-0.514193
H	-3.109420	-7.179131	0.238188
H	-3.411105	-6.971096	-1.523150
H	-4.764480	-7.434933	-0.431047
C	1.722699	4.000003	4.276551
H	2.299402	4.774447	4.807376
H	0.855974	4.464688	3.778741
H	1.324978	3.299753	5.035508
C	6.275096	2.215285	2.900371
H	6.656789	3.038237	3.526407
H	6.454404	1.269530	3.447669
H	6.858400	2.168871	1.966240
C	5.866885	-2.258860	-1.511737
H	5.397521	-3.078155	-2.089022
H	6.934006	-2.221036	-1.785403
H	5.771216	-2.518679	-0.444387
C	5.507636	1.955987	-4.317112
H	6.607422	1.911111	-4.386842
H	5.105513	1.590758	-5.281535
H	5.192775	3.006670	-4.204988
C	2.744886	-5.708011	1.917630
H	2.139098	-6.208562	2.697035

H	2.479523	-6.168399	0.951166
H	3.803431	-5.920969	2.140724
C	3.696993	-1.074848	3.773710
H	3.151023	-1.008709	4.734213
H	4.702882	-1.470970	3.991796
H	3.786065	-0.050716	3.377345
C	-3.373778	-4.509160	-2.868406
H	-3.358484	-3.683482	-3.600157
H	-2.840227	-5.365756	-3.323092
H	-4.418119	-4.817515	-2.696279
C	-3.219019	-4.565130	2.215822
H	-3.415866	-5.650081	2.207577
H	-2.525930	-4.335567	3.041957
H	-4.178419	-4.062515	2.436016
C	-6.068071	-2.958288	0.324491
H	-5.904711	-3.901510	0.871050
H	-7.137464	-2.698996	0.433966
H	-5.864968	-3.150319	-0.740586
C	-4.529689	-0.019326	4.171257
H	-3.549343	0.350532	4.514342
H	-5.269698	0.783339	4.356121
H	-4.818525	-0.888955	4.784540
C	-1.631293	5.630036	1.489708
H	-1.652474	6.669060	1.121649
H	-2.010890	5.630992	2.529461
H	-0.583261	5.286153	1.519702
C	-5.334770	5.030874	-1.925435
H	-6.195665	5.348915	-1.308360
H	-4.970625	5.932353	-2.448017
H	-5.702395	4.308819	-2.672956

4.4.4 Optimized Structure Coordinates for Truncated (^{Ar}P₃B)Fe(NNH) (TPSS)

Fe	-0.135888	-0.488147	0.146160
P	1.980569	-1.160243	0.574042
P	0.100526	1.655924	0.520383
P	-2.280116	-0.887778	0.597705
O	3.892429	4.263002	-3.404467
O	-6.194611	0.832734	-3.652627
O	-2.802068	-6.857698	1.320923
O	6.588514	1.420085	3.476865
O	4.427325	-3.507134	-4.401426
N	-0.266980	-0.863383	-1.504257
O	-4.831044	5.122279	0.549295
C	0.887289	0.767615	2.930507
C	1.161894	2.492039	-0.760555
C	-2.556041	-2.718487	0.737087
C	1.858161	1.707223	-1.694520
H	1.702626	0.622546	-1.694210
C	1.361335	3.887156	-0.763723
H	0.800399	4.520020	-0.066309
C	-1.370569	2.766027	0.541941
C	1.625146	0.762192	4.133170
H	1.623662	-0.139670	4.757504
C	4.034812	-1.057017	2.518759
H	3.691550	-2.053929	2.816307
C	1.677185	3.071568	2.530417
H	1.721002	3.963662	1.897882
C	3.386885	-0.380164	1.471343
C	0.955342	1.934554	2.130739
C	-1.704420	-3.584015	0.030629
H	-0.935772	-3.157126	-0.621878
C	2.958065	3.668144	-2.569568
C	-3.645138	-1.100901	-1.826600
H	-3.022639	-1.990745	-1.967888
C	2.261828	4.492553	-1.654457
C	2.081530	-2.884307	-1.628107
H	1.068543	-3.156480	-1.321272
C	2.768019	2.270810	-2.606506
C	-2.766996	-0.246350	2.239016
C	2.594340	-3.409798	-2.823509
C	3.837229	0.894491	1.090051
H	3.344358	1.423991	0.270289
C	2.827271	-1.996880	-0.830886
C	-2.012820	3.089096	1.751952
H	-1.614001	2.708559	2.697546

C	-1.624494	-0.039886	3.049070
C	0.241702	-1.934210	2.504619
C	-4.073155	-0.006119	2.703403
H	-4.936441	-0.180403	2.051987
C	-3.542850	-0.359249	-0.632918
C	-3.504846	-3.262390	1.621910
H	-4.147852	-2.601471	2.212128
C	-2.746275	-5.492153	1.075187
C	-4.327183	0.799885	-0.474807
H	-4.222615	1.418662	0.422450
C	3.892394	-3.015742	-3.217453
C	4.137539	-1.664076	-1.225709
H	4.743167	-0.997361	-0.602195
C	-5.334394	0.419759	-2.642273
C	1.296736	-2.443625	1.681992
C	-4.519391	-0.714349	-2.854355
C	1.632802	-3.808745	1.647318
H	2.441457	-4.156694	0.994656
C	3.425637	4.564001	-4.722429
H	3.143267	3.647042	-5.275597
H	4.258914	5.060146	-5.245012
H	2.551386	5.244464	-4.695689
C	5.518442	0.828168	2.818592
C	2.387129	3.042269	3.738637
H	2.967623	3.917220	4.052695
C	-5.257401	1.185326	-1.457571
C	-1.910476	3.230653	-0.670049
H	-1.435427	2.952141	-1.617671
C	-0.152951	-4.255851	3.227937
H	-0.740681	-4.969911	3.816038
C	-3.613072	-4.649237	1.805926
C	5.107239	-0.466305	3.206872
C	-0.472254	-2.892564	3.267074
H	-1.310378	-2.554735	3.887962
C	2.377036	1.879211	4.526638
H	2.959842	1.847755	5.454423
C	0.903742	-4.718916	2.425699
H	1.142384	-5.787606	2.390410
C	-3.659868	4.372582	0.534463
C	4.906610	1.518289	1.750060
C	-3.169977	3.883312	1.766000
C	-4.261430	0.483283	4.003620
H	-5.271614	0.701061	4.367824
C	4.687226	-2.164521	-2.418304
C	-1.780098	-4.978442	0.185730

C	-3.146887	0.704286	4.828586
H	-3.290586	1.091907	5.844036
C	-3.049958	4.051099	-0.697843
C	-3.584758	-7.605859	0.388059
H	-3.563728	-8.653702	0.727834
H	-3.167543	-7.545870	-0.636109
H	-4.634067	-7.250218	0.363022
C	-7.495747	0.243093	-3.610706
H	-8.060120	0.664010	-4.458002
H	-8.021464	0.486084	-2.666261
H	-7.446385	-0.858893	-3.714969
C	6.223397	2.223693	4.601718
H	5.722174	1.621197	5.384254
H	5.546781	3.048651	4.307645
H	7.158417	2.641493	5.006474
C	4.132821	-2.709250	-5.550960
H	3.042495	-2.663880	-5.743492
H	4.634840	-3.188842	-6.405666
H	4.513714	-1.675403	-5.435023
B	-0.148602	-0.373736	2.450620
C	-4.643289	6.539403	0.556660
H	-4.126354	6.885566	-0.360011
H	-4.057189	6.863828	1.438601
H	-5.646933	6.990195	0.599366
N	-0.423231	-1.308357	-2.637709
H	-0.470101	-0.548356	-3.353469
C	-0.814010	-5.895481	-0.527573
H	0.164099	-5.402537	-0.653808
H	-0.668011	-6.824439	0.046790
H	-1.180228	-6.171210	-1.534547
C	-6.176888	2.369245	-1.259940
H	-7.171710	2.035297	-0.907353
H	-5.783897	3.073895	-0.512028
H	-6.334178	2.903924	-2.210972
C	-4.591287	-1.487663	-4.151916
H	-3.627309	-1.978874	-4.366065
H	-5.363042	-2.280340	-4.108765
H	-4.850794	-0.818955	-4.989056
C	-3.606105	4.551679	-2.011864
H	-2.978784	5.364068	-2.424731
H	-3.628169	3.736552	-2.756234
H	-4.629899	4.935596	-1.888321
C	-3.891044	4.206606	3.053911
H	-3.752971	5.266701	3.339805
H	-4.976802	4.044196	2.942714

H	-3.518228	3.576414	3.876156
C	2.511775	5.983290	-1.642756
H	2.098024	6.470531	-2.545615
H	2.043823	6.455788	-0.763531
H	3.594162	6.197455	-1.632790
C	3.539985	1.395381	-3.568679
H	4.527431	1.834296	-3.788122
H	3.677588	0.385451	-3.148260
H	3.004240	1.280235	-4.530687
C	6.087500	-1.794279	-2.852766
H	6.072005	-0.945958	-3.564877
H	6.698972	-1.486875	-1.988355
H	6.576649	-2.640635	-3.362311
C	1.755264	-4.328858	-3.680754
H	0.973108	-3.750751	-4.207126
H	2.374932	-4.852789	-4.424873
H	1.234682	-5.077197	-3.059379
C	5.365426	2.900477	1.350046
H	5.125374	3.104036	0.293101
H	4.849183	3.670447	1.954625
H	6.449590	3.019294	1.511370
C	5.795859	-1.176386	4.349772
H	6.866091	-0.913969	4.386267
H	5.352737	-0.884784	5.321800
H	5.692100	-2.270745	4.256458
C	-4.591391	-5.246287	2.790713
H	-5.407255	-5.787756	2.276028
H	-4.087966	-5.979112	3.444893
H	-5.049888	-4.462584	3.415885
C	-1.851450	0.439378	4.358412
H	-0.993773	0.629310	5.014517

4.4.5 Optimized Structure Coordinates for Truncated [(^{Ar}P₃B)Fe(NNH)]⁺ (TPSS)

Fe	0.137425	0.649134	0.416500
P	-2.055012	1.136503	0.586460
P	-0.174727	-1.534447	0.485525
P	2.360605	0.813876	0.801291
O	-3.771967	-3.634305	-3.887397
O	6.253402	-1.127208	-3.357661
O	3.393674	6.728175	1.286725
O	-6.744884	-1.302542	3.395345
O	-4.494492	3.927198	-4.139090
N	0.369557	0.891364	-1.237301
O	4.510005	-5.308375	0.386774
C	-0.982803	-0.973200	2.965842
C	-1.173620	-2.163615	-0.947804
C	2.776512	2.611578	0.895169
C	-1.882560	-1.291448	-1.794122
H	-1.792923	-0.210155	-1.665521
C	-1.318779	-3.553799	-1.140373
H	-0.766427	-4.253595	-0.503209
C	1.266551	-2.675028	0.451401
C	-1.713065	-1.107438	4.163371
H	-1.648436	-0.326686	4.930988
C	-3.924998	0.951667	2.668543
H	-3.448134	1.850244	3.074670
C	-1.924981	-3.119333	2.201068
H	-2.018384	-3.894727	1.434901
C	-3.431386	0.363306	1.492192
C	-1.120153	-1.988730	1.993647
C	2.026887	3.515952	0.123168
H	1.230665	3.139731	-0.527318
C	-2.866040	-3.164845	-2.959827
C	3.691643	0.872008	-1.643284
H	3.095371	1.772782	-1.820746
C	-2.168276	-4.074344	-2.130413
C	-2.039878	2.846334	-1.641079
H	-0.974324	2.972265	-1.427190
C	-2.735924	-1.767894	-2.802769
C	2.740748	0.077265	2.430242
C	-2.585072	3.478086	-2.765918
C	-4.057936	-0.777904	0.955554
H	-3.668071	-1.226560	0.038617
C	-2.838688	2.055209	-0.788460
C	1.793808	-3.189903	1.650894
H	1.351822	-2.903387	2.609195

C	1.585460	-0.240673	3.190309
C	-0.127328	1.693905	2.466173
C	4.039297	-0.175544	2.912740
H	4.916602	0.072350	2.306152
C	3.563178	0.167975	-0.427596
C	3.753615	3.106865	1.778796
H	4.323077	2.420998	2.413888
C	3.220564	5.370684	1.103199
C	4.343331	-0.984547	-0.213300
H	4.221536	-1.574592	0.700124
C	-3.961029	3.287502	-3.040879
C	-4.213673	1.923397	-1.059781
H	-4.851111	1.338049	-0.389666
C	5.392232	-0.679961	-2.374272
C	-1.142807	2.296454	1.635452
C	4.581485	0.448049	-2.641012
C	1.789813	-0.848429	4.447899
H	0.920980	-1.128125	5.054192
C	-1.281713	3.706705	1.536126
H	-2.047739	4.127561	0.877296
C	-3.230671	-4.027160	-5.157412
H	-2.710875	-3.181843	-5.648391
H	-4.086254	-4.339153	-5.774632
H	-2.524351	-4.872577	-5.054708
C	-5.630113	-0.757898	2.786224
C	-2.642240	-3.227866	3.399539
H	-3.290527	-4.094321	3.569667
C	5.295073	-1.400956	-1.162209
C	1.852278	-3.040341	-0.774108
H	1.464314	-2.625988	-1.711587
C	0.523193	3.985401	3.137223
H	1.158844	4.644663	3.736859
C	3.986872	4.485745	1.898678
C	-5.025519	0.393959	3.339743
C	0.710239	2.610716	3.185476
H	1.498211	2.200964	3.825638
C	-2.546868	-2.216434	4.369890
H	-3.131265	-2.294354	5.293319
C	-0.469280	4.538962	2.297775
H	-0.598807	5.625476	2.246737
C	3.413728	-4.465414	0.389380
C	-5.940151	-2.519558	0.974378
H	-6.223921	-3.185229	1.809989
C	-5.176896	-1.345469	1.579798
C	2.881740	-4.074864	1.640157

C	4.206290	-0.774519	4.168695
H	5.212856	-0.986833	4.543689
C	-4.794863	2.533011	-2.185345
C	2.230667	4.902741	0.212226
C	3.078809	-1.112728	4.933299
H	3.207285	-1.587398	5.911917
C	2.920434	-3.950643	-0.831023
C	4.256902	7.379557	0.343177
H	4.310640	8.435243	0.649217
H	3.855042	7.315008	-0.685857
H	5.272106	6.938946	0.359534
C	-5.118105	-3.339149	-0.032407
H	-4.904699	-2.764700	-0.951167
H	-5.678892	-4.239112	-0.336906
H	-4.152970	-3.662784	0.392385
C	7.581958	-0.587572	-3.312631
H	8.127365	-1.034638	-4.157335
H	8.091508	-0.850862	-2.366218
H	7.572256	0.514117	-3.421274
C	-7.250347	-2.008118	0.329826
H	-7.868756	-1.476287	1.071350
H	-7.836554	-2.851857	-0.075675
H	-7.022960	-1.315451	-0.501366
C	-6.481357	-2.182221	4.497710
H	-5.978625	-1.654839	5.329894
H	-5.849663	-3.034245	4.181915
H	-7.459272	-2.552604	4.838441
C	-4.652324	3.118858	-5.314067
H	-3.678761	2.714057	-5.651904
H	-5.063546	3.779577	-6.091835
H	-5.349994	2.278152	-5.139225
B	0.124128	0.127973	2.625535
C	4.225751	-6.704408	0.214869
H	3.746872	-6.899078	-0.763602
H	3.566486	-7.079380	1.020553
H	5.193356	-7.225805	0.258520
N	0.579178	0.824819	-2.427302
H	0.643693	-0.140947	-2.818004
C	-1.743472	4.337097	-3.680145
H	-0.745549	4.514660	-3.248389
H	-1.604403	3.853309	-4.664199
H	-2.235195	5.306142	-3.868473
C	-6.271577	2.389884	-2.469365
H	-6.841137	2.254994	-1.535419
H	-6.654867	3.277287	-2.998632

H	-6.469833	1.506712	-3.106766
C	-3.530344	-0.820809	-3.672426
H	-4.604404	-1.075757	-3.639856
H	-3.402089	0.222018	-3.340639
H	-3.221343	-0.888112	-4.731899
C	-2.372331	-5.563477	-2.283343
H	-3.412713	-5.780673	-2.575600
H	-1.714114	-5.985017	-3.066203
H	-2.145641	-6.092383	-1.343182
C	3.527192	-4.348669	-2.156820
H	3.655533	-3.465912	-2.806439
H	4.511576	-4.818722	-2.013651
H	2.876782	-5.066785	-2.690806
C	3.480717	-4.606301	2.921016
H	3.118595	-4.032599	3.788107
H	3.217344	-5.668655	3.078372
H	4.581895	-4.551635	2.886160
C	-5.556099	1.011737	4.612180
H	-6.643335	0.852388	4.699466
H	-5.079046	0.559424	5.502146
H	-5.346576	2.093966	4.642768
C	6.211713	-2.573966	-0.902514
H	5.762701	-3.305161	-0.213978
H	6.466773	-3.081414	-1.846383
H	7.160147	-2.229657	-0.448448
C	4.690086	1.175824	-3.961038
H	3.762001	1.727455	-4.184564
H	5.518147	1.909773	-3.947695
H	4.896506	0.465909	-4.778506
C	5.000374	5.039507	2.872136
H	5.383385	4.250768	3.539215
H	5.863488	5.484401	2.343774
H	4.555264	5.844142	3.482217
C	1.372250	5.865913	-0.573858
H	1.249614	6.812628	-0.022886
H	1.823529	6.106382	-1.554477
H	0.375998	5.432606	-0.765731

4.4.6 Optimized Structure Coordinates for Truncated [(^{Ar}P₃B)Fe(NNH₂)]⁺ (TPSS)

Fe	-0.073094	0.639925	-0.113304
P	2.128847	1.116151	-0.272047
P	0.193565	-1.539508	-0.420544
P	-2.287827	0.862873	-0.486455
O	3.826753	-4.129056	3.661118
O	-6.321950	-1.366660	3.388349
O	-3.209499	6.812674	-0.345476
O	6.696040	-0.923997	-3.563454
O	4.772055	3.294430	4.667621
N	-0.371844	0.807217	1.608735
O	-4.516916	-5.279616	-0.755249
C	1.028675	-0.713388	-2.821780
C	1.204987	-2.344340	0.917869
C	-2.674817	2.666959	-0.386368
C	1.952459	-1.565942	1.821761
H	1.873180	-0.475601	1.789341
C	1.329677	-3.748738	0.977901
H	0.750281	-4.377390	0.292620
C	-1.250016	-2.679401	-0.510652
C	1.758985	-0.733005	-4.027552
H	1.726504	0.135458	-4.695907
C	3.990476	1.256802	-2.360061
H	3.547129	2.234325	-2.578695
C	1.895612	-2.968182	-2.315453
H	1.969978	-3.826157	-1.640199
C	3.477820	0.471684	-1.312237
C	1.129203	-1.841651	-1.975921
C	-1.920512	3.467324	0.489764
H	-1.147939	3.002287	1.110402
C	2.925214	-3.553323	2.789975
C	-3.704627	0.742153	1.913291
H	-3.132140	1.642680	2.163685
C	2.191215	-4.371154	1.896583
C	2.198316	2.449249	2.200779
H	1.112704	2.530486	2.077202
C	2.819107	-2.145494	2.763791
C	-2.671813	0.310044	-2.183466
C	2.796823	2.942085	3.367167
C	4.057054	-0.774637	-1.015186
H	3.666694	-1.381316	-0.190860
C	2.967362	1.835820	1.190286
C	-1.794355	-3.033366	-1.760399
H	-1.360392	-2.627224	-2.678618

C	-1.516153	0.084003	-2.975644
C	0.214229	1.916447	-2.050007
C	-3.971650	0.106149	-2.685134
H	-4.846731	0.282340	-2.050750
C	-3.516649	0.118652	0.661994
C	-3.628048	3.272163	-1.226510
H	-4.196946	2.668728	-1.941147
C	-3.065417	5.439535	-0.303003
C	-4.272907	-1.025378	0.345115
H	-4.109798	-1.551944	-0.600552
C	4.196517	2.790406	3.520499
C	4.362371	1.739904	1.348093
H	4.972997	1.291582	0.557837
C	-5.420014	-0.862530	2.471505
C	1.222804	2.414415	-1.142546
C	-4.634765	0.253843	2.841230
C	-1.724972	-0.379344	-4.293310
H	-0.857821	-0.586718	-4.930502
C	1.371905	3.799473	-0.871873
H	2.131687	4.129160	-0.155681
C	3.289331	-4.588612	4.909283
H	2.829185	-3.756748	5.477300
H	4.137149	-4.996212	5.480135
H	2.532708	-5.381899	4.758521
C	5.614812	-0.468051	-2.835506
C	2.600607	-2.966434	-3.526291
H	3.209561	-3.833398	-3.804529
C	-5.259002	-1.508967	1.225458
C	-1.829628	-3.198257	0.660857
H	-1.431690	-2.917462	1.642842
C	-0.411706	4.277907	-2.447215
H	-1.037143	5.008564	-2.970025
C	-3.834441	4.660298	-1.200226
C	5.066729	0.799729	-3.136776
C	-0.606447	2.920285	-2.665595
H	-1.390424	2.597232	-3.358238
C	2.544191	-1.844025	-4.370297
H	3.119015	-1.837982	-5.302621
C	0.572388	4.723629	-1.535775
H	0.702713	5.795289	-1.351238
C	-3.412335	-4.452560	-0.658483
C	5.134939	-1.261241	-1.767526
C	-2.887952	-3.907271	-1.853049
C	-4.141430	-0.350443	-3.998850
H	-5.148419	-0.525417	-4.391909

C	4.998147	2.213844	2.510136
C	-2.099478	4.859491	0.547282
C	-3.014742	-0.594643	-4.800063
H	-3.144760	-0.958805	-5.825061
C	-2.904917	-4.100313	0.612537
C	-4.067981	7.381477	0.652997
H	-4.101459	8.463582	0.454068
H	-3.675307	7.207857	1.673263
H	-5.090602	6.962974	0.587471
C	-7.661356	-0.860734	3.289940
H	-8.237087	-1.349992	4.089686
H	-8.114396	-1.104418	2.310476
H	-7.688148	0.236669	3.434272
C	6.371267	-1.679695	-4.737596
H	5.808276	-1.066751	-5.467564
H	5.772365	-2.575272	-4.485406
H	7.328306	-1.990391	-5.181977
C	5.100522	2.328963	5.677216
H	4.198728	1.776434	6.005458
H	5.511972	2.895658	6.525732
H	5.855680	1.603543	5.320563
B	-0.052755	0.376473	-2.366715
C	-4.248735	-6.688969	-0.734921
H	-3.780600	-6.997253	0.219319
H	-3.586348	-6.980352	-1.572079
H	-5.221300	-7.191498	-0.843146
N	-0.619515	0.113805	2.642024
H	-0.936822	0.559086	3.513809
H	-0.522645	-0.917443	2.649425
C	-4.823956	0.901667	4.193421
H	-3.953828	1.523802	4.462892
H	-5.713289	1.559378	4.202567
H	-4.980649	0.137509	4.972799
C	-6.151049	-2.671330	0.857174
H	-6.413987	-3.256278	1.753164
H	-7.097455	-2.307392	0.414303
H	-5.679793	-3.337751	0.120335
C	-3.506267	-4.655699	1.883336
H	-2.873713	-5.459054	2.305175
H	-3.598202	-3.864553	2.647337
H	-4.507231	-5.071985	1.695577
C	-3.504328	-4.265086	-3.184542
H	-3.289816	-5.314735	-3.457639
H	-4.602280	-4.164200	-3.142693
H	-3.114470	-3.614873	-3.982886

C	2.354455	-5.873363	1.923935
H	1.695217	-6.337431	2.681677
H	2.095337	-6.317769	0.948890
H	3.391140	-6.145202	2.180838
C	3.637162	-1.292017	3.706435
H	3.618689	-0.233756	3.398423
H	3.253350	-1.353115	4.742416
H	4.683252	-1.641475	3.735169
C	5.758424	-2.601883	-1.466411
H	5.539949	-2.914166	-0.432405
H	5.352075	-3.381124	-2.138781
H	6.849538	-2.571963	-1.620028
C	5.626166	1.626960	-4.270297
H	6.710914	1.461753	-4.374289
H	5.156461	1.348308	-5.232927
H	5.435441	2.701217	-4.110019
C	6.497964	2.120200	2.666317
H	6.793739	1.161340	3.133707
H	6.998855	2.171605	1.686233
H	6.875196	2.935843	3.304807
C	1.991681	3.621172	4.450253
H	2.436502	4.595177	4.714802
H	0.950019	3.781242	4.126601
H	1.977443	3.019392	5.377495
C	-4.817838	5.335704	-2.126688
H	-5.671379	5.760042	-1.567200
H	-4.338471	6.176704	-2.656306
H	-5.218645	4.625497	-2.867824
C	-1.234693	5.715467	1.443498
H	-1.070676	6.707542	0.991522
H	-1.703897	5.874595	2.432690
H	-0.255892	5.235139	1.613184

4.4.7 Optimized Structure Coordinates for Alternative Structure B (TPSS)

Fe	0.875232	-0.080475	0.225086
P	1.339983	2.137778	0.220905
P	-1.306341	0.278612	0.183668
P	0.825787	-2.268187	0.747708
O	-3.258657	3.931989	-4.229185
O	-2.607150	-6.094398	-2.422443
O	6.058481	-5.267374	0.306744
O	-1.062369	6.877549	3.036531
O	4.084866	4.989328	-4.331391
N	2.068844	-0.491042	-1.340314
O	-5.439627	-4.114917	0.351210
C	-0.793040	1.251649	2.627857
C	-1.910829	1.268708	-1.276015
C	2.418728	-3.202575	0.537634
C	-0.998438	1.899421	-2.137113
H	0.066326	1.679953	-2.031941
C	-3.288750	1.508484	-1.463898
H	-4.024146	0.999456	-0.830939
C	-2.554050	-1.083998	0.227444
C	-0.963795	2.037964	3.786563
H	-0.179444	2.048845	4.553870
C	1.220023	4.097217	2.245723
H	2.158430	3.662627	2.606835
C	-2.970774	2.066851	1.816945
H	-3.745836	2.099355	1.044839
C	0.570508	3.530075	1.135674
C	-1.804510	1.303474	1.643471
C	3.635728	-2.497174	0.551225
H	3.622572	-1.405194	0.639568
C	-2.798732	3.021524	-3.287269
C	-0.234914	-3.395526	-1.577156
H	0.377106	-2.636485	-2.077335
C	-3.750607	2.384696	-2.458048
C	3.008869	2.310297	-2.049875
H	3.076344	1.220237	-1.946156
C	-1.415674	2.790424	-3.142090
C	0.384414	-2.463703	2.515437
C	3.623151	2.952821	-3.135040
C	-0.622564	4.101017	0.661140
H	-1.121985	3.672880	-0.213410
C	2.270387	3.038306	-1.092971
C	-3.023227	-1.558048	1.463847
H	-2.632546	-1.132651	2.393696

C	0.001861	-1.243553	3.125649
C	1.902751	0.380176	2.249906
C	0.382078	-3.681713	3.221089
H	0.748575	-4.598717	2.746169
C	-0.308348	-3.407799	-0.171466
C	2.442426	-4.606390	0.421304
H	1.500907	-5.167386	0.391850
C	4.857665	-4.572072	0.346064
C	-1.176971	-4.315528	0.458170
H	-1.290763	-4.304393	1.546301
C	3.477169	4.351934	-3.259365
C	2.180908	4.439211	-1.221437
H	1.633624	5.024988	-0.477287
C	-1.808436	-5.224249	-1.688601
C	2.508820	1.305426	1.321763
C	-0.987060	-4.289362	-2.355785
C	-0.507142	-1.319223	4.441764
H	-0.845590	-0.401993	4.937499
C	3.920111	1.458808	1.231513
H	4.336881	2.159319	0.500122
C	-3.398917	3.410026	-5.553404
H	-2.426366	3.083346	-5.969496
H	-3.802448	4.227338	-6.172272
H	-4.099180	2.551324	-5.577300
C	-0.530803	5.753707	2.418582
C	-3.124696	2.824108	2.985726
H	-4.026991	3.429561	3.129557
C	-1.932028	-5.239722	-0.284515
C	-3.028530	-1.671817	-0.960557
H	-2.638610	-1.335391	-1.926853
C	4.194686	-0.153219	3.026402
H	4.850618	-0.701412	3.711747
C	3.653655	-5.310817	0.335014
C	0.680107	5.213660	2.904863
C	2.823486	-0.366044	3.062649
H	2.416749	-1.091396	3.775034
C	-2.112449	2.822572	3.960217
H	-2.223016	3.437525	4.860730
C	4.751472	0.760371	2.097119
H	5.835307	0.922952	2.066264
C	-4.492467	-3.096150	0.326395
C	-1.189763	5.219840	1.289087
C	-3.983938	-2.581502	1.536274
C	-0.097915	-3.717992	4.537104
H	-0.112830	-4.663553	5.090784

C	2.780368	5.114736	-2.298205
C	4.869904	-3.164585	0.455826
C	-0.568280	-2.536415	5.135440
H	-0.959543	-2.563015	6.158819
C	-4.011716	-2.671545	-0.932420
C	6.625833	-5.424931	-0.996476
H	7.548388	-6.012605	-0.868296
H	6.876256	-4.447508	-1.452494
H	5.937870	-5.967078	-1.675212
C	-1.949925	-7.275138	-2.887824
H	-2.710857	-7.870168	-3.418091
H	-1.544044	-7.867928	-2.044151
H	-1.122383	-7.037252	-3.584082
C	-1.989863	6.597466	4.088886
H	-1.505517	6.046995	4.919008
H	-2.847524	6.000394	3.724594
H	-2.349304	7.570529	4.457800
C	3.226639	5.203385	-5.455886
H	2.831024	4.246149	-5.849217
H	3.838318	5.691225	-6.231346
H	2.371992	5.858860	-5.197494
B	0.332232	0.142459	2.364001
C	-6.790835	-3.685114	0.527708
H	-7.102603	-2.995932	-0.281536
H	-6.934249	-3.176652	1.500941
H	-7.415494	-4.591540	0.497207
N	0.847034	-0.441336	-1.711764
C	-0.953498	-4.223842	-3.865742
H	-0.738450	-3.196786	-4.204505
H	-0.166357	-4.878724	-4.287296
H	-1.917941	-4.548820	-4.290322
C	-2.885877	-6.198511	0.388108
H	-3.932132	-5.936483	0.151143
H	-2.720684	-7.238237	0.053535
H	-2.767218	-6.160850	1.484250
C	-4.543704	-3.299288	-2.199464
H	-5.614558	-3.064066	-2.346128
H	-3.988625	-2.928636	-3.076331
H	-4.452389	-4.398190	-2.168555
C	-4.435325	-3.126502	2.872590
H	-5.288090	-2.551715	3.281794
H	-4.755819	-4.176660	2.773930
H	-3.614759	-3.068044	3.608170
C	-5.223382	2.669484	-2.644073
H	-5.600539	2.244131	-3.592728

H	-5.816952	2.235045	-1.822833
H	-5.409905	3.756482	-2.686277
C	-0.401368	3.490563	-4.019056
H	0.537739	3.661613	-3.467699
H	-0.150100	2.881704	-4.908754
H	-0.794276	4.458415	-4.372118
C	-2.481333	5.820003	0.788087
H	-2.620302	5.612552	-0.285994
H	-3.344996	5.377453	1.320365
H	-2.504379	6.908782	0.960178
C	1.357563	5.818963	4.112537
H	1.208768	6.911282	4.139504
H	0.936738	5.406285	5.049607
H	2.438221	5.598002	4.113199
C	2.679180	6.617537	-2.428486
H	1.788122	6.909713	-3.017655
H	2.584578	7.093314	-1.438437
H	3.565188	7.025914	-2.941799
C	4.411381	2.177353	-4.166281
H	5.353780	2.695145	-4.411947
H	4.637931	1.162024	-3.804012
H	3.844930	2.076627	-5.111436
C	3.689099	-6.818763	0.237482
H	3.917725	-7.151701	-0.792995
H	4.475282	-7.234656	0.889862
H	2.717153	-7.255537	0.519201
C	6.176079	-2.403806	0.479493
H	6.971479	-3.010373	0.943746
H	6.508057	-2.142795	-0.543615
H	6.064918	-1.459937	1.035550
H	2.529918	-1.428151	-1.433705

4.4.8 Optimized Structure Coordinates for Alternative Structure G (TPSS)

Fe	0.635045	-0.091171	0.206503
P	1.339813	2.043883	0.342392
P	-1.553967	0.419329	0.338897
P	0.619600	-2.319518	0.548051
O	-3.675167	4.222462	-3.853188
O	-1.669710	-6.173037	-3.470823
O	6.446780	-3.791432	0.925661
O	-0.495846	6.878999	3.363348
O	4.098264	3.926216	-4.644115
N	0.645340	-0.283985	-1.680345
O	-5.670839	-3.980720	0.392577
C	-0.793977	1.146431	2.797143
C	-2.192979	1.505873	-1.025285
C	2.377425	-2.887214	0.607496
C	-1.330398	2.173769	-1.912394
H	-0.251881	2.006451	-1.853871
C	-3.578853	1.752382	-1.121609
H	-4.272901	1.236092	-0.448905
C	-2.829856	-0.911726	0.349823
C	-0.786149	1.885661	3.997224
H	0.027150	1.744188	4.718944
C	1.524184	3.973572	2.357959
H	2.446010	3.457562	2.648405
C	-2.873983	2.297426	2.147607
H	-3.668939	2.481565	1.418921
C	0.763590	3.499104	1.273904
C	-1.841491	1.384517	1.879133
C	3.320399	-2.197045	-0.172815
H	2.986367	-1.373092	-0.815720
C	-3.205645	3.295717	-2.945364
C	0.568208	-3.750336	-1.847315
H	1.530583	-3.261434	-2.031825
C	-4.104612	2.652556	-2.062899
C	3.085012	1.793817	-1.843981
H	3.268894	0.776430	-1.476804
C	-1.813253	3.069042	-2.880183
C	-0.107295	-2.653985	2.193751
C	3.688823	2.200251	-3.042447
C	-0.410771	4.170214	0.889443
H	-1.004388	3.805415	0.044734
C	2.294088	2.684367	-1.080399
C	-3.305252	-1.434383	1.567654
H	-2.932393	-1.035924	2.514922

C	-0.295470	-1.485187	2.977325
C	1.755568	0.056564	2.179930
C	-0.473840	-3.928275	2.667125
H	-0.329869	-4.816117	2.042093
C	-0.137344	-3.488005	-0.653921
C	2.816362	-3.904745	1.473593
H	2.100412	-4.428014	2.115523
C	5.101198	-3.524921	0.767500
C	-1.379030	-4.118111	-0.435993
H	-1.965859	-3.890378	0.459208
C	3.479501	3.531351	-3.479107
C	2.142732	4.011142	-1.519105
H	1.555894	4.717608	-0.921929
C	-1.143889	-5.304902	-2.535160
C	2.437963	1.035403	1.366377
C	0.067794	-4.633436	-2.815633
C	-0.883054	-1.648633	4.250797
H	-1.061027	-0.764713	4.873996
C	3.855517	1.067802	1.278240
H	4.339069	1.813141	0.638813
C	-4.173048	3.689921	-5.089685
H	-3.389929	3.115256	-5.621077
H	-4.471929	4.554784	-5.700447
H	-5.049528	3.035091	-4.926312
C	-0.083401	5.745895	2.691640
C	-2.852930	3.007845	3.355593
H	-3.648169	3.728069	3.577666
C	-1.876318	-5.064427	-1.349080
C	-3.320993	-1.434714	-0.860968
H	-2.969477	-1.031063	-1.817790
C	3.988792	-0.774219	2.853376
H	4.593359	-1.468632	3.445511
C	4.177045	-4.235581	1.570045
C	1.113307	5.102911	3.082948
C	2.602723	-0.854887	2.895908
H	2.132456	-1.615547	3.526631
C	-1.801888	2.814957	4.267929
H	-1.776533	3.395327	5.196813
C	4.621584	0.184725	2.032125
H	5.715141	0.235083	1.990435
C	-4.763582	-2.937411	0.357335
C	-0.847072	5.305606	1.586459
C	-4.264483	-2.457970	1.590439
C	-1.049963	-4.055932	3.938502
H	-1.347828	-5.043028	4.307021

C	2.736674	4.458417	-2.713719
C	4.691560	-2.495454	-0.108169
C	-1.254332	-2.913493	4.728573
H	-1.710747	-3.011279	5.719357
C	-4.295823	-2.446336	-0.882032
C	7.012571	-4.720461	-0.010952
H	8.068093	-4.844137	0.274166
H	6.953659	-4.335669	-1.047002
H	6.500475	-5.700245	0.037290
C	-1.186890	-7.522643	-3.408962
H	-1.703527	-8.073840	-4.208689
H	-1.420219	-7.987021	-2.431887
H	-0.093713	-7.569067	-3.576948
C	-1.302130	6.647617	4.526406
H	-0.746105	6.080608	5.297308
H	-2.223777	6.092041	4.269827
H	-1.568063	7.638757	4.922042
C	3.260860	3.979898	-5.809436
H	2.824982	2.986676	-6.029828
H	3.909899	4.288725	-6.641956
H	2.441694	4.713483	-5.689187
B	0.175130	-0.060912	2.408267
C	-7.052309	-3.618134	0.252532
H	-7.248405	-3.144415	-0.727950
H	-7.364900	-2.925374	1.056768
H	-7.627067	-4.553113	0.327414
N	-0.054130	-0.854834	-2.571102
H	-0.802037	-1.388283	-2.081000
C	0.799633	-4.867412	-4.116421
H	1.346152	-3.961020	-4.425186
H	1.538317	-5.685808	-4.021570
H	0.090838	-5.147090	-4.912001
C	-3.141769	-5.844103	-1.080930
H	-3.698816	-6.011380	-2.016636
H	-2.897398	-6.841993	-0.669498
H	-3.795388	-5.336788	-0.356726
C	-4.808053	-2.995757	-2.193566
H	-5.283201	-3.977650	-2.049590
H	-5.554023	-2.315575	-2.646130
H	-3.981157	-3.112385	-2.914684
C	-4.761518	-3.049889	2.888038
H	-5.824525	-2.802157	3.062315
H	-4.690753	-4.150923	2.864040
H	-4.175202	-2.672610	3.739944
C	-5.586684	2.943201	-2.124813

H	-6.097066	2.285731	-2.853789
H	-6.063935	2.776668	-1.144811
H	-5.764040	3.984853	-2.438005
C	-0.880803	3.784682	-3.829720
H	0.170303	3.639691	-3.532514
H	-0.997251	3.409216	-4.863521
H	-1.104999	4.865068	-3.856292
C	-2.110076	6.031247	1.192429
H	-2.419340	5.756805	0.171377
H	-2.940756	5.767822	1.874083
H	-1.973057	7.123359	1.255585
C	1.918557	5.621511	4.251228
H	1.819980	6.715918	4.336004
H	1.564719	5.182507	5.203421
H	2.984569	5.360323	4.145651
C	2.589781	5.893352	-3.161185
H	1.675204	6.027669	-3.769729
H	2.507743	6.567543	-2.293113
H	3.452118	6.200493	-3.774736
C	4.553794	1.270703	-3.860157
H	5.540045	1.725782	-4.052620
H	4.698428	0.306264	-3.347417
H	4.100519	1.069853	-4.847543
C	4.672018	-5.292584	2.528961
H	5.013167	-6.195904	1.990229
H	5.537482	-4.921614	3.104178
H	3.877377	-5.598165	3.227886
C	5.704976	-1.704143	-0.901034
H	6.680016	-1.704013	-0.388199
H	5.855525	-2.130663	-1.910265
H	5.371879	-0.659864	-1.027263
H	1.403624	0.252588	-2.152785

4.4.9 Optimized Structure Coordinates for Alternative Structure I (TPSS)

Fe	0.875543	-0.095282	0.172938
P	1.328503	2.182164	0.243715
P	-1.363976	0.279216	0.186199
P	0.883533	-2.315119	0.709428
O	-3.413503	4.171874	-3.936922
O	-2.517152	-5.997082	-2.638163
O	6.243310	-5.053975	0.430658
O	-1.098198	6.910238	3.023292
O	4.194785	4.672184	-4.406320
N	1.972395	-0.635812	-1.275752
O	-5.502631	-4.082379	0.124409
C	-0.744060	1.184775	2.634748
C	-1.976818	1.324977	-1.219371
C	2.517197	-3.158559	0.511644
C	-1.098478	2.026332	-2.065755
H	-0.027282	1.814288	-2.020779
C	-3.364545	1.549009	-1.346710
H	-4.069610	0.992589	-0.719383
C	-2.571045	-1.106618	0.177800
C	-0.846808	1.972333	3.799559
H	-0.032406	1.967094	4.534068
C	1.222784	4.169495	2.219543
H	2.180929	3.764256	2.561249
C	-2.933243	2.040113	1.910460
H	-3.735405	2.093735	1.168799
C	0.549896	3.572616	1.137395
C	-1.789580	1.254199	1.690783
C	3.708055	-2.406377	0.525284
H	3.659391	-1.313508	0.572540
C	-2.962462	3.189811	-3.078228
C	-0.004796	-3.511548	-1.663390
H	0.781037	-2.915897	-2.145520
C	-3.876966	2.485322	-2.259673
C	3.099377	2.192167	-1.939031
H	3.248273	1.132125	-1.707915
C	-1.571261	2.963529	-2.998719
C	0.396793	-2.535074	2.455660
C	3.756275	2.757925	-3.039765
C	-0.666041	4.113948	0.683655
H	-1.183832	3.664559	-0.167952
C	2.247148	2.968756	-1.126471
C	-3.078406	-1.607210	1.388798
H	-2.709093	-1.211322	2.340710

C	0.031213	-1.323983	3.087866
C	1.930569	0.348266	2.186066
C	0.347662	-3.770739	3.128040
H	0.681212	-4.688844	2.633133
C	-0.203124	-3.436762	-0.269066
C	2.592410	-4.563487	0.435858
H	1.672861	-5.160008	0.410809
C	5.006181	-4.444444	0.406722
C	-1.187879	-4.247142	0.318772
H	-1.388814	-4.176569	1.391281
C	3.524432	4.122573	-3.334191
C	2.063983	4.334553	-1.419878
H	1.424730	4.952276	-0.781375
C	-1.723113	-5.199366	-1.836346
C	2.509050	1.384651	1.371064
C	-0.769314	-4.368365	-2.468004
C	-0.487131	-1.408909	4.399115
H	-0.808297	-0.495200	4.911030
C	3.902041	1.623881	1.352215
H	4.308670	2.391634	0.686009
C	-3.919132	3.719939	-5.201643
H	-3.150489	3.148497	-5.756987
H	-4.185301	4.624340	-5.768639
H	-4.817741	3.086445	-5.080274
C	-0.557266	5.793175	2.417912
C	-3.024551	2.794871	3.086451
H	-3.908502	3.416005	3.266727
C	-1.946370	-5.153325	-0.444045
C	-3.018678	-1.652216	-1.041734
H	-2.612293	-1.282407	-1.989250
C	4.203725	-0.092549	3.046539
H	4.862118	-0.650834	3.720057
C	3.828958	-5.228546	0.395513
C	0.681339	5.286706	2.875259
C	2.845142	-0.393200	3.001328
H	2.454871	-1.191858	3.639475
C	-1.972905	2.777781	4.017849
H	-2.033575	3.398345	4.918538
C	4.738722	0.910335	2.210983
H	5.810573	1.134674	2.240542
C	-4.544489	-3.086250	0.162856
C	-1.234977	5.231062	1.311769
C	-4.062651	-2.611306	1.402761
C	-0.143928	-3.819729	4.438998
H	-0.193978	-4.776584	4.969430

C	2.698088	4.931652	-2.521822
C	4.962639	-3.032553	0.470187
C	-0.580302	-2.639398	5.064565
H	-0.979371	-2.679748	6.083540
C	-4.015148	-2.637199	-1.070428
C	6.764828	-5.481024	-0.836321
H	7.756030	-5.911974	-0.631985
H	6.870737	-4.626542	-1.532349
H	6.121128	-6.248748	-1.305289
C	-2.125452	-7.371617	-2.767687
H	-2.837114	-7.829793	-3.470638
H	-2.173446	-7.902954	-1.799526
H	-1.099479	-7.456850	-3.173843
C	-1.923757	6.649581	4.165877
H	-1.348809	6.163207	4.977177
H	-2.782362	6.004126	3.900245
H	-2.290699	7.626271	4.513999
C	3.432450	4.810483	-5.613906
H	3.062942	3.827732	-5.964973
H	4.116018	5.234473	-6.364730
H	2.569883	5.489664	-5.477182
B	0.353657	0.063723	2.354263
C	-6.858533	-3.654891	0.317985
H	-7.158567	-2.923358	-0.456428
H	-7.004668	-3.201316	1.316143
H	-7.482457	-4.557194	0.233736
N	0.900920	-0.143380	-1.880938
H	0.330835	-0.892740	-2.329879
C	-0.609276	-4.416785	-3.968738
H	0.093430	-3.644310	-4.321272
H	-0.232389	-5.399661	-4.304830
H	-1.583871	-4.267957	-4.465250
C	-2.986478	-6.033894	0.204594
H	-3.915857	-6.048273	-0.386338
H	-2.626659	-7.075859	0.296642
H	-3.225612	-5.673494	1.216338
C	-4.520434	-3.221847	-2.367683
H	-5.611664	-3.085167	-2.471547
H	-4.027353	-2.743008	-3.229059
H	-4.324494	-4.307055	-2.417176
C	-4.574644	-3.173377	2.709521
H	-5.416863	-2.575971	3.106413
H	-4.932704	-4.206893	2.574769
H	-3.777863	-3.165944	3.472846
C	-5.361298	2.758980	-2.345261

H	-5.843341	2.141139	-3.126153
H	-5.862156	2.527315	-1.390516
H	-5.545466	3.815770	-2.598617
C	-0.619092	3.743446	-3.875972
H	0.419057	3.407626	-3.724864
H	-0.872774	3.637106	-4.945953
H	-0.674221	4.822852	-3.644227
C	-2.547288	5.807916	0.838940
H	-2.764791	5.496441	-0.195412
H	-3.379831	5.451145	1.474405
H	-2.537911	6.908502	0.899260
C	1.393480	5.933682	4.040303
H	1.180949	7.014530	4.074360
H	1.057619	5.499413	5.001297
H	2.483698	5.780182	3.973743
C	2.511372	6.399839	-2.824392
H	1.650502	6.560244	-3.501567
H	2.314103	6.969840	-1.901837
H	3.406747	6.813021	-3.316417
C	4.691208	1.950326	-3.909687
H	5.664809	2.458687	-4.014774
H	4.854097	0.945511	-3.487930
H	4.284764	1.830451	-4.930586
C	3.905842	-6.737527	0.364223
H	3.969505	-7.118910	-0.672513
H	4.800955	-7.090850	0.901888
H	3.010772	-7.187809	0.823617
C	6.248344	-2.240111	0.501864
H	6.908402	-2.603235	1.309194
H	6.813300	-2.349559	-0.442262
H	6.045330	-1.168747	0.658201
H	2.247351	-1.612425	-1.506322

4.4.10 Optimized Structure Coordinates for Truncated $[(\text{ArP}_3\text{B})\text{Fe}(\text{N}_2)]^-$ (TPSS)

P	2.270057	0.354216	0.982575
P	-1.037116	-1.930853	0.708379
P	-1.163696	1.498754	0.525347
O	4.501582	5.950779	0.390850
O	0.023239	6.400148	-2.821203
O	5.343450	-3.357110	-2.656557
O	-5.580962	-2.621193	-3.238652
O	2.945716	-6.462142	0.312408
O	-7.050191	0.240766	-0.066083
C	1.391553	-0.549105	3.370764
C	4.355814	2.272831	0.349764
H	4.983082	1.432299	0.031187
C	-3.785356	-2.488918	-0.025873
H	-4.031101	-2.513441	1.039143
C	4.853980	3.581978	0.224926
C	2.718399	4.453724	1.100171
C	1.541200	-1.165549	4.637093
H	0.647780	-1.506420	5.174627
C	2.272877	3.130141	1.238562
H	1.259043	2.951097	1.608239
C	-4.831000	-2.644344	-0.951942
C	4.022829	4.658333	0.603959
C	2.590489	-0.172219	2.714689
C	3.064672	2.032848	0.858162
C	3.503462	-0.424661	-1.412194
H	3.040554	0.483381	-1.812939
C	-1.717929	-2.068972	2.410370
C	1.929693	-4.641143	1.576449
C	-4.527264	-2.546551	-2.323409
C	-2.977864	1.176891	0.355187
C	3.854875	-0.291600	3.316560
H	4.751389	0.050369	2.784779
C	1.952765	-5.484937	0.445167
C	0.323886	3.094374	-1.205265
H	1.058398	2.300081	-1.037307
C	3.403628	-0.707551	-0.032478
C	-2.458129	-2.270925	-0.439279
C	4.010270	-1.878237	0.457671
H	3.956362	-2.110988	1.525714
C	-4.941377	0.828029	-1.072803
C	0.031817	-3.445352	0.571501
C	-0.944976	2.953904	-0.623658
C	-0.300060	1.471209	3.090667

C	-3.579762	1.125711	-0.918738
H	-2.976641	1.333970	-1.810058
C	3.965044	-0.890888	4.580782
H	4.947984	-1.017663	5.050575
C	-2.581778	-3.066116	2.904754
H	-2.854390	-3.923840	2.278366
C	-3.745403	0.834820	1.482150
H	-3.271580	0.811585	2.470128
C	-1.901099	3.967578	-0.837426
H	-2.906011	3.868013	-0.409712
C	-1.815018	-0.907278	4.516620
H	-1.520672	-0.068660	5.160918
C	1.040333	-5.331410	-0.618497
C	2.802806	-1.348128	5.225765
H	2.881837	-1.836173	6.205449
C	-0.291612	5.227959	-2.133820
C	0.685827	4.230174	-1.949372
C	0.963435	-3.625443	1.612016
H	0.953366	-2.935498	2.463751
C	-1.251952	-1.008671	3.220699
C	4.138922	-1.304034	-2.297817
C	-3.220160	-2.276825	-2.778714
C	0.079834	-4.308123	-0.537269
H	-0.636973	-4.187349	-1.357645
C	-5.106209	0.499674	1.368143
C	4.709054	-2.484763	-1.772328
C	-1.383475	3.615962	2.511030
H	-1.924539	4.234302	1.786021
C	4.689701	-2.769597	-0.393078
C	-1.006596	2.301133	2.183806
C	-1.019544	4.156013	3.753731
H	-1.284594	5.190249	4.003765
C	-2.735660	-1.850213	4.996250
H	-3.159123	-1.741751	6.002931
C	0.055640	2.048446	4.332541
H	0.633022	1.451165	5.049977
C	-1.591852	5.111625	-1.591567
C	-0.286455	3.370071	4.658081
H	0.024010	3.793857	5.621798
C	-2.202289	-2.150987	-1.820415
H	-1.194009	-1.904404	-2.162629
C	4.953440	6.614896	1.568639
H	5.323289	7.604342	1.253376
H	5.776557	6.055616	2.058171
H	4.137399	6.752668	2.305874

C	-3.098792	-2.953342	4.202414
H	-3.789290	-3.712873	4.589523
C	-5.693919	0.547617	0.088526
C	-5.733044	-3.891482	-3.864967
H	-6.607574	-3.814807	-4.532692
H	-5.912158	-4.692964	-3.119959
H	-4.842579	-4.165199	-4.465450
C	-0.030670	6.287388	-4.240527
H	0.201689	7.285369	-4.648063
H	-1.038053	5.978722	-4.586046
H	0.708681	5.558600	-4.626572
C	4.557792	-4.500340	-3.003366
H	5.142041	-5.071308	-3.744570
H	3.589177	-4.201550	-3.450774
H	4.352005	-5.143472	-2.126222
C	2.696368	-7.672176	1.022515
H	3.534911	-8.352391	0.796324
H	1.746624	-8.143357	0.697087
H	2.649078	-7.506576	2.116952
C	-7.928101	1.332880	0.185029
H	-8.952399	0.970489	-0.006286
H	-7.713837	2.189956	-0.485247
H	-7.858773	1.683741	1.234388
B	-0.016226	-0.085459	2.676673
N	0.385483	-0.172070	-1.417020
N	0.483059	-0.146373	-2.560263
Fe	0.214750	-0.178880	0.367970
C	2.090472	4.380693	-2.487849
H	2.800275	3.814478	-1.862608
H	2.173818	3.992323	-3.521807
H	2.396368	5.440673	-2.496907
C	-2.597182	6.220976	-1.807458
H	-2.878758	6.314292	-2.873315
H	-3.518328	6.035073	-1.230498
H	-2.179342	7.197449	-1.504906
C	-5.901664	0.074212	2.582388
H	-5.261289	-0.498219	3.275790
H	-6.296332	0.945923	3.140643
H	-6.759683	-0.551815	2.285959
C	-5.596944	0.781099	-2.434291
H	-6.052265	-0.205676	-2.624154
H	-6.402213	1.534947	-2.525910
H	-4.854623	0.973453	-3.226227
C	4.196831	-1.030134	-3.782900
H	3.819347	-0.019825	-4.009113

H	5.226630	-1.129637	-4.169235
H	3.572398	-1.750681	-4.343679
C	5.397459	-3.990384	0.150463
H	6.283226	-4.226808	-0.463868
H	5.720527	-3.818163	1.190701
H	4.742002	-4.880835	0.152062
C	6.227771	3.860471	-0.342444
H	6.165605	4.552133	-1.201795
H	6.885674	4.343458	0.404924
H	6.712580	2.926569	-0.671704
C	1.785652	5.606337	1.395093
H	1.768458	5.853604	2.473593
H	2.086763	6.505994	0.833332
H	0.755492	5.336731	1.109379
C	2.909469	-4.795090	2.719142
H	2.498158	-5.449770	3.512519
H	3.859736	-5.236824	2.378005
H	3.117451	-3.817038	3.184902
C	1.116561	-6.248270	-1.819275
H	0.959761	-7.307263	-1.538837
H	0.353216	-5.976311	-2.567170
H	2.110416	-6.193493	-2.298454
C	-2.928728	-2.067962	-4.248341
H	-2.047082	-1.417476	-4.374396
H	-2.711708	-3.023456	-4.766002
H	-3.795015	-1.608037	-4.754381
C	-6.255650	-2.868520	-0.499300
H	-6.890266	-2.000644	-0.748521
H	-6.700070	-3.758273	-0.982248
H	-6.295057	-3.009288	0.593834

References

- (1) Burgess, B. K.; Lowe, D. J. *Chem. Rev.* **1996**, *96*, 2983.
- (2) Eady, R. R. *Chem. Rev.* **1996**, *96*, 3013.
- (3) Chatt, J.; Dilworth, J. R.; Richards, R. L. *Chem. Rev.* **1978**, *78*, 589.
- (4) Hidai, M.; Mizobe, Y. *Chem. Rev.* **1995**, *95*, 1115.
- (5) Yandulov, D. V.; Schrock, R. R. *Inorg. Chem.* **2005**, *44*, 1103.
- (6) Yandulov, D. V.; Schrock, R. R. *Science* **2003**, *301*, 76.
- (7) Buscagan, T. M.; Oyala, P. H.; Peters, J. C. *Angew. Chem. Int. Ed.* **2017**, *56*, 6921.
- (8) Chalkley, M. J.; Del Castillo, T. J.; Matson, B. D.; Roddy, J. P.; Peters, J. C. *ACS Cent. Sci.* **2017**, *3*, 217.
- (9) Anderson, J. S.; Rittle, J.; Peters, J. C. *Nature* **2013**, *501*, 84.
- (10) Rittle, J.; Peters, J. C. *J. Am. Chem. Soc.* **2016**, *138*, 4243.
- (11) Hoffman, B. M.; Dean, D. R.; Seefeldt, L. C. *Acc. Chem. Res.* **2009**, *42*, 609.
- (12) Del Castillo, T. J.; Thompson, N. B.; Peters, J. C. *J. Am. Chem. Soc.* **2016**, *138*, 5341.
- (13) Hill, P. J.; Doyle, L. R.; Crawford, A. D.; Myers, W. K.; Ashley, A. E. *J. Am. Chem. Soc.* **2016**, *138*, 13521.
- (14) Thompson, N. B.; Green, M. T.; Peters, J. C. *J. Am. Chem. Soc.* **2017**, *139*, 15312.
- (15) Chatt, J.; Pearman, A. J.; Richards, R. L. *J. Chem. Soc., Dalton Trans.* **1976**, 1520.
- (16) Anderson, J. S.; Cutsail, G. E.; Rittle, J.; Connor, B. A.; Gunderson, W. A.; Zhang, L.; Hoffman, B. M.; Peters, J. C. *J. Am. Chem. Soc.* **2015**, *137*, 7803.
- (17) Dilworth, J. R. *Coord. Chem. Rev.* **2017**, *330*, 53.

- (18) Takahashi, T.; Mizobe, Y.; Sato, M.; Uchida, Y.; Hidai, M. *J. Am. Chem. Soc.* **1980**, *102*, 7461.
- (19) Geri, J. B.; Shanahan, J. P.; Szymczak, N. K. *J. Am. Chem. Soc.* **2017**, *139*, 5952.
- (20) Yandulov, D. V.; Schrock, R. R. *Can. J. Chem.* **2005**, *83*, 341.
- (21) Lehnert, N.; Tucek, F. *Inorg. Chem.* **1999**, *38*, 1659.
- (22) Yandulov, D. V.; Schrock, R. R.; Rheingold, A. L.; Ceccarelli, C.; Davis, W. M. *Inorg. Chem.* **2003**, *42*, 796.
- (23) George, T. A.; Koczon, L. M.; Tisdale, R. C.; Gebreyes, K.; Ma, L.; Shaikh, S. N.; Zubieta, J. *Polyhedron* **1990**, *9*, 545.
- (24) Hinrichsen, S.; Kindjajev, A.; Adomeit, S.; Krahmer, J.; Näther, C.; Tucek, F. *Inorg. Chem.* **2016**, *55*, 8712.
- (25) Labios, L. A.; Heiden, Z. M.; Mock, M. T. *Inorg. Chem.* **2015**, *54*, 4409.
- (26) Labios, L. A.; Weiss, C. J.; Egbert, J. D.; Lense, S.; Bullock, R. M.; Dougherty, W. G.; Kassel, W. S.; Mock, M. T. *Z. Anorg. Allg. Chem.* **2015**, *641*, 105.
- (27) Weiss, C. J.; Egbert, J. D.; Chen, S.; Helm, M. L.; Bullock, R. M.; Mock, M. T. *Organometallics* **2014**, *33*, 2189.
- (28) Sönksen, L.; Gradert, C.; Krahmer, J.; Näther, C.; Tucek, F. *Inorg. Chem.* **2013**, *52*, 6576.
- (29) Romer, R.; Gradert, C.; Bannwarth, A.; Peters, G.; Nather, C.; Tucek, F. *Dalton Trans.* **2011**, *40*, 3229.
- (30) Yuki, M.; Miyake, Y.; Nishibayashi, Y. *Organometallics* **2009**, *28*, 5821.
- (31) Arashiba, K.; Miyake, Y.; Nishibayashi, Y. *Nat. Chem.* **2011**, *3*, 120.

- (32) Anderson, S. N.; Fakley, M. E.; Richards, R. L.; Chatt, J. *J. Chem. Soc., Dalton Trans.* **1981**, 1973.
- (33) Matson, B. D., Interplay of Proton Transfer, Electron Transfer and Proton-Coupled Electron Transfer in Transition Metal Mediated Nitrogen Fixation; PhD Dissertation, California Institute of Technology, 2018.
- (34) Rittle, J.; Peters, J. C. *J. Am. Chem. Soc.* **2017**, *139*, 3161.
- (35) Moret, M.-E.; Peters, J. C. *J. Am. Chem. Soc.* **2011**, *133*, 18118.
- (36) Suess, D. L. M.; Peters, J. C. *J. Am. Chem. Soc.* **2013**, *135*, 4938.
- (37) Lee, Y.; Mankad, N. P.; Peters, J. C. *Nat. Chem.* **2010**, *2*, 558.
- (38) Chiswell, B.; Venanzi, L. M. *J. Chem. Soc. A: Inorg., Phys., Theor.* **1966**, 417.
- (39) Provencher, L.; Wynn, H.; Jones, J. B.; Krawczyk, A. R. *Tetrahedron: Asymmetry* **1993**, *4*, 2025.
- (40) Moret, M.-E.; Peters, J. C. *Angew. Chem. Int. Ed.* **2011**, *50*, 2063.
- (41) Lucken, E. A. C. *Nuclear Quadrupole Coupling Constants*; Academic Press: London, 1969.
- (42) Townes, C. H.; Dailey, B. P. *J. Chem. Phys.* **1949**, *17*, 782.
- (43) Fong, H.; Moret, M.-E.; Lee, Y.; Peters, J. C. *Organometallics* **2013**, *32*, 3053.
- (44) Creutz, S. E.; Peters, J. C. *J. Am. Chem. Soc.* **2014**, *136*, 1105.
- (45) Del Castillo, T. J.; Thompson, N. B.; Suess, D. L. M.; Ung, G.; Peters, J. C. *Inorg. Chem.* **2015**, *54*, 9256.
- (46) Weitz, I. S.; Rabinovitz, M. *J. Chem. Soc., Perkin Trans. 1* **1993**, 117.
- (47) Robbins, J. L.; Edelstein, N.; Spencer, B.; Smart, J. C. *J. Am. Chem. Soc.* **1982**, *104*, 1882.

- (48) Vicente, J.; Chicote, M.-T.; Guerrero, R.; Jones, P. G. *J. Chem. Soc., Dalton Trans.* **1995**, 1251.
- (49) Xu, Y.; Alcock, N. W.; Clarkson, G. J.; Docherty, G.; Woodward, G.; Wills, M. *Org. Lett.* **2004**, 6, 4105.
- (50) Berto, T. C.; Hoffman, M. B.; Murata, Y.; Landenberger, K. B.; Alp, E. E.; Zhao, J.; Lehnert, N. *J. Am. Chem. Soc.* **2011**, 133, 16714.
- (51) Stoll, S.; Schweiger, A. *J. Magn. Reson.* **2006**, 178, 42.
- (52) Sheldrik, G. M.; Universität Göttingen: Göttingen, Germany, 2000.
- (53) Grimme, S.; Antony, J.; Ehrlich, S.; Krieg, H. *J. Chem. Phys.* **2010**, 132, 154104.

Appendix A

ADDITIONAL CHARACTERIZATION DATA AND SYNTHETIC DETAILS

Experimental:

General Considerations: All operations were carried out using standard Schlenk or glovebox techniques under inert atmospheres of N₂ or argon. Unless otherwise noted all solvents were deoxygenated and dried by thoroughly sparging with N₂ gas followed by passage through an activated alumina column in the solvent purification system by SG Water, USA LLC and storage over 3 Å molecular sieves prior to use. Non-halogenated solvents were tested with a standard purple solution of sodium benzophenone ketyl in tetrahydrofuran in order to confirm effective oxygen and moisture removal. All reagents were purchased from commercial vendors and used without further purification unless otherwise stated. [Cp₂Fe][BAr^F₂₄], [(TPB)Fe][BAr^F₂₄], (TPB)FeOH, [(P₃B)Co][BAr^F₂₄] were synthesized according to literature procedures.¹⁻³ ArP₃B was prepared according to the procedure given in Chapter 4. Deuterated solvents were purchased from Cambridge Isotope Laboratories, Inc., degassed and stored over activated 3 Å molecular sieves prior to use. Elemental analyses were performed by California Institute of Technology's Elemental Analysis facility or by Midwest Microlab, LLC, Indianapolis, IN.

Nuclear Magnetic Resonance Spectroscopy: ¹H and ¹³C chemical shifts are reported in ppm relative to tetramethylsilane, using residual solvent resonances as internal standards. ³¹P chemical shifts are reported in ppm and referenced externally to 85% aqueous H₃PO₄. ¹⁹F chemical shifts are reported in ppm and referenced externally to trifluorotoluene at -63.72 ppm. Solution phase magnetic measurements were performed by the method of Evans.

Infrared Spectroscopy: Solid IR measurements were obtained on a Bruker Alpha spectrometer equipped with a diamond ATR probe.

EPR Spectroscopy: Continuous wave X-band EPR spectra were obtained on a Bruker EMX spectrometer on 2-9 mM solutions prepared as frozen glasses in 2-MeTHF, toluene or methylcyclohexane. Spectra were simulated using the EasySpin suite of programs with Matlab 2016.⁴

X-Ray Crystallography: XRD studies were carried out at the Beckman Institute Crystallography Facility on a Bruker AXS KAPPA APEXII diffractometer (Mo K α radiation) or a Bruker AXS D8 VENTURE (Mo K α or Cu K α). Structures were solved using SHELXS or SHELXT and refined against F² on all data by full-matrix least squares with SHELXL.⁵ The crystals were mounted on a mitegen loops under Paratone N oil. With the exception of any S-H or O-H hydrogen atoms which were located in the difference map, all hydrogen atoms were placed at geometrically calculated positions and refined using a riding model. The isotropic displacement parameters of all hydrogen atoms were fixed at 1.2 (1.5 for methyl groups) times the U_{eq} of the atoms to which they are bonded.

Electrochemistry. Electrochemical measurements were carried out using a CD instruments 600B electrochemical analyzer. A freshly-polished glassy carbon electrode was used as the working electrode and a graphite rod was used as the auxiliary electrode. Solutions (THF) of electrolyte (0.1 M tetra-n-butylammonium hexafluorophosphate) contained ferrocene (0.1 mM), to serve as an internal reference, and analyte (0.2 mM). All reported potentials are referenced to the ferrocene/ferrocenium couple, Cp₂Fe/[Cp₂Fe]⁺.

(TPB)Co(SH), Method 1: 171.8 mg (0.114 mmol) of [(TPB)Co][BAr^F₄] was dissolved in ~ 5 mL Et₂O giving a dark red-purple solution. This solution was added to a stirring suspension of NaSH (34.8 mg, 0.612 mmol) in 5 mL Et₂O and allowed to stir for 14 hours. The stirring solution gradually turned from dark red-purple to yellow-orange. The solvent was removed under reduced

pressure and the remaining solids were extracted in pentane (~50 mL) and filtered through celite giving a clear yellow-orange solution. Removal of solvent under reduced pressure yielded (TPB)Co(SH) as an orange powder. This powder was then washed with cold MeCN (3 x 3 mL) to remove residual NaBAr^F₂₄. Crystals suitable for X-ray diffraction studies were grown by slow vapor diffusion of a concentrated Et₂O solution into HMDSO. Yield 77.6 mg (0.113 mmol) 99%. Elemental Analysis % C; H; N: Found (Calc): C: 63.39 (63.35); H: 8.12 (8.12); N: 0.00 (0.00). ¹H NMR (300 MHz, C₆D₆) δ 119.91 (s, br), 27.18 (s, br), 17.84 (s, br), 16.76 (s), 5.49 (s, br), 0.99 (s, br), 0.01 (s, br), -0.17 (s, br), -1.18 (s, br), -7.83 (s). Solution magnetic moment (C₆D₆, RT) 3.2 μ_B.

(TPB)Co(SH), Method 2: 54.4 mg (0.08 mmol) of (TPB)Co(N₂) was dissolved in ~ 6 mL C₆H₆ giving a yellow solution. This solution was degassed via 3 freeze-pump-thaw cycles turning from yellow to brown. The frozen solution was then exposed to a calibrated bulb charged with 0.088 mmol of H₂S gas and the solution was allowed to thaw. The stirring solution rapidly turned from brown to green and was allowed to stir for ca. 14 hours resulting in an orange-brown solution. The solvent was removed under reduced pressure yielding (TPB)Co(SH) as a fine orange powder. Samples prepared by this method gave spectroscopic signatures identical to those observed in samples prepared by method 1. Yield 51.7 mg (0.075 mmol) 94.3 %.

Reaction of (TPB)Co(SH) with FeCp₂][BAr^F₂₄]: 40.4 mg (0.059 mmol) (TPB)Co(SH) was suspended in ~ 5 mL Et₂O and cooled to -78 °C in the glovebox cold well. A chilled solution of 62.0 mg (0.059 mmol) [FeCp₂][BAr^F₄] in ~ 3 mL Et₂O was added to (TPB)Co(SH) causing a rapid color change from brown to bright green. The reaction was allowed to stir cold for 3.5 hours and then at room temperature for 15 minutes causing a color change from green to dark brown. All volatiles were removed *in vacuo* and the remaining dark solids were washed with pentane to

remove FeCp_2 . $[(\text{TPB})\text{Co}][\text{BAr}^{\text{F}}_{24}]$ was identified in the remaining solids along with a dark insoluble powder.

(TPB)Co(OH): 168.8 mg (0.112 mmol) of $[(\text{TPB})\text{Co}][\text{BAr}^{\text{F}}_4]$ was dissolved in ~ 5 mL Et_2O giving a dark red-purple solution. This solution was added to a stirring suspension of NaOH (194.7 mg, 4.87 mmol) in 5 mL Et_2O and allowed to stir for 14 hours. The stirring solution gradually turned from dark red-purple to yellow-orange. The solvent was removed under reduced pressure and the remaining solids were extracted in pentane (~ 50 mL) and filtered through celite giving a clear yellow-orange solution. Removal of solvent under reduced pressure yielded *(TPB)Co(OH)* as a yellow powder. This powder was then washed with cold MeCN (3 x 3 mL) to remove residual $\text{NaBAr}^{\text{F}}_{24}$. Crystals suitable for X-ray diffraction studies were grown by slow vapor diffusion of a concentrated Et_2O solution into HMDSO. Yield 72.8 mg (0.109 mmol) 97%. Elemental Analysis % C; H; N: Found (Calc): C: 64.86 (64.88); H: 8.14 (8.32); N: 0.23 (0.00) ^1H NMR (300 MHz, C_6D_6) δ 164.69 (s, br), 22.73 (s, br), 15.90 (s), 9.36 (s, br), 5.75 (s, br), 2.36 (s, br), 0.09 (s, br), -5.37 (s, br), -8.88 (s). Solution magnetic moment (C_6D_6 , RT) $2.9 \mu_{\text{B}}$.

(TPB)Fe(SH): 106.6 mg (0.071 mmol) of $[(\text{TPB})\text{Fe}][\text{BAr}^{\text{F}}_4]$ was dissolved in ~ 5 mL Et_2O giving an orange solution. This solution was added to a stirring suspension of NaSH (54.3 mg, 0.97 mmol) in 5 mL Et_2O and allowed to stir for 14 hours. The solvent was removed under reduced pressure and the remaining solids were extracted in pentane (~ 50 mL) and filtered through celite giving a clear yellow-orange solution. Removal of solvent under reduced pressure yielded *(TPB)Fe(SH)* as a brown powder. This powder was then washed with cold MeCN (3 x 3 mL) to remove residual $\text{NaBAr}^{\text{F}}_{24}$. Crystals suitable for X-ray diffraction studies were grown by slow vapor diffusion of a concentrated Et_2O solution into HMDSO. Yield 47.1 mg (0.69 mmol) 97%. Elemental Analysis % C; H; N: Found (Calc): C: 63.59 (63.64); H: 8.11 (8.16); N: 0.00 (0.00) ^1H

NMR (300 MHz, C₆D₆) δ 91.65 (s, br), 32.28 (s), 23.89 (s, br), 17.75 (s, br), 6.01 (s, br), 4.29 (s, br), 1.37 (s, br), -0.23 (s), -1.65 (s, br), -21.44 (s, br). Solution magnetic moment (C₆D₆, RT) 4.1 μ_B .

Reaction of (TPB)Fe(SH) with [FeCp₂][BAr^F₄]: 43.1 mg (0.0634 mmol) (TPB)Fe(SH) was dissolved in ~ 5 mL Et₂O and cooled to -78 °C in the glovebox cold well. A chilled solution of 66.9 mg (0.0638 mmol) [FeCp₂][BAr^F₄] in ~ 3 mL Et₂O was added to (TPB)Fe(SH) causing a rapid color change from brown to dark brown. The reaction was allowed to stir cold for 3.5 hours and then at room temperature for 15 minutes. All volatiles were removed *in vacuo* and the remaining dark solids were washed with pentane to remove FeCp₂. The remaining dark solids were dissolved in minimal Et₂O and layered with pentane and stored at -35 °C. [(TPB)Fe][BAr^F₂₄] was identified in the remaining solids along with a dark insoluble powder.

(^{Ar}P₃B)CoBr: 656.3 mg (0.444 mmol) of ^{Ar}P₃B and 109.0 mg (0.498 mmol) of CoBr₂ were dissolved in THF giving an inky black-brown solution. Volatiles were removed *en vacuo* and the remaining solids were triturated in Et₂O and evaporated to dryness. The remaining solids were then dissolved in benzene and stirred vigorously over freshly prepared 1 % Na/Hg amalgam (0.496 mmol) for ca. 14 hours. The solution was filtered through Celite and volatiles were removed *in vacuo* leaving a dark orange foam. The solids were extracted in pentane and filtered through Celite again removing some blue-green solids (presumably unreacted cobalt halide solvates). After standing an orange microcrystalline solid began to precipitate and the solution was transferred to a -35 °C freezer for ca. 12 hours after which time the mother liquor was decanted and the solids were washed with a 1 mL portion of cold pentane. Crystals of quality suitable for X-ray diffraction studies were grown by slow evaporation of a pentane solution into HMDSO. Yield 423.6 mg (.262

mmol) 58.8 %. ^1H NMR (400 MHz, C_6D_6) δ 23.63 (s), 15.65 (s), 3.80 (s, br), 2.91 (s), 2.73 (s), 1.77 (s, br), 1.02 (s), 0.44 (s), 0.16 (s), -5.69 (s, br), -8.04 (s).

$(^{\text{Ar}}\text{P}_3\text{B})\text{Co}(\text{N}_2)$: 246.0 mg (0.152 mmol) of $(^{\text{Ar}}\text{P}_3\text{B})\text{CoBr}$ was dissolved in benzene (ca. 10 mL) and stirred vigorously over an excess of freshly prepared 1 % Na/Hg amalgam (0.761 mmol) for ca. 14 hours. The orange solution was then filtered through Celite and lyophilized giving $(^{\text{Ar}}\text{P}_3\text{B})\text{Co}(\text{N}_2)$ as a fine orange powder. Crystals of quality suitable for X-ray diffraction studies were grown by slow evaporation of a pentane solution into HMDSO. Yield 200.9 mg (0.128 mmol) 84 %. ^1H NMR (400 MHz, C_6D_6) δ 13.91 (s, br), 11.39 (s, br), 5.38 (s, br), 3.43 (s, br), 3.14 (s, br), 2.23 (s, br), 1.30 (s, br), 0.73 (s, br), -3.28 (s, br). IR (thin film from C_6D_6): $\nu_{\text{N}_2} = 2106\text{ cm}^{-1}$.

$[(^{\text{Ar}}\text{P}_3\text{B})\text{Co}][\text{BAr}^{\text{F}}_{24}]$: 200.9 mg (0.128 mmol) of $(^{\text{Ar}}\text{P}_3\text{B})\text{Co}(\text{N}_2)$ was dissolved in ca. 4 mL Et_2O and chilled to $-78\text{ }^\circ\text{C}$ and combined with a chilled solution of $[\text{FeCp}_2][\text{BAr}^{\text{F}}_{24}]$ (34.5 mg, 0.128 mmol) in ca. 4 mL Et_2O . The solution turns from dark orange to dark green on addition of $[\text{FeCp}_2][\text{BAr}^{\text{F}}_{24}]$. The solution was allowed to slowly warm to room temperature overnight (ca 14 hours) yielding a dark green solution. The solution was concentrated to ca. 2 mL and layered with pentane and stored at $-35\text{ }^\circ\text{C}$ for several days over which time large dark green blocks of $[(^{\text{Ar}}\text{P}_3\text{B})\text{Co}][\text{BAr}^{\text{F}}_{24}]$ formed. After decanting of the mother liquor the solids were washed with pentane. Crystals obtained via this method were of sufficient quality for X-ray diffraction studies. Yield 209.8 mg (0.0873 mmol) 68.2 %. ^1H NMR (400 MHz, Benzene- d_6) δ 8.42 (s, 8H), 7.72 (s, 4H), 7.48-7.28 (m, br, 3H) 7.26 (d, $^3J_{\text{HH}} = 7.4\text{ Hz}$, 3H), 6.93 (d, $^3J_{\text{HH}} = 7.7\text{ Hz}$, 3H), 6.74-6.64 (m, br, 9H), 6.27 (s, 6H), 3.49 (s, 9H), 3.31 (s, 9 H), 3.27-3.19 (m, 6H), 3.09-2.98 (m, 6H), 1.11 (d, $^3J_{\text{HH}} = 7.6\text{ Hz}$, 18H), 0.89 (d, $^3J_{\text{HH}} = 7.1\text{ Hz}$, 18H), 0.84 (d, $^3J_{\text{HH}} = 7.6\text{ Hz}$, 18H), 0.78 (d, $^3J_{\text{HH}} = 7.5\text{ Hz}$, 18H).

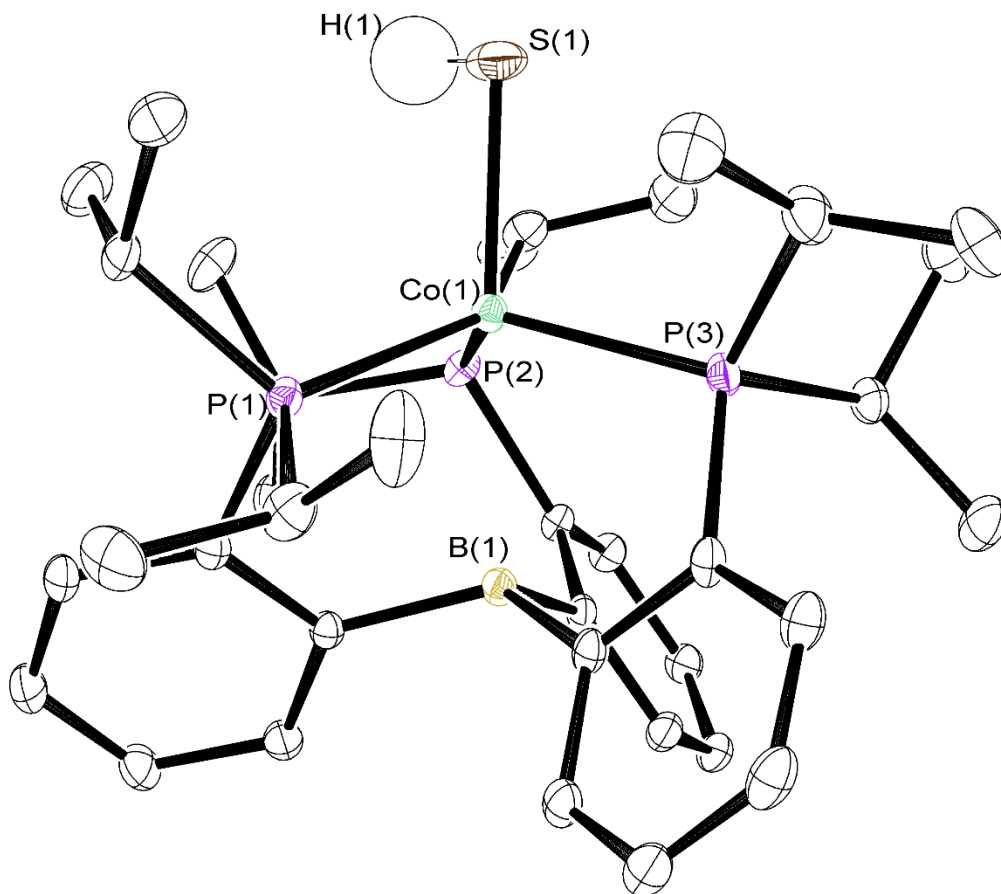


Figure A.1: ORTEP representation of $(P_3B)Co(SH)$. H atoms not attached to S omitted for clarity.

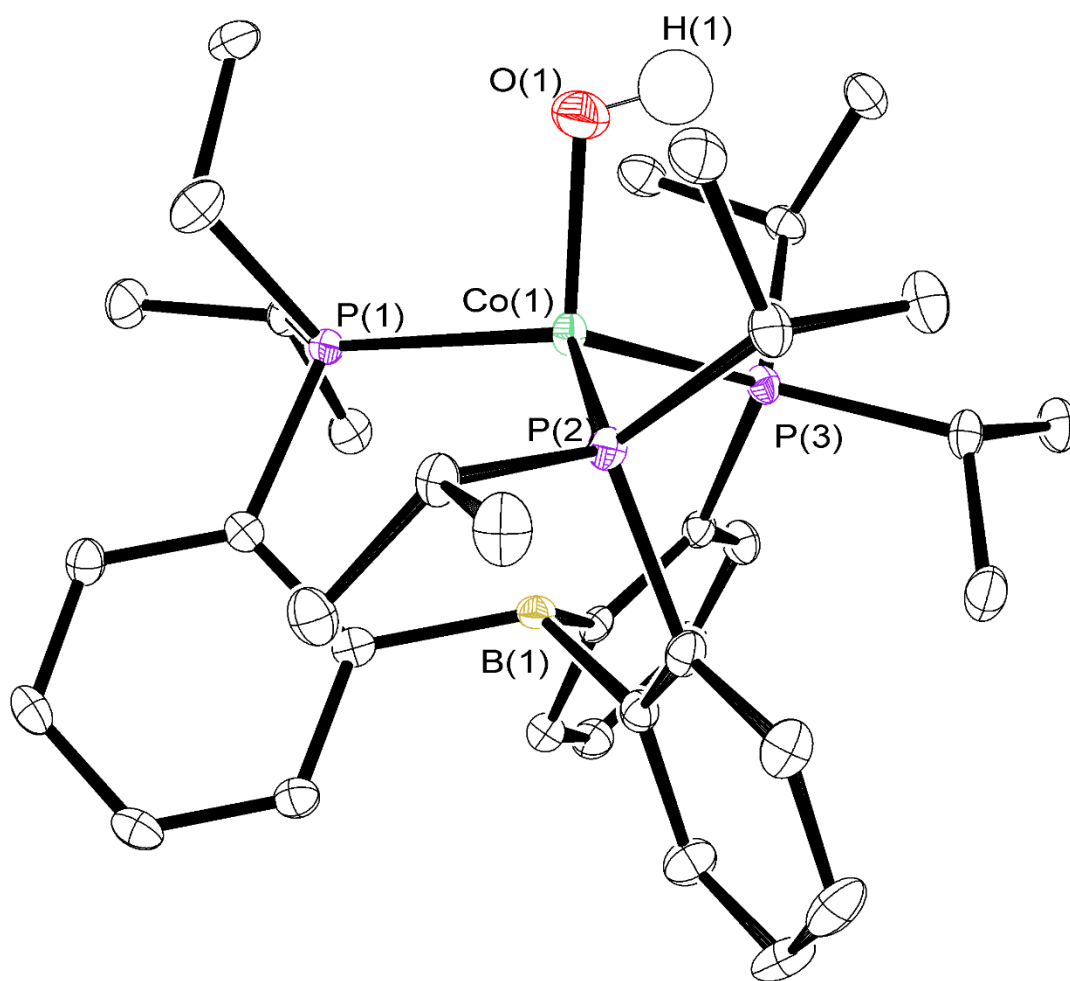


Figure A.2: ORTEP representation of (P₃B)Co(OH). H atoms not attached to O omitted for clarity.

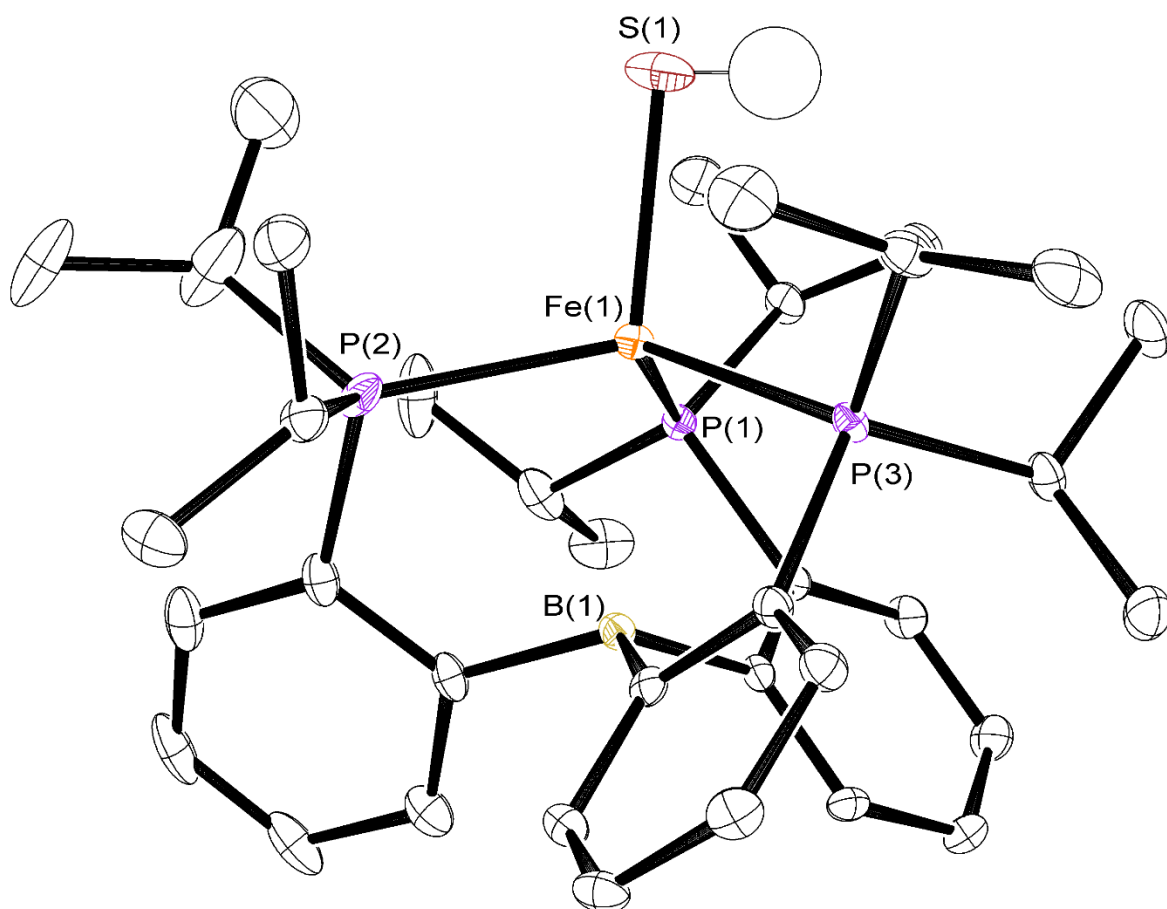


Figure A.3: ORTEP representation of $(P_3B)Fe(SH)$. H atoms not attached to S omitted for clarity.

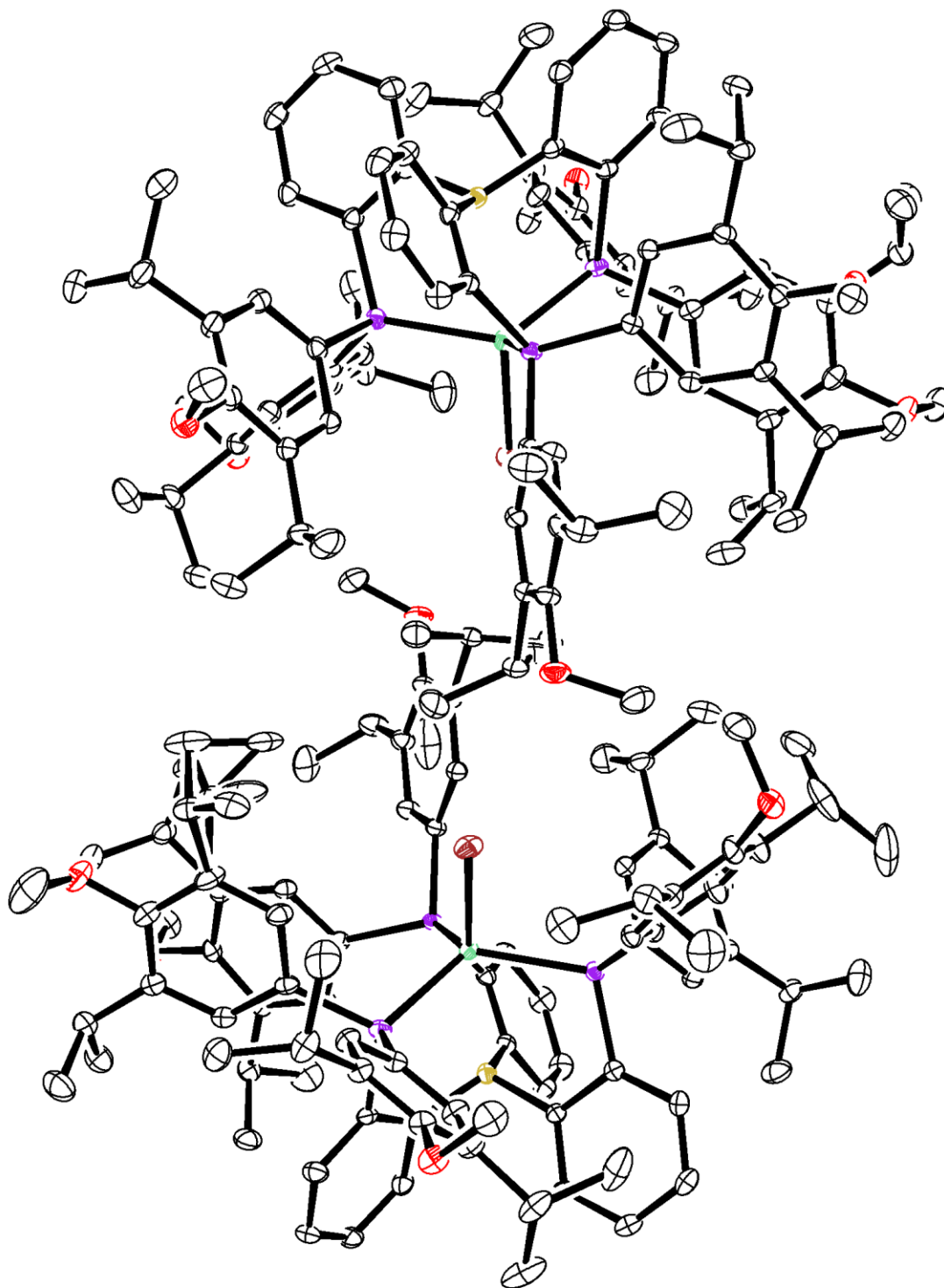


Figure A.4: ORTEP representation of $(\text{ArP}_3\text{B})\text{CoBr}$. H atoms omitted for clarity. C is shown in black, O is shown in red, P is shown in purple, B is shown in yellow, Br is shown in maroon and Co is shown in green.

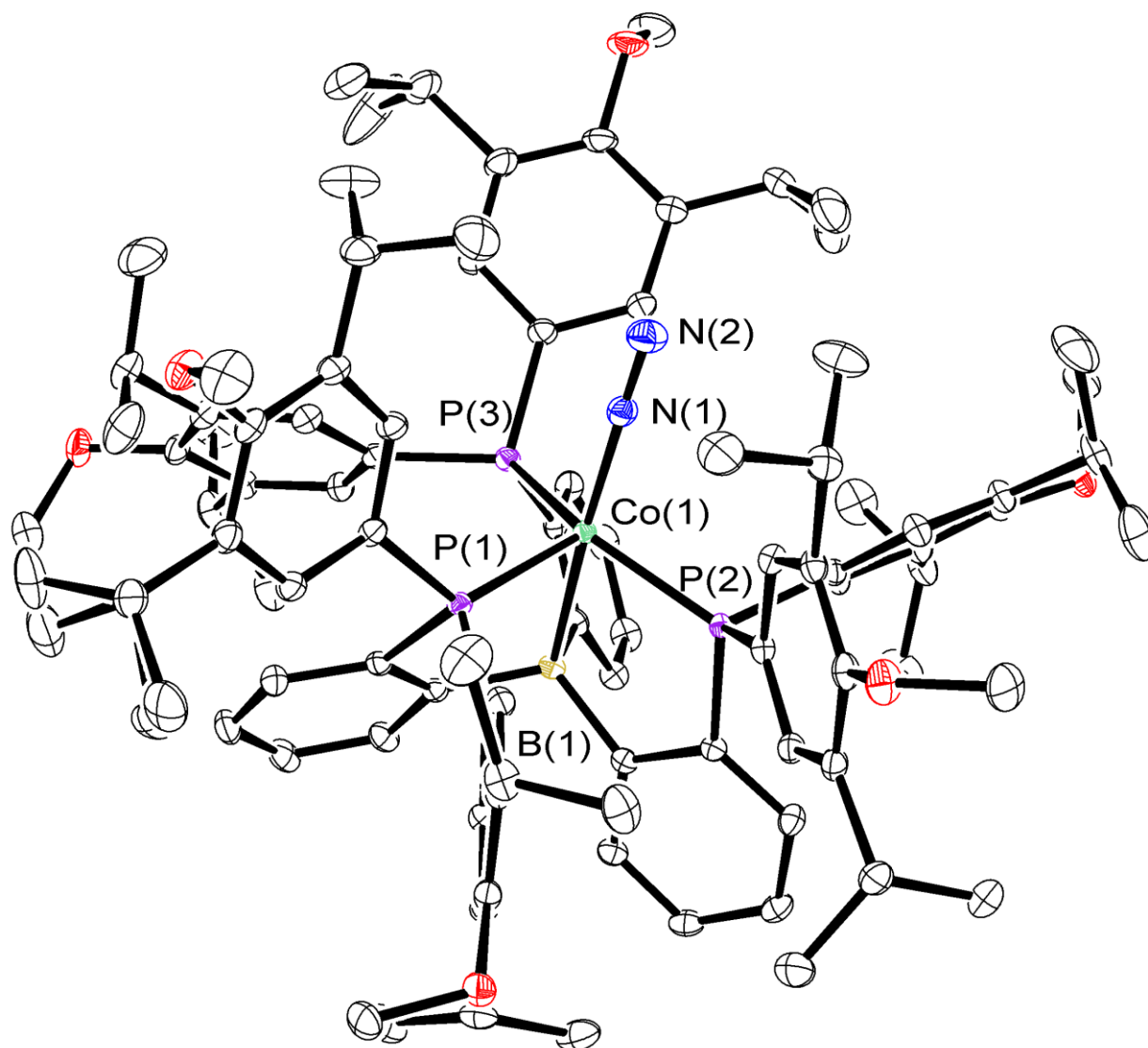


Figure A.5: ORTEP representation of $(\text{ArP}_3\text{B})\text{Co}(\text{N}_2)$. H atoms omitted for clarity.

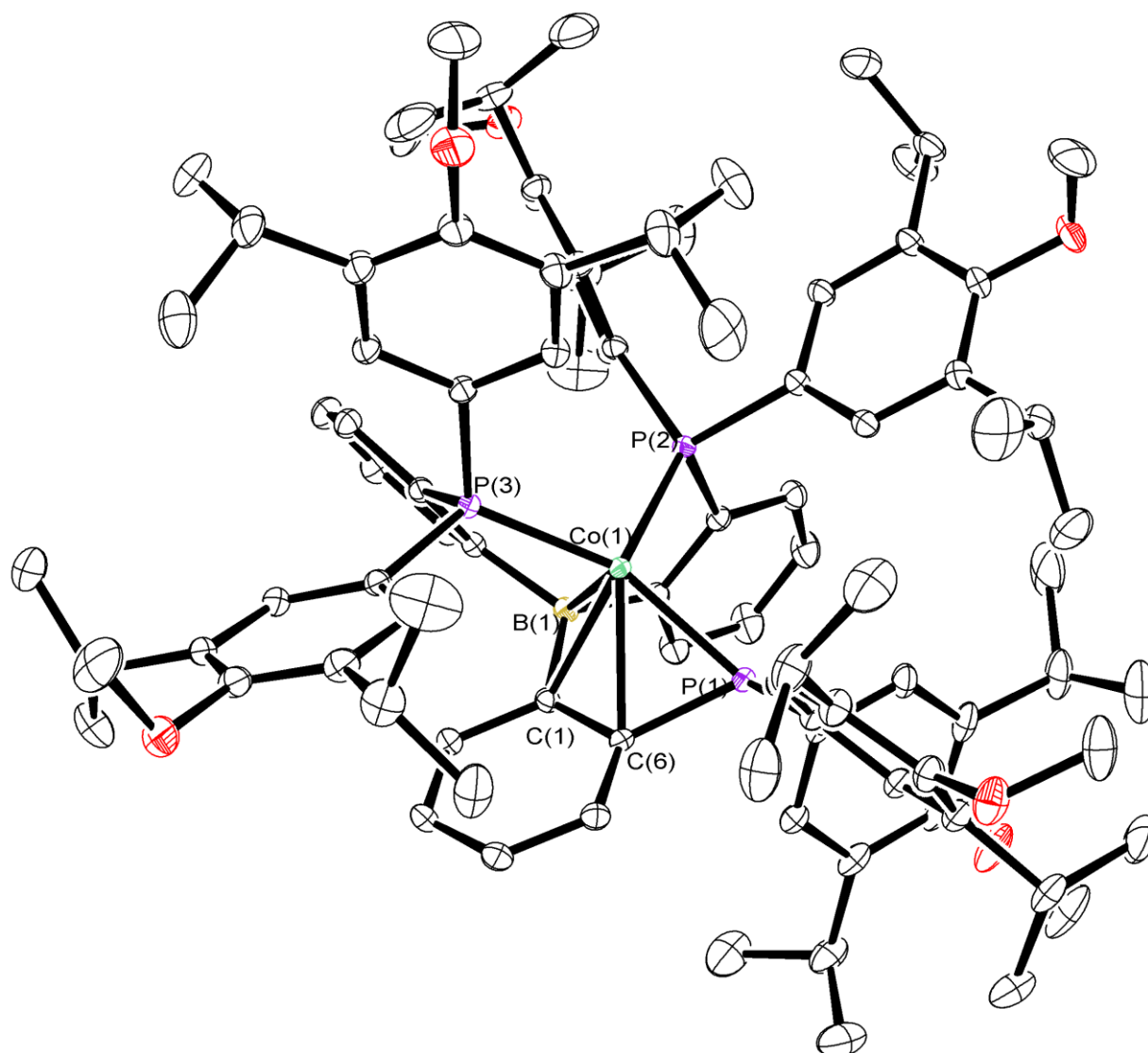


Figure A.6: ORTEP representation of $[(^{\text{Ar}}\text{P}_3\text{B})\text{Co}][\text{BAr}^{\text{F}}_{24}]$. H atoms and $[\text{BAr}^{\text{F}}_{24}]^-$ counterion omitted for clarity.

Table A.1: XRD experimental parameters for (P₃B)Fe(SH), (P₃B)Co(SH), (P₃B)Co(OH).

Compound	(P ₃ B)Fe(SH)	(P ₃ B)Co(SH)	(P ₃ B)Co(OH)
	C ₃₆ H ₅₅ BP ₃ SFe	C ₃₆ H ₅₅ BP ₃ SCo	C ₃₆ H ₅₅ BP ₃ OC ₃
Formula	679.43	682.51	666.45
Weight			
<i>T</i> (K)	100(2)K	100(2)K	100(2)K
λ (Å)	0.71073	0.71073	0.71073
Space Group	P-1	P-1	P-1
A	10.9198(8)	10.8507(7)	10.9419(10)
B	11.5109(8)	11.4883(8)	11.1785(11)
C	15.9173(11)	15.9445(10)	16.6401(16)
A	91.377(2)	91.442(4)	77.741(3)
B	96.073(3)	97.328(4)	78.211(3)
Γ	117.640(2)	117.446(4)	61.796(3)
Volume	1756.4(2)	1741.5(2)	1739.9(3)
Z	2	2	2
Density (calc)	1.285	1.302	1.272
R1, wr2	0.0688, 0.1427	0.056, 0.1418	0.0442, 0.1020

$$R1 = \sum ||F_o| - |F_c|| / \sum |F_o|, wR2 = \{ \sum [w(F_o^2 - F_c^2)^2] / \sum w(F_o^2)^2 \}^{1/2}$$

Table A.2: XRD experimental parameters for (^{Ar}P₃B)CoBr, (^{Ar}P₃B)Co(N₂), [(^{Ar}P₃B)Co][BAr^F₂₄]

Compound	(^{Ar} P ₃ B)CoBr	(^{Ar} P ₃ B)Co(N ₂)	[(^{Ar} P ₃ B)Co][BAr ^F ₂₄]
	C ₉₆ H ₁₂₆ BP ₃ BrO ₆ Co	C ₉₆ H ₁₂₆ BP ₃ N ₂ O ₆ Co	C ₁₂₈ H ₁₃₈ B ₂ F ₂₄ P ₃ O ₆ Co
Formula	1618.52	1566.63	2401.84
Weight			
<i>T</i> (K)	100(2)K	100(2)K	100(2)K
λ (Å)	0.71073	0.71073	0.71073
Space Group	P-1	P-1	P2 ₁ /c
<i>a</i>	14.9957(9)	14.9679(13)	24.607(3)
<i>b</i>	23.1625(13)	15.2834(15)	19.200(2)
<i>c</i>	28.2467(17)	22.363(2)	26.038(3)
α	66.575(3)	93.602(3)	90
β	85.815(3)	102.974(3)	97.372(3)
γ	79.983(3)	114.644(3)	+0
Volume	8865.2(9)	4459.8(7)	12200(3)
<i>Z</i>	4	2	4
Density (calc)	1.213	1.167	1.308
R1, wr2	0.0437, 0.1077	0.0416, 0.1008	0.0554, 0.1492

$$R1 = \sum ||F_o| - |F_c|| / \sum |F_o|, \text{ wr2} = \{ \sum [w(F_o^2 - F_c^2)^2] / \sum w(F_o^2)^2 \}^{1/2}$$

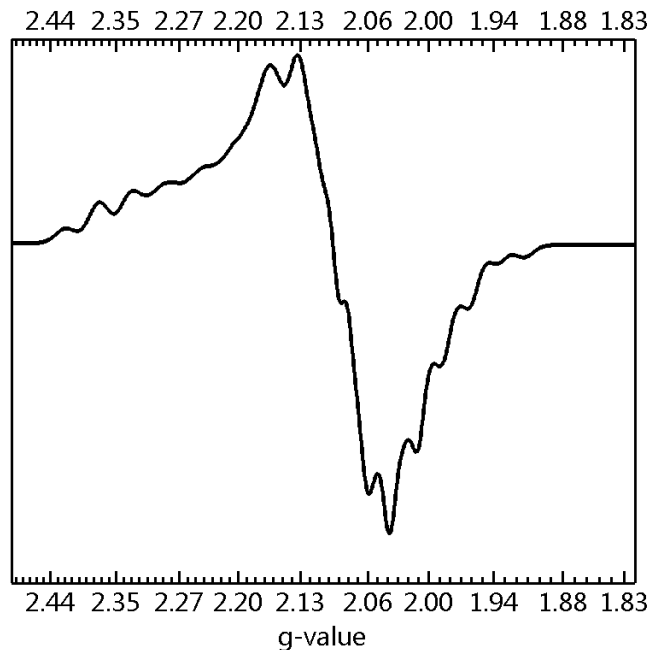


Figure A.7: CW X-band EPR spectrum of ($^{Ar}P_3B$)Co(N₂) in MeCy glass (77 K).

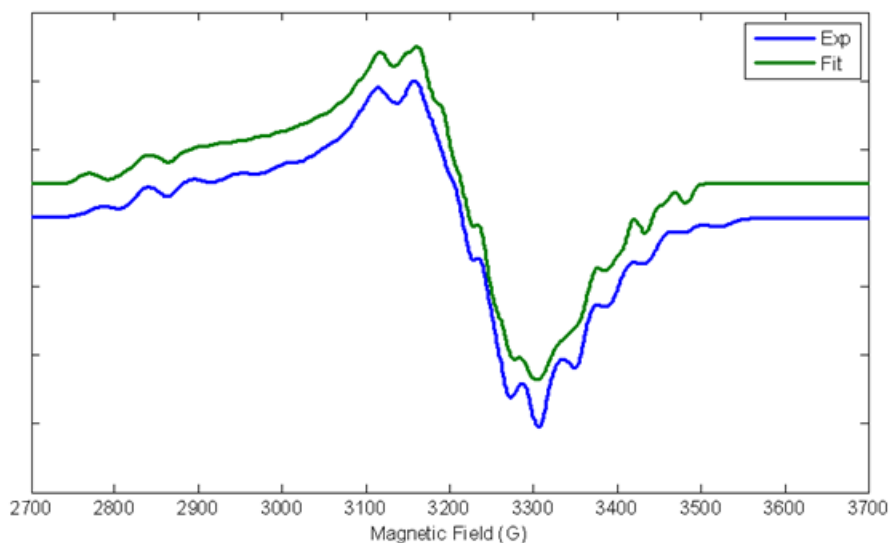


Figure A.8: CW X-band EPR spectrum of ($^{Ar}P_3B$)Co(N₂) in MeCy glass with simulation (77 K). Simulation parameters: g : [2.2413 2.0900 2.0375]; H_{Strain} : [68 173 48]; g_{Strain} : [0.0070 0.0020 0]; A_{Co} : [146, 38, 70], A_{P1} : [219, 66, 121], A_{P2} : [223, 72, 144], A_{P3} : [43, 127, 244]. MW-Freq = 9.431 GHz.

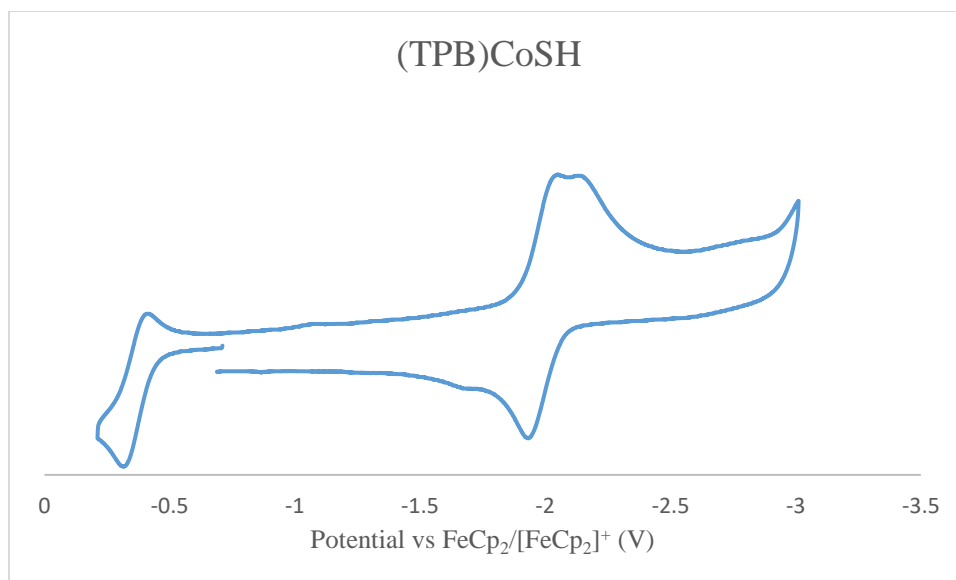


Figure A.9: Cyclic Voltammogram of (TPB)CoSH in THF (0.1 M [TBA][PF₆]). Scanning anodically from the open circuit potential.

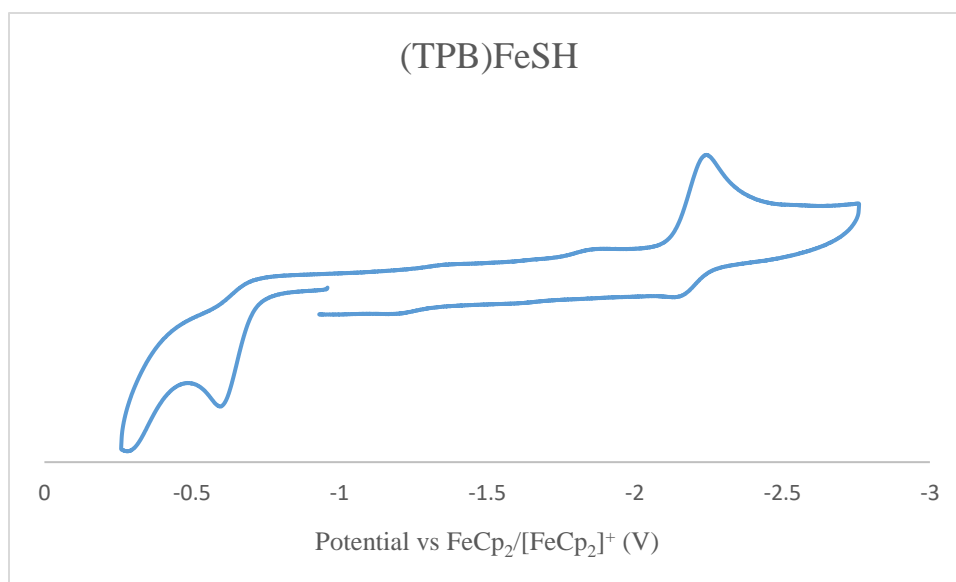


Figure A.10: Cyclic Voltammogram of (TPB)FeSH in THF (0.1 M [TBA][PF₆]). Scanning anodically from the open circuit potential.

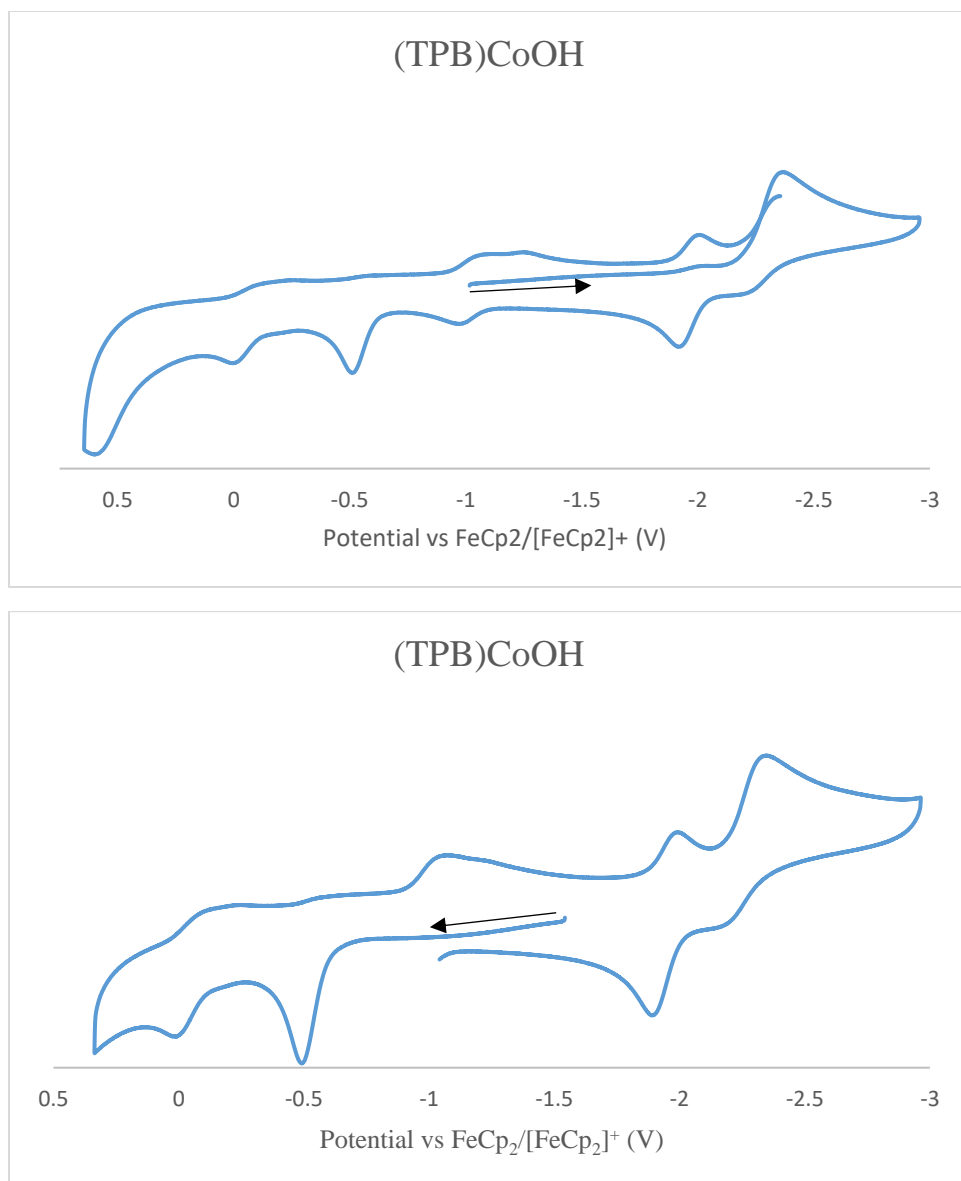


Figure A.11: Cyclic Voltammograms of (TPB)CoOH in THF (0.1 M [TBA][PF₆]). Top: Scanning cathodically from the open circuit potential. Bottom: Scanning anodically from the open circuit potential.

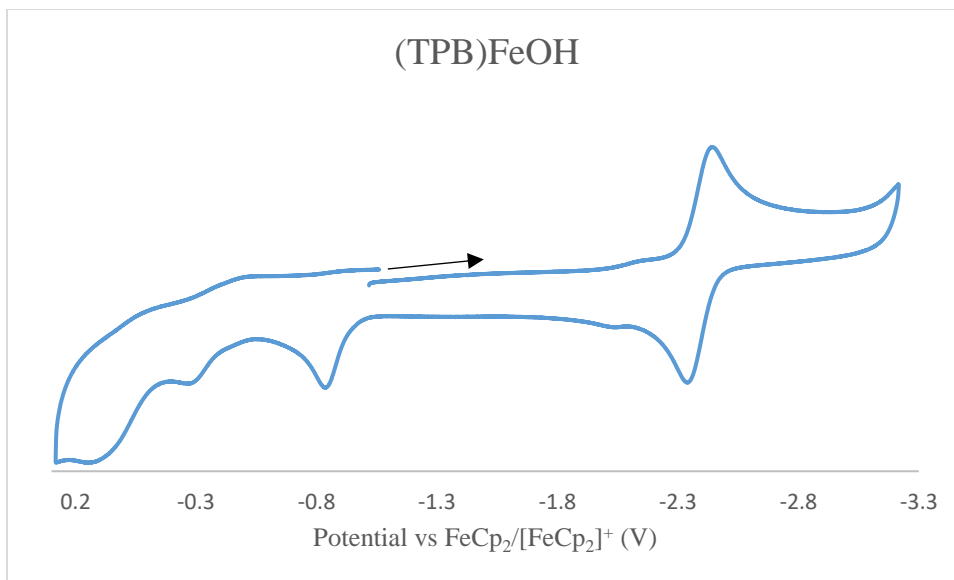


Figure A.12: Cyclic Voltammogram of (TPB)FeOH in THF (0.1 M [TBA][PF₆]).

References

- (1) Del Castillo, T. J.; Thompson, N. B.; Suess, D. L. M.; Ung, G.; Peters, J. C. *Inorg. Chem.* **2015**, *54*, 9256.
- (2) Anderson, J. S.; Moret, M.-E.; Peters, J. C. *J. Am. Chem. Soc.* **2013**, *135*, 534.
- (3) Meyer, W. E.; Amoroso, A. J.; Jaeger, M.; Le Bras, J.; Wong, W.-T.; Gladysz, J. A. *J. Organomet. Chem.* **2000**, *616*, 44.
- (4) Stoll, S.; Schweiger, A. *J. Magn. Reson.* **2006**, *178*, 42.
- (5) Sheldrik, G. M.; Universität Göttingen: Göttingen, Germany, 2000.